TAILORING THE SYNTHESIS AND THE FUNCTIONALIZATION OF NANOPARTICLES FOR NANOMEDICINE

Autor

Pelaz García, Beatriz

Director/es

Martínez de la Fuente, Jesús
Pino González de la Higuera, Pablo Alfonso del

FACULTAD DE CIENCIAS
Departamento de Química Orgánica
2012

CAESARAVGVSTANAE STVDIVM GENERALE CIVITATIS

INSTITUTO UNIVERSITARIO
DE INVESTIGACIÓN EN
NANOCIENCIA DE ARAGÓN

Tailoring the Synthesis and the Functionalization of Nanoparticles for Nanomedicine

Memoria que presenta Beatriz Pelaz García para optar al grado de doctor europeo

Zaragoza, Enero 2012

D. Jesús Martínez de la Fuente, Investigador ARAID del grupo de Nanodiagnóstico y Nanoterapia del Instituto de Nanociencia de Aragón de la Universidad de Zaragoza, y D. Pablo Alfonso del Pino González de la Higuera, Investigador del mismo grupo

INFORMAN:

Que Beatriz Pelaz García, licenciada en Química y Bioquímica, ha realizado en el grupo de Nanodiagnóstico y Nanoterapia del Instituto de Nanociencia de Aragón (INA) de la Universidad de Zaragoza bajo su dirección el trabajo descrito en la presente memoria, que lleva por título "Tailoring the Synthesis and Functionalization of Nanoparticles for Nanomedicine", y que presenta para optar al grado de Doctor Europeo.

Zaragoza, Enero de 2012

Fdo. Dr. Jesús Martínez de la Fuente

Fdo. Dr. Pablo A. del Pino
González de la Higuera

Acknowledgment

In the years of this research work, I benefited from the knowledge, encouragement and support of several people. At this stage, I would like to express my gratitude.

First of all, I would like to thank Dr. Jesús Martínez de la Fuente and Dr. Pablo del Pino. They gave me the opportunity to perform this challenging work under their supervision. I thank them for the consistent support allowing me the opportunity to find my own preferences and priorities.

I am thankful to Prof. Dr. Ricardo Ibarra for providing me with the facilities in the Instituto de Nanociencia de Aragón (INA) where I have achieved most of the results presented in this work. In this regard, I would also like to express my gratitude to Prof. Soledad Penadés & Prof. Manuel Martín-Lomas for providing with the facilities (Instituto de Investigaciones Químicas, Sevilla) where I started this work. I am also grateful to Prof. Asunción Fernández for financial support.

I would like to thanks Dr. Catherine Berry for her valuable help and work and the rest of the people who made my time in Glasgow easier, Mathis, Adam, Dimitris, Hakim,..; to Dr. Jose Montenegro, Prof Wolfgang Parak, Dr. Susana Carregal, Dr. Pilar Rivera and the rest of the guys for made of my time in Marburg unforgettable.

I want to thank to all the INA technicians for their technical support.

I want to thank to whole BioNanoSurf group, María, Sara P, Ester, Sara R. Carlos, Yulán, Jorge, Iñiguín, Scott, Jesús, Pablo y Vale, for our fruitful discussions (…). Their enthusiasm for Bio-Nano was always a motivation for me, and they get that every day was different from the others. I must say that working with them have been always like a prize. I will miss you guys.

I do not want forget the rest of the INA friends, Teito, Lauri, Rochilín, Carlos, Alfonso, Luis, Pilar, David, and the people who are now working far away, Abertito, Boada, Campana, Aida who left an incredible vacant (I will miss you too!).

I do not want to finish without thanking my friends from Sevilla, where my time was short but I got some good friends, Antonio, Macarena, Oli y Diego. Also, I want to remember the people from my old lab in Valladolid who guided my work when I started in a Laboratory, Prof. Espinet, Dr. Juan Casares, Dr. Gorka, Antonio, Bea, Dr. Nora, Dr. Cris, Dr. Javi, and Dr. Mónica who was always with me, since the very beginning.

Specially, I want to thank Pablo for all his sleepless nights, his unconditional help every day, and all the effort he put in this work, professionally and personally. I also want to thank Emma who brought happiness to my life in the worst thesis times.

Of course, I want to thank my friends and family for their unconditional support and patient. I am here because of you!!!

Thank you!

Objectives

The general aim of the present work is the development of nanomaterials for applications in biology and medicine. Unarguably, nanotechnology can provide with novel, or enhanced, devices and systems for the development of novel therapies and improved diagnosis tools.

This work focuses on engineered inorganic NPs which in fact, are hybrid nanomaterials composed of an inorganic core (*i.e.* superparamagnetic iron oxide and/or metallic gold) and an organic complex coating (*i.e.* amphiphilic chains, polymers, carbohydrates, proteins, peptides, fluorescent dyes, *etc.*). Importantly, the inorganic core provides the nanomaterial with physical properties related to their size (such as superparamagnetism or surface plasmons) whereas a multicomponent organic coating allows for improving the colloidal stability of the nanomaterials and tailoring for control over the interface of nanomaterials with biological systems.

To this end, the present work has been divided in two main parts:

Part I: core@shell iron oxide@gold NPs

The main aim of this part is the development of superparamagnetic nanocomposites which surface (metallic Au) prevents the oxidation and degradation of the superparamagnetic core (iron oxide) and furthermore, can be easily hybridized with an organic functional coating based on thiolated chains. The surface modifications addressed herein include: (i) molecules for surface passivation which will give to the nanocomposites stability in physiological media and (ii) biomolecules such as peptides and carbohydrates which will add biological activity. Once achieved the final hybridized nanocomposites, these nanocomposites will be evaluated in terms of their ability as (i) superparamagnetic materials, (ii) carriers to shuttle "drugs" into cells, and (iii) nanoheaters (hyperthermia agents).

Part II: Au Nanoprisms or NanoNachos (NNs)

In the second part of this work (and more significant in terms of results and length), the first objective is the development of a straightforward and new method to produce biocompatible NIR absorbing gold NPs which allows for tuning the shape and size of the NPs; thus, it is possible to control the optical properties of the material. Importantly, the NIR band of such NPs (*nanoheaters*) can be excited to produce heat very efficiently. NIR excitation of NPs is the most favorable scenario for biomedical applications; this is motivated for the suitable penetration depth that NIR radiation has in biological tissues; currently, NIR sources are widely used in multi-photon microscopy, photo-acoustic imaging or photothermal therapy. Herein, the potential of newly synthesized NIR absorbing NPs as photon-to-heat transducers will be evaluated both at macroscopic and molecular level.

Second, the stability, viability and internalization efficiency of newly synthesized nanoheaters, derivatized with molecules of biological relevance, will be addressed *in vitro*. Finally, the effect of laser irradiation will be evaluated at the single cell level and in areas containing thousands of cells; this studies allow for evaluation of the heating ability of NPs to impair cell viability and/or trigger changes in the cell-morphology.

Table of Contents

Section I : Fe_3O_4@Au NPs

Introduction

Chapter 1

Although the definition of nanomaterial is relatively broad and depends largely on the author and media where it is expressed, recently, the European Commission has defined it as "a natural, incidental or manufactured material containing particles, in an unbound state or as an aggregate or as an agglomerate and where, for 50% or more of the particles in the number size distribution, one or more external dimensions is in the size range 1 nm – 100 nm". Thus, the prefix *nano-* makes reference to at least one of the dimensions of any the material (or any of its constituents) being in the range of *ca.* 1 - 100×10^{-9} m. This broad definition covers a large diversity of materials, such as inorganic NPs (or nanocrystals), organic NPs, nanowires, thin films, surface coatings, *etc.* Furthermore, nanomaterials can be originated intentionally, *i.e.* engineered nanomaterials (the subject of this work), or unintentionally (*e.g.* wear of prosthesis,[1] fumes,[2] mechanical wear of materials, chemical powder waste, *etc.*[3]). Also recently, as for a general definition of nanosciences and nanotechnologies, European authorities have defined them as "approaches to research, development and manufacturing that aim to control the structure and behavior of matter at the level of atoms and molecules. Nanosciences offer the possibility of furthering our understanding of phenomena at the atomic level. Nanotechnologies make possible the development of materials and devices with novel properties, functions and performance". Interestingly, these definitions lack of any reference to the dimension of the materials at the nanoscale.

For the sake of clarity, it should be noted that this work is restricted to (i) engineered colloidal inorganic NPs (made of iron oxide and/or gold), (ii) some their fascinating properties (*e.g.* superparamagnetism, surface plasmons, radiation-to-heat transduction, *etc.*), and (iii) some of their uses in nanotechnology applied to medicine (such as interaction of NPs with cell cultures, hyperthermia, etc.)

Importantly, inorganic materials down to the nanoscale present very interesting and useful properties, such as intense fluorescence, surface plasmons, superparamagnetism, *etc.*, which do not show their bulk counterparts, or other organic NPs. Many efforts in the field of nanoscience have been devoted to evaluate the different parameters that determine these *nano* properties of NPs made of a variety of materials.[4] In general, most of the *nano* properties are determined by the spatial confinement of electrons, phonons, and electric fields around the particles as well as due to their large surface to volume ratio. When compared to bulk materials, larger proportions of constituent atoms or molecules lie at the surface of nanomaterials (Figure 1.1), leading to a large surface to volume ratio which can dictate their reactivity, hardness, as well as magnetic, catalytic, and opto-electronic properties. These *nano* properties have found a great deal of interest in many different fields, such as in electrochemistry, electrocatalysis, optics, electronics, analytical devices, energy devices, and in nanomedicine (diagnosis, drug delivery, imaging, treatment, theranostics, *etc.*).[5]

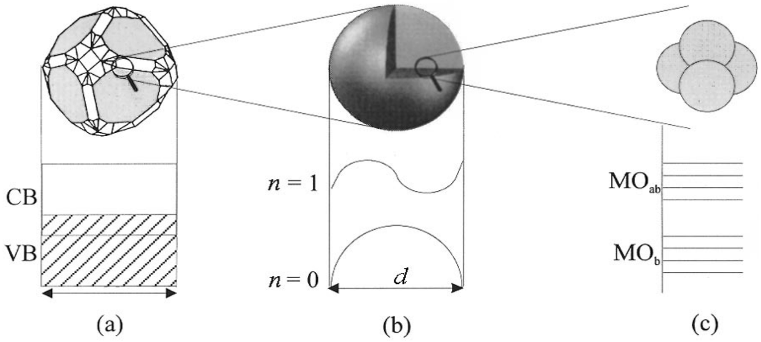

Figure 1.1. *Representation of the size-dependence of the orbital structure variations for a metal; a) typical metallic band structure for bulk metals; b) discrete electronic level where the particle diameter corresponds with the de Broglie wavelength; c) bonding and antibonding molecular orbital, occupied by electrons localized in bonds. Adapted from Schmid et al.*[6]

Inorganic NPs (or nanocrystals) can be composed of a variety of materials, such as noble metals (*e.g.* Au,[7] Ag,[8] Pt,[9,10] Pd,[11], *etc.*), metals (*e.g.* Rh,[12] Ir,[13] Ru,[14] *etc.*), semiconductors (*e.g.* CdSe, CdS, ZnS,[7,15] TiO_2,[16] PbS,[17] InP,[17] Si,[18] *etc.*), magnetic compounds (*e.g.* Fe_3O_4,[19] Co,[20] $CoFe_2O_4$,[21] FePt,[11] CoPt,[22] *etc.*) and many possible combinations of the materials aforementioned (core@shell NPs and other nanocomposites).[23]

The term "inorganic NP" makes reference to the nature of the main component of the material. However, there are not "bare" inorganic NPs, at least colloidally stable, as they require a coating to prevent irreversible agglomeration due to van der Waals attraction inter-NPs. The nature of the coating can be very diverse, ranging from small molecules (*e.g.* forming highly charged monolayers that prevent inter-NPs interactions *via* charge repulsion) to large polymers (that prevent inter-NPs interactions *via* steric hindrance). Also the interplay between the inorganic core, the coating and the exterior media can be quite complex; for instance, the coating can be ionically adsorbed or covalently coupled to the surface of the NP, and NPs suspended in biological fluids will normally adsorb organic molecules, typically proteins, to form the so called protein corona.[24] In summary, inorganic NPs are in fact hybrid nanomaterials formed by an inorganic core and a coating, intentionally designed (*e.g.* for improved colloidal stability or a particular function) or unintentionally derived from the interaction with the surrounding medium.

1.1. Formation of Nanocrystals

Over the past 30 years, the development of synthetic methods to produce nanocrystals with controlled composition, size, shape and structure (solid or hollow) have attracted a lot of interest; this trend is motivated by the enormous variety of applications where well-defined nanocrystals are keystone.

There are two main approaches to synthesize nanocrystals, *i.e.* the "top-down" using physical methods such laser ablation,[25] and the "bottom-up" which employs solution-phase colloidal chemistry. Typically, by using colloidal chemical synthetic methods, a variety of NPs sizes and shapes can be accessed synthetically enabling tailoring for specific purposes. In general, chemical synthetic methods to obtain nanocrystals from a precursor are based on its decomposition or its reduction to zero-valent atoms; in this context, the crystallization of these atoms to form a nanocrystal can be typically described by the model proposed by LaMer and coworkers.[26] In this model, the concentration of atoms steadily increases as the precursor is decomposed or reduced; then, once the concentration of atoms reaches a supersaturation state, the atoms start to aggregate to form small clusters or so-called nuclei (nucleation process). Following nucleation, clusters grow up to a critical size, where structural fluctuations become so energetically costly that the cluster becomes locked into a well-defined structure, the so called "seed". Importantly, the crystal structure of the seed (single-crystal, singly twinned, or multiply twinned structure) determines ultimately the shape and monodispersity of the final product(s). For instance, in the case that different seeds coexist, different nanocrystal (in shape and/or size) will result. Then, seeds will grow into nanocrystals of increasingly larger size until an equilibrium state is reached between the atoms on the surface of the nanocrystal and the atoms in the solution.[27] Alternatively to the atom-by-atom addition, the final nanocrystals can be formed *via* agglomeration of the nuclei and preformed nanocrystals.[28,29] Importantly, the shape of the final NPs is determined by a combinations of thermodynamic (*e.g.* temperature, reduction potential, *etc.*) and kinetic factors (*e.g.* reactant concentration, diffusion, solubility concentration rate, *etc.*), as well as the presence of capping agents. In principle, by finely tuning the reaction conditions (*i.e.* seeds structure), it is possible to access different shapes such as octahedral,[30] tetrahedra,[31] hexagonal plates,[32] nanorods,[33] triangular plates,[34] dendrites, [35] *etc.* (Figure 5.2). For more details in this matter, see an excellent review on the shape of metallic NPs by Xia and coworkers.[27]

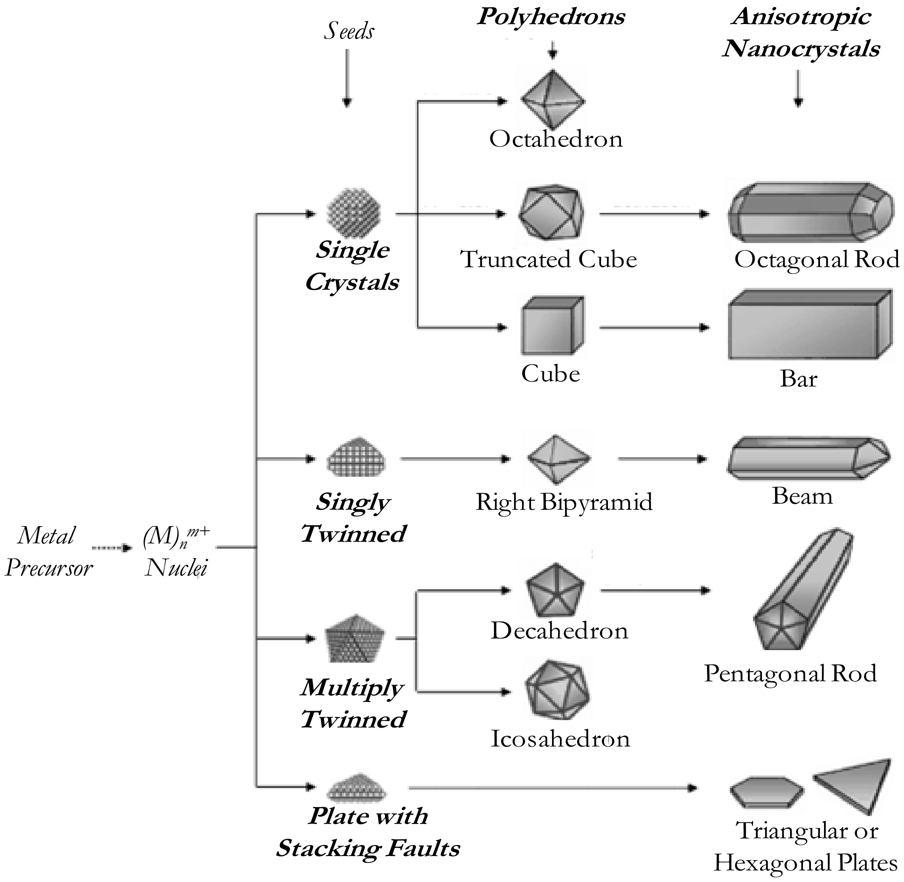

Figure 1.2. *Reaction pathways which lead to fcc metal nanocrystals of different shapes (adapted from Xia et al.[36]).*

1.2. Interfacing Nanomaterials & Biological Systems

In the last decade, nanoscience has grown to what appears to be one of the research areas of the most impact to our society.[37] There has been (maybe since the pioneering work of Alivisatos and coworkers in 1998 where for the first time nanocrystals were proposed as cellular probes) a widely extended interest for "mixing" NPs with living organisms and biomolecules.[38] This is motivated by two main reasons: (i) NPs size lays in the "right" range where most of bio-interactions occurs, and (ii) the highly useful properties of materials when reduced down to the nanoscale.[39] Recent progress in nanotechnology applied to medicine and biology, also called bionanotechnology or nanomedicine depending on the context, has spread the general optimism that this applied discipline can solve "all" the medical (therapy and diagnosis) and biology (sensing, limits of detection) issues.[40] However, many challenges must be overcome until nanomedicine or bionanotechnology becomes available for all and an actual breakthrough for our society.[41,42] Engineered nanomaterials have found in the bio-context a huge diversity of applications in fields such as sensing, imaging, therapy or diagnosis which is normally grouped together into a field called bionanotechnology (also nanomedicine).[39,43,44] Nanomaterials designed for their use in biological environments (cells, macromolecules, organic and inorganic molecules present in physiological media, etc.) possess a coating (surfactant) corona, typically of choice on the final synthetic product,[45] which ultimately determine their interaction with macromolecules such as nucleic acids, proteins, carbohydrates, and lipids.[46] These interactions at the nano-bio interface represent normally a complex scenario which greatly influence on the success of a particular engineered nanomaterial for a certain application (as a sensor, diagnostic tool, drug carrier or more complex multitask systems).[41,47] Therefore, in a bio-context, materials scientists have to ask themselves how both, a particular complex nanomaterial and their constituents (surfactants, precursors, macromolecules or organic polymers, etc.) interface with physiological environments that normally are quite different from the environment where the synthesis of the nanomaterials took place, *i.e.* polar or non-polar solvents with very particular attributes such as ionic strength, pH or presence of multivalent ions, salts or polymers, to name a few. For instance, synthesis of highly monodisperse inorganic nanocrystals made of metals (*e.g.* Au, FePt), metal oxides (*e.g.* ferrites, Fe oxides, ZnO) and semiconductor (*e.g.* CdSe, CdSe/ZnS, CdS, CdTe) are typically (preferably) done in organic solvents in the presence of capping agents containing aliphatic chains including alkyl phosphine oxides, alkyl phosphonic acids, alkyl phosphines or fatty acids.[45] In order to use nanocrystals made in organic solvents for bio-applications, they have to be transformed into water soluble materials as physiological media contains mainly water, among other constituents such as proteins, lipids, salts or multivalent ions. Over the past decade different approaches have been used for water-transfer of nanocrystals by *e.g.* ligand-exchange (exchanging aliphatic chains by hydrophilic containing molecules), silanization (growing a glass shell around the NPs) and polymer coating methods (intercalating amphiphilic polymers in the aliphatic shell of the NPs).[48,49] All these methods provide material scientists with the tools for designing, at the molecular level, the outermost shell of nanomaterials and therefore the bio-interface. The possibility of custom-made nanomaterials with a wide variety of chemical groups (neutral, positively or negatively charged) allows for tailoring the net charge of the nanomaterials as well as a well-defined surface charge-pattern.[50] The surface can be further modified by conjugation with biological molecules, such as peptides[51] or proteins (*e.g.* antibodies,[52] enzymes,[53] *etc.*), nucleic acids,[54] carbohydrates,[55] *etc.*, in order to interface the NPs with the environment and thus to tune their properties.[56] Independently of the synthetic route (in polar or non-polar solvent, inorganic or organic core material), shape, size, surface area, roughness, porosity or crystallinity (if applies), the charge and distribution of charges arising from different functional groups (either from the coating surfactants, attached biomolecules or the protein corona) play a critical role in the fate of nanomaterials for bio-applications; this is motivated because coulomb interactions (as well as hydrophobic/hydrophilic interactions) lead a nanomaterial to interact with macromolecules in the physiological milieu such proteins or carbohydrates, both in the media or in the cell (membrane receptors, chaperones, genetic material, etc.).[47] It is worth noting that when a NP is presented to a cell, what the cell sees is a patchwork made of the organic molecules (and corresponding functional groups) covering the NP which can be as originally designed or result of unspecific protein absorption.

Importantly, in the context of bioapplications, the physico-chemical properties of nanomaterials have to be critically evaluated as typically, they determine the suitability (potential application) of a particular nanomaterial for a defined purpose.[42,57] Most relevant physico-chemical properties, of nanomaterials in a defined medium (such as complete cell culture medium, body fluids, *in vivo*, etc.), are (i) a defined composition (*i.e.* inorganic core, organic layer, functional biomolecules attached, protein corona, etc.), (ii) dose for a given model, (ii) colloidal stability, purity, and inertness, (iv) shape and size (of the whole nanomaterial including organic coatings), and (v) charge of the nanomaterial.

1.3. Bioapplications of Nanomaterials

As previously stated, nanotechnology offers presently a variety of opportunities for biosciences and health. Nanotechnology can provide with novel or improved devices and systems that greatly contribute to the progress of our society. As the degree of control to fabricate such structures evolves, new applications based on these materials can be explored.[2] Photothermal therapy (PTT), photoacoustic imaging or surface enhanced resonance spectroscopy (SERS) are examples of applications where NPs such as nanorods,[3] hollow nanospheres[4] and nanostars,[5] among others, can act as transducers.

In the following, and as examples where nanotechnology is increasingly being explored, two important areas will be put into perspective, *i.e.* (i) cancer treatment by hyperthermia (or thermoablation) and (ii) superparamagnetic NPs as MRI contrast agents.

(i) Hyperthermia

The suitability of increased temperatures to achieve therapeutic gain has been known for centuries; where the earliest report is likely to have been in 3000 BC, known as the Egyptian Edwin Smith surgical papyrus.[58] Hippocrates (460 – 360 BC) already describes in one of his aphorisms "hot-irons, concerns higher temperatures, such as those used in cauterization". In the 19th and 20th centuries, researchers started to use artificial fever - generated by infection and toxins - and novel radiofrequency approaches as treatments based on increased temperature. Although at the end of the 19th century, technology was able to match the need of hyperthermia researchers regarding the use of radiation to heat tissue, a wider interest in hyperthermia had to wait until 1975, during the first international congress on hyperthermia in oncology (Washington, 1975). In recent years, hyperthermia appears to have gained renewed interest from the scientific community. This might well have been motivated by the latest progress in the generation and control of non-ionizing radiation and the capability of nanotechnology to deliver materials which can act as heat transducers (nanoheaters). The general consensus now is that hyperthermia is a very promising treatment which has remarkable biological effect in tumor cells *in vivo*; however, suitable heat delivery and control represents a challenge, both from the technical and physiological point of view.[59]

What stands for oncological hyperthermia? It is the use of heat to kill tumor cells or at least, make them more susceptible to be killed by other methods such as chemo- and/or radiotherapy. A more general definition of hyperthermia is "the elevation of temperature above the physiological level with the objective to achieve therapeutic gain".[59] Hyperthermia can kill cells directly; however, clinical results have shown that the combination of radiotherapy & hyperthermia and chemotherapy & hyperthermia (thermochemotherapy) translates into a substantial (not only additive) therapeutic improvement.[60-62] There are currently two main hyperthermia approaches for fighting cancer:

(i) Mild hyperthermia where the temperature (of the region to treat) is raised to 40 °C – 44 °C. Given that *in vivo* tumor cells are more vulnerable to heat than healthy cells, mild hyperthermia can be used to weaken tumor cells prior to radio- and/or chemotherapy. In addition, heat can be used to stimulate the immune response for non-specific immunotherapies.[63]

(ii) Thermal ablation (thermoblation) where temperature is raised above 46 °C and leads to tumor elimination via necrosis, coagulation or carbonization.[64]

Cancerous cells are not inherently more susceptible to damage by heat than healthy cells. With the exception of tumor cells of cancers that affect blood, bone marrow, and lymph nodes (hematological malignancies),[65] normal and tumor cells are equally susceptible to increased temperatures *in vitro*. In general, the thermal energy dose required for induction of cell death in cell cultures appears to be related to the amount of energy to produce protein denaturation; it ultimately affects the cell by damaging structures like cytoskeleton and membrane, and enzyme complexes for DNA synthesis and repair. [66] Therefore, the energy dose required should carry the cell above a threshold temperature; this temperature might slightly vary between cell lines and cell in different stages of the cell cycle. Another scenario applies however *in vivo* where tumor cells, in contrast to normal tissue, can be irreversibly damaged when exposed to temperatures between 40ºC and 44 °C; this is motivated by the characteristic physiology which most of types of tumors share, *i.e.* the vasculature of solid tumors is chaotic and the blood supply is therefore deficient, resulting in regions with hypoxia and low pH which ultimately makes cells more susceptible to hyperthermia treatment. This is normally not the case in non-tumor tissues which remain unaffected even after an exposure time of 1 h to an environment temperature of 44°C.[67] Only nervous tissues seem to be more temperature-sensitive.[68]

It has been demonstrated that after hyperthermia treatment, a class of proteins called heat-shock proteins (HSPs) are expressed on the surface of tumor cells but not on the corresponding normal tissues.[69,70] HSPs mediate the stability of tumor cells following environmental stress, and they are commonly regarded as chaperones assisting protein folding and translocation; however, HSPs can also serve as cytokines that can stimulate dendritic cells and macrophages to produce proinflammatory cytokines and chemokines. Tumor cells expressing on their surface HSPs are more susceptible to lysis by natural killer cells. Moreover, the release of HSPs following necrotic cell death, but no apoptotic death, stimulates macrophages and dendritic cells to produce cytokines and therefore, activate antigen-presenting cells.[71] There is direct evidence for important role of releasable HSPs in the initiation of antitumor immunity.[72]

As previously mentioned hyperthermia works very well as an adjuvant for the more classical radio- and chemotherapy. Hyperthermia has been proven to drastically enhance the suitability of radiotherapy.[60] Two main mechanisms are responsible for this more than additive enhancement. First, hyperthermia has been reported to increase blood flow into the tumor; thus, an improved tissue oxygenation can prevent the hypoxic problem and radio-sensitize the hypoxic area.[73] How persistent is the improved tissue oxygenation is a controversial matter.[74] Second, it has been demonstrated that also *in vitro*, where the hypoxic problem do not applies, hyperthermia foster radiation effects as well. This may well be result of destructive interference of hyperthermia with DNA repair after radiotherapy, probably by damaging cellular proteins.[75] Overall hyperthermia seems to palliate radioresistance of tumors and to greatly improve the killing efficiency of ionizing radiation (without entering in "forbidden" radiation doses) by affecting the DNA repair mechanism.[76]

On the other hand, and despite the lack of interaction of some typical antitumor drugs and heat, the suitability of hyperthermia to enhance the cytotoxicity of many chemotherapeutic agents has been widely confirmed *in vivo*.[62] Mechanisms for the thermal enhancement include increased rate constants of alkylation, increased drug uptake and inhibition of repair of drug-induced lethal or sublethal damage. Studies on drug-heat sequence show, in general, that drugs administered immediately before hyperthermia is most effective.[77]

Modalities of classical oncological hyperthermia may be classified according to the nature of the applicator, from the whole body to the tumor cell level (Table 1.1). There are three main heat sources; contact with externally heated liquid, contactless applicator (*e.g.* ultrasound, microwave radiofrequency and infrared devices), and inserted heat sources (e.g. antennas, laser fibers, probes and mediators). Nevertheless, none of these devices is able to destroy selectively deeply situated cancer, without destroying the surrounding normal tissues. This fact has led to the development of technologies based on inserted heat sources.[78]

Nanotechnology can offer a wide variety of nanomaterials with great potential as "ideal" nanoheaters. As the degree of control to fabricate "smart" nanomaterials evolves, the application of nanotechnology to medicine (nanomedicine) can find more applications where it can have a great impact. This is the case of hyperthermia field where superparamagnetic NPs as well as plasmonic NPs are currently investigated as nanoheaters or nanotransducers which can be remotely activated by radiation which do not (or minimally) interact with physiological tissue and fluids. In addition, the design of complex functional nanomaterials has undergone an extraordinary development in recent years; this has provided us with complex nanomaterials not only with extraordinary physical properties but also with a vast array of molecules with of biological relevance such as antibodies, genetic material or tumoral markers of the most diverse nature; these molecules can be also thought as functional surfactants.

Nanotechnology provide us with the opportunity of achieving smart nanostructures with complex functionalities including local heating, targeting (passive or active), improved uptake, delivery, biocompatibility, suitable biodistribution or non-immunogenicity, to name a few. The use of local heating by bio-active NPs can drastically reduce the side effects (cell toxicity and/or tissue radiation damage) of traditional treatments when used in combined therapies.

There is also another approach to destroy tumors by NP-based heating, *i.e.* increasing the temperature above 46 °C and therefore, causing cell death by necrosis; in contrast to apoptosis (the other known cellular death) necrosis occurs when cells suffer an irreversible damage.

Hyperthermia Strategy		Overheated Region			
		Whole-body	Organ	Tumor	Cell
Hot source		Hot bath, air, wax, blanket, suits, etc.	Isolated organ perfusion (e.g. liver)	Direct injection of hot water (96ºC)	
Ultrasound applicator				Scanned focused ultrasound monitored by MRI	
Electro-magnetic Source	Radiative applicator	Water-filtrated infrared exposure		Interstitial laser photocoagulation (direct insertion of laser fiber)	
	Capacitive applicator	Radio-frequency capacitance hyperthermia through two electrodes coupled at the body surface	Focalized microwave beam through one single element applicator coupled at the body surface	RF-antennas based on unipolar or bipolar interstitial electrodes or interstitial microwave antennas	
	Inductive applicator (magnetic hyperthermia)			Magnetic interstitial implants hyperthermia Arterial embolization hyperthermia or direct injection hyperthermia of magnetic nanoparticles	Intracellular hyperthermia through ligand-mediates magnetic particle (i.v. administration)
	NIR light source			Gold nanoparticles[79,80] (Subject of Chapter 8)	

Table 1.1. *Typical hyperthermia strategies in oncology (Adapted from Mornet).*[78]

(ii) Superparamagnetic NPs as MRI contrast agents (T_2-agents)

Magnetic Resonance Imaging (MRI) is an imaging technique based on the contrast given by the magnetic relaxation processes of the nuclear spins of hydrogen atoms (^1H) in water and fat, the major hydrogen containing components of the human body. When the nuclear spins are exposed to an external magnetic field gradient (field amplitude B_0 of values up to 2T in clinical MRI systems), these will align parallel to the applied field (Z axis), giving rise to a net magnetic moment (m in Figure 1.3). Then, the ^1H can be excited with a resonant radio frequency (RF) transverse pulse which will bring the net magnetization to the plane perpendicular to the applied field, where it will rotate about the Z axis at a frequency equal to the frequency of the photon which would cause a transition between the two energy levels of the spin (the Larmor frequency that for ^1H is 42.58 MHz/T); in addition to the rotation, the net magnetization starts to dephase because each of the spin packets making it up is experiencing a slightly different magnetic field and rotates at its own Larmor frequency. The recovery of net magnetization to the equilibrium takes place via two different relaxation mechanisms which occur simultaneously: (i) the longitudinal (or spin-lattice) relaxation process (T_1) or in other words, the recovery of the net magnetic moment along the Z axis, and (ii) the transverse (or spin-spin) relaxation process (T_2) accounting for the loss of signal in the perpendicular plane (Figure 1.3); T_1 and T_2 are normally expressed in terms of the longitudinal r_1 or transverse r_2 relaxivities, their corresponding inverses respectively. Figure 1.4 shows schematically the typical relaxation times of various tissues in the human body at field amplitude of 1.5 T.

It should be noted that it is the gradient in the magnetic field that causes different regions (with their corresponding ^1H) to experience a unique magnetic field; ultimately, this makes nuclear spins (^1H) in different regions to relax differently and allow for imaging their positions.

Contrast agents can be used to improve the visibility (contrast) of internal body structures; historically, the most commonly used compounds for contrast enhancement are based on Gadolinium (III) chelates (Gd-complex). These contrast agents (paramagnetic) typically work by shortening the relaxation T_1 of ^1H in their vicinity (they also shorten T_2).

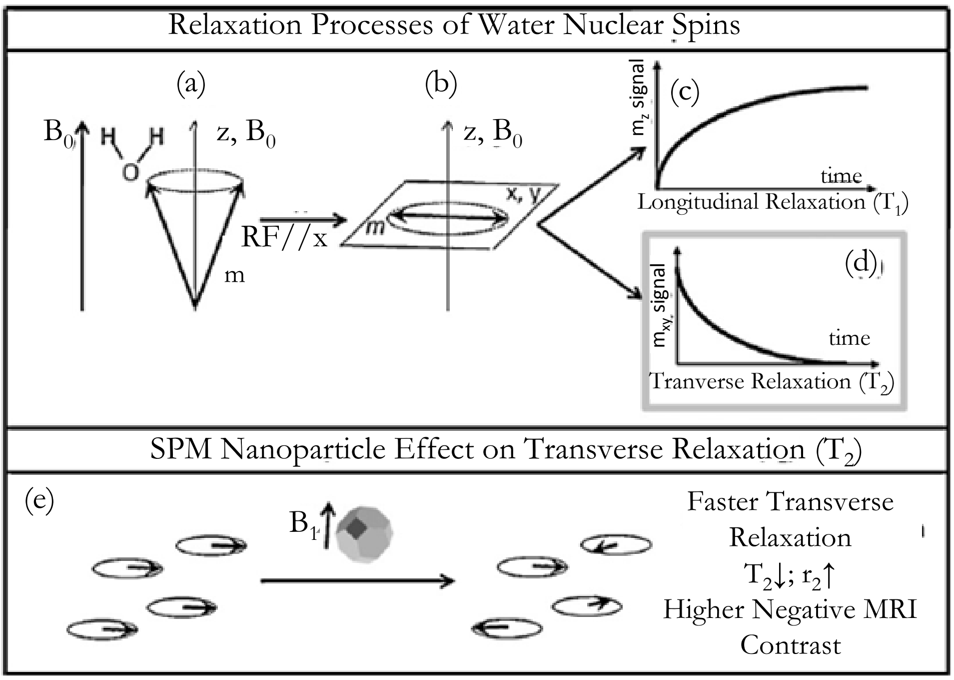

Figure 1.3. *Scheme of magnetic resonance (MR) principle and the role of magnetic nanoparticles as contrast agents. Above: (a) net magnetization (m) of* ^{1}H *rotates around the direction of the applied external magnetic field (*B_0*); (b) upon application of a resonant RF pulse, m begins precessing perpendicularly to* B_0*; (c) m relaxes back to its original equilibrium states through longitudinal (*T_1*) and (d) transverse (*T_2*) modes; (e) in the presence of magnetic nanoparticles, the spins of* ^{1}H *start precessing inhomogeneously under the additional effect of the local dipolar field (*B_1*) originated by the nanoparticles. Consequently they relax faster and induce a strong MRI signal, which produces strong MR contrast effects. Adapted from Figuerola et al.*[81]

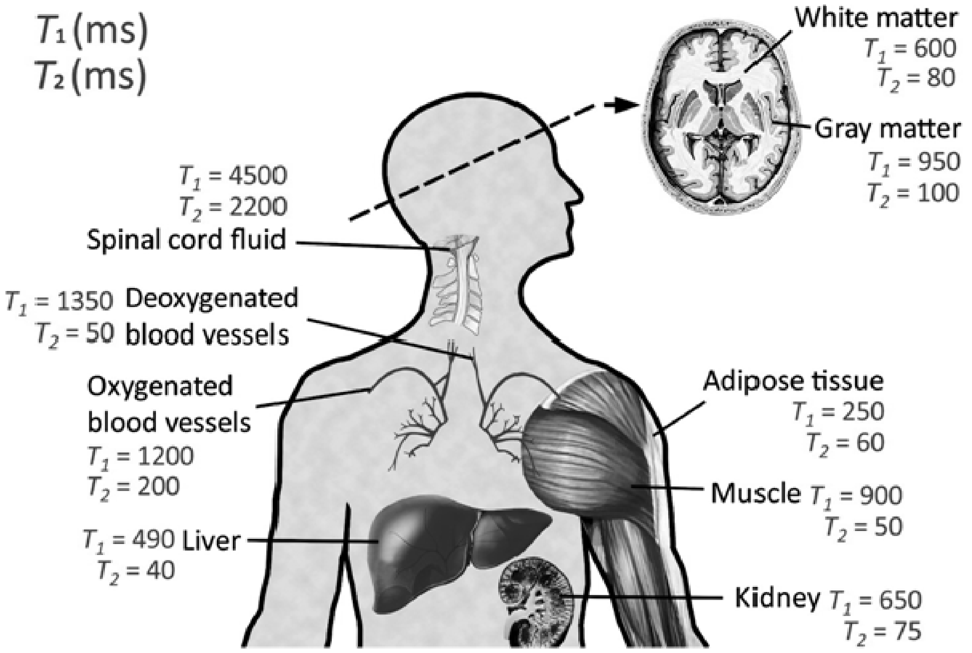

Figure 1.4. *Approximate values of the two relaxation time constants (*T_1 *and* T_2*) of various tissues in the human body at field amplitude of 1.5 T. Reproduced from Mahmoudi et al.*[82]

More recently, iron oxide NPs have gained attention as T_2-weighted MRI contrast agents.[82] The presence of SPM NPs in organs or tissues creates an additional magnetic field (B_1) which induces local field inhomogeneities that significantly increase the speed of proton transverse relaxation (decrease of T_2), leading to a negative contrast or a darkening of the image. This is why magnetic nanoparticles such as iron oxide are predominantly considered T_2-contrast agents.

Most used MRI agents are gadolinium based, but due to the toxicity of heavy metal ions, this must be applied in the form of ionic complexes with chelating ligands, which are less toxic. Indeed, human biochemistry is not based in gadolinium. For this, this kind of MRI agents are being substituted by others such as iron oxide nanoparticles.[83]

Some relevant parameters for common contrast agents are given in the following Table 1.2.

MR contrast agent	**Main use**	**Molecular weight or size**	**Relaxativity($mM^{-1}s^{-1}$)**
Gd-DTPA	T_1-agents	0.6 kDa	R_1= 3.7
Dextran-Gd-DTPA	T_1-agents	75 kDa	R_1=11
Resovist® (Carboxi-dextran SPIO SHU-555)	T_2-agents	62 nm	R_1=12;R_2=188(0.94 T)
Endorem® (Dextran SPIO AMI-25)	T_2-agents	58 nm	R_1=24;R_2=107(0.47 T)
Feridex® (Dextran USPIO MION 46L)	T_2-agents	18-024 nm	R_1=16;R_2=35(0.47 T)
Sinerem® (Dextran SPIO)	T_2-agents	17-20 nm	R_1=23;R_2=53(0.47 T)
Fe3O4@Au core/shell	T_2-agents	120 nm	R_2=465(1.5 T)(Halas, AdvFucntMat093901)
Fe3O4@Au core/shell	T_2-agents	7.5 nm	R_1=10.3;R_2=90.9(0.47 T)

Table 1.2. *T_1 and T_2 contrast agents and their characteristics (adapted from Mornet et. al.).*[78]

REFERENCES

(1) Papageorgiou, I.; Brown, C.; Schins, R.; Singh, S.; Newson, R.; Davis, S.; Fisher, J.; Ingham, E.; Case, C. P.: The effect of nano- and micron-sized particles of cobalt–chromium alloy on human fibroblasts in vitro. *Biomaterials* **2007**, *28*, 2946-2958.

(2) Balas, F.; Arruebo, M.; Urrutia, J.; Santamaria, J.: Reported nanosafety practices in research laboratories worldwide. *Nature Nanotechnology* **2010**, *5*, 93-96.

(3) Gottschalk, F.; Nowack, B.: The release of engineered nanomaterials to the environment. *Journal of Environmental Monitoring* **2011**, *13*, 1145-1155.

(4) Sajanlal, P. R.; Sreeprasad, T. S.; Samal, A. K.; Pradeep, T.: Anisotropic nanomaterials: structure, growth, assembly, and functions. *Nano Reviews* **2011**, *2*.

(5) Peng, X. G.: Band Gap and Composition Engineering on a Nanocrystal (BCEN) in Solution. *Accounts of Chemical Research* **2010**, *43*, 1387-1395.

(6) Schmid, G.; Bäumle, M.; Geerkens, M.; Heim, I.; Osemann, C.; Sawitowski, T.: Current and future applications of nanoclusters. *Chemical Society Reviews* **1999**, *28*, 179-185.

(7) Boisselier, E.; Astruc, D.: Gold nanoparticles in nanomedicine: preparations, imaging, diagnostics, therapies and toxicity. *Chemical Society Reviews* **2009**, *38*, 1759-1782.

(8) Podsiadlo, P.; Paternel, S.; Rouillard, J. M.; Zhang, Z.; Lee, J.; Lee, J. W.; Gulari, E.; Kotov, N. A.: Layer-by-layer assembly of nacre-like nanostructured composites with antimicrobial properties. *Langmuir* **2005**, *21*, 11915-11921.

(9) Chiu, C. Y.; Li, Y. J.; Ruan, L. Y.; Ye, X. C.; Murray, C. B.; Huang, Y.: Platinum nanocrystals selectively shaped using facet-specific peptide sequences. *Nature Chemistry* **2011**, *3*, 393-399.

(10) Pankhurst, Q. A.; Thanh, N. K. T.; Jones, S. K.; Dobson, J.: Progress in applications of magnetic nanoparticles in biomedicine. *Journal of Physics D-Applied Physics* **2009**, *42*.

(11) Ung, D.; Tung, L. D.; Caruntu, G.; Delaportas, D.; Alexandrou, I.; Prior, I. A.; Thanh, N. T. K.: Variant shape growth of nanoparticles of metallic Fe-Pt, Fe-Pd and Fe-Pt-Pd alloys. *CrystEngComm* **2009**, *11*, 1309-1316.

(12) Biacchi, A. J.; Schaak, R. E.: The Solvent Matters: Kinetic versus Thermodynamic Shape Control in the Polyol Synthesis of Rhodium Nanoparticles. *Acs Nano* **2011**, *5*, 8089-8099.

(13) Rueping, M.; Koenigs, R. M.; Borrmann, R.; Zoller, J.; Weirich, T. E.; Mayer, J.: Size-Selective, Stabilizer-Free, Hydrogenolytic Synthesis of Iridium Nanoparticles Supported on Carbon Nanotubes. *Chemistry of Materials* **2011**, *23*, 2008-2010.

(14) Salas, G.; Podgorsek, A.; Campbell, P. S.; Santini, C. C.; Padua, A. A. H.; Gomes, M. F. C.; Philippot, K.; Chaudret, B.; Turmine, M.: Ruthenium nanoparticles in ionic liquids: structural and stability effects of polar solutes. *Physical Chemistry Chemical Physics* **2011**, *13*, 13527-13536.

(15) Jamieson, T.; Bakhshi, R.; Petrova, D.; Pocock, R.; Imani, M.; Seifalian, A. M.: Biological applications of quantum dots. *Biomaterials* **2007**, *28*, 4717-4732.

(16) Drbohlavova, J.; Adam, V.; Kizek, R.; Hubalek, J.: Quantum dots - characterization, preparation and usage in biological systems. *International Journal of Molecular Sciences* **2009**, *10*, 656-673.

(17) Rogach, A. L.; Eychmüller, A.; Hickey, S. G.; Kershaw, S. V.: Infrared-emitting colloidal nanocrystals: Synthesis, assembly, spectroscopy, and applications. *Small* **2007**, *3*, 536-557.

(18) O'Farrell, N.; Houlton, A.; Horrocks, B. R.: Silicon nanoparticles: applications in cell biology and medicine. *International journal of nanomedicine* **2006**, *1*, 451-472.

(19) Salado, J.; Insausti, M.; Lezama, L.; de Muro, I. G.; Goikolea, E.; Rojo, T.: Preparation and Characterization of Monodisperse Fe(3)O(4) Nanoparticles: An Electron Magnetic Resonance Study. *Chemistry of Materials* **2011**, *23*, 2879-2885.

(20) Wen, T. L.; Krishnan, K. M.: Cobalt-based magnetic nanocomposites: fabrication, fundamentals and applications. *Journal of Physics D-Applied Physics* **2011**, *44*.

(21) Lacroix, L. M.; Malaki, R. B.; Carrey, J.; Lachaize, S.; Respaud, M.; Goya, G. F.; Chaudret, B.: Magnetic hyperthermia in single-domain monodisperse FeCo nanoparticles: Evidences for Stoner-Wohlfarth behavior and large losses. *Journal of Applied Physics* **2009**, *105*.

(22) Qin, W. Q.; Yang, C. R.; Ma, X. H.; Lai, S. S.: Selective synthesis and characterization of metallic cobalt, cobalt/platinum, and platinum microspheres. *Journal of Alloys and Compounds* **2011**, *509*, 338-342.

(23) Thanh, N. T. K.; Green, L. A. W.: Functionalisation of nanoparticles for biomedical applications. *Nano Today* **2010**, *5*, 213-230.

(24) Cedervall, T.; Lynch, I.; Lindman, S.; Berggård, T.; Thulin, E.; Nilsson, H.; Dawson, K. A.; Linse, S.: Understanding the nanoparticle–protein corona using methods to quantify exchange rates and affinities of proteins for nanoparticles. *Proc. Natl. Acad. Sci. U. S. A.* **2007**, *104*, 2050-2055.

(25) Barcikowski, S.; Mafune, F.: Trends and Current Topics in the Field of Laser Ablation and Nanoparticle Generation in Liquids. *J. Phys. Chem. C* **2011**, *115*, 4985-4985.

(26) LaMer, V. K.; Dinegar, R. H.: Theory, Production and Mechanism of Formation of Monodispersed Hydrosols. *Journal of the American Chemical Society* **1950**, *72*, 4847-4854.

(27) Xia, Y. N.; Xiong, Y. J.; Lim, B.; Skrabalak, S. E.: Shape-Controlled Synthesis of Metal Nanocrystals: Simple Chemistry Meets Complex Physics? *Angewandte Chemie-International Edition* **2009**, *48*, 60-103.

(28) Watzky, M. A.; Finke, R. G.: Transition metal nanocluster formation kinetic and mechanistic studies. A new mechanism when hydrogen is the reductant: Slow, continuous nucleation and fast autocatalytic surface growth. *Journal of the American Chemical Society* **1997**, *119*, 10382-10400.

(29) Jana, N. R.; Gearheart, L.; Murphy, C. J.: Seed-Mediated Growth Approach for Shape-Controlled Synthesis of Spheroidal and Rod-like Gold Nanoparticles Using a Surfactant Template. *Advanced Materials* **2001**, *13*, 1389-1393.

(30) Lim, B.; Xiong, Y. J.; Xia, Y. N.: A water-based synthesis of octahedral, decahedral, and icosahedral Pd nanocrystals. *Angewandte Chemie-International Edition* **2007**, *46*, 9279-9282.

(31) Zhang, J. G.; Gao, Y.; Alvarez-Puebla, R. A.; Buriak, J. M.; Fenniri, H.: Synthesis and SERS properties of nanocrystalline gold octahedra generated from thermal decomposition of HAuCl4 in block copolymers. *Advanced Materials* **2006**, *18*, 3233-+.

(32) Ah, C. S.; Yun, Y. J.; Park, H. J.; Kim, W.-J.; Ha, D. H.; Yun, W. S.: Size-Controlled Synthesis of Machinable Single Crystalline Gold Nanoplates. *Chemistry of Materials* **2005**, *17*, 5558-5561.

(33) Murphy, C. J.; Thompson, L. B.; Chernak, D. J.; Yang, J. A.; Sivapalan, S. T.; Boulos, S. P.; Huang, J.; Alkilany, A. M.; Sisco, P. N.: Gold nanorod crystal growth: From seed-mediated synthesis to nanoscale sculpting. *Current Opinion in Colloid & Interface Science* **2011**, *16*, 128-134.

(34) Millstone, J. E.; Hurst, S. J.; Métraux, G. S.; Cutler, J. I.; Mirkin, C. A.: Colloidal Gold and Silver Triangular Nanoprisms. *Small* **2009**, *5*, 646-664.

(35) Guerrero-Martínez, A.; Barbosa, S.; Pastoriza-Santos, I.; Liz-Marzán, L. M.: Nanostars shine bright for you. *Current Opinion in Colloid & Interface Science* **2011**, *16*, 118-127.

(36) Xia, Y.; Xiong, Y.; Lim, B.; Skrabalak, S. E.: Shape-Controlled Synthesis of Metal Nanocrystals: Simple Chemistry Meets Complex Physics? *Angewandte Chemie International Edition* **2008**, *48*, 60-103.

(37) Weiss, P. S.: Nanoscience and Nanotechnology: Present and Future. *ACS Nano* **2010**, *4*, 1771-1772.

(38) Bruchez, M.; Moronne, M.; Gin, P.; Weiss, S.; Alivisatos, A. P.: Semiconductor Nanocrystals as Fluorescent Biological Labels. *Science* **1998**, *281*, 2013-2016.

(39) Parak, W. J.; Gerion, D.; Pellegrino, T.; Zanchet, D.; Micheel, C.; Williams, S. C.; Boudreau, R.; Le Gros, M. A.; Larabell, C. A.; Alivisatos, A. P.: Biological applications of colloidal nanocrystals. *Nanotechnology* **2003**, *14*, R15-R27.

(40) Rannard, S.; Owen, A.: Nanomedicine: Not a case of "One size fits all". *Nano Today* **2009**, *4*, 382-384.

(41) Nel, A.; Xia, T.; Mädler, L.; Li, N.: Toxic Potential of Materials at the Nanolevel. *Science* **2006**, *311*, 622-627.

(42) Rivera Gil, P.; Oberdörster, G. n.; Elder, A.; Puntes, V. c.; Parak, W. J.: Correlating Physico-Chemical with Toxicological Properties of Nanoparticles: The Present and the Future. *ACS Nano* **2010**, *4*, 5527-5531.

(43) De, M.; Ghosh, P. S.; Rotello, V. M.: Applications of Nanoparticles in Biology. *Advanced Materials* **2008**, *20*, 4225-4241.

(44) Sperling, R. A.; Rivera gil, P.; Zhang, F.; Zanella, M.; Parak, W. J.: Biological applications of gold nanoparticles. *Chemical Society Reviews* **2008**, *37*, 1896-1908.

(45) Yin, Y.; Alivisatos, A. P.: Colloidal nanocrystal synthesis and the organic-inorganic interface. *Nature* **2005**, *437*, 664-670.

(46) Niemeyer, C. M.: Nanoparticles, proteins, and nucleic acids: Biotechnology meets materials science. *Angewandte Chemie-International Edition* **2001**, *40*, 4128-4158.

(47) Nel, A. E.; Madler, L.; Velegol, D.; Xia, T.; Hoek, E. M. V.; Somasundaran, P.; Klaessig, F.; Castranova, V.; Thompson, M.: Understanding biophysicochemical interactions at the nano-bio interface. *Nat Mater* **2009**, *8*, 543-557.

(48) Pellegrino, T.; Manna, L.; Kudera, S.; Liedl, T.; Koktysh, D.; Rogach, A. L.; Keller, S.; Radler, J.; Natile, G.; Parak, W. J.: Hydrophobic nanocrystals coated with an amphiphilic polymer shell: A general route to water soluble nanocrystals. *Nano Letters* **2004**, *4*, 703-707.

(49) Pellegrino, T.; Kudera, S.; Liedl, T.; Javier, A. M.; Manna, L.; Parak, W. J.: On the development of colloidal nanoparticles towards multifunctional structures and their possible use for biological applications. *Small* **2005**, *1*, 48-63.

(50) Verma, A.; Uzun, O.; Hu, Y.; Hu, Y.; Han, H.-S.; Watson, N.; Chen, S.; Irvine, D. J.; Stellacci, F.: Surface-structure-regulated cell-membrane penetration by monolayer-protected nanoparticles. *Nat Mater* **2008**, *7*, 588-595.

(51) Dejardin, T.; de la Fuente, J.; del Pino, P.; Furlani, E. P.; Mullin, M.; Smith, C. A.; Berry, C. C.: Influence of both a static magnetic field and penetratin on magnetic nanoparticle delivery into fibroblasts. *Nanomedicine* **2011**, *6*, 1719-1731.

(52) Puertas, S.; Batalla, P.; Moros, M. a.; Polo, E.; del Pino, P.; Guisán, J. M.; Grazú, V.; de la Fuente, J. s. M.: Taking Advantage of Unspecific Interactions to Produce Highly Active Magnetic Nanoparticle−Antibody Conjugates. *ACS Nano* **2011**, *5*, 4521-4528.

(53) Bahshi, L.; Freeman, R.; Gill, R.; Willner, I.: Optical Detection of Glucose by Means of Metal Nanoparticles or Semiconductor Quantum Dots. *Small* **2009**, *5*, 676-680.

(54) Parak, W. J.; Gerion, D.; Zanchet, D.; Woerz, A. S.; Pellegrino, T.; Micheel, C.; Williams, S. C.; Seitz, M.; Bruehl, R. E.; Bryant, Z.; Bustamante, C.; Bertozzi, C. R.; Alivisatos, A. P.: Conjugation of DNA to silanized colloidal semiconductor nanocrystalline quantum dots. *Chemistry of Materials* **2002**, *14*, 2113-2119.

(55) Moros, M.; Pelaz, B.; Lopez-Larrubia, P.; Garcia-Martin, M. L.; Grazu, V.; de la Fuente, J. M.: Engineering biofunctional magnetic nanoparticles for biotechnological applications. *Nanoscale* **2010**, *2*, 1746-1755.

(56) Algar, W. R.; Prasuhn, D. E.; Stewart, M. H.; Jennings, T. L.; Blanco-Canosa, J. B.; Dawson, P. E.; Medintz, I. L.: The Controlled Display of Biomolecules on Nanoparticles: A Challenge Suited to Bioorthogonal Chemistry. *Bioconjugate Chemistry* **2011**, *22*, 825-858.

(57) Soenen, S. J.; Rivera-Gil, P.; Montenegro, J.-M.; Parak, W. J.; De Smedt, S. C.; Braeckmans, K.: Cellular toxicity of inorganic nanoparticles: Common aspects and guidelines for improved nanotoxicity evaluation. *Nano Today* **2011**, *6*, 446-465.

(58) Nielsen, O. S.; Horsman, M.; Overgaard, J.: A future for hyperthermia in cancer treatment? *European Journal of Cancer* **2001**, *37*, 1587-1589.

(59) van der Zee, J.; Vujaskovic, Z.; Kondo, M.; Sugahara, T.: The Kadota Fund International Forum 2004–Clinical group consensus*. *International Journal of Hyperthermia* **2008**, *24*, 111-122.

(60) van der Zee, J.; González, D.; van Rhoon, G. C.; van Dijk, J. D. P.; van Putten, W. L. J.; Hart, A. A. M.: Comparison of radiotherapy alone with radiotherapy plus hyperthermia in locally advanced pelvic tumours: a prospective, randomised, multicentre trial. *The Lancet* **2000**, *355*, 1119-1125.

(61) Rolf D, I.: Hyperthermia adds to chemotherapy. *European Journal of Cancer* **2008**, *44*, 2546-2554.

(62) URANO, M.: Invited Review: For the clinical application of thermochemotherapy given at mild temperatures. *International Journal of Hyperthermia* **1999**, *15*, 79-107.

(63) Sheng, W.-Y.; Huang, L.: Cancer Immunotherapy and Nanomedicine. *Pharmaceutical Research* **2011**, *28*, 200-214.

(64) El-Sayed, I. H.; Huang, X. H.; El-Sayed, M. A.: Selective laser photo-thermal therapy of epithelial carcinoma using anti-EGFR antibody conjugated gold nanoparticles. *Cancer Letters* **2006**, *239*, 129-135.

(65) Moriyama, Y.; Narita, M.; Sato, K.; Urushiyama, M.; Koyama, S.; Hirosawa, H.; Kishi, K.; Takahashi, M.; Takai, K.; Shibata, A.: APPLICATION OF HYPERTHERMIA TO THE TREATMENT OF HUMAN ACUTE-LEUKEMIA - PURGING HUMAN-LEUKEMIC PROGENITOR CELLS BY HEAT. *Blood* **1986**, *67*, 802-804.

(66) Hildebrandt, B.; Wust, P.; Ahlers, O.; Dieing, A.; Sreenivasa, G.; Kerner, T.; Felix, R.; Riess, H.: The cellular and molecular basis of hyperthermia. *Critical Reviews in Oncology Hematology* **2002**, *43*, 33-56.

(67) Fajardo, L. F.: PATHOLOGICAL EFFECTS OF HYPERTHERMIA IN NORMAL-TISSUES. *Cancer Research* **1984**, *44*, 4826-4835.

(68) Wondergem, J.; Haveman, J.; Rusman, V.; Sminia, P.; Vandijk, J. D. P.: EFFECTS OF LOCAL HYPERTHERMIA ON THE MOTOR FUNCTION OF THE RAT SCIATIC-NERVE. *International Journal of Radiation Biology* **1988**, *53*, 429-438.

(69) van der Zee, J.: Heating the patient: a promising approach? *Annals of Oncology* **2002**, *13*, 1173-1184.

(70) Multhoff, G.; Botzler, C.; Wiesnet, M.; Müller, E.; Meier, T.; Wilmanns, W.; Issels, R. D.: A stress-inducible 72-kDa heat-shock protein (HSP72) is expressed on the surface of human tumor cells, but not on normal cells. *International Journal of Cancer* **1995**, *61*, 272-279.

(71) Basu, S.; Binder, R. J.; Suto, R.; Anderson, K. M.; Srivastava, P. K.: Necrotic but not apoptotic cell death releases heat shock proteins, which deliver a partial maturation signal to dendritic cells and activate the NF-κB pathway. *International Immunology* **2000**, *12*, 1539-1546.

(72) Chen, T.; Guo, J.; Han, C.; Yang, M.; Cao, X.: Heat Shock Protein 70, Released from Heat-Stressed Tumor Cells, Initiates Antitumor Immunity by Inducing Tumor Cell Chemokine Production and Activating Dendritic Cells via TLR4 Pathway. *The Journal of Immunology* **2009**, *182*, 1449-1459.

(73) Sun, X.; Li, X.-F.; Russell, J.; Xing, L.; Urano, M.; Li, G. C.; Humm, J. L.; Ling, C. C.: Changes in tumor hypoxia induced by mild temperature hyperthermia as assessed by dual-tracer immunohistochemistry. *Radiotherapy and oncology : journal of the European Society for Therapeutic Radiology and Oncology* **2008**, *88*, 269-276.

(74) Kelleher, D. K.; Vaupel, P.: No Sustained Improvement in Tumor Oxygenation After Localized Mild Hyperthermia
Oxygen Transport to Tissue XXXI. Takahashi, E., Bruley, D. F., Eds.; Springer US, 2010; Vol. 662; pp 393-398.

(75) Dikomey, H. H. K. E.: Hyperthermic radiosensitization: mode of action and clinical relevance. *International Journal of Radiation Biology* **2001**, *77*, 399-408.

(76) Franckena, M.; Fatehi, D.; Bruijne, M. d.; Canters, R. A. M.; Norden, Y. v.; Mens, J. W.; Rhoon, G. C. v.; Zee, J. v. d.: Hyperthermia dose-effect relationship in 420 patients with cervical cancer treated with combined radiotherapy and hyperthermia. *European journal of cancer (Oxford, England : 1990)* **2009**, *45*, 1969-1978.

(77) Hohenberger, P.; Wysocki, W. M.: Neoadjuvant Treatment of Locally Advanced Soft Tissue Sarcoma of the Limbs: Which Treatment to Choose? *The Oncologist* **2008**, *13*, 175-186.

(78) Mornet, S.; Vasseur, S.; Grasset, F.; Duguet, E.: Magnetic nanoparticle design for medical diagnosis and therapy. *Journal of Materials Chemistry* **2004**, *14*, 2161-2175.

(79) Dickerson, E. B.; Dreaden, E. C.; Huang, X.; El-Sayed, I. H.; Chu, H.; Pushpanketh, S.; McDonald, J. F.; El-Sayed, M. A.: Gold nanorod assisted near-infrared plasmonic photothermal therapy (PPTT) of squamous cell carcinoma in mice. *Cancer Letters* **2008**, *269*, 57-66.

(80) Dreaden, E. C.; Mackey, M. A.; Huang, X.; Kang, B.; El-Sayed, M. A.: Beating cancer in multiple ways using nanogold. *Chemical Society Reviews* **2011**, *40*, 3391.

(81) Figuerola, A.; Di Corato, R.; Manna, L.; Pellegrino, T.: From iron oxide nanoparticles towards advanced iron-based inorganic materials designed for biomedical applications. *Pharmacological Research* **2010**, *62*, 126-143.

(82) Mahmoudi, M.; Hosseinkhani, H.; Hosseinkhani, M.; Boutry, S.; Simchi, A.; Journeay, W. S.; Subramani, K.; Laurent, S.: Magnetic Resonance Imaging Tracking of Stem Cells in Vivo Using Iron Oxide Nanoparticles as a Tool for the Advancement of Clinical Regenerative Medicine. *Chemical Reviews* **2010**, *111*, 253-280.

(83) Na, H. B.; Song, I. C.; Hyeon, T.: Inorganic Nanoparticles for MRI Contrast Agents. *Advanced Materials* **2009**, *21*, 2133-2148.

Introduction to Bioapplications of Superparamagnetic NPs

Chapter 2

Over the last decade, a wide variety of iron oxide NPs (mostly maghemite, γ-Fe_2O_3, or magnetite, Fe_3O_4, single domains of about 5 – 20 nm in diameter) have received a great deal of interest in the fields of biotechnology and nanomedicine.[1,2] This interest has been motivated by the fascinating superparamagnetic behavior that iron oxide NPs exhibit and which make them very suitable candidates for bio-applications such as targeted drug delivery,[1,3,4] magnetofection,[5-7] magnetic hyperthermia,[1-3,8-13] magnetic resonance imaging (MRI),[4,14-16] biosensing[17,18] or magnetic separation (Figure 2.1).[9,19]

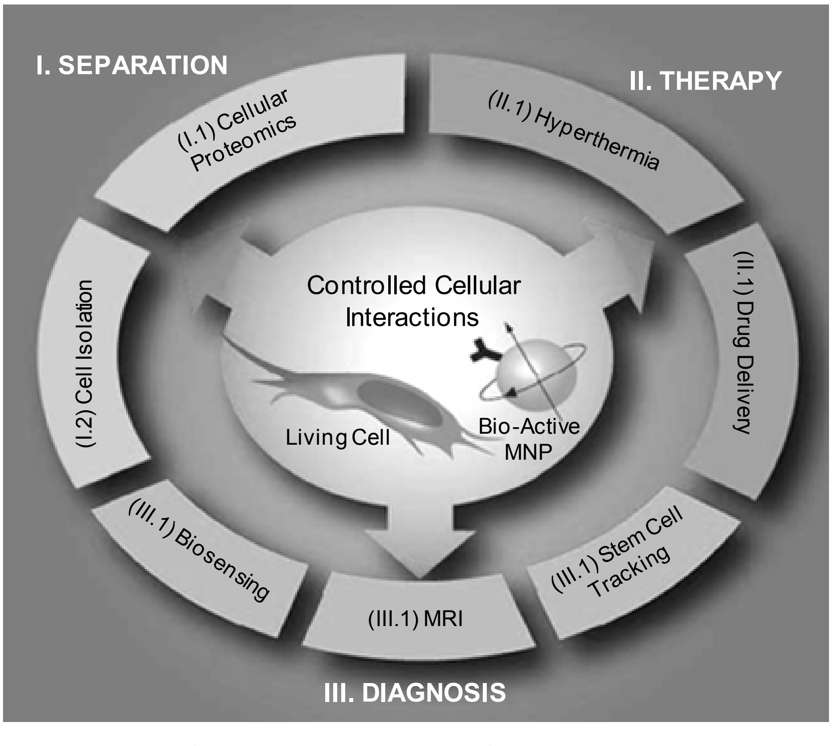

Figure 2.1. *Bio-applications of magnetic NP (adapted from Barakat).*[20]

The superparamagnetic behavior of iron oxide NPs confers two crucial properties of remarkable potential in the context of bio-applications: (i) iron oxide NP-based nanosystems (also assemblies based on superparamagnetic NPs) can be remotely manipulated by an external magnetic field (EMF)[5,21] and (ii) they can resonantly couple to an alternating magnetic field (AMF).[10,11,13,22,23] Theoretically, at 400 kHz for example, 99% of radiation can be transferred to magnetic NPs located 15 cm inside the body;[24,25] thus, due to the suitable penetration depth of AMF in tissue, hybrid (inorganic/organic) nanoheaters based on iron oxide NPs can be used both for remote controlled drug release in targeted tissues[24] and for destroying tumors containing iron oxide NPs by hyperthermia.[10,23,26]

In addition to their use as "nanoheaters" in AMF based hyperthermia therapy, magnetic NPs (MNPs) have also received a great deal of attention due to their potential as contrast agents for nuclear magnetic resonance imaging (MRI). MRI is a widely extended non-invasive imaging technique which produces high resolution images of the body (or animals in general); this technique tracks changes in the relaxation times of the nuclear spin of hydrogen protons following irradiation of the body by radiofrequency (RF) pulses. In this context, MNPs are able to modify the relaxation times of the nuclear spins in their most immediate vicinity to yield signal of contrast. These changes can be interpreted and used for imaging of tissue targeted with MNPs.[27-30]

2.1. Synthesis of Iron Oxide NPs

A variety of approaches have been used to synthesize iron oxide NPs with controlled properties. Importantly, engineered NPs should present a homogeneous size distribution as well as uniform physico-chemical properties (such as superparamagnetism, colloidal stability, *etc.*). The most important synthetic methods to produce iron oxide NPs (briefly introduced in the following) are (i) coprecipitation, (ii) the uses of micelles, (iii) thermal decomposition process and (iv) synthesis of hybrids materials (nanocomposites).

(i) **Coprecipitation** is an easy and extended way to obtain iron oxide nanoparticles. The synthesis evolves though the dissolution of iron salts (Fe^{2+} and Fe^{3+}) in alkaline aqueous phase, under inert atmosphere to avoid the magnetite oxidation to maghemite and it is carry on commonly at room temperature. [31] Nanoparticles are form through the following reaction,

$$\mathrm{Fe^{2+} + 2Fe^{3+} + 8OH^- \rightarrow Fe_3O_4 + 4H_2O} \qquad (2.1)$$

Nanoparticles size, shape and composition depend on the reagents used (sulphates, chlorides, nitrates), the Fe^{2+}/Fe^{3+} ratio, temperature, pH and strength of the media. *e.g.* high pH and ionic strength generate small particles.[32] Polymers such as polyethylenglycol (PEG), polyvinyl alcohol (PVA), or poly (lactic-*co*-glycolic) acid (PLGAs), or molecules such as dextranes or phospholipids are also used as surfactants and as agents to control the nanoparticles size.[33]

The major advantages of this method are its simplicity, versatility and the possibility to obtain nanoparticles at large scale. The clinical contrast agent Fedirex® is synthesized by this method. This method does not provide a good control on the final size and the distribution of the NPs. Also, NPs synthesized by this methodology exhibit low crystallinity which leads to lower magnetization values.

(ii) The use of micelles or microemulsions water-oil are other possibilities to obtain this kind of iron oxide NPs.[34] In this case, seeding and growing NPs processes occur in the inner part of the surfactant micelles. This fact limits the NPs size leading to a major control in the final NPs size distribution. Micelle size is controlled by the molar ratio between surfactants and water. Most typical surfactants are bromide cetylammonium (CTAB) or sodium dodecylsulphate among the ionic ones, or Triton X-100 or Igepal among non-ionic surfactants.[29] Once synthesized, NPs must be extracted from the micelles; this can be achieved by a polarity change inside the system by precipitation, or by an organic solvent addition, such as acetone.[35]

Although the NPs obtained by this method allow for a lower polydispersity than NPs synthesized by coprecipitation, it is still far from ideal and also, NPs present low crystallinity.[36] As a particular drawback, the high solvent volume use in this method makes difficult to scale up the amount of NPs.[35]

(iii) Thermal decomposition is the method that provides iron oxide NPs with best properties including narrow size distribution, best crystallinity and best magnetic behavior. This technique uses organometallic iron precursors which are soluble in the organic solvents in which the reaction is performed. Organic solvents allow for the use of higer temperatures than in aqueous conditions, which is a crucial factor to improve the quality of the NPs. A typical thermal decomposition requires the presence of a metallic complex, such as acetylacetonate ($M(acac)_n$, where M= Fe, Mn, Co, Ni and n =2 or 3), metallic cupferronates, or carbonyls; and a surfactant, both dissolved in an organic solvent at boiling temperature. Most common surfactants are oleic acid (OA) and fatty acids. Parameters which control the NPs size and morphology are the molar ratio between the metallic precursors, the surfactants and solvent. Also the boiling temperature of the organic solvent is an important parameter of control. Changes in reaction time and temperature are also possible changing the properties of the final products.

In 1993, Bawendi and coworkers were the first ones to use the thermal decomposition method to produce high quality quantum dots.[37] Then, Alivisatos and coworkers used the thermal decomposition to obtain maghemite NPs.[38] Hyeon and coworkers were the firsts to apply the iron (III) pentacarbonyl and the oleic acid, as precursor and surfactant respectively.[39] Sun and coworkers use the iron (III) acetylacetonate, oleic acid and oleylamine solved in diphenyl ether to generate 4 nm magnetite NPs.[40] Using this method, it is possible to obtain NPs up to 22 nm of diameter. [41] This technique is really versatile and it is possible to modulate the size and shape of the final NPs.

(iv) Assembling several inorganic materials into a single nanocomposite, which exhibits the physical and chemical properties of their constituents, represents an innovative and relatively new way to design multifunctional materials.[42-44] Engineered hybrid nanocomposites have been proven to offer novel and often unique properties that originate from collective interactions between the constituents. Furthermore, precise hybridization of nanocrystals with on-demand optical, electronic and magnetic properties into hybrid nanocomposites might provides a route to enhanced metamaterials.[45,46]. In literature, a vast variety of nanocomposites have been reported to date;[44] the most general and extended strategy to synthesize these hybrid materials consists of two steps: (i) synthesis of nanoparticles of one material, and (ii) use of the newly prepare NPs as nucleation seeds to deposit the other components (Figure 2.2).

Given the multiple potential applications of SPM-NPs in bionanotechnology, nanocomposites which carry the superparamagnetic properties of an iron oxide core and the shielding/surface as well as the optical properties of an Au shell add an extra value to the suitability of bare iron oxide NPs for bioapplications. In literature, there is a wide variety of composite nanomaterials composed by iron oxide and another inorganic material.

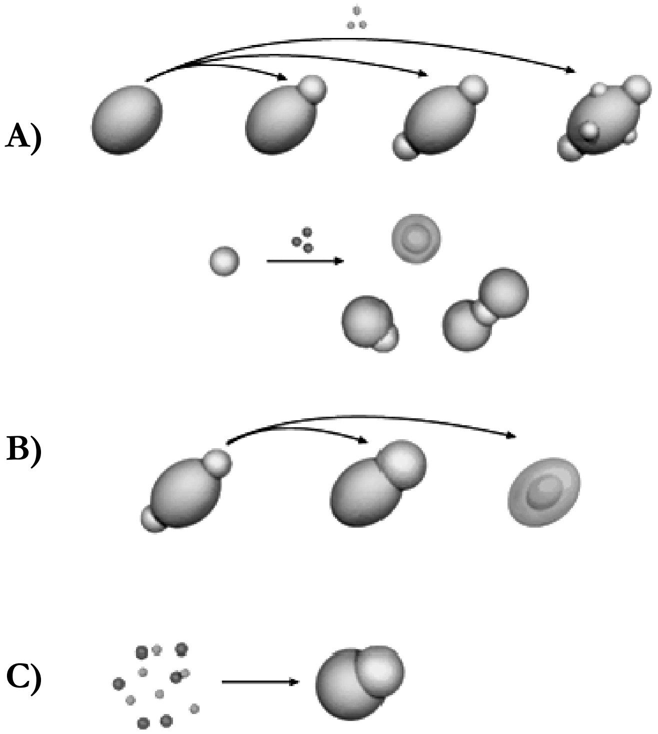

***Figure* 2.2.** *Schemes of different growth mechanisms during the synthesis of hybrid nanoparticles. (A) Surface nucleation and growth of a second phase on a seed nanoparticle (material-1). Top: growth of islands (material-2) on "seeds" of material 1; bottom: growth of material 2 from a material 1 seed. (B) Surface nucleation followed by surface diffusion of material-2 on top of material-1. (C) Simultaneous nucleation and growth of both materials. Adapted from Costi et al.*[44]

The structure of an inorganic nanocomposite containing iron oxide NPs can be classified into the following subgroups (Figure 2.3): core-shell, mosaic, shell-core, shell-core-shell, and dumbbell.[47,48]

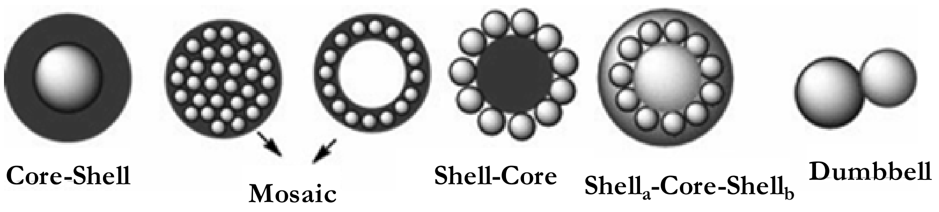

***Figure* 2.3.** *Scheme of representative nanostructures composed by iron oxide and another material (adapted from Wu).*[47]

One of the most addressed multicomponent nanomaterials based on iron oxide is based on the core-shell structure containing a core of iron oxide and a thin shell of metallic gold (iron oxide@gold NPs); a myriad of strategies have been described to synthesized this structure, *i.e.* thermal decomposition,[48] reverse micelle method using cetyltrimethylammonium bromide (CTAB) as surfactant,[49,50] chemical coprecipitation[51] or growing the gold on the iron oxide by an iterative hydroxylamine seeding.[52]

Even in the absence of external magnetic fields, one of the major challenges in the synthesis and stabilization of magnetic nanomaterials is the prevention of anisotropic magnetic dipolar attraction.[53] Experimentally, providing the magnetic core with an external coating is one of the successful approaches. A shell also provides oxidative stability to the magnetic core which is crucial for the efficient of magnetic materials in applications such as hyperthermia, magnetofection or MRI. Some experimental works have also pointed out that core-shell structures can enhance the capability of these core-shell NPs to heat under AMF.[25,54]

2.2. Shielding & Functionalization of Iron Oxide NPs for Bioapplications

Colloidal suspensions of iron oxide particles possess a unique combination of fluidity and the capability to interact with magnetic fields as result of their magnetic behavior whatever it is, *i.e.* ferro-, ferrimagnetic or superparamagnetic. However, an appropriate derivatization with a hydrophilic coating is crucial to provide the particles with colloidal stability; in the absence of any surface coating, magnetic iron oxide particles (as well as all inorganic NPs) exhibit an inherent hydrophobic surface with a large surface area to volume ratio. Then, due to hydrophobic interactions between uncoated particles, these will agglomerate to form large clusters which exhibit strong magnetic dipole–dipole attractions between them and which typically result in ferromagnetic clusters. Thus, the magnetization of newly formed cluster increases as the size of the cluster increases by addition of more particles to the cluster. Since iron oxide particles are attracted magnetically, in addition to the usual flocculation due to Vander Waals force, surface modification is even more important to produce stable particles.[1]

Besides the required colloidal stability, iron oxide NPs designed for their use in biological environments (cells, macromolecules, organic and inorganic molecules present in physiological media, etc.) require a coating, typically of choice on the final synthetic product, which ultimately determine their interaction with macromolecules such as nucleic acids, proteins, carbohydrates, and lipids. These interactions at the nano-bio interface represent normally a complex scenario which greatly influence on the success of a particular engineered nanomaterial for a certain application where iron oxide NPs can act as a sensor, diagnostic tool, drug carrier or more complex multitask (theranostic) systems. Therefore, in a bio-context, the properties of engineered iron oxide NPs in physiological environments have to be critically analyzed; normally, the characteristic and components of physiological media are quite different from the environment where the synthesis of the nanosystems took place, *i.e.* polar or non-polar solvents with very particular attributes such as ionic strength, pH or presence of multivalent ions, salts or polymers, to name a few.

Importantly, syntheses of highly monodisperse iron oxide nanocrystals are typically performed in in organic solvents in the presence of capping agents containing aliphatic chains.[30,55] In order to use nanocrystals made in organic solvents for bio-applications, they have to be transformed into water soluble materials as physiological media contains mainly water, among other constituents such as proteins, lipids, salts or multivalent ions.

Over the past decade different approaches have been used for water-transfer of iron oxide nanocrystals by the following methods (see Figure 2.4): (i) ligand-exchange by exchanging aliphatic chains by bifunctional molecules containing hydrophilic groups,[1] (ii) gold coating by growing a shell of metallic gold on top the iron oxide NP,[56] (iii) polymer coating methods by intercalating amphiphilic polymers in the aliphatic shell of the NPs, [57,58] and (iii) silanization by growing a glass shell around the NPs.[59] All these methods allows for designing, at the molecular level, the outermost shell of nanomaterials and therefore the bio-interface.

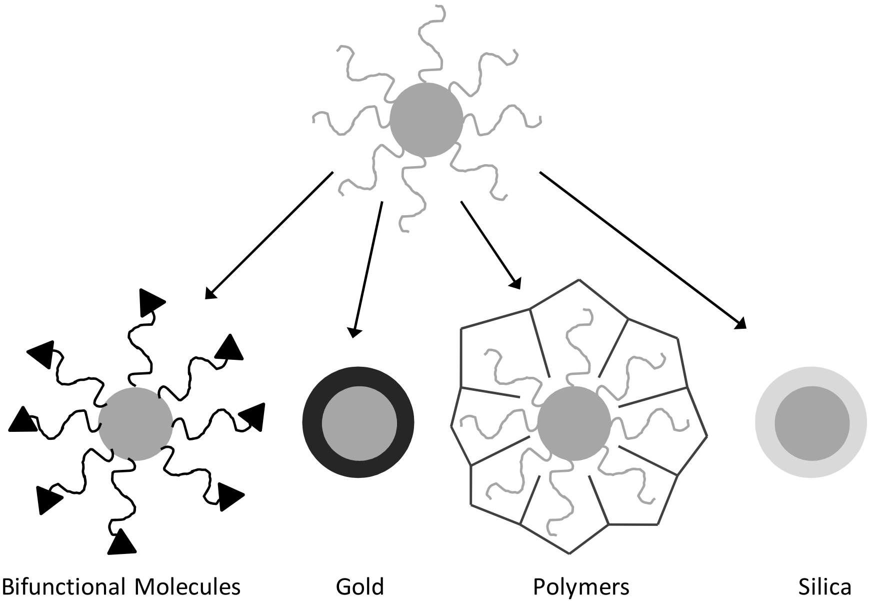

Figure 2.4. *Different approached to transfer to water iron oxide NPs made in organic solvents.*

From the aforementioned water-transfer methods, gold coating presents very beneficial features such very efficient shielding of iron oxide degradation, enhanced optical properties (surface plasmons), biocompatibility owing to its low reactivity and ease of functionalisation with a wide variety of thiolated chains.

The possibility of custom-made organic coatings with a wide variety of chemical groups (neutral, positively or negatively charged) allows for tailoring the net charge of the nanomaterials as well as a well-defined surface charge-pattern.[60] Independently of the synthetic route, shape, size, surface area, roughness, porosity or crystallinity of iron oxide NPs, the charge and distribution of charges arising from different functional groups play a critical role in the fate of nanomaterials for bio-applications; this is motivated because Coulomb interactions (as well as hydrophobic/hydrophilic interactions) lead a nanomaterial to interact with macromolecules in the physiological milieu such proteins or carbohydrates, both in the media or in the cell (membrane receptors, chaperones, genetic material, etc.).[61] It is worth noting that when a NP is into to a cell, what the cell sees is a patchwork made of the organic molecules (and corresponding functional groups) covering the NP which can be as originally designed or result of unspecific protein absorption.

The charge of iron oxide NPs, and inorganic NPs in general, can also be greatly modified in physiological media due to the absorption of biomolecules present in the physiological milieu; absorption of proteins and following physiochemical surface changes on nanomaterials are the focus of several studies.[62-67] Thus the adsorption of serum proteins on the surface of nanomaterials can hide the synthetic organic layer and lead to unspecific uptake of nanomaterials into cells by receptor-mediated endocytosis.[68-70] Protein absorption onto nanoparticles can also adversely affect the function and structure of proteins;[61,71,72] for instance, disease-related fibrils made of human β2-microglobulin are formed in the surface of different nanoparticles.[65] Given that adsorption of proteins changes the nano-bio interface, it is worth noting that both the uptake and toxicity of NPs can be greatly influenced by the absorption of serum proteins.[68,69,71,73,74] Therefore, the design of a functional organic coating for iron oxide NPs is of the most importance for any bioapplication; ideally, the organic coating should add extra capabilities to the nanosystems including enhanced colloidal stability, avoiding unspecific proteins absorption and targeting to drive the nanosystem where desired, among others.

2.3. Bioapplications of Iron Oxide NPs

Combination of gold and Fe_xO_y to obtain hybrid nanocomposites can generate useful systems which combine the advantages from individual magnetic and gold NPs (Figure 2.5).[75-77]Among different magnetic materials, iron oxide is the most used in bioapplications due its "good" biocompatibility. For this reason, magnetic nanoparticles (MNPs) made of iron oxide has found a lot of attractive applications in nanomedicine; iron oxide MNPs have demonstrated great promise for diagnostic and therapeutic applications.[78] On the other hand, a gold shell would provide the system of good oxidation stability, a major biocompatibility and of course an easy way to modify the surface in order to reach more stable nanosystems under biological conditions. In addition, the presence of gold to a nanocomposite add optical features very suitable for cellular optical imaging, hyperthermia, and sensitive bio-detection for DNA and proteins among others.[56]

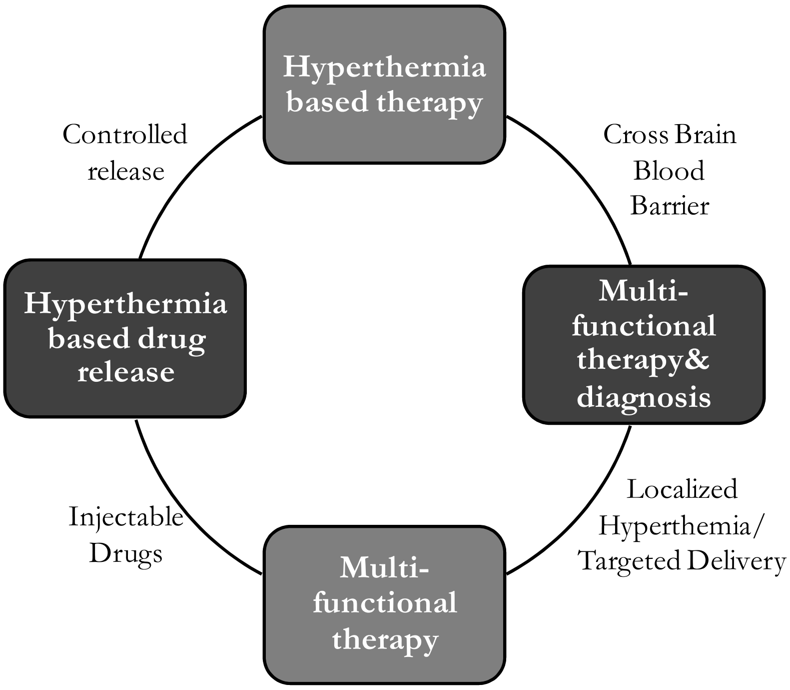

***Figure* 2.5.** *MNPs application spectra(adapted from Kumar).*[53]

Currently, MNPs are providing good results in nanomedicine; there are many ongoing clinical trials using them in diagnosis and therapy (Table 2.1).Bare MNPs can be used to target tumor cells passively by the enhanced permeability effect (EPR effect),[79] or they can be modified with ligands of biological relevance which can add functions to the MNPs system as drug carriers, theranostic agents, etc. A variety of targeting ligands have been used for derivatized MNPs, depending on the specific target, such as peptides (e.g. chlorotoxin,[80] RGD,[81] CREKA,[82] bombesin,[83] etc.), antibodies,[84] and small molecules like folate.[85]

Magnetic nanosystems can be also manipulated by an external magnetic field gradient. The remote control of magnetic nanocarriers by external magnetic fields, also called magnetic targeting, combined with the intrinsic penetrability of magnetic fields into human tissue, opens up many applications involving the transport and/or immobilization of magnetic nanoparticles, or of magnetically tagged biological entities. In this way they can be made to deliver a package, such as an anticancer drug, or a group of radionuclide atoms, to a targeted region of the body, such as a tumor.[86]

Status/Starting Date	Title/Condition	Sponsor
Recruiting / Jan10	Inflammatory cell labeling and tracking with magnetic resonance imaging after myocardial infarction /Myocardial infarction; inflammation	University of Edinburg
Ongoing / Jul08	Evaluation of magnetic nanoparticle enhanced imaging in autoimmune diabetes / Diabetes mellitus, type I	Joslin Diabetes Center
Recruiting/ Jul08	Improved pre-operative staging of pancreatic cancer using superparamagnetic iron oxide magnetic resonance imaging/Pancreatic cancer	Massachusetts General Hospital Institute
Recruiting/ Oct08	Assessing dynamic magnetic resonance(MR) imaging in patients with recurrent high grade glioma receiving chemotherapy / Brain neoplasm	OHSU Knight Cancer Institute
Terminated/ Jul05	A validation study of MR lymphangiography using SPIO, a new lynphotropic superparamagnetic NP contrast/ Bladder genitourinary and prostate cancers	M.D. Anderson Cancer Center

Table 2.1. *Recently initiated clinical trials evaluating the utility of MNPs in diagnostic applications.*[85]

Superparamagnetic NPs can be made to resonantly respond to a time-varying magnetic field, with advantageous results related to the transfer of energy from the exciting field to the nanoparticle for applications (hyperthermia). In diagnosis, superparamagnetic NPs are used currently as T_2-contrast agents (Table 2.2); molecular targeting has been extensively explored in the development of tumor-selective MRI agents and has showed promise for further therapeutic applications.[87] However, most of the superparamagnetic NPs tested *in vivo* models have been shown to be taken up nonspecifically by the reticuloendothelial system (RES); this fact makes their detection not very useful. Therefore, it is clear the importance of the use of MNPs modified specifically to target the region of interest.

In literature, it is possible to find uses of iron oxide/gold nanocomposites in theranostics,[88] gene delivery,[89] biosensors,[90-94] cell sorting[95] and separation[96] and catalysis.[97-100] Iron oxide-gold nanosystems are suitable for the aforementioned bioapplications based on the properties of GNPs and MNPs, independently. In this context and following with the previously described, iron oxide-gold materials have been applied in MRI; note that T_2 is affected by the structure of the materials.[83,84,93] Recently, Fe_3O_4@Au nanocomposites have been also used as multimodal agent contrast using CT and MRI techniques.[101] Hyperthermia is currently investigated as a treatment modality using nanoheater, *i.e.* MNPs under AMF fields and GNPs under NIR illumination; therefore, joining the properties of MNPs and GNPs in one theranostic nanosystem opens a variety of choices for treatment and MRI/CT imaging.[88,102]

Pre-clinical Agent	Commercial Name	MR target	Status
AMI-25	Ferumoxide, Fedirex, Endorem	Liver	Approved
OMP	Abdoscan	Bowel	Approved
AMI-121	Gastromark, Ferumoxsil, Lumirem	Bowel	Approved
SHU555A	Resovist	Liver	Approved (EU, Japan, Australia), Phase III (USA)
AMI-227	Combidex, Sinerem, Ferumoxtran	Lymph, Node metastases	Phase III
CODE 7228	Feraheme, Ferumoxtyol	Vasculature	Phase II

Table 2.2.*Commercially available MNPs for MRI currently approved or in clinical trials.*

2.4 Hyperthermia Based on Superparamagnetic NPs: Magnetic Fluid Hyperthermia (MFH)

The original idea of using magnetic NPs (MNPs) to heat and destroy tumors was first introduced by Gilchrist[103] back in 1957 and further explored by the groups of Gordon, Hines and Nielsen.[104] However, following studies lacked of suitable animal models, temperature control or the adequate technology (frequency and amplitude of AMF) to push this new technique to any reasonable clinical study. Hyperthermia based on magnetic materials had to wait until the 1990s when the group of A. Jordan introduced the concept of magnetic fluid hyperthermia (MFH).[105,106] They found that subdomain magnetic particles (nanometer in size) absorb much more power at tolerable AMF than is obtained by well-known hysteresis heating of multidomain (microns in size) magnetic particles. The development of MFH has gained since increasingly attention of both materials and oncology researchers. At present, MFH has obtained successful results in clinical trials in humans.[107]

In general, magnetic materials present magnetic dipoles generated by the spinning of some of their electrons; these polarized electrons can be aligned parallel or antiparallel with respect to the neighboring ones and respond very differently to an applied magnetic field. Depending on how these polarized electrons interact with each other, magnetic materials fall into one of the following categories: paramagnets, ferromagnets, ferrimagnets or antiferromagnets. However, it is important to highlight here that falling into one of these categories strongly depends on the size of the material; therefore, the magnetic behavior of a particular materials can be tuned by adjusting its size.[35]

When the magnetic dipoles of a material are randomly oriented and can be only oriented by the presence of an external magnetic field, this material is considered to be in a paramagnetic phase. In this phase, magnetic dipoles will randomly relax to their equilibrium state (initial zero net magnetic moment), as the magnetic field is switched off, with no extra energy required.

Alternatively, a ferromagnetic phase is characterized by an enhanced collective parallel alignment of magnetic dipoles, even in the absence of a magnetic field. Bulk metals such as Fe, Pt or Co, as well as some of their alloys (FePt, FeCo) are ferromagnetic materials. In contrast to the ferromagnetic phase, neighboring magnetic dipoles can collectively align in an antiparallel fashion. This type of magnetic exchange coupling gives rise to antiferromagnetic and ferrimagnetic phases. The former one applies when the material shows a net zero magnetization which results from the destructive coupling of magnetic dipoles with the same magnetic moment; typical examples of antiferromagnetic bulk materials include hematite (one of the many mineral forms of Fe_2O_3), metals such as Cr, alloys such as FeMn, and oxides such as NiO. In contrast, if the neighboring antiparallel magnetic moments have different values, their destructive coupling gives rise to a net magnetization in the so called ferrimagnetic phase. The principal examples of ferrimagnetic materials are magnetite (iron (II, III) oxide; Fe_3O_4) and a variety of ferrites such as Co ferrite ($CoFe_2O_4$), MnZn ferrite ($Mn_aZn_{(1-a)}Fe_2O_4$), NiZn ferrite ($Ni_aZn_{(1-a)}Fe_2O_4$), etc.

The main parameters required to define the behavior of magnetic materials are:

(i) Coercive field (H_c), the external field (of opposite sign) required to reduce the net magnetization back to zero; this parameter defines the minimum energy required for the reversal of the magnetization of the material. H_c is strictly related to the magnetic anisotropic constant (K_a); this determines the energy barrier to be overcome in order to invert the direction of the magnetic dipoles of the material. In the case of NPs, K_a is determined by the symmetry of the crystal lattice, size and shape of the NP.

(ii) Saturation magnetization (M_s), the maximum value of net magnetization of a material under the influence of sufficiently high magnetic fields.

(iii) Remanent magnetization (M_R), the residual magnetization at zero applied field. These three parameters define the hysteresis loop generated in field-dependent magnetization measurements (Figure 2.7).

Magnetic parameters like the coercivity can be finely tuned by adjusting the size, shape and structure of materials in the nanometer range (also in the micrometer range); this represents an important advantage of magnetic nanoparticles compared to their bulk counterparts since for instance, they can be custom made for specific bioapplications with particular practical requirements such magnetic hyperthermia. In fact, for spherical magnetic NPs with sizes bellow the so-called superparamagnetic radius (r_{SP}), ferro- and ferrimagnetic NPs become superparamagnetic; in the superparamagnetic regime, the application of an external magnetic field induces high magnetic moments in NPs whereas switching-off the field leaves zero remanence (M_R). Reduce the size of magnetic NPs impairs the presence of domain walls in the particle (multi domain, MD) and gives rise to single domain particles which are energetically favorable for sizes bellow the r_{SP}; in the superparamagnetic regime the thermal energy is sufficiently high to overcome the energy of magnetic stabilization of the particle (Figure 2.8).

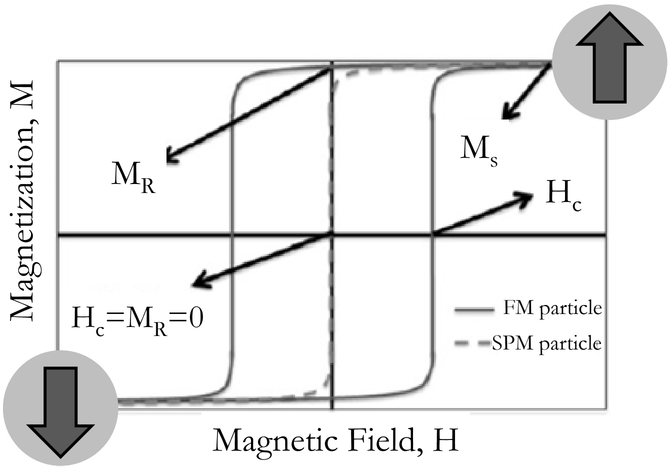

Figure 2.7. *Magnetization vs. magnetic field curve for superparamagnetic particles (SPM) and ferro- and ferrimagnetic particles (FM). Coercive field (H_c), saturation magnetization (M_s) and remanence magnetization are indicated. Adapted from Figuerola et. al.*[108]

The concept of superparamagnetism is intrinsically linked to the nanometer range. Superparamagnetic NPs are very suitable candidates for *in vivo* bioapplications since the absence of coercivity, among other reasons, prevents potential NP aggregation; in the context of *in vivo* experimentation, NPs aggregation represents a potential danger that can lead to embolisms.[108]

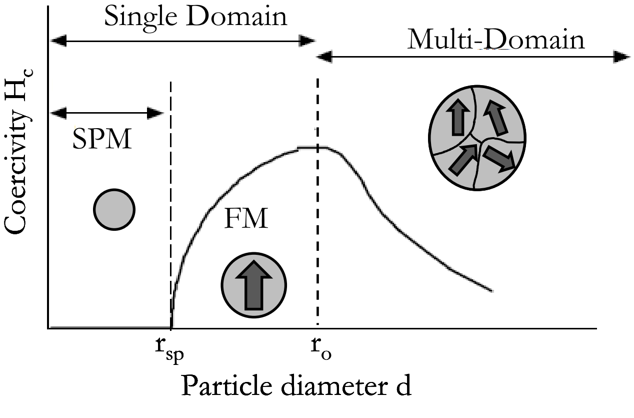

Figure 2.8. *Size-dependence of the coercivity showing the different regimes as the size of particles increases from the nano- to the micro-range. Adapted from Figuerola et al.*[108]

In principle, ferromagnetic and ferrimagnetic particles (FM particles, in the micrometric size range) release heat by the hysteresis loss mechanism; in these regimes, the heating efficiency comes determined here by the area of the hysteresis loop, which in turn, depends on three parameters given by the sample, *i.e.* coercivity, remanence and saturation at a given AMF (defined by values of magnetic field B_0 and frequency f); thus, the most efficient heater is the one that exhibits the greatest values of these three parameters.

Large FM particles contain several domains characterized by a variety of magnetization vectors. When FM particles are exposed to an applied magnetic field those domains "parallel" to the external field will "grow" whereas the remaining domains will "shrink"; this phenomenon gives rise to irreversible domain wall displacements, *i.e.* magnetization curves for increasing and decreasing magnetic field amplitudes are different (left panel in Figure 2.9). The heat produced per unit of volume is proportional to the hysteresis loop as shown in the following expression (Equation 2.2):

$$\mathrm{P_{FM}} = \mu_0 \mathrm{f} \oint \mathrm{H\delta M} \qquad (2.2)$$

where μ_0 and f are the magnetic permeability in vacuum and the applied frequency, respectively. According to equation (2.2), the value of P_{FM} can be experimentally determined with magnetometers of the type VSM (vibrating sample magnetometer) or SQUID (superconducting quantum interference device).

In single domain particles (superparamagnetic regime, in the nanosize range) the scenario changes drastically; heating due to hysteresis losses cannot occur due to the absence of domain walls. However, superparamagnetic nanoparticles (SPM-NPs) can produce heat by the Néel and/or Brown relaxations mechanisms; although both mechanisms can be present simultaneously, the fastest mechanism for a particular superparamagnetic material under AMF (defined by B_0 and f) will predominate in the heating process. Briefly, the Néel relaxation time depends on the anisotropic energy barrier (ΔE) between the parallel and antiparallel states (middle panel in Figure 2.9). Ultimately, ΔE is dictated by the anisotropy (material, surface and shape) and volume of the SPM-NPs. On the other hand, the Brown relaxation time depends on the probability of SPM-NPs to invert its magnetization by physically rotating in the medium (right panel in Figure 2.9); the ability to rotate depends on the viscosity of the immersion medium and the hydrodynamic radius of the SPM-NPs, *i.e.* inorganic core plus organic and hydration layers. In theory, there is a critical diameter at which both mechanisms contribute equally (same relaxation time). Above this critical size, Brownian heating will predominate whereas bellow it, Néel heating will apply.

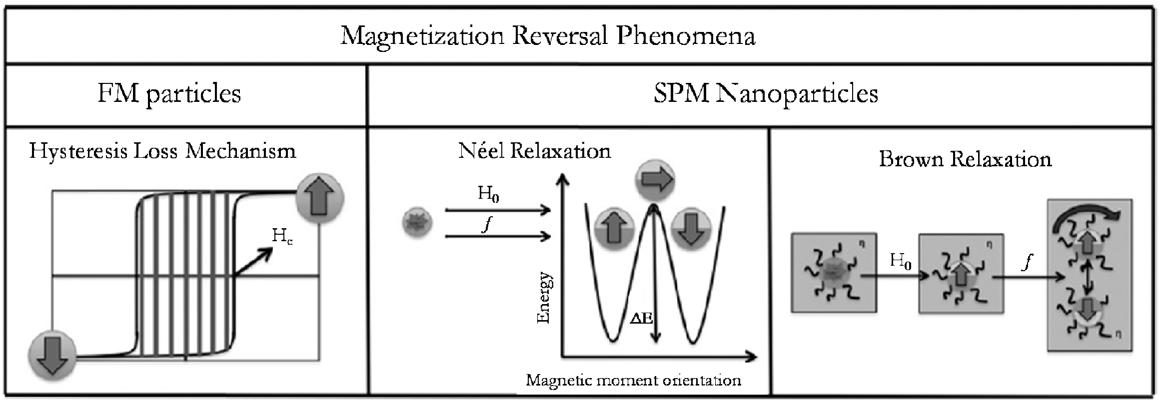

***Figure 2.9**. Relaxation processes involved in heating mechanism driven by AMF. Left panel, hysteresis losses in ferro- and ferromagnetic particles (FM); middle and right panels correspond to Néel and Brown relaxation processes in SPM-NPs, respectively. Adapted from Figuerola et al.*[108]

The heating ability of MNPs under AMF is defined by the parameter called specific absorption rate (SAR) which can be calculated with the following expression:

— (2.3)

where m is the amount of the magnetic material used in the assay, C is the specific heat capacity of the sample (both the nanoparticle material and the dispersion medium are considered) and $\Delta T/\Delta t$ is the initial slope of the temperature increment *vs.* time.

The heat produced per unit of volume (P_{FM} or P_{SPM}) can be experimentally obtained from the product of the SAR value and the concentration of NPs. It is very challenging to give a general theoretical expression of SAR due to the vast number of parameters which should be taken into account including size, size distribution, shape and chemical composition of the particles as well as the experimental conditions of AMF (B_0 and f).

Table 2.3 lists the SAR values corresponding to different iron oxide based NPs under different experimental conditions.

Magnetic NP			**Experimental conditions**			
Magnetic compound	Core diameter (nm)	Corona	H (kAm^{-1})	f (kHz)	Dispersion medium	SAR (W/g)
SD ferrite[109]	10-12	Dextran	7.2	880	Physiological solution	210±8
SD ferrite	6-12	Carboxymethyl dextran	7.2	880	Physiological solution	90±4
MD Fe_3O_4	100-150	None	7.2	880	Physiological solution	90±4
MD γ-Fe_2O_3	100-150	None	7.2	880	Physiological solution	42±3
SD Fe_3O_4 [110]	8	None	6.5	300	Water	21
Fe_3O_4 (Endorem®)	6	Dextran	6.5	300	Water	<0.1
SD γ-Fe_2O_3 [111]	3	Dextran	12.5	500	Water	106
SD γ-Fe_2O_3	5	Dextran	12.5	500	Water	524
SD γ-Fe_2O_3	7	Dextran	12.5	500	Water	626
Fe_3O_4	7.5	None	32.5	80	Water	15.6
Fe_3O_4	13	None	32.5	80	Water	39.4
Fe_3O_4	46	None	32.5	80	Water	75.6
Fe_3O_4	81	None	32.5	80	Water	63.7
Fe_3O_4	282	None	32.5	80	Water	32.5
Fe_3O_4	416	None	32.5	80	Water	28.9

Table 2.3. *SAR values for different iron oxide particles.*

Given the vast amount of parameters and AMF conditions to take into account regarding SAR values (Table 2.3), the answer is far from simple. In principle, SAR values of iron oxide particles vary following the same trend as the corresponding coercivity values (Figure 2.10).[112] In order to reach the maximum SAR values, the sample should be brought to saturation, which in the case of FM particles, usually requires very high magnetic fields (B_0), normally above 100 kA×m^{-1}. Besides the technical limitations to reach such AMF working conditions, there are also physiological limitations to the application of very high B_0 and f conditions since they can lead to damage of untargeted (without particles) healthy tissue. For *in vivo* experimentation, the general consensus is that the upper limit for B_0 and f are 15 kA×m^{-1} and 1.2 MHz, respectively; in addition the product $B_0 \times f$ should be below 5×10^9 A×(m×s)$^{-1}$.[10] For FM NPs, this limitation adds to the aforementioned possible problems associated with aggregation due to remanence after treatment and thus, limits the use of FM particles as hyperthermia agents.

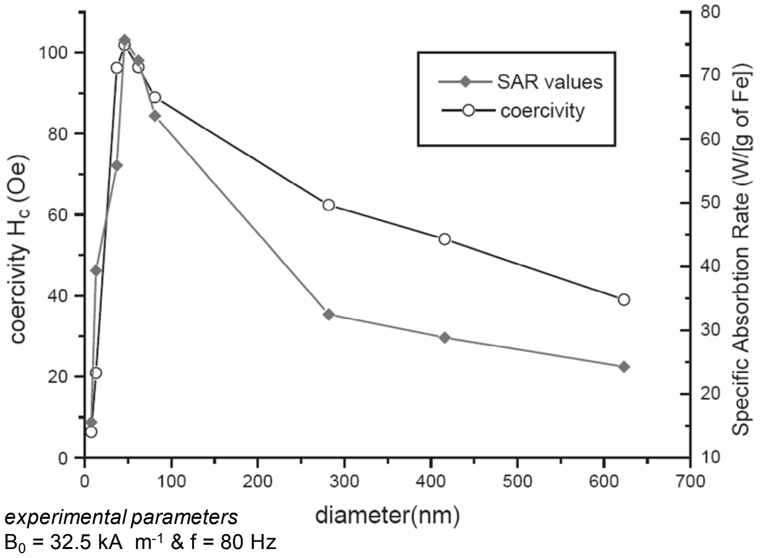

Figure 2.10. *Coercivity (H_C) and the SAR values as functions of the average particle diameters of magnetite (reproduced from Ma et al.).*[112]

In contrast, at "physiological AMF regimes", SPM-NPs in the range of 10-20 nm exhibit higher SAR values than their equivalent micrometric counterparts (FM particles), although larger NPs can achieve greater coercivity values.[112] Figure 2.11 shows theoretical (panel A) and experimental (panel B) SAR values for iron oxide NPs. In summary, SPM-NPs are the most suitable candidates for applications where a large value of SAR is required such as hyperthermia treatment or drug release mediated by heat.

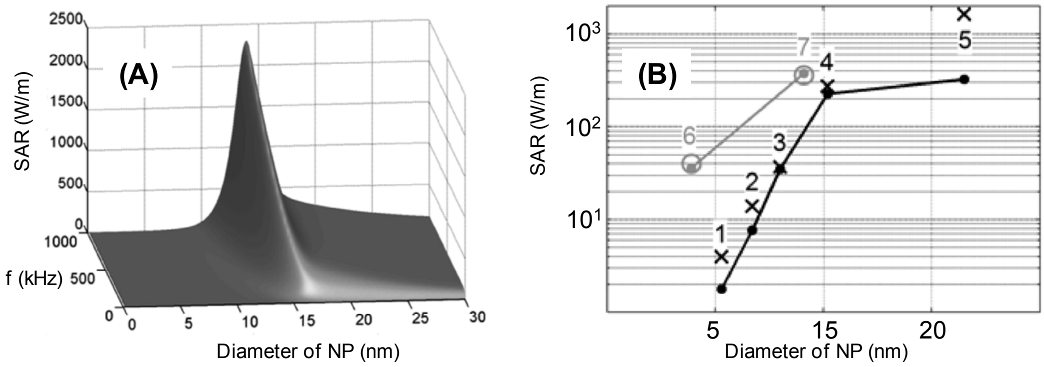

Figure 2.11. *(A) Theoretical SAR values of monodispersed iron oxide (maghemite) nanoparticles as a function of particle diameter and magnetic field frequency at a fixed field amplitude B_0 = 24.8 kA×m^{-1}. (B) Experimental SAR values for maghemite (1-5 black cross) and cobalt ferrite (6 and 7 gray circle) compared to the corresponding theoretical lines (black and gray solid lines). Reproduced from Fortin et al.*[8]

REFERENCES

(1) Gupta, A. K.; Gupta, M.: Synthesis and surface engineering of iron oxide nanoparticles for biomedical applications. *Biomaterials* **2005**, *26*, 3995-4021.

(2) Pankhurst, Q. A.; Connolly, J.; Jones, S. K.; Dobson, J.: Applications of magnetic nanoparticles in biomedicine. *Journal of Physics D-Applied Physics* **2003**, *36*, R167-R181.

(3) Neuberger, T.; Schopf, B.; Hofmann, H.; Hofmann, M.; von Rechenberg, B.: Superparamagnetic nanoparticles for biomedical applications: Possibilities and limitations of a new drug delivery system. *Journal of Magnetism and Magnetic Materials* **2005**, *293*, 483-496.

(4) Nasongkla, N.; Bey, E.; Ren, J. M.; Ai, H.; Khemtong, C.; Guthi, J. S.; Chin, S. F.; Sherry, A. D.; Boothman, D. A.; Gao, J. M.: Multifunctional polymeric micelles as cancer-targeted, MRI-ultrasensitive drug delivery systems. *Nano Letters* **2006**, *6*, 2427-2430.

(5) del Pino, P.; Munoz-Javier, A.; Vlaskou, D.; Rivera Gil, P.; Plank, C.; Parak, W. J.: Gene Silencing Mediated by Magnetic Lipospheres Tagged with Small Interfering RNA. *Nano Letters* **2010**, *10*, 3914-3921.

(6) Mykhaylyk, O.; Antequera, Y. S.; Vlaskou, D.; Plank, C.: Generation of magnetic nonviral gene transfer agents and magnetofection in vitro. *Nature Protocols* **2007**, *2*, 2391-2411.

(7) Schillinger, U.; Brill, T.; Rudolph, C.; Huth, S.; Gersting, S.; Krotz, F.; Hirschberger, J.; Bergemann, C.; Plank, C.: Advances in magnetofection - magnetically guided nucleic acid delivery. *Journal of Magnetism and Magnetic Materials* **2005**, *293*, 501-508.

(8) Fortin, J. P.; Wilhelm, C.; Servais, J.; Menager, C.; Bacri, J. C.; Gazeau, F.: Size-sorted anionic iron oxide nanomagnets as colloidal mediators for magnetic hyperthermia. *Journal of the American Chemical Society* **2007**, *129*, 2628-2635.

(9) Goya, G. F.; Grazu, V.; Ibarra, M. R.: Magnetic nanoparticles for cancer therapy. *Current Nanoscience* **2008**, *4*, 1-16.

(10) Hergt, R.; Dutz, S.: Magnetic particle hyperthermia-biophysical limitations of a visionary tumour therapy. *Journal of Magnetism and Magnetic Materials* **2007**, *311*, 187-192.

(11) Hergt, R.; Dutz, S.; Muller, R.; Zeisberger, M.: Magnetic particle hyperthermia: nanoparticle magnetism and materials development for cancer therapy. *Journal of Physics-Condensed Matter* **2006**, *18*, S2919-S2934.

(12) Johannsen, M.; Gneveckow, U.; Eckelt, L.; Feussner, A.; Waldofner, N.; Scholz, R.; Deger, S.; Wust, P.; Loening, S. A.; Jordan, A.: Clinical hyperthermia of prostate cancer using magnetic nanoparticles: Presentation of a new interstitial technique. *International Journal of Hyperthermia* **2005**, *21*, 637-647.

(13) Jordan, A.; Scholz, R.; Maier-Hauff, K.; van Landeghem, F. K. H.; Waldoefner, N.; Teichgraeber, U.; Pinkernelle, J.; Bruhn, H.; Neumann, F.; Thiesen, B.; von Deimling, A.; Felix, R.: The effect of thermotherapy using magnetic nanoparticles on rat malignant glioma. *Journal of Neuro-Oncology* **2006**, *78*, 7-14.

(14) Huh, Y. M.; Jun, Y. W.; Song, H. T.; Kim, S.; Choi, J. S.; Lee, J. H.; Yoon, S.; Kim, K. S.; Shin, J. S.; Suh, J. S.; Cheon, J.: In vivo magnetic resonance detection of cancer by using multifunctional magnetic nanocrystals. *Journal of the American Chemical Society* **2005**, *127*, 12387-12391.

(15) Lee, J. H.; Huh, Y. M.; Jun, Y.; Seo, J.; Jang, J.; Song, H. T.; Kim, S.; Cho, E. J.; Yoon, H. G.; Suh, J. S.; Cheon, J.: Artificially engineered magnetic nanoparticles for ultra-sensitive molecular imaging. *Nature Medicine* **2007**, *13*, 95-99.

(16) Martina, M. S.; Fortin, J. P.; Menager, C.; Clement, O.; Barratt, G.; Grabielle-Madelmont, C.; Gazeau, F.; Cabuil, V.; Lesieur, S.: Generation of superparamagnetic liposomes revealed as highly efficient MRI contrast agents for in vivo imaging. *Journal of the American Chemical Society* **2005**, *127*, 10676-10685.

(17) Mannix, R. J.; Kumar, S.; Cassiola, F.; Montoya-Zavala, M.; Feinstein, E.; Prentiss, M.; Ingber, D. E.: Nanomagnetic actuation of receptor-mediated signal transduction. *Nature Nanotechnology* **2008**, *3*, 36-40.

(18) Wang, S. X.; Li, G.: Advances in giant magnetoresistance biosensors with magnetic nanoparticle tags: Review and outlook. *Ieee Transactions on Magnetics* **2008**, *44*, 1687-1702.

(19) Ramadan, Q.; Samper, V.; Poenar, D.; Yu, C.: Magnetic-based microfluidic platform for biomolecular separation. *Biomedical Microdevices* **2006**, *8*, 151-158.

(20) Barakat, N. S.: Magnetically modulated nanosystems: a unique drug-delivery platform. *Nanomedicine* **2009**, *4*, 799-812.

(21) Erb, R. M.; Son, H. S.; Samanta, B.; Rotello, V. M.; Yellen, B. B.: Magnetic assembly of colloidal superstructures with multipole symmetry. *Nature* **2009**, *457*, 999-1002.

(22) Gazeau, F.; Levy, M.; Wilhelm, C.: Optimizing magnetic nanoparticle design for nanothermotherapy. *Nanomedicine* **2008**, *3*, 831-844.

(23) Thiesen, B.; Jordan, A.: Clinical applications of magnetic nanoparticles for hyperthermia. *International Journal of Hyperthermia* **2008**, *24*, 467-474.

(24) Derfus, A. M.; von Maltzahn, G.; Harris, T. J.; Duza, T.; Vecchio, K. S.; Ruoslahti, E.; Bhatia, S. N.: Remotely Triggered Release from Magnetic Nanoparticles. *Advanced Materials* **2007**, *19*, 3932-3936.

(25) Lee, J.-H.; Jang, J.-t.; Choi, J.-s.; Moon, S. H.; Noh, S.-h.; Kim, J.-w.; Kim, J.-G.; Kim, I.-S.; Park, K. I.; Cheon, J.: Exchange-coupled magnetic nanoparticles for efficient heat induction. *Nat Nano* **2011**, *6*, 418-422.

(26) Fortin, J. P.; Gazeau, F.; Wilhelm, C.: Intracellular heating of living cells through Neel relaxation of magnetic nanoparticles. *European Biophysics Journal with Biophysics Letters* **2008**, *37*, 223-228.

(27) Gao, J. H.; Gu, H. W.; Xu, B.: Multifunctional Magnetic Nanoparticles: Design, Synthesis, and Biomedical Applications. *Accounts of Chemical Research* **2009**, *42*, 1097-1107.

(28) Kim, J.; Piao, Y.; Hyeon, T.: Multifunctional nanostructured materials for multimodal imaging, and simultaneous imaging and therapy. *Chemical Society Reviews* **2009**, *38*, 372-390.

(29) Laurent, S.; Forge, D.; Port, M.; Roch, A.; Robic, C.; Elst, L. V.; Muller, R. N.: Magnetic iron oxide nanoparticles: Synthesis, stabilization, vectorization, physicochemical characterizations, and biological applications. *Chemical Reviews* **2008**, *108*, 2064-2110.

(30) Sun, C.; Lee, J. S. H.; Zhang, M. Q.: Magnetic nanoparticles in MR imaging and drug delivery. *Advanced Drug Delivery Reviews* **2008**, *60*, 1252-1265.

(31) Massart, R.; Cabuil, V.: EFFECT OF SOME PARAMETERS ON THE FORMATION OF COLLOIDAL MAGNETITE IN ALKALINE-MEDIUM - YIELD AND PARTICLE-SIZE CONTROL. *Journal De Chimie Physique Et De Physico-Chimie Biologique* **1987**, *84*, 967-973.

(32) Pedro, T.; María del Puerto, M.; Sabino, V.-V.; Teresita, G.-C.; Carlos, J. S.: The preparation of magnetic nanoparticles for applications in biomedicine. *Journal of Physics D: Applied Physics* **2003**, *36*, R182.

(33) Dave, S. R.; Gao, X.: Monodisperse magnetic nanoparticles for biodetection, imaging, and drug delivery: a versatile and evolving technology. *Wiley Interdisciplinary Reviews: Nanomedicine and Nanobiotechnology* **2009**, *1*, 583-609.

(34) Santra, S.; Tapec, R.; Theodoropoulou, N.; Dobson, J.; Hebard, A.; Tan, W.: Synthesis and Characterization of Silica-Coated Iron Oxide Nanoparticles in Microemulsion: The Effect of Nonionic Surfactants. *Langmuir* **2001**, *17*, 2900-2906.

(35) Lu, A.-H.; Salabas, E. L.; Schüth, F.: Magnetic Nanoparticles: Synthesis, Protection, Functionalization, and Application. *Angewandte Chemie International Edition* **2007**, *46*, 1222-1244.

(36) Ayyub, P.; Multani, M.; Barma, M.; Palkar, V. R.; Vijayaraghavan, R.: SIZE-INDUCED STRUCTURAL PHASE-TRANSITIONS AND HYPERFINE PROPERTIES OF MICROCRYSTALLINE FE2O3. *Journal of Physics C-Solid State Physics* **1988**, *21*, 2229-2245.

(37) Murray, C. B.; Norris, D. J.; Bawendi, M. G.: Synthesis and characterization of nearly monodisperse CdE (E = sulfur, selenium, tellurium) semiconductor nanocrystallites. *Journal of the American Chemical Society* **1993**, *115*, 8706-8715.

(38) Rockenberger, J.; Scher, E. C.; Alivisatos, A. P.: A New Nonhydrolytic Single-Precursor Approach to Surfactant-Capped Nanocrystals of Transition Metal Oxides. *Journal of the American Chemical Society* **1999**, *121*, 11595-11596.

(39) Hyeon, T.; Lee, S. S.; Park, J.; Chung, Y.; Na, H. B.: Synthesis of Highly Crystalline and Monodisperse Maghemite Nanocrystallites without a Size-Selection Process. *Journal of the American Chemical Society* **2001**, *123*, 12798-12801.

(40) Sun, S. H.; Zeng, H.; Robinson, D. B.; Raoux, S.; Rice, P. M.; Wang, S. X.; Li, G. X.: Monodisperse MFe2O4 (M = Fe, Co, Mn) nanoparticles. *Journal of the American Chemical Society* **2004**, *126*, 273-279.

(41) Park, J.; An, K.; Hwang, Y.; Park, J.-G.; Noh, H.-J.; Kim, J.-Y.; Park, J.-H.; Hwang, N.-M.; Hyeon, T.: Ultra-large-scale syntheses of monodisperse nanocrystals. *Nat Mater* **2004**, *3*, 891-895.

(42) Carbone, L.; Cozzoli, P. D.: Colloidal heterostructured nanocrystals: Synthesis and growth mechanisms. *Nano Today* **2010**, *5*, 449-493.

(43) Levin, C. S.; Hofmann, C.; Ali, T. A.; Kelly, A. T.; Morosan, E.; Nordlander, P.; Whitmire, K. H.; Halas, N. J.: Magnetic-Plasmonic Core-Shell Nanoparticles. *ACS Nano* **2009**, *3*, 1379-1388.

(44) Costi, R.; Saunders, A. E.; Banin, U.: Colloidal Hybrid Nanostructures: A New Type of Functional Materials. *Angewandte Chemie-International Edition* **2010**, *49*, 4878-4897.

(45) Shevchenko, E. V.; Talapin, D. V.; Kotov, N. A.; O'Brien, S.; Murray, C. B.: Structural diversity in binary nanoparticle superlattices. *Nature* **2006**, *439*, 55-59.

(46) Urban, J. J.; Talapin, D. V.; Shevchenko, E. V.; Kagan, C. R.; Murray, C. B.: Synergism in binary nanocrystal superlattices leads to enhanced p-type conductivity in self-assembled PbTe/Ag2Te thin films. *Nat Mater* **2007**, *6*, 115-121.

(47) Wu, W.; He, Q. G.; Jiang, C. Z.: Magnetic Iron Oxide Nanoparticles: Synthesis and Surface Functionalization Strategies. *Nanoscale Research Letters* **2008**, *3*, 397-415.

(48) Wang, L. Y.; Luo, J.; Fan, Q.; Suzuki, M.; Suzuki, I. S.; Engelhard, M. H.; Lin, Y. H.; Kim, N.; Wang, J. Q.; Zhong, C. J.: Monodispersed core-shell Fe3O4@Au nanoparticles. *Journal of Physical Chemistry B* **2005**, *109*, 21593-21601.

(49) Carpenter, E. E.; Sangregorio, C.; O'Connor, C. J.: Effects of shell thickness on blocking temperature of nanocomposites of metal particles with gold shells. *Ieee Transactions on Magnetics* **1999**, *35*, 3496-3498.

(50) Cho, S. J.; Idrobo, J. C.; Olamit, J.; Liu, K.; Browning, N. D.; Kauzlarich, S. M.: Growth mechanisms and oxidation resistance of gold-coated iron nanoparticles. *Chemistry of Materials* **2005**, *17*, 3181-3186.

(51) Mikhaylova, M.; Kim, D. K.; Bobrysheva, N.; Osmolowsky, M.; Semenov, V.; Tsakalakos, T.; Muhammed, M.: Superparamagnetism of magnetite nanoparticles: Dependence on surface modification. *Langmuir* **2004**, *20*, 2472-2477.

(52) Lyon, J. L.; Fleming, D. A.; Stone, M. B.; Schiffer, P.; Williams, M. E.: Synthesis of Fe oxide core/Au shell nanoparticles by iterative hydroxylamine seeding. *Nano Letters* **2004**, *4*, 719-723.

(53) Kumar, C.; Mohammad, F.: Magnetic nanomaterials for hyperthermia-based therapy and controlled drug delivery. *Advanced Drug Delivery Reviews* **2011**, *63*, 789-808.

(54) Habib, A. H.; Ondeck, C. L.; Chaudhary, P.; Bockstaller, M. R.; McHenry, M. E.: Evaluation of iron-cobalt/ferrite core-shell nanoparticles for cancer thermotherapy. *Journal of Applied Physics* **2008**, *103*.

(55) Sun, S.; Zeng, H.; Robinson, D. B.; Raoux, S.; Rice, P. M.; Wang, S. X.; Li, G.: Monodisperse MFe2O4 (M = Fe, Co, Mn) Nanoparticles. *Journal of the American Chemical Society* **2003**, *126*, 273-279.

(56) Leung, K. C.-F.; Xuan, S.; Zhu, X.; Wang, D.; Chak, C.-P.; Lee, S.-F.; Ho, W. K. W.; Chung, B. C. T.: Gold and iron oxide hybrid nanocomposite materials. *Chemical Society Reviews* **2012**.

(57) Pellegrino, T.; Manna, L.; Kudera, S.; Liedl, T.; Koktysh, D.; Rogach, A. L.; Keller, S.; Radler, J.; Natile, G.; Parak, W. J.: Hydrophobic nanocrystals coated with an amphiphilic polymer shell: A general route to water soluble nanocrystals. *Nano Letters* **2004**, *4*, 703-707.

(58) Pellegrino, T.; Kudera, S.; Liedl, T.; Javier, A. M.; Manna, L.; Parak, W. J.: On the development of colloidal nanoparticles towards multifunctional structures and their possible use for biological applications. *Small* **2005**, *1*, 48-63.

(59) Giersig, M.; Liz-Marzan, L. M.; Ung, T.; Su, D. S.; Mulvaney, P.: Chemistry of nanosized silica-coated metal particles EM-study. *Berichte Der Bunsen-Gesellschaft-Physical Chemistry Chemical Physics* **1997**, *101*, 1617-1620.

(60) Verma, A.; Uzun, O.; Hu, Y.; Hu, Y.; Han, H.-S.; Watson, N.; Chen, S.; Irvine, D. J.; Stellacci, F.: Surface-structure-regulated cell-membrane penetration by monolayer-protected nanoparticles. *Nat Mater* **2008**, *7*, 588-595.

(61) Nel, A. E.; Madler, L.; Velegol, D.; Xia, T.; Hoek, E. M. V.; Somasundaran, P.; Klaessig, F.; Castranova, V.; Thompson, M.: Understanding biophysicochemical interactions at the nano-bio interface. *Nat Mater* **2009**, *8*, 543-557.

(62) Moros, M.; Pelaz, B.; Lopez-Larrubia, P.; Garcia-Martin, M. L.; Grazu, V.; de la Fuente, J. M.: Engineering biofunctional magnetic nanoparticles for biotechnological applications. *Nanoscale* **2010**, *2*, 1746-1755.

(63) Rocker, C.; Potzl, M.; Zhang, F.; Parak, W. J.; Nienhaus, G. U.: A quantitative fluorescence study of protein monolayer formation on colloidal nanoparticles. *Nat Nano* **2009**, *4*, 577-580.

(64) Gref, R.; Lück, M.; Quellec, P.; Marchand, M.; Dellacherie, E.; Harnisch, S.; Blunk, T.; Müller, R. H.: 'Stealth' corona-core nanoparticles surface modified by polyethylene glycol (PEG): influences of the corona (PEG chain length and surface density) and of the core composition on phagocytic uptake and plasma protein adsorption. *Colloids and Surfaces B: Biointerfaces* **2000**, *18*, 301-313.

(65) Linse, S.; Cabaleiro-Lago, C.; Xue, W.-F.; Lynch, I.; Lindman, S.; Thulin, E.; Radford, S. E.; Dawson, K. A.: Nucleation of protein fibrillation by nanoparticles. *Proceedings of the National Academy of Sciences* **2007**, *104*, 8691-8696.

(66) Walczyk, D.; Bombelli, F. B.; Monopoli, M. P.; Lynch, I.; Dawson, K. A.: What the Cell "Sees" in Bionanoscience. *Journal of the American Chemical Society* **2010**, *132*, 5761-5768.

(67) Monopoli, M. P.; Walczyk, D.; Campbell, A.; Elia, G.; Lynch, I.; Baldelli Bombelli, F.; Dawson, K. A.: Physical−Chemical Aspects of Protein Corona: Relevance to in Vitro and in Vivo Biological Impacts of Nanoparticles. *Journal of the American Chemical Society* **2011**, *133*, 2525-2534.

(68) Alkilany, A. M.; Nagaria, P. K.; Hexel, C. R.; Shaw, T. J.; Murphy, C. J.; Wyatt, M. D.: Cellular Uptake and Cytotoxicity of Gold Nanorods: Molecular Origin of Cytotoxicity and Surface Effects. *Small* **2009**, *5*, 701-708.

(69) Chithrani, B. D.; Ghazani, A. A.; Chan, W. C. W.: Determining the Size and Shape Dependence of Gold Nanoparticle Uptake into Mammalian Cells. *Nano Letters* **2006**, *6*, 662-668.

(70) Zhao, F.; Zhao, Y.; Liu, Y.; Chang, X.; Chen, C.; Zhao, Y.: Cellular Uptake, Intracellular Trafficking, and Cytotoxicity of Nanomaterials. *Small* **2011**, *7*, 1322-1337.

(71) Deng, Z. J.; Liang, M.; Monteiro, M.; Toth, I.; Minchin, R. F.: Nanoparticle-induced unfolding of fibrinogen promotes Mac-1 receptor activation and inflammation. *Nat Nano* **2011**, *6*, 39-44.

(72) Lacerda, S. H. D. P.; Park, J. J.; Meuse, C.; Pristinski, D.; Becker, M. L.; Karim, A.; Douglas, J. F.: Interaction of Gold Nanoparticles with Common Human Blood Proteins. *ACS Nano* **2009**, *4*, 365-379.

(73) Xie, J.; Xu, C.; Kohler, N.; Hou, Y.; Sun, S.: Controlled PEGylation of Monodisperse Fe3O4 Nanoparticles for Reduced Non-Specific Uptake by Macrophage Cells. *Advanced Materials* **2007**, *19*, 3163-3166.

(74) Hauck, T. S.; Ghazani, A. A.; Chan, W. C. W.: Assessing the Effect of Surface Chemistry on Gold Nanorod Uptake, Toxicity, and Gene Expression in Mammalian Cells. *Small* **2008**, *4*, 153-159.

(75) Bao, Z. H.; Sun, Z. H.; Li, Z. F.; Tian, L. W.; Ngai, T.; Wang, J. F.: Plasmonic Gold-Superparamagnetic Hematite Heterostructures. *Langmuir* **2011**, *27*, 5071-5075.

(76) Wang, C.; Xu, C. J.; Zeng, H.; Sun, S. H.: Recent Progress in Syntheses and Applications of Dumbbell-like Nanoparticles. *Advanced Materials* **2009**, *21*, 3045-3052.

(77) Wang, C.; Yin, H. F.; Dai, S.; Sun, S. H.: A General Approach to Noble Metal-Metal Oxide Dumbbell Nanoparticles and Their Catalytic Application for CO Oxidation. *Chemistry of Materials* **2010**, *22*, 3277-3282.

(78) Brigger, I.; Dubernet, C.; Couvreur, P.: Nanoparticles in cancer therapy and diagnosis. *Advanced Drug Delivery Reviews* **2002**, *54*, 631-651.

(79) Kievit, F. M.; Zhang, M.: Surface Engineering of Iron Oxide Nanoparticles for Targeted Cancer Therapy. *Accounts of Chemical Research* **2011**, *44*, 853-862.

(80) Jana, N. R.; Gearheart, L.; Murphy, C. J.: Wet chemical synthesis of high aspect ratio cylindrical gold nanorods. *Journal of Physical Chemistry B* **2001**, *105*, 4065-4067.

(81) Boisselier, E.; Astruc, D.: Gold nanoparticles in nanomedicine: preparations, imaging, diagnostics, therapies and toxicity. *Chemical Society Reviews* **2009**, *38*, 1759-1782.

(82) Bell, C. S.; Yu, S. S.; Giorgio, T. D.: The Multistrata Nanoparticle: an FeOx/Au Core/Shell Enveloped in a Silica-Au Shell. *Small* **2011**, *7*, 1158-1162.

(83) Bardhan, R.; Chen, W. X.; Perez-Torres, C.; Bartels, M.; Huschka, R. M.; Zhao, L. L.; Morosan, E.; Pautler, R. G.; Joshi, A.; Halas, N. J.: Nanoshells with Targeted Simultaneous Enhancement of Magnetic and Optical Imaging and Photothermal Therapeutic Response. *Advanced Functional Materials* **2009**, *19*, 3901-3909.

(84) Garcia, I.; Gallo, J.; Genicio, N.; Padro, D.; Penades, S.: Magnetic Glyconanoparticles as a Versatile Platform for Selective Immunolabeling and Imaging of Cells. *Bioconjugate Chemistry* **2011**, *22*, 264-273.

(85) Cole, A. J.; Yang, V. C.; David, A. E.: Cancer theranostics: the rise of targeted magnetic nanoparticles. *Trends in Biotechnology* **2011**, *29*, 323-332.

(86) Lim, Y. T.; Cho, M. Y.; Kim, J. K.; Hwangbo, S.; Chung, B. H.: Plasmonic magnetic nanostructure for bimodal imaging and photonic-based therapy of cancer cells. *Chembiochem* **2007**, *8*, 2204-2209.

(87) McCarthy, J. R.; Weissleder, R.: Multifunctional magnetic nanoparticles for targeted imaging and therapy. *Advanced Drug Delivery Reviews* **2008**, *60*, 1241-1251.

(88) Rai, P.; Mallidi, S.; Zheng, X.; Rahmanzadeh, R.; Mir, Y.; Elrington, S.; Khurshid, A.; Hasan, T.: Development and applications of photo-triggered theranostic agents. *Advanced Drug Delivery Reviews* **2010**, *62*, 1094-1124.

(89) Kamei, K.; Mukai, Y.; Kojima, H.; Yoshikawa, T.; Yoshikawa, M.; Kiyohara, G.; Yamamoto, T. A.; Yoshioka, Y.; Okada, N.; Seino, S.; Nakagawa, S.: Direct cell entry of gold/iron-oxide magnetic nanoparticles in adenovirus mediated gene delivery. *Biomaterials* **2009**, *30*, 1809-1814.

(90) Wei, Q.; Xiang, Z.; He, J.; Wang, G. L.; Li, H.; Qian, Z. Y.; Yang, M. H.: Dumbbell-like Au-Fe(3)O(4) nanoparticles as label for the preparation of electrochemical immunosensors. *Biosensors & Bioelectronics* **2010**, *26*, 627-631.

(91) Zhuo, Y.; Yuan, P. X.; Yuan, R.; Chai, Y. Q.; Hong, C. L.: Bienzyme functionalized three-layer composite magnetic nanoparticles for electrochemical immunosensors. *Biomaterials* **2009**, *30*, 2284-2290.

(92) Qiu, J. D.; Peng, H. P.; Liang, R. P.; Xia, X. H.: Facile preparation of magnetic core-shell Fe(3)O(4)@Au nanoparticle/myoglobin biofilm for direct electrochemistry. *Biosensors & Bioelectronics* **2010**, *25*, 1447-1453.

(93) Yigit, M. V.; Zhu, L. Y.; Ifediba, M. A.; Zhang, Y.; Carr, K.; Moore, A.; Medarova, Z.: Noninvasive MRI-SERS Imaging in Living Mice Using an Innately Bimodal Nanomaterial. *Acs Nano* **2011**, *5*, 1056-1066.

(94) Zhao, J.; Zhang, Y. Y.; Li, H. T.; Wen, Y. Q.; Fan, X. Y.; Lin, F. B.; Tan, L. A.; Yao, S. Z.: Ultrasensitive electrochemical aptasensor for thrombin based on the amplification of aptamer-AuNPs-HRP conjugates. *Biosensors & Bioelectronics* **2011**, *26*, 2297-2303.

(95) Liu, H. L.; Sonn, C. H.; Wu, J. H.; Lee, K. M.; Kim, Y. K.: Synthesis of streptavidin-FITC-conjugated core-shell Fe3O4-Au nanocrystals and their application for the purification of CD4(+) lymphocytes. *Biomaterials* **2008**, *29*, 4003-4011.

(96) Wang, C. G.; Irudayaraj, J.: Multifunctional Magnetic-Optical Nanoparticle Probes for Simultaneous Detection, Separation, and Thermal Ablation of Multiple Pathogens. *Small* **2010**, *6*, 283-289.

(97) Liu, Y.; Jia, C. J.; Yamasaki, J.; Terasaki, O.; Schuth, F.: Highly Active Iron Oxide Supported Gold Catalysts for CO Oxidation: How Small Must the Gold Nanoparticles Be? *Angewandte Chemie-International Edition* **2010**, *49*, 5771-5775.

(98) Edwards, J. K.; Solsona, B.; Landon, P.; Carley, A. F.; Herzing, A.; Watanabe, M.; Kiely, C. J.; Hutchings, G. J.: Direct synthesis of hydrogen peroxide from H-2 andO(2) using Au-Pd/Fe2O3 catalysts. *Journal of Materials Chemistry* **2005**, *15*, 4595-4600.

(99) Lee, Y. M.; Garcia, M. A.; Huls, N. A. F.; Sun, S. H.: Synthetic Tuning of the Catalytic Properties of Au-Fe(3)O(4) Nanoparticles. *Angewandte Chemie-International Edition* **2010**, *49*, 1271-1274.

(100) Ge, J. P.; Huynh, T.; Hu, Y. P.; Yin, Y. D.: Hierarchical magnetite/silica nanoassemblies as magnetically recoverable catalyst-supports. *Nano Letters* **2008**, *8*, 931-934.

(101) Kim, D.; Yu, M. K.; Lee, T. S.; Park, J. J.; Jeong, Y. Y.; Jon, S.: Amphiphilic polymer-coated hybrid nanoparticles as CT/MRI dual contrast agents. *Nanotechnology* **2011**, *22*.

(102) Cherukuri, P.; Glazer, E. S.; Curleya, S. A.: Targeted hyperthermia using metal nanoparticles. *Advanced Drug Delivery Reviews* **2010**, *62*, 339-345.

(103) Gilchrist, R. K.; Medal, R.; Shorey, W. D.; Hanselman, R. C.; Parrott, J. C.; Taylor, C. B.: SELECTIVE INDUCTIVE HEATING OF LYMPH NODES. *Annals of Surgery* **1957**, *146*, 596-606.

(104) Gordon, R. T.; Hines, J. R.; Gordon, D.: Intracellular hyperthermia a biophysical approach to cancer treatment via intracellular temperature and biophysical alterations. *Medical Hypotheses* **1979**, *5*, 83-102.

(105) Jordan, A.; Scholz, R.; Maier-Hauff, K.; Johannsen, M.; Wust, P.; Nadobny, J.; Schirra, H.; Schmidt, H.; Deger, S.; Loening, S.; Lanksch, W.; Felix, R.: Presentation of a new magnetic field therapy system for the treatment of human solid tumors with magnetic fluid hyperthermia. *Journal of Magnetism and Magnetic Materials* **2001**, *225*, 118-126.

(106) Jordan, A.; Scholz, R.; Wust, P.; Fahling, H.; Felix, R.: Magnetic fluid hyperthermia (MFH): Cancer treatment with AC magnetic field induced excitation of biocompatible superparamagnetic nanoparticles. *Journal of Magnetism and Magnetic Materials* **1999**, *201*, 413-419.

(107) Maier-Hauff, K.; Ulrich, F.; Nestler, D.; Niehoff, H.; Wust, P.; Thiesen, B.; Orawa, H.; Budach, V.; Jordan, A.: Efficacy and safety of intratumoral thermotherapy using magnetic iron-oxide nanoparticles combined with external beam radiotherapy on patients with recurrent glioblastoma multiforme. *Journal of Neuro-Oncology* **2011**, *103*, 317-324.

(108) Figuerola, A.; Di Corato, R.; Manna, L.; Pellegrino, T.: From iron oxide nanoparticles towards advanced iron-based inorganic materials designed for biomedical applications. *Pharmacological Research* **2010**, *62*, 126-143.

(109) Bogdanov, A. A.; Martin, C.; Weissleder, R.; Brady, T. J.: TRAPPING OF DEXTRAN-COATED COLLOIDS IN LIPOSOMES BY TRANSIENT BINDING TO AMINOPHOSPHOLIPID - PREPARATION OF FERROSOMES. *Biochimica Et Biophysica Acta-Biomembranes* **1994**, *1193*, 212-218.

(110) Hergt, R.; Andra, W.; d'Ambly, C. G.; Hilger, I.; Kaiser, W. A.; Richter, U.; Schmidt, H. G.: Physical limits of hyperthermia using magnetite fine particles. *Ieee Transactions on Magnetics* **1998**, *34*, 3745-3754.

(111) Chan, D. C. F.; Kirpotin, D. B.; Bunn, P. A.: *Physical chemistry and in vivo tissue heating properties of colloidal magnetic iron oxides with increased power absorption rates*, 1997.

(112) Ma, M.; Wu, Y.; Zhou, J.; Sun, Y.; Zhang, Y.; Gu, N.: Size dependence of specific power absorption of Fe3O4 particles in AC magnetic field. *Journal of Magnetism and Magnetic Materials* **2004**, *268*, 33-39.

Synthesis & Characterization of Fe_3O_4@Au NPs

Chapter 3

The main aim of this chapter is the development of superparamagnetic nanocomposites which surface (metallic Au) prevents the oxidation and degradation of the superparamagnetic core and furthermore, can be easily hybridized with an organic functional coating based on thiolated chains. The surface modifications addressed herein include: (i) molecules for surface passivation which will give to the nanocomposites stability in physiological media and (ii) biomolecules such as peptides and carbohydrates which will add biological activity. These biomolecules define the nanocomposites regarding the interaction cell-material. Once achieved the final hybridized nanocomposites, the superparamagnetic character of these nanocomposites will be evaluated for the following applications: (i) as carriers to shuttle "drugs" into cells and (ii) as nanoheaters (hyperthermia agents).

3.1. Synthesis of Fe_3O_4@Au

Herein the synthetic method followed to obtain Fe_3O_4@Au NPs is briefly discussed.[1] The first step is the synthesis of the core, iron oxide "seeds" of *ca.* 4 nm, by thermal decomposition of iron (III) acetylacetonate ($Fe(acac)_3$) following a modified synthetic route of the popular method originally described by Sun and coworkers.[2] Briefly, $Fe(acac)_3$ is dissolved, under argon atmosphere with vigorous stirring, in diphenyl ether in the presence of 1,2-hexadecanediol, oleic acid, and oleylamine (Figure 3.1.(a)); the solution was then heated to 210 °C and refluxed for 2 h. 1,2-Hexadecanediol functions as an organic reducing agent to facilitate the formation of Fe_3O_4 NPs. The decomposition is done in presence of oleic acid and oleylamine which ultimately act as surfactants; whether oleylamine act here as reductant remains unclear though.[3] In literature, there are many variations of this method where the solvent, molar ratio of surfactants and heating rates, among other synthetic parameters, play a determining role in the characteristics of the resulting NPs.[4] The combination of synthetic parameters used here was chosen due to the high monodispersity of the resulting NPs.

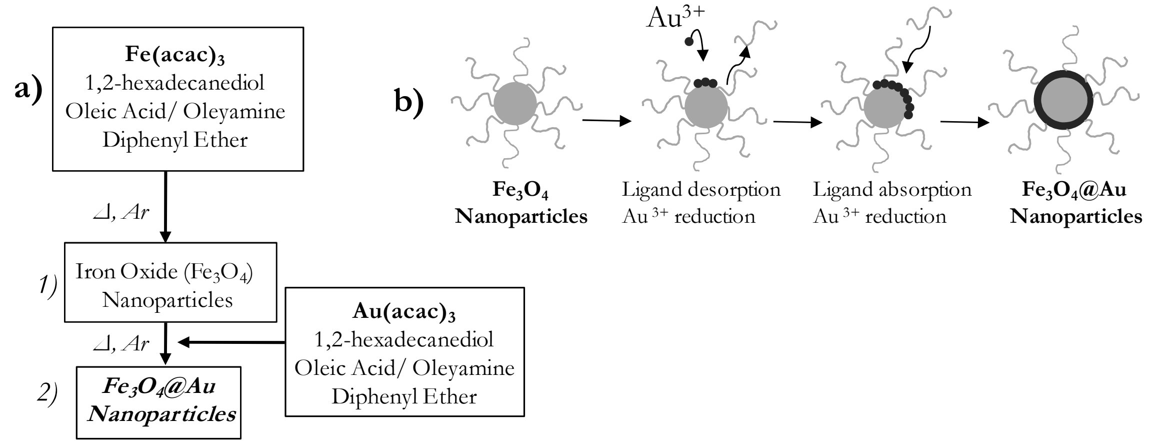

Figure 3.1. *a) Scheme of the synthesis of Fe_3O_4@Au (MGNPs). b) Graph of gold coating of iron oxide nanoparticles (adapted from Wang).*[1]

The second component of this nanocomposite is a shell *ca.* 3 nm made of metallic gold. Likewise, this shell is produced by thermal decomposition of gold acetate ($Au(OOCCH_3)_3$) and subsequent deposition of metallic gold on top of the previously formed Fe_3O_4 seeds (experimental details can be found in Annex A). Ethanol was added into the solution and a dark-purple material was precipitated and separated by centrifuging. The precipitated product was washed with ethanol, and redispersed in hexane in the presence of oleic acid and oleylamine. The NPs solution appeared dark purple, which can be speculatively interpreted as a sign for the successful grow of a metallic gold coating.

The size of the "seeds" and the final product, in hexane, were characterized by electron microscopy (Figure 3.2); Fe_3O_4 cores presented an average diameter of 3.9±0.8 nm whereas Fe_3O_4@Au NPs (supposed product) had an average diameter of 6.7±0.9 nm. Transmission electron micrographs showed the presence of Au-uncoated iron oxide NPs (Figure 3.2, panel d). However, most of the "seeds" appeared to be coated by Au as both the contrast and the size of the final product are homogeneous. This new Au shell provides the NPs with optical features, *i.e.* a surface plasmon resonance (SPR) band centered at 524 nm; this band was not present in the naked iron oxide nuclei. Importantly, a plasmon band at ca. 524 nm is indicative of solid Au NPs of diameter larger than 20 nm;[5] this argument can be used speculatively to claim the iron oxide@gold core@shell structure.

Given the average diameters of the "seeds" and the final NPs, 3.9 nm and 6.7 nm, respectively, the resultant NPs should have a constituents ratio [Au : Fe_3O_4] of *ca.* 4:1 (in volume), taken into consideration geometrical calculations.

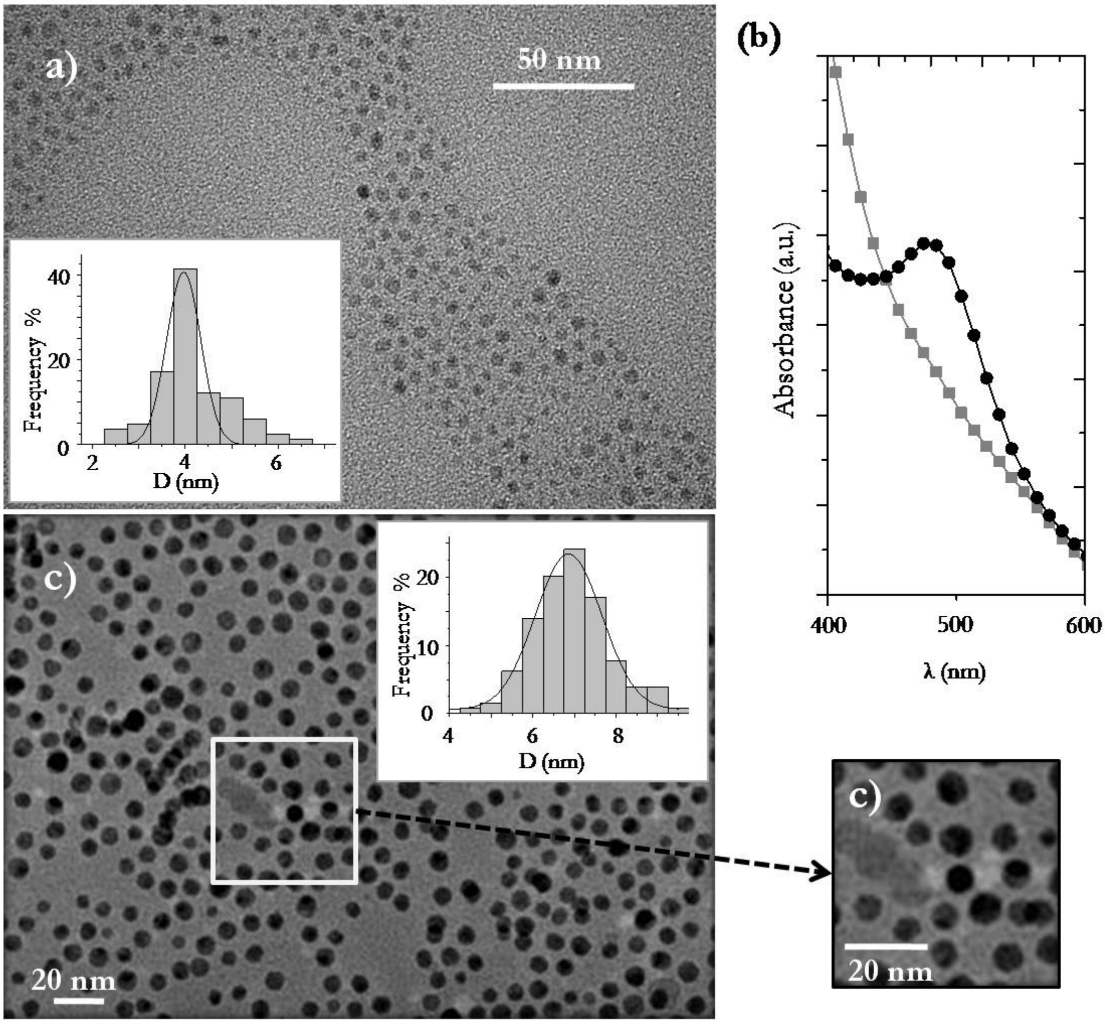

Figure 3.2. *TEM micrographs and corresponding histograms of b) Fe_3O_4 NPs and c) Fe_3O_4@Au NPs; b) UV/Vis spectra of Fe_3O_4 NPs (gray line) and Fe_3O_4@Au NPs in hexane; d) inset from c) where it is possible to distinguish uncoated iron oxide NPs.*

3.2. Water transfer of Fe_3O_4@Au NPs

In the context of applications of engineered NPs to biology and medicine, water transfer of non-polar soluble NPs is the most critical step as it is required for actually using the NPs in physiological-related fluids. [6,7] In this work, for the newly engineered Fe_3O_4@Au NPs in organic solvent, the approach to water transfers these NPs involve the formation of gold-sulfide bonds between the metallic shell of the NPs and on demand thiolated chains. The nature of this kind of bond is still matter of debate; however, the most widely accepted explanation for the formation of the Au-S bond is assuming its nature as a dative covalent bond. This kind of chemistry has been extensively used to attach a variety of thiolated molecules to Au^0 surfaces which are then referred to as monolayer protected surfaces. [6]The key of the success to water transfer Fe_3O_4@Au NPs is to protect the Au^0 shell with a monolayer of hydrophilic (at least partially) thiolated chains; thus, it is crucial the proper orientation of the thiol group onto Au^0 surface to achieve monolayer protected NPs. Herein, the general procedure proposed consists of mixing equal volumes of a hexane solution containing the NPs and a water solution containing the thiolated chains.[8] In the following the strategies used here to achieve monolayer protected NPs are described:

(i) The use of sodium borohydride to reduce thiol groups with the aim of preventing the formation of disulfide bonds between thiolated chains. To improve the miscibility of the two phases, vigorous shaking was used. This strategy allowed to water-transfer the NPs in the time course of days until the colors of the two phases interchange completely, *i.e.* the hexane and water phases turned colorless dark purple, respectively. Alternatively, the use of ultrasounds as shaking source speeds up the water-transfer, thus the reaction occurs in the time course of 2 hours.

(ii) The use of thiolated chains of the type mixed chains containing an aliphatic chain of eleven carbons and a hydrophilic part consisting on a tetraethylene glycol chain. The aliphatic part is ended by a thiol group whereas the hydrophilic was oxidized to get a carboxylic group for further chemical modifications with carbohydrates. By using mixed chains, the gold-sulfide interaction is promoted by the amphipathic nature of the ligand which directs the thiol group towards the non-polar phase.

Table 3.1 summarizes the different samples obtained by the methods aforementioned.

Sample	Chain	Transfer Method
PEG	HS-PEG(7)-OMe	(ii)Ultrasound/$NaBH_4$
MUA	11-Mercaptoundecanoic Acid (MUA)	(ii)Ultrasound/$NaBH_4$
CM-OH	Hydroxylated Mix Chain	(i)Vigorous Shaking$NaBH_4$
CM-CO_2H	Carboxylated Mix Chain	(i)Vigorous Shaking/$NaBH_4$
CM-Glc	Glucosylated Mix Chain	(i)Vigorous Shaking/$NaBH_4$
CM-Gal	Galactosylated Mix Chain	(i)Vigorous Shaking /$NaBH_4$
CM-Cellob	Cellobyose Modified Mix Chain	(i)Vigorous Shaking/$NaBH_4$
CM-Lacto	Lactose Modified Mix Chain	(i)Vigorous Shaking/$NaBH_4$

Table 3.1. *List of samples water-transferred by thiolated chains.*

MUA & PEG samples

For samples where ultrasound was used to water-transfer the NPs (samples PEG and MUA in Table 3.1), NPs in the water phase appeared to be aggregates made of iron oxide and newly formed gold nanoparticles (Figure 3.3) embedded in organic micelle-like structures. The formation of water-transferred aggregates can only be explained as result of the reduction of the Au-shell by the sodium borohydride, further enhanced by ultrasound application for extended periods of time.[9] As result of the formation of aggregates, the LSPR band red-shifts to 570 nm and 583 nm for aggregates capped by PEG and MUA, respectively (Figure 3.3a); note that the original NPs before water-transfer exhibited the plasmon band at 524 nm (Figure 3.3b). High resolution (HR) electron microscopy confirmed the heterogeneous composition of MUA and PEG samples; electron microscopy micrographs showed the presence of heterogeneous composites made of iron oxide and gold (Figure 3.7 b-d). Moreover, ICP analysis confirmed the inorganic weight (iron oxide and gold) to be extraordinarily low; this evidence is in agreement with the presence of organic micelle-like structures capable of stabilizing these aggregates.

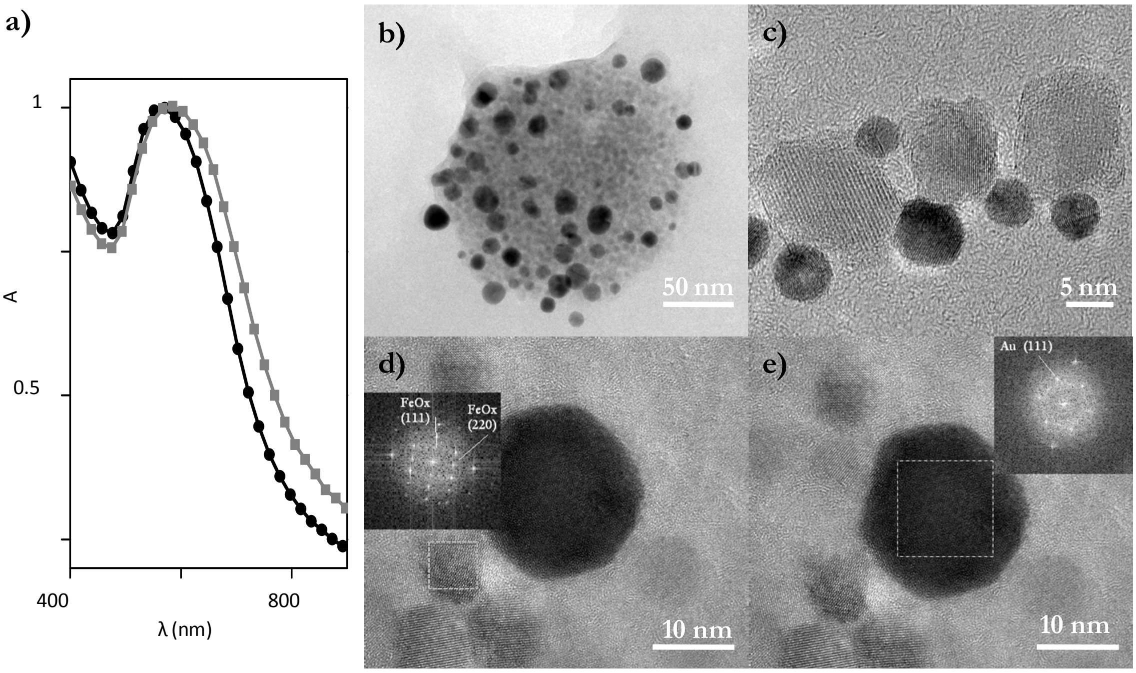

Figure 3.3. *a) UV-Vis spectra from aggregates, gray and black line correspond to PEG and MUA samples. b) TEM micrograph of iron oxide/gold aggregates. HR-TEM micrographs showing heterogeneous aggregates made of iron oxide and gold. The diffraction patterns of iron oxide (inset d) and gold (inset e) are conclusive regarding the heterogeneity of the aggregates.*

Nevertheless, although made of heterogeneous aggregates, PEG and MUA samples exhibited superparamagnetic behavior as shown in Figure 3.4; hysteresis loops of these two samples were measured with a vibrating sample magnetometer (VSM) at room temperature

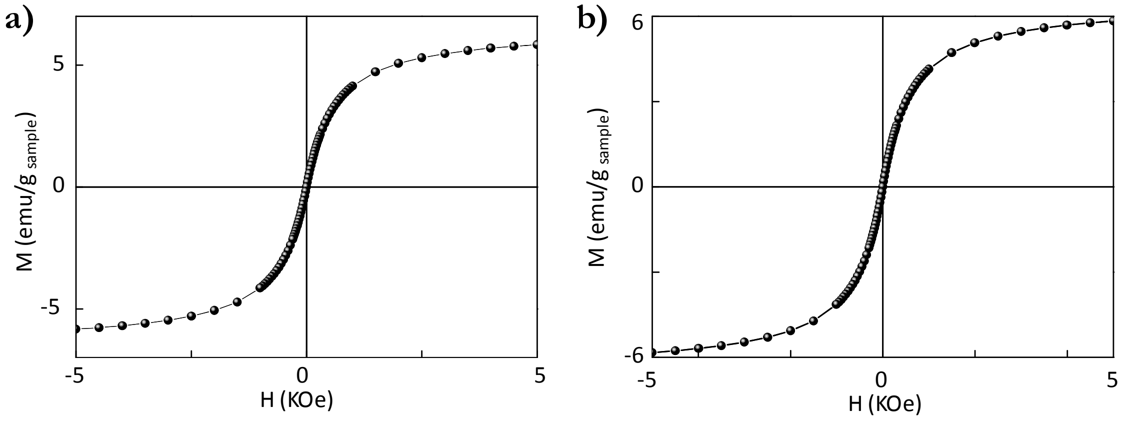

Figure 3.4. *Hysteresis loops corresponding to samples PEG (a) and MUA (b).*

As for a final proof, a colorimetric assay was used to exclude the presence of the core-shell iron oxide-gold structure; a selected PEG sample was treated with

HCl for carrying out an acidic digestion of iron. Under acidic treatment, only the unprotected (by an Au shell) iron content will be degraded into a yellow solution; in contrast, noble metals like gold will remain unalterable. X-ray photoelectron spectroscopy (XPS) was used to quantify the metal content in one PEG sample and the corresponding HCl-treated sample (Table 3.2). Results are conclusive in this matter; the HCl-treated sample showed no iron content whereas the untreated sample does. The iron digestion can be only explained in the absence of the core-shell structure.

Sample	**Binding Energy (eV)**	
	Fe 2p	**Au 4f**
w/o treatment	709.0 2.44%	83.8 2.60%
acid treatment	----	83.8 4.91%

Table 3.2. *XPS results regarding the iron and gold content for the HCl-treated sample and the equivalent untreated sample.*

Samples water-transferred by MIXED CHAINS

The different mixed chains were obtained by organic synthesis. The synthetic process involves a three-step synthesis (Annex) where importantly, the reaction of 11-bromideundec-1-ene with a slight excess of 50% sodium hydroxide and 4 equivalents of tetra (ethylene glycol) provide the chain with a thiol group. This group is introduced by a photochemical addition of thioacetate. Finally, the thiol group is deprotected via sodium methoxide. At this point, the hydroxylated chain is susceptible to produce glycosytated products if activated sugars (trichloroacetimidate, Annex) are added in acidic conditions. Also, the same process is used to obtain chains modified with glucose, galactose, cellobiose and lactose. Carboxylic chain is obtained by the use of Jones reagents to oxidize the hydroxyl group to a carboxylic.

As shown Figure 3.5, they all share following structural design:

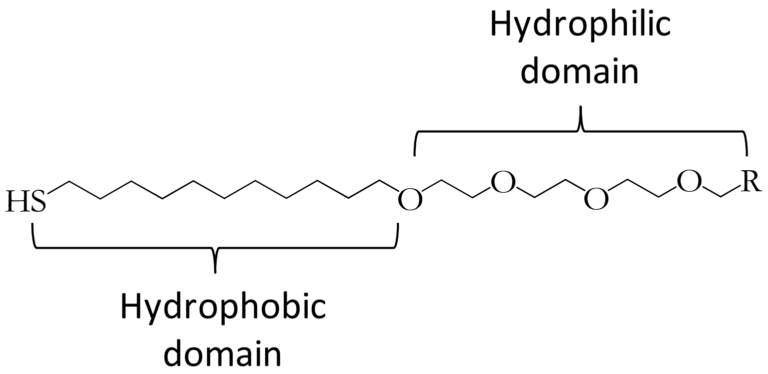

Figure 3.5. *General scheme of the structural composition of mixed chains used for NPs water-transferred.*

As for end terminal groups (R in Figure 3.5), the following organic compounds, listed in Table 3.3, were used:

Sample	R	Structure
CM-OH	CH_2OH	CH_2OH
CM-CO_2H	CO_2H	CO_2H
CM-Glc	50% CH_2O Glucose/ 50% CO_2H	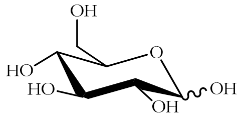
CM-Gal	50% CH_2O Galactose/ 50% CO_2H	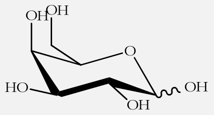
CM-Cellob	50% CH_2O Cellobiose/ 50% CO_2H	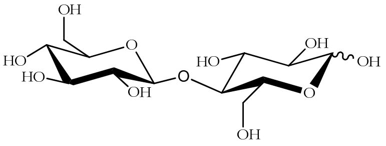
CM-Lacto	50% CH_2O Lactose/ 50% CO_2H	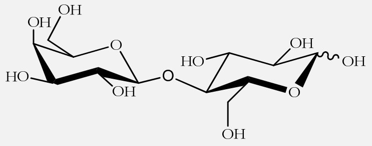

Table 3.3. *Different end terminal organic compounds incorporated into mixed chains.*

Water transfer by mixed chains required vigorous shaking in the presence of sodium borohydride; these conditions enhance the interphase and promote the NPs coating (see scheme shown in Figure 3.6). However, ultrasound was avoided to prevent the formation of aggregates such as the ones formed in samples MUA and PEG.

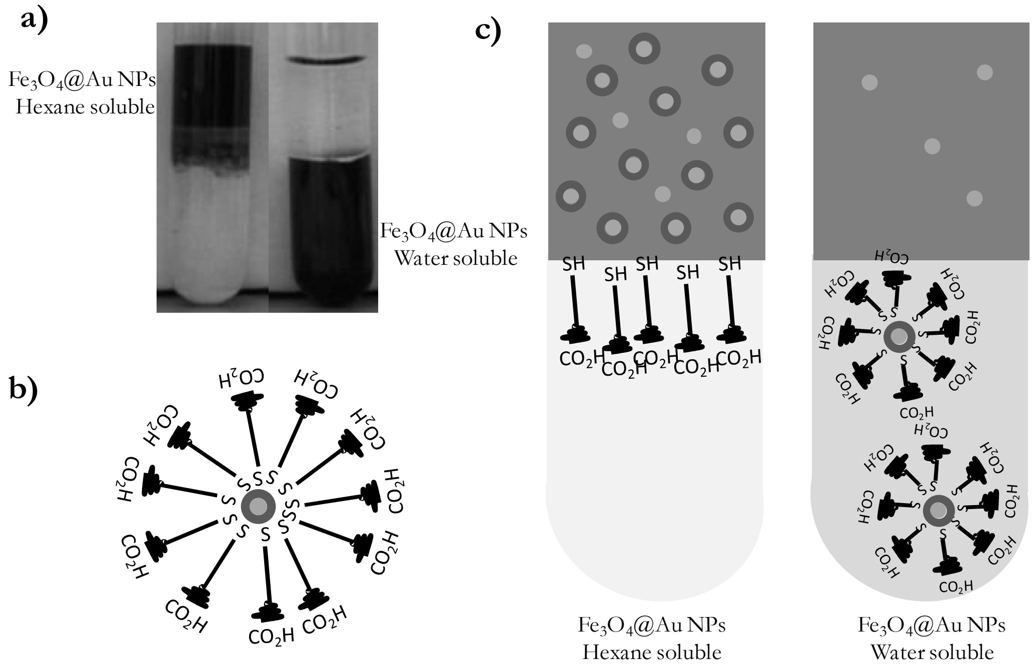

Figure 3.6. *a) Photographs of Fe_3O_4@Au NPs in the organic phase before water transfer (left) and Fe_3O_4@Au NPs in the water phase after water transfer (right). b) Scheme of Fe_3O_4@Au NPs protected by a monolayer of carboxylated mixed chains. c) Scheme of the strategy used for water transfer of Fe_3O_4@Au NPs; left, particles stabilized in the organic phase and the mixed chain orientation through the interphase water-hexane; right, mixed chain protected NPs in the water-phase whereas gold-uncoated iron oxide NPs remain in organic phase.*

Water-transfer of Fe_3O_4@Au NPs by mixed chains resulted in colloids very stable over time (years), and allowed for their purification by centrifugation, dialysis or magnetic separation following solvent precipitation (acetone). Remarkably, colloids tolerated lyophilization and subsequent resuspension in water, as well as in a vast variety of buffers with high ionic strength, without any sign of aggregation; this demonstrates the excellent "quality" of the organic coating provided by mixed chains. UV-Vis spectra of the mixed chain coated NPs (Figure 3.7) did not show any indication of aggregation and remained very similar to the spectrum of bare Fe_3O_4@Au NPs in hexane (plasmon band at 524 nm).

In principle, the use of thiol-gold chemistry aiming water transfer of NPs in hexane should prevent the transfer of Au-uncoated iron oxide "seeds". The facts that the resulting colloids in the water phase after several steps of purification exhibited optical features (surface plasmon band) as well as superparamagnetic behavior are clear indications of the core-shell structure of the Fe_3O_4@Au NPs; the different samples of mixed chain coated NPs were characterized by UV-Vis spectroscopy, electron microscopy (TEM and STEM), SQUID, thermogravimetric analysis (TGA), XPS and Fourier transform infrared spectroscopy (FTIR).

UV-Vis spectroscopy showed narrow surface plasmon bands centered at *ca.* 528 for all the mixed chain protected NPs (Figure 3.7); these narrow bands are indicative of homogeneous NPs dispersions with narrow size distributions. However, small changes in the resonant position among the samples, especially with respect to the original NPs in hexane, were found; this shows the influence of the terminal ligand chains used to form the organic monolayer (Table 3.4).

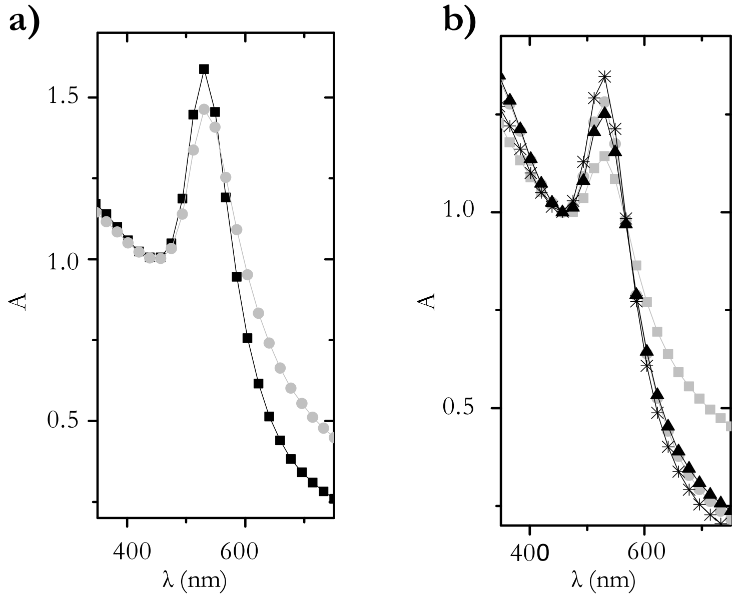

Figure 3.7. *UV-Vis spectra of water solubilized NPs. a) Black solid squares and grey solid circles correspond to hydroxylated mixed chain (CM-OH) capped NPs and carboxylated mixed chain capped NPs, respectively. b) NPs coated with sugar modified mixed chains; glucose modification is represented by a black star, galactose with a gray circle; cellobiose is the gray square and lactose corresponds with the black triangle.*

Sample	λ_{MAX} (nm)
CM-OH	531
CM-CO_2H	533
CM-Glc	525
CM-Gal	527
CM-Cellob	528
CM-Lacto	528

Table 3.4. *Summary of the position of the maximum absorbance for each mixed chain sample.*

Electron transmission micrographs showed that particles present gold contrast and a narrow size distribution (Figure 3.8). The average size was founded to be 7.1 ± 1.6 nm (Histogram in inset on Figure 3.8a). The homogeneous contrast found in STEM images confirmed the presence of only one species which can be presumed to be Fe_3O_4@Au NPs.

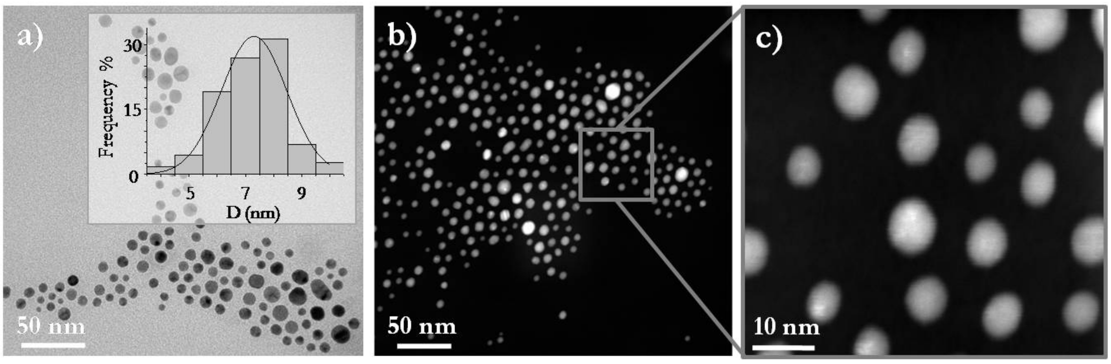

***Figure* 3.8.** *a) Micrograph and size distribution of water stabilized Fe_3O_4@Au NPs. b) STEM image of a dispersion of Fe_3O_4@Au NPs and c) corresponding 5x magnification where contrast uniformity arisen from NPs indicates the presence of only one species.*

As for a final assay to elucidate whether the NPs were core-shell, the metal contents of three relevant samples were determined by inductively coupled plasma optical emission spectrometry (ICP-OES) (Figure 3.11). Sample 1 (CM-Lacto) consisted of the product of the gold and iron digestion with aqua regia of water soluble CM-Lacto NPs. Sample 2 was treated with chlorhydric acid to digest the available iron not protected by gold; and sample 3 consisted of the product after digestion with aqua regia sample 2. Figure 3.11(a) represents the sample preparation schematically. The original concentration of NPs was 50 mg/L.

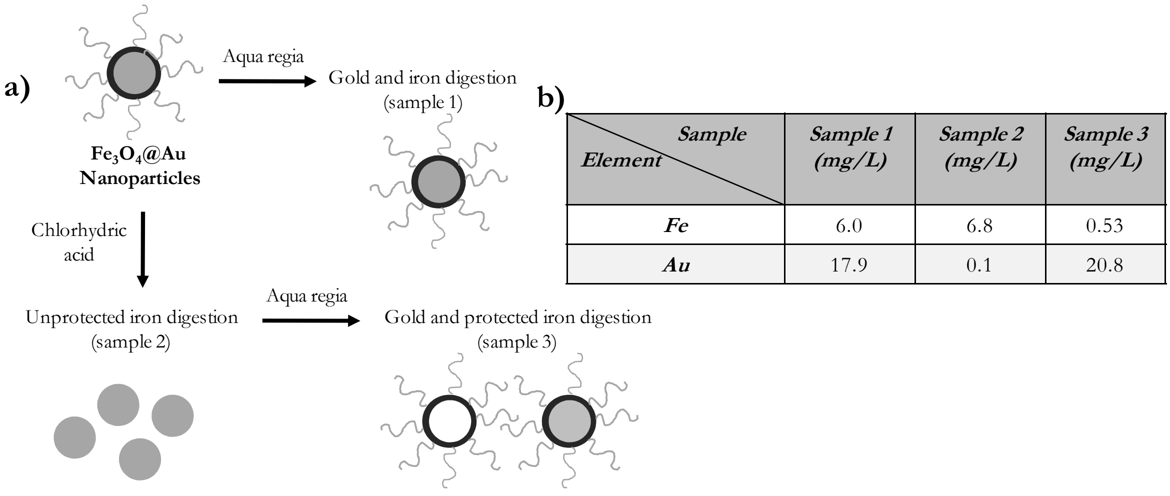

Element \ Sample	*Sample 1 (mg/L)*	*Sample 2 (mg/L)*	*Sample 3 (mg/L)*
Fe	6.0	6.8	0.53
Au	17.9	0.1	20.8

***Figure* 3.11.** *a)Scheme of the design of the experiment; b) results from the ICP-OES measurements of gold and iron concentration.*

Results shows that with the chlorhydric digestion (sample 2), iron result digested almost in its totality. Combining the amounts obtained in the fractionated digestion (sample 2 and 3), gold/iron ratio is almost the same that in the total digestion in sample 1. This result manifests that the Au shell coating is not homogeneous and allows the acid molecules to reach the iron atoms. This fact in addition with STEM observations, in which images showed uniform Au-like contrast and no evidences of holes in the gold shell, indicated that particles seems to be core-shell but presenting some kind of pores which led acid moieties to reach the core of the structure.

3.3. Magnetic characterization.

The magnetic properties of bare Fe_3O_4 NPs ("seeds") were examined and were compared with the magnetic properties of Au-coated NPs (supposed core-shell Fe_3O_4@Au NPs) by using a magnetometer of the type SQUID (Superconducting Quantum Interference Device). In both cases, the content of Fe was calculated assumig that the superparamagnetic component is magnetite (Fe_3O_4) as claimed in literature.[2]

Plots of the magnetization *vs.* the applied magnetic field (M–H loop) at room temperature (300 K) and 10 K were collected for samples of "seeds" (Fe_3O_4) (a) and Au-coated NPs (c) as shown Figure 3.9. At room temperature no hysteresis loops were observed, but at 10 K the clear hysteresis loops revealed the examined samples ("seeds" and Au-coated NPs) to be superparamagnetic in nature. At room temperature, the values of saturation (M_s) were 89 and 95 emu×g^{-1} for the "seeds" and the Au-coated NPs, respectively; the saturation (M_s) of bulk Fe_3O_4 is 92 emu×g^{-1}.

Figure 3.9 shows the temperature dependence of the magnetization for Fe_3O_4 NPs (panel b) and Fe_3O_4@Au NPs (panel d). These measurements include two steps; first, the samples are cooled down to 5 K in the absence of field where the magnetization approximates to zero as the magnetic moments of the particles are blocked in a randomly oriented fashion. The application of a constant small magnetic field (100 Oe, always less than the H_C of the corresponding samples) induces however a net magnetic moment along the field direction, which will

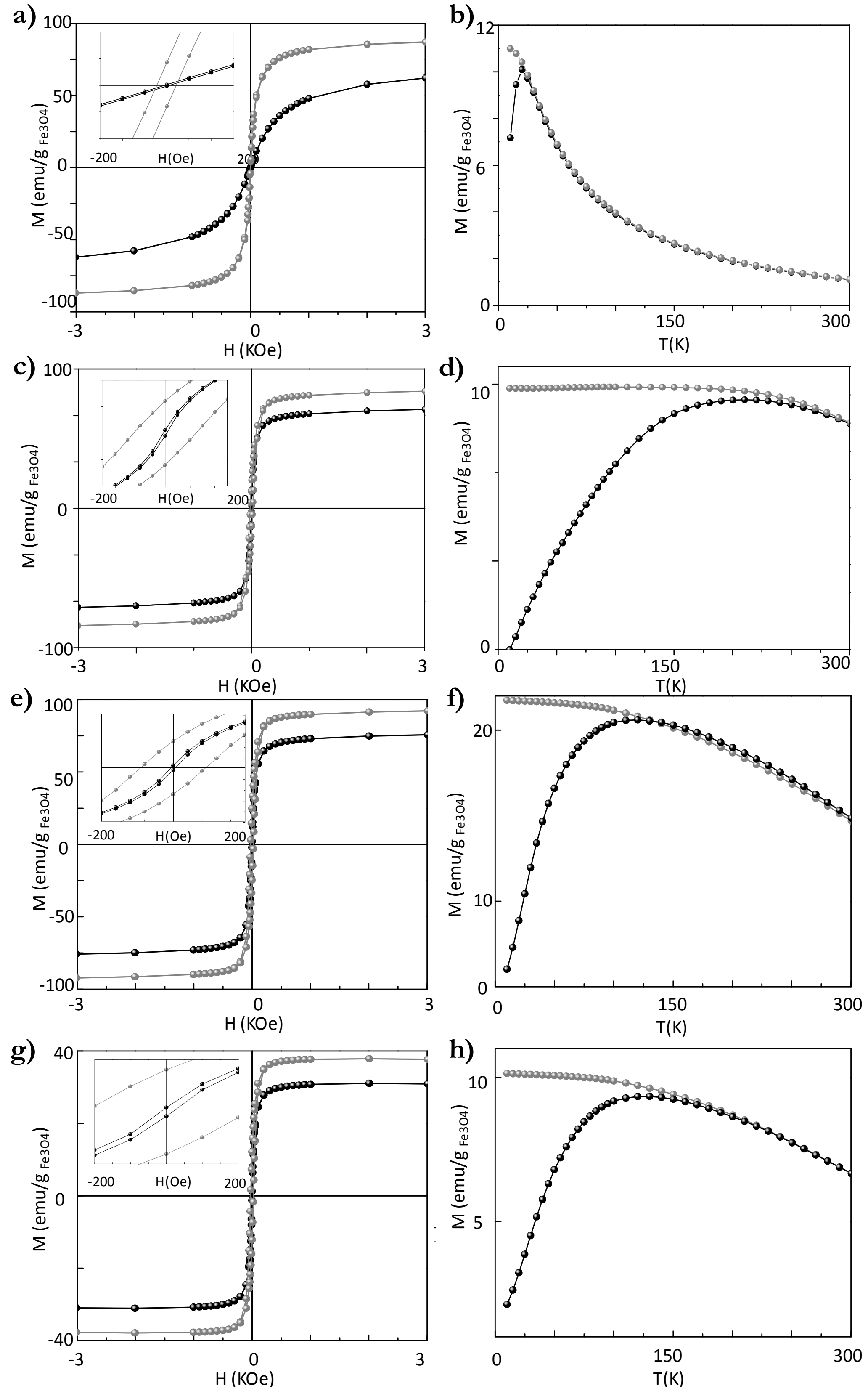

Figure 3.9. *Panels a) and c) show magnetization vs. applied field for ca. 4 nm Fe_3O_4 NPs ("seeds") and ca. 6.7 nm Fe_3O_4@Au NPs, respectively. Gray and black lines represent the magnetization measured at 10K and 300K, respectively. Panels b) and d) display the ZFC/FC curves corresponding to Fe_3O_4 NPs and Fe_3O_4@Au NPs, respectively; gray and black lines correspond to*

the FC and ZFC curves taken at 100 Oe. e) and g) Shows magnetization vs field of CM-Gal and CM-Lacto respectively. Gray line represents the magnetization measured at 10K and black at 300K.f) and h) are the ZFC/FC curves from CM-Gal (f) and CM-Lacto (g). Gray line corresponds with FC at 100 Oe field, and black one corresponds with ZFC.

increase with temperature as more NPs orient their magnetic moments parallel to the field (Zero Field Cooled curve, ZFC). ZFC curve comes to a maximum which corresponds to the case when most of the NPs behave as superparamagnets; as a result of the balance between the disorder thermal and magnetic moment blocking of NPs. This temperature is called blocking temperature (T_B) and its broadening is size distribution dependent. At temperatures higher than T_B the magnetization steadily decrease as the thermal fluctuations increases and contributes to the random orientation of the NPs magnetic moments. In the second step, the samples are cooled in the presence of the constant small magnetic field to generate the Field Cooled curve (FC). Above T_{irr} both the FC and ZFC curves are coincidental (equilibrium magnetization); below T_{irr}, the FC curve splits from the ZFC curve, since then the magnetization does not correspond to the equilibrium. T_{irr} is the temperature when bigger NPs started to block with the field. Moreover, the ZFC curve relaxes toward the FC curve. That is, below T_{irr}, blocking of the magnetic moments occurs for times longer than the experimental resolution time. The temperature dependence of the magnetization curves (ZFC and FC) provides information about the average T_B and T_{irr}, the size distribution of the NPs and the possible presence of NP-NP interactions.[10]

The FC magnetization curve for Fe_3O_4@Au NPs (panel d) decreases very slowly as the temperature increases and tends to flatten off in the range of 5-200 K; this temperature behavior differs from the T^{-1} Curie-like law expected for non-interacting NPs and suggests the presence of interparticle interactions, presumably of the dipole–dipole type [10,11]. The high value for the T_B of Fe_3O_4@Au NPs can be explained by the presence of interparticle interactions produced because either the gold shell is insufficient to prevent interparticle interactions or the organic layer is insufficient to stabilize the Fe_3O_4@Au NPs. In the case of Fe_3O_4 NPs ("seeds"), the magnetic behavior is the expected for superparamagnetic NPs showing a small T_B (*ca.* 50 K).

Two samples were selected, *i.e.* CM-Gal and CM-Lacto, to study the magnetic behavior of mixed chain coated NPs; acquisition parameters equivalent to the ones used for the original bare NPs in hexane were selected for proper comparison (Figure 3.9); results yielded similar high blocking temperatures and confirmed the superparamagnetic character expected for Au-coated iron oxide NPs.

To give the magnetization per gram of iron oxide (assumed magnetite), it is mandatory to assess the amount of iron oxide present in the sample; therefore, the composition of the hybridized NPs was determined by Inductively Coupled Plasma Mass Spectrometry (ICP-MS). Surprisingly, ICP results showed that the sample MS-Lacto posses a higher amount of inorganic material than the sample MS-Gal; this fact can be explained if one assumes that the monolayer of mixed chains is packed differently in samples were the mixed chain is ended by a disaccharide (CM-Lacto) or a monosaccharide (CM-Gal); given the high organic content on the sample CM-Gal, mixed chains ended by galactose molecule appeared to pack very densely on the surface of Au-coated NPs.

Sample	% Fe	% Au	% Fe_3O_4	% Inorganic Material
CM-Gal	11	37	15	51.6
CM-Lacto	14.8	63.4	20	83.4

***Table* 3.5.** *ICP results of sugar modified NPs.*

The superparamagnetic behavior of both samples can be extrapolated from the typical superposition of the hysteresis loops at 10 K and 300 K, characteristic of superparamagnetic systems (Figure 3.9 panel e and g). At room temperature, CM-Gal and CM-Lacto samples achieved saturation at 92 $emu \times g^{-1}_{(Fe3O4)}$ and 89 $emu \times g^{-1}_{(Fe3O4)}$, respectively. Bulk magnetite and magnetite NPs (4 nm) have saturation values of 94 and 98 $emu \times g^{-1}_{(Fe3O4)}$, respectively. Blocking temperatures of CM-Gal and CM-Lacto were 130 K and 160 K respectively. Elsewhere, previous work of Carpenter & coworkers reported on the synthesis of core-shell Fe-Au NPs synthesized by a reverse micelle method; NPs exhibited there a broad size distribution of 5-15 nm (average diameter *ca.* 10 nm) and a T_B of 42 K,[12] much lower than the blocking temperatures of samples CM-Lacto and CM-Gal. In other work, Cho and coworkers synthesized core-shell iron oxide-gold NPs with a size of 18 ± 4 nm which showed a T_B of 150K,[13] which is of a similar value to the T_B obtained CM-Gal and CM-Lacto; note that the size of mixed chain Au-coated NPs is *ca.* half of the diameter reported by Cho and coworkers.

Magnetization values for iron oxide gold coated NPs has been also reported for 18-30 nm structures which show a magnetization of 38 emu g^{-1} (T = 10 K).[10]

Monodispersed 30 nm gold-coated Fe_3O_4 NPs prepared via sonolysis on a solution mixture of gold ions and amino-modified Fe_3O_4 NPs present a saturation magnetization (Ms) of 63 emu g^{-1} (T = 300 K).[14] Recently , Halas and coworkers published the magnetization values for Au nanoshells coated with Fe_3O_4 and SiO_2 resulting in 17.98 emu g^{-1},[15] authors claim that this value is higher than other similar structures. The sugar-modified iron oxide@gold NPs synthesized here exhibit magnetization values equivalent to that of the bare iron oxide NPs of equivalent size (*ca.* 4 nm).

Relaxativity time (r_2)

The use of superparamagnetic NPs as contrast agents for T_2-weighted MRI was introduced as one of the popular bioapplications of these materials. As T_2-weighting contrast agents, superparamagnetic NPs induce a perturbation in the nuclear spin of water protons that typically shortens T_2 (or enhances the relaxivity $R_2 = 1/T_2$). Such changes results in darkening the corresponding area in T_2-weigthed images. Typically, the "quality" of contrast agent for T_2-weighted MRI (as a standardized contrast enhancement indicator) is given by the relaxivity coefficient r_2; the greater r_2, the better contrast. This coefficient can be deduced by plotting the $R_2(s^{-1})$ values of a given sample *vs.* the concentration of iron in the sample (mM Fe); r_2 is the slope of the R_2 dependence on concentration.

Measurements of R_2 values for selected samples (CM-Gal and CM-Lacto) were carried out in a time domain (TD) MRI instrument (Bruker mq60 Minispec). This instrument is specially designed to characterize MRI contrast agents for clinical use; the model used operates at 1.47 T (60 MHz).

The relaxivity coefficients r_2 of CM-Gal and CM-Lacto (Table 3.10) were calculated as previously described from the plots shown in Figure 4.3. The r_2 coefficients of selected samples, CM-Gal and CM-Lacto, were found to be very similar to those of commercially available T_2 contrast agents and other GMNPs stabilize by similar ligands (Table3.5). The gold shell and the coating do not have a negative contribution to the T_2 contrast enhancement; however, the coating represents an advantage in terms of stabilization and functionalization which can be very suitable for *in vivo* applications.

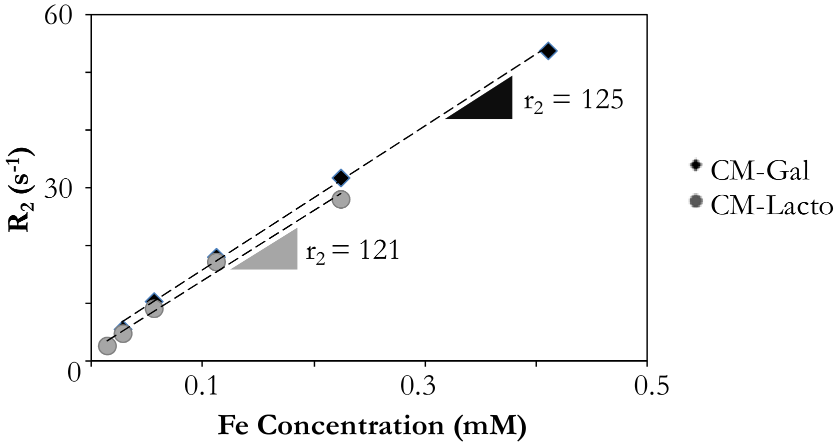

Figure 3.10. *R_2 values vs iron concentration. Samples were measured in water, pH 7 at room temperature.*

Name	Core size(nm)	Total size/nm	Coating	r2 ($mM^{-1}×s^{-1}$)
AMI-25 (Feridex; Endorem)	5–6	80–150	Dextran	*ca.* 100
CLIO, MION	2.8	10–30	Dextran	69
Fe_3O_4@Au	3.2	12	mixed chains*	155
CM-Gal	4	12.6	CM-Gal	125
CM-Lacto	4	12.6	CM-Lacto	121

Table 3.5. *Relaxivity coefficients of water soluble modified MGNPs. Measurements at 1.47 T.*

** The coating by mixed chains used in the work of Gallo et. al. is equivalent to the present work.*[8]

3.4. Conclusions

Superparamagnetic Fe_3O_4@Au NPs were synthesized by a thermal decomposition method in organic solvent; the composite NPs presented a Fe_3O_4 core of *ca.* 4 nm of diameter and a Au outer shell of *ca.* 3 nm. Aiming for applications in physiological media, NPs were water transferred using a variety of organic molecules which provide the nanocomposites with a suitable hydrophilic coating. Importantly, the NPs transferred to the aqueous phase show a good stability in aqueous solution; these can be centrifuged, precipitated and lyophilized which confirm that the phase transfer strategy work properly. Values of magnetization saturation depend on the chain used for the water transfer. ICP measurements demonstrated that monosaccharide-modified chains form an improved densely packed monolayer which translates into a greater amount of organic material onto the NPs surface. Nevertheless, the core@shell nature of these particles could not be confirmed 100%; results are not conclusive in this regards and likely, the gold shell does not fully cover the iron oxide core. On the other hand, the products exhibited Au-like uniform contrast in STEM measurements, surface plasmon resonance and superparamagnetic behavior.

REFERENCES

(1) Wang, L. Y.; Luo, J.; Fan, Q.; Suzuki, M.; Suzuki, I. S.; Engelhard, M. H.; Lin, Y. H.; Kim, N.; Wang, J. Q.; Zhong, C. J.: Monodispersed core-shell Fe3O4@Au nanoparticles. *Journal of Physical Chemistry B* **2005**, *109*, 21593-21601.

(2) Sun, S. H.; Zeng, H.; Robinson, D. B.; Raoux, S.; Rice, P. M.; Wang, S. X.; Li, G. X.: Monodisperse MFe2O4 (M = Fe, Co, Mn) nanoparticles. *Journal of the American Chemical Society* **2004**, *126*, 273-279.

(3) Xu, Z.; Shen, C.; Hou, Y.; Gao, H.; Sun, S.: Oleylamine as Both Reducing Agent and Stabilizer in a Facile Synthesis of Magnetite Nanoparticles. *Chemistry of Materials* **2009**, *21*, 1778-1780.

(4) Niederberger, M.: Nonaqueous Sol–Gel Routes to Metal Oxide Nanoparticles. *Accounts of Chemical Research* **2007**, *40*, 793-800.

(5) Jain, P. K.; Lee, K. S.; El-Sayed, I. H.; El-Sayed, M. A.: Calculated Absorption and Scattering Properties of Gold Nanoparticles of Different Size, Shape, and Composition: Applications in Biological Imaging and Biomedicine. *The Journal of Physical Chemistry B* **2006**, *110*, 7238-7248.

(6) Love, J. C.; Estroff, L. A.; Kriebel, J. K.; Nuzzo, R. G.; Whitesides, G. M.: Self-assembled monolayers of thiolates on metals as a form of nanotechnology. *Chemical Reviews* **2005**, *105*, 1103-1169.

(7) Ma, Y.; Chechik, V.: Aging of Gold Nanoparticles: Ligand Exchange with Disulfides. *Langmuir* **2011**, *27*, 14432-14437.

(8) Gallo, J.; Garcia, I.; Padro, D.; Arnaiz, B.; Penades, S.: Water-soluble magnetic glyconanoparticles based on metal-doped ferrites coated with gold: Synthesis and characterization. *Journal of Materials Chemistry* **2010**, *20*, 10010-10020.

(9) Radziuk, D. V.; Zhang, W.; Shchukin, D.; Mohwald, H.: Ultrasonic Alloying of Preformed Gold and Silver Nanoparticles. *Small* **2010**, *6*, 545-553.

(10) Mandal, M.; Kundu, S.; Ghosh, S. K.; Panigrahi, S.; Sau, T. K.; Yusuf, S. M.; Pal, T.: Magnetite nanoparticles with tunable gold or silver shell. *Journal of Colloid and Interface Science* **2005**, *286*, 187-194.

(11) del Barco, E.; Asenjo, J.; Zhang, X. X.; Pieczynski, R.; Julia, A.; Tejada, J.; Ziolo, R. F.; Fiorani, D.; Testa, A. M.: Free rotation of magnetic nanoparticles in a solid matrix. *Chemistry of Materials* **2001**, *13*, 1487-1490.

(12) Carpenter, E. E.; Sangregorio, C.; O'Connor, C. J.: Effects of shell thickness on blocking temperature of nanocomposites of metal particles with gold shells. *Ieee Transactions on Magnetics* **1999**, *35*, 3496-3498.

(13) Cho, S. J.; Idrobo, J. C.; Olamit, J.; Liu, K.; Browning, N. D.; Kauzlarich, S. M.: Growth mechanisms and oxidation resistance of gold-coated iron nanoparticles. *Chemistry of Materials* **2005**, *17*, 3181-3186.

(14) Wu, W.; He, Q. G.; Chen, H.; Tang, J. X.; Nie, L. B.: Sonochemical synthesis, structure and magnetic properties of air-stable Fe3O4/Au nanoparticles. *Nanotechnology* **2007**, *18*.

(15) Bardhan, R.; Chen, W. X.; Perez-Torres, C.; Bartels, M.; Huschka, R. M.; Zhao, L. L.; Morosan, E.; Pautler, R. G.; Joshi, A.; Halas, N. J.: Nanoshells with Targeted Simultaneous Enhancement of Magnetic and Optical Imaging and Photothermal Therapeutic Response. *Advanced Functional Materials* **2009**, *19*, 3901-3909.

Bioapplications of Fe_3O_4@Au NPs

Chapter 4

In this chapter some of the potential uses of the Fe_3O_4@Au nanocomposite (in the following referred to as MGNPs) described in chapter 3 will be addressed; the functionality of these as nanocarriers will be evaluated *in vitro* and as hyperthermia agents. Previously, the viability of these particles in *in vitro* systems should be evaluated.

4.1. Viability Evaluation of MGNPs

The efficient use of the modified water soluble MGNPs in bioapplications is determined ultimately by their stability in physiological media and viability at cellular level; the cell line HeLa (human cervix cancer cells) was used to evaluate the viability of MGNPs in cell cultures. To account for cytotoxicity effects, the respiration activity of the cells was analyzed by a test based on 3-(4,5-dimethylthiazol-2-yl)-2,5-diphenyltetrazolium (MTT) (Figure 4.1). This assay is a colorimetric method based on the metabolic reduction of MTT by the mitochondrial succinate dehydrogenase; the product generated by this enzymatic reaction is formazan, a compound with a characteristic blue color. The amount of formazan can be correlated with the metabolic activity of cells, one of many viability-related parameters.

Prior to the MTT-test, selected MGNPs were sterilized by UV-light exposure and filtration (0.2 µm filters); filtered NPs were suspended in cell culture media DMEM (Dulbecco's Modified Eagle Medium) at a variety of concentration of NPs (1 - 100 µg/mL). 5×10^3 HeLa cells per well were seeded onto 96-well dishes and cultured at 37 °C and 5% CO_2 during 24 h. Then, cells were supplemented with fresh media containing different concentrations of MGNPs under evaluation; cells were challenged with MGNPs for 24 h prior to viability assessment. After the incubation time concluded, wells were emptied out washed with PBS; then they were supplemented with fresh medium containing MTT (0.25 mg/mL). 96-well dishes were incubated during 4 hours and then, the plates were centrifuged at

5000 rpm during 15 minutes to promote the adhesion of formazan crystals onto the plate. By a flip the supernatant media was removed from the plate; formazan crystals were solubilized by adding 200 µl of DMSO per well. The respiration activity of cells challenged with NPs is determined indirectly by the formazan-absorbance (570 nm) of samples relative to controls (NPs-unchallenged cells).

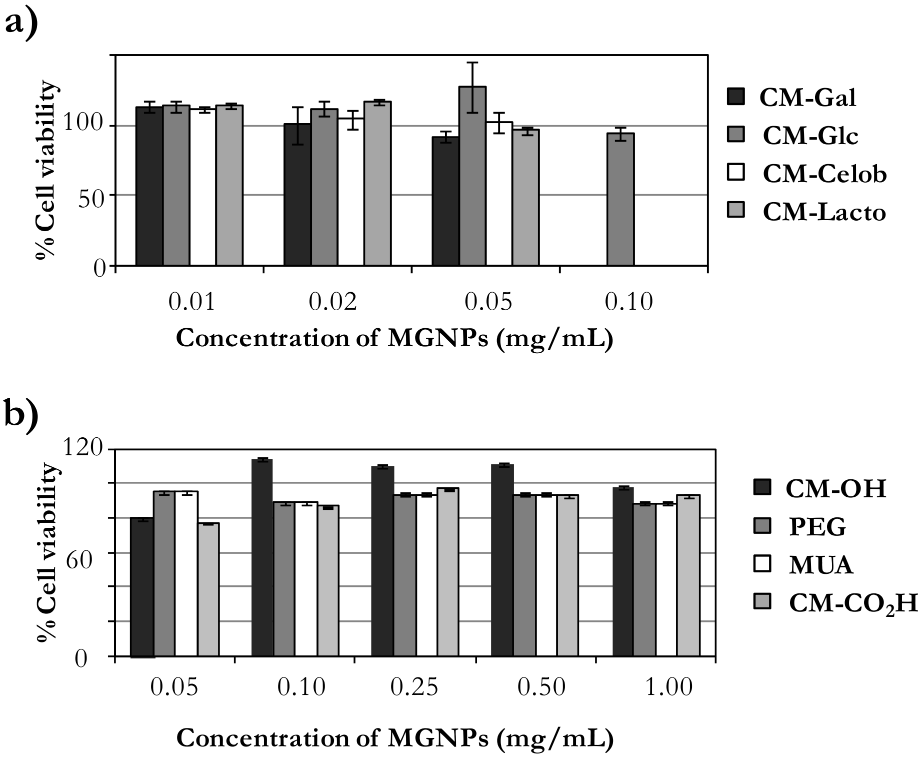

Figure 4.1. *MTT-viability results of a) sugar modified water soluble MGNPs; b) hydroxylated and carboxylated water soluble MGNPs and MUA and PEG iron oxide/gold aggregates.*

Figure 4.1 shows the viability results concerning samples of MGNPs (synthesized as described in Chapter 3), *i.e.* Fe_3O_4@Au NPs stabilized by polyethylene glycol (PEG), mercaptoundecanoic acid (MUA), and a variety of mixed chains derivatized with the following end terminal groups: hydroxyl group (CM-OH), carboxyl group (CM-CO_2H), glucose (CM-Glc), galactose (CM-Gal), lactose (CM-Lacto) and celobiose (CM-Celob); error bars represent the statistical standard deviation (quintuplicates). Cell survival is above 80% in all the cases, even when the concentration of MGNPS is as high as 1 mg/mL; a material could be considered cytotoxic for humans when viability values drop below 80%. In addition, cell viability appears to be independent of the sample and concentration. These results indicate that these NPs do not impair mitochondrial respiration. Although there are not standardized protocols for assessing cytotoxicity of NPs, MTT-assays are widely used as a preliminary test to evaluate the biocompatibility of engineered NPs. Thus, MGNPs used in this work appear to be suitable candidates for bioapplications.

4.2. Vectorization of MGNPs

Most of biomedical applications regarding NPs require cellular uptake; no matter whether for imaging or therapy, *in vitro* or *in vivo*, in general NPs should be able to cross cellular membranes as efficiently as possible. However, the impermeable nature of the cell plasma membrane and nuclear envelope limit the therapeutic use of nanocarriers as well as other proteins, peptides, genes, etc. To date different methods have been developed to improve cell uptake including microinjection, electroporation, bacterial toxins, viral transfection or receptor mediated endocytosis.[1] However, important issues such as transfer efficiency, cell viability or technical challenges limit the general applicability of these techniques.[2-5] Recently, two independent approaches involving nanotechnology have gained popularity, i.e. magnetofection and conjugation of nanocarriers with cell penetrating peptides (CPPs).

First, the use of an external magnetic fields to improve internalization of magnetic carriers by magnetic force; this technique is usually referred to as magnetofection.[6,7] Using this technique is possible to obtain high nanoparticle concentration inside cells using a low concentration of magnetic nanoparticles. As example, gene expression for short time rise up 100 times compared with standard transfection method.[8] Nowadays, magnetofection is available commercially (Quemicell.com) and it is offered as an alternative to the most common transfection techniques.

Second, the use of nanocarriers hybridized with cell-penetrating peptides (CPPs) as enhanced shuttles for cell internalization. CPPs are a family of peptides that show great potential in drug delivery as they facilitate cell entry of various hydrophilic macromolecules.[9]. In 1988, the first CPP, *i.e.* the purified HIV transactivator of transcription (tat) peptide, was described. Since then, a variety of CPPs have been described.[10-12] An original study in 1999 demonstrated that iron oxide-tat conjugates increased cellular uptake more than 100-fold.[13] In following studies, the effect of different CPPs on nanocarriers has been demonstrated to greatly improve uptake efficiency.[2,14-16]

To date, the consensus about the cellular uptake of NPs is that there are two routes, *i.e.* receptor mediated endocytosis or a non-specific route, typically pinocytosis;[17] Independently of the route and besides the varying degrees of success with regards uptake, these method do not allow for achieving nuclear uptake and ultimately, any attached cargo (such as drugs or genes) get degraded in the endosome.

In this section, the potential use of MGNPs as Trojan horses to shuttle drugs into cells is evaluated *in vitro*. Experimental details for cell culture, immunostaining techniques, Western blots analysis, fluorescence and electronic microscopy are given in Annex A. The two approaches aforementioned, magnetofection and derivatization with CPPs, were compared in terms of uptake efficiency and cell response.

Water soluble carboxylated mixed chain MGNPs (previously referred to as sample CM-CO_2H) were modified with tat peptides. NPs were derivatized with peptides by carboxyl-to-amine conjugation (tat-MGNPs); the conjugation was achieved using the well known activation protocol via EDC/NHS chemistry where EDC and NHS are 1-Ethyl-3-[3-dimethylaminopropyl] carbodi-imide hydrochloride and N-hydroxysuccinimide, respectively (Figure 4.2).

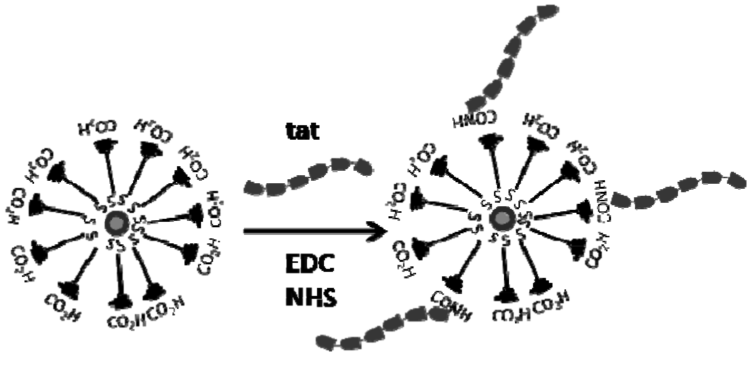

Figure 4.2. *Scheme of derivatization of CM-CO_2H with tat peptides to yield conjugates tat-MGNPs.*

To assess the influence of tat and an external magnetic field on internalization, human fibroblasts (Infinity Telomerase Inmortalised primary human fibroblast, hTERT-BJ1 of Clontech Laboratories) were challenged with the tat-modified MGNPs (in the following, MGNPs@tat) with (+) and without (−) the presence of a static magnetic field of 350 mT (MF). The influence on relevant proteins involved in the cell morphology was analyzed by standard immunostaining techniques.

With regards to nanoparticle uptake, there are various possible pathways involved, and understanding the key molecules involved allows bioengineering of specially tailored complexes for highly specialized delivery.[18,19] NP uptake and subsequent intracellular pathways depend on cell type, size, shape, charge and chemistry of the particles.[20,21] In the present case the size of tat-MGNPs is *ca* 7 nm. The actual mechanism of CPP (tat) uptake into cells remains under debate. There is a general consensus that early suggestions of receptor-independent uptake were misleading,[22,23] and that endocytosis is responsible, however the actual type of endocytosis (mediated by clathrin, caveolin or others) is still unclear.[24]

Previous studies have shown that actin plays a role in internalization, and it is known that microtubules are required for efficient transfer of cargo once inside the cell.[25] In this case F-actin and β -tubulin were well organized in the control cells, both +MF and −MF (Figure 4.3). F-actin was well structured around the cell periphery, with stress fibres across the cell body (Figure 4.3 Controls), while β-tubulin was observed as individual fibers radiating out from the organizing centre located by the nucleus to the cell periphery. However, images of cells challenged with tat-MGNPs indicated a strong actin response, observed as punctuate and diffuse actin staining throughout the cell body (Figure 4.3, MGNPs +MF and −MF). Similarly, tubulin staining appeared denser in the presence of NPs (Figure 4.7 MGNPs +MF and −MF); no difference was observed with (+MF) or without (–MF) a magnetic field.

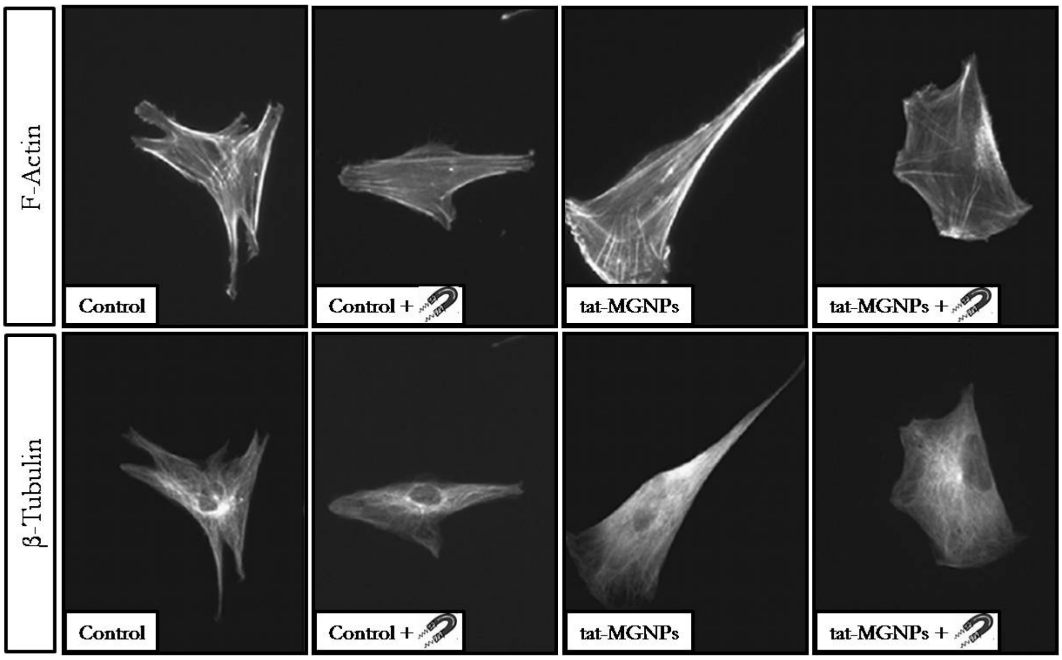

Figure 4.3. *F-actin(top) and β-tubulin(down) immunostaining of first column cells control, second column cell under MF control, third and fourth column cell incubated with tat-MGNPs with or without the presence of MF, respectively.*

Caveolin and clathrin immunofluorescence images are represented in Figure 4.4.

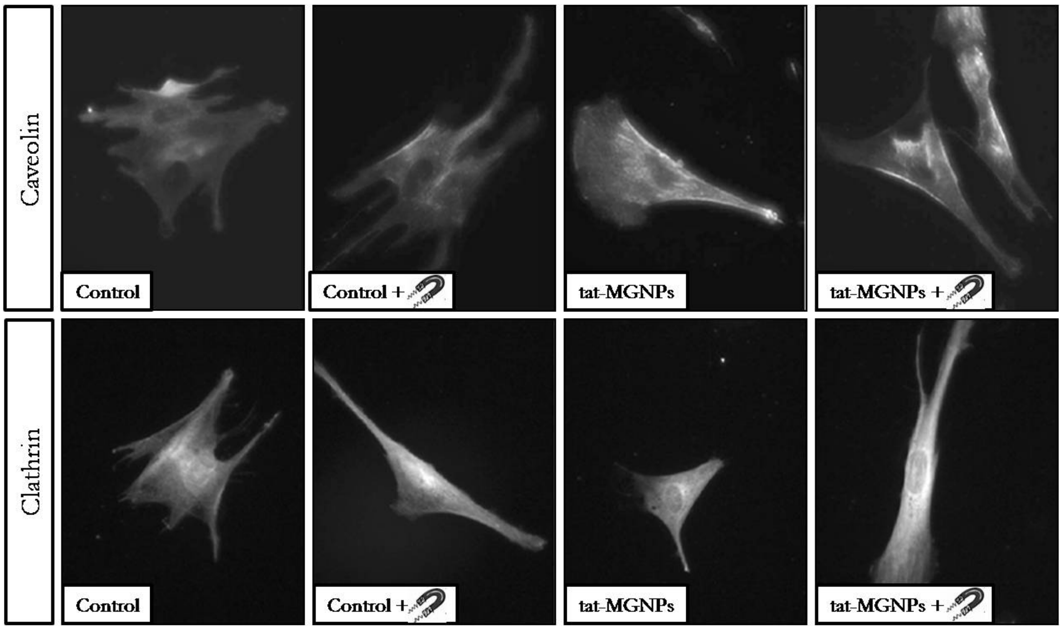

Figure 4.4. *Caveolin(top) and clathrin (down) immunostaining of first column cells control, second column cell under MF control, third and fourth column cell incubated with MNPs with or without the presence of MF, respectively.*

A comparison of caveolin staining intensity of control samples (1st and 2nd column) and those challenged with tat-MGNPs (3rd and 4th column) suggested that particle uptake may be caveolin mediated. Caveolin staining certainly appeared more concentrated in cells incubated with the MNPs. No difference was observed with or without a magnetic field. Meanwhile clathrin staining of the control samples (1st and 2nd column) mirrored those of cells exposed to the MNPs (3rd and 4th column), with no obvious difference in stain intensity noted. No difference was observed with and without a magnetic field. Caveolae are found on the surface of many, but not all cell types, and are buds consisting of caveolin with a bilayer containing cholesterol and glycolipids.[19] Caveloae constitute 10–20% of the cell surface of endothelial cells, but are also found in smooth muscle cells and fibroblasts.[26] They are typically 50–80 nm in size, thus making them slightly smaller than clathrin coated pits[19]. Caveolin- mediated endocytosis is the route of entry not only for various proteins and viruses, but it is also being investigated as a means of drug delivery using NPs.[26,27] Unlike clathrin-mediated endocytosis, caveolin-mediated endocytosis is a highly regulated process involving complex signaling, which may be controlled by the tat-MGNPs entry itself. Also, the lysosomal degradation pathway can be by-passed, thus avoiding breakdown of the functionalized particles, allowing them to reach their target.[26]. Results herein showed that the particles were indeed uptaken into the cell, a view supported by the actin/tubulin staining,[26], and suggested a caveolin dependent uptake route as opposed to clathrin.

Western blots analysis of caveolin and clathrin further demonstrated that uptake appeared to be caveolin dependent as opposed to clathrin mediated, whereby a clear increase in caveolin band intensity in the presence of tat-MGNPs was noted compared to the control cells (Figure 4.5). Furthermore, the intensity increased in the presence of the field, suggesting a higher uptake. Meanwhile clathrin band intensities were of a similar level. Band intensities for both caveolin and clathrin were quantified using Image J imaging software (http://www.rsb.info.nih.gov/nih-image).

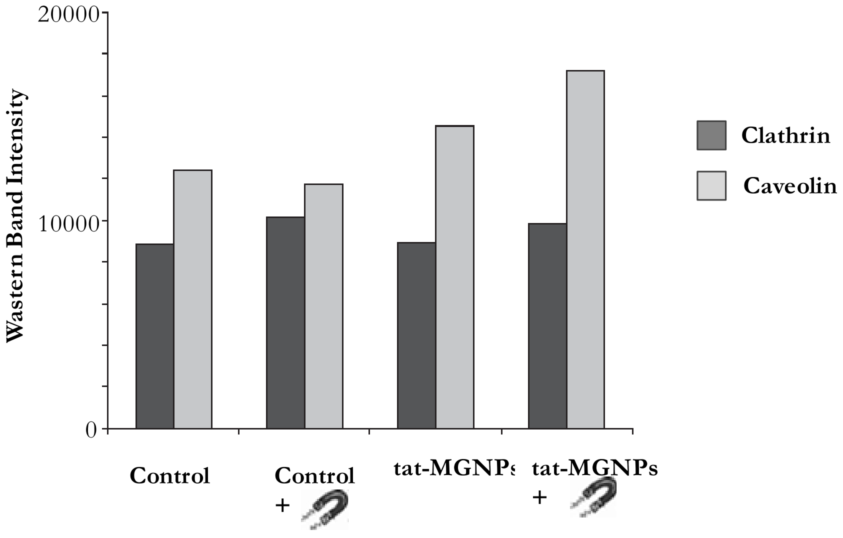

Figure 4.5. *Western-blot analysis results.*

Scanning micrographs were done to determine if any morphological change occurs in cell membrane. These cells present a smooth membrane. Cell exposed under magnetic field show striated membrane which is typical in the early stages of alignment. This fact is unusual in the cases of shorts exposures under magnetic fields. In the case of cells incubated with nanoparticles a clear response is observed. Many protusion and philopodia are present in the membrane. Cell treated with tat-MGNPs and magnetic field presents also an alignment with the MF (Figure 4.6).

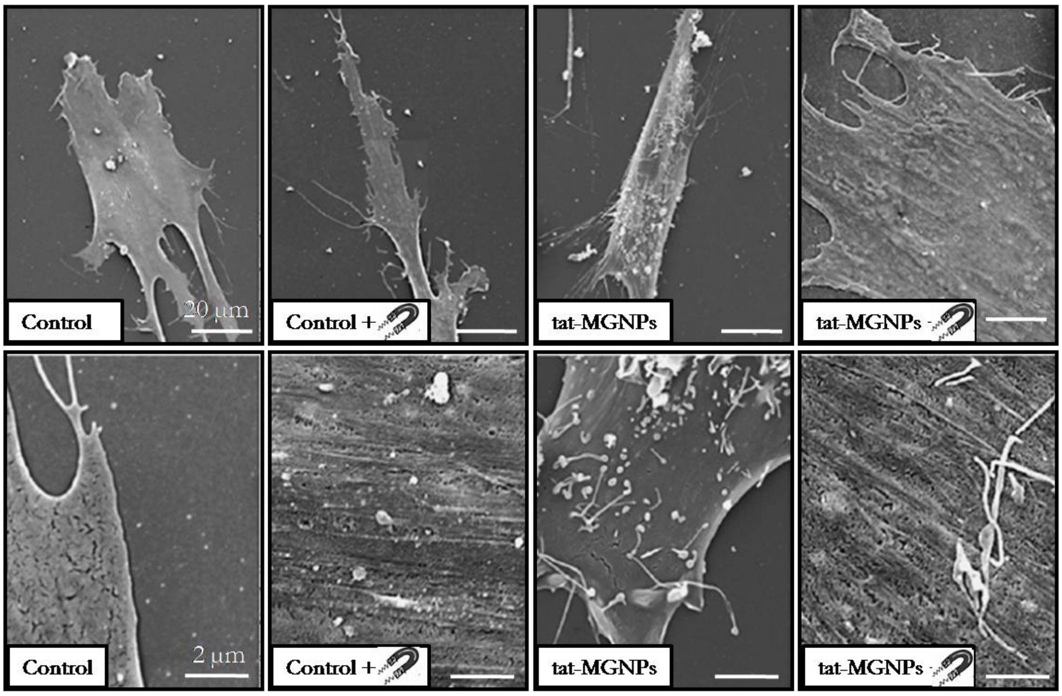

Figure 4.6. *Scanning electron micrographs with different magnifications to observe morphology cell changes, first column correspond with cells control, second column with cell under MF control, third and fourth column with cell incubated with MGNPs with or without the presence of MF, respectively.*

As last observation, cells were observed by transmission microscopy (Figure 4.7). In the cells incubated with tat-MGNPs with and without magnetic field exposure tat-MGNPs were founded inside nuclear membrane. On the other hand, untreated cells present no modification.

CPPs internalization mechanism is still unclear. In the beginning was thought it was an independent receptor-mediated process. So internalization must occur by endocytosis, but this endocytosis mechanism is not described yet. These results show that internalization of these tat-MGNPs occurs by a caveolin-mediated via and show clathrin independence. TEM micrographs confirm the tat-MGNPs internalization, and it is possible to see their localization in the celular inner. Tat-modification must be the responsible of the pass through nuclear membrane, presumably by nuclear pores.

There is no significant differences respect the internalization with and without magnetic field. This could be due the small size of the nanoparticles. The typical size of a particle use for magnetofection rounds 100 nm of diameter.

I would like to highlight that this work was done in collaboration with the group of Dr. Berry from the Centre for Cell Engineering of University of Glasgow. In particular, immunostaining, western-blot analysis and the assessment of morphology changes *via* electron microscopy was done in the facilities of the University of Glasgow.

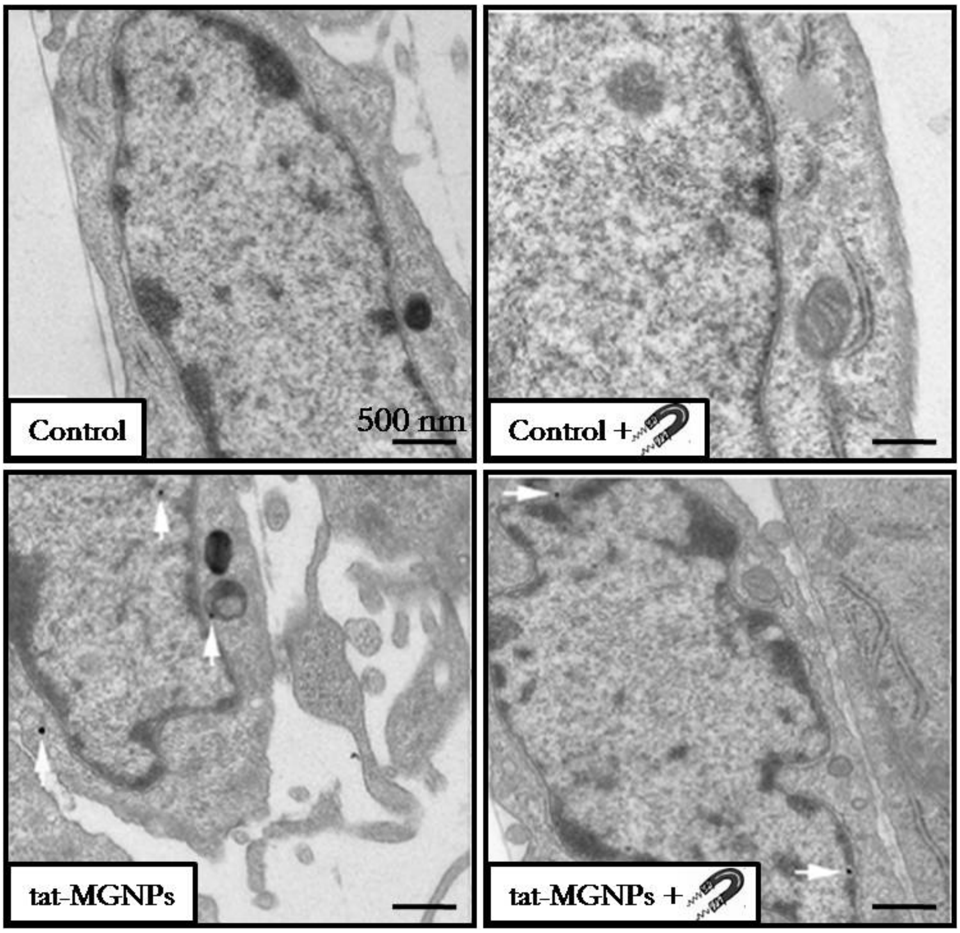

Figure 4.7. *Transmission electron micrographs; controls images shows no morphology changes, whereas in the cell incubated with MNPs and MF (3rd and 4th images respectively) MNPs are visible in the inner of the cell.*

4.3. Application for magnetic hyperthermia

The treatment referred to as magnetic hyperthermia (also called magnetic fluid hyperthermia) can be defined as the local heating of regions containing MNPs under a time-varying magnetic field (AC field); generally, local heating is used to destroyed solid tumors. Biocompatible superparamagnetic NPs are injected into the region of interest which can be then heated selectively until tumor destruction is achieved; superparamagnetic NPs are the preferred choice over "more magnetic" particles such as ferromagnetic particles because of physiological boundaries, *i.e.* at physiological-allowed values of the AC field, superparamagnetic NPs exhibit higher SAR values than their equivalent micrometric counterparts (FM particles). Therefore, iron oxide NPs, single-domain NPs in the size of 5 -20 nm, have become the most popular agents for magnetic hyperthermia. Magnetic hyperthermia has been recently approved to treat humans (Magforce AG). So far this treatment is only available in Germany at the Charité-Universitäts medizin Berlin; here, they use *ca.* 15 nm iron oxide NPs with an aminosilane coating (NanoTherm®) and AC fields with a frequency of 100 kHz and variable field strength (0 – 18 $kA\times m^{-1}$).

Ideally, NPs engineered for magnetic hyperthermia should exhibit enhanced capability towards thermal energy transfer; this parameter is normally given by the specific absorption rate (SAR) value which depends on the experimental parameters (AC field) and the characteristic of the nanoheater, *i.e.* composition, size and anisotropy.

To evaluate the potential use of MGNPs developed in this work as nanoheaters in magnetic hyperthermia, selected samples of MGNPs (UV-Vis spectra in Figure 4.8(a)) were evaluated with an instrument specially designed for testing nanoheaters for magnetic hyperthermia (DM100 series of nB nanoScale Biomagnetics); the instrument was operated at 800 KHz and *ca.* 19 $kA\times m^{-1}$. Under these AC field conditions, the temperature increment over time was collected for different samples; the instrument uses an adiabatic-like Dewar flask to minimize heat losses.

In order to calculate the experimental SAR of the particles, the following equation was used:[28]

$$\mathrm{SAR} = \frac{\Delta T}{\Delta t}\frac{C_{liq}\rho_{liq}}{\Phi} \tag{4.1}$$

where C_{liq} and ρ_{liq} are the specific heat capacity and density of the liquid, respectively, and Φ the weight concentration of the MNPs in the colloid. Note that the maximum slope dT/dt occurs along the first seconds after turning on the magnetic field. The experimental value of $\Delta T/\Delta t$ is calculated by performing a linear fit of the hyperthermia data (temperature versus time) in the initial time interval, t = [1-10] s. In the present case, the liquid is water and therefore, C_{liq} and ρ_{liq} were 4.18 J/gK and 1 g/L, respectively. Note that in addition to the samples discussed in this chapter (mixed chains derivatized NPs), polymer coated Fe_3O_4 NPs (6 nm)[29] and PEG capped Au NPs (13 nm) were also measured as controls. Figure 4.8(b) represents the temperature increment in one minute for each sample.

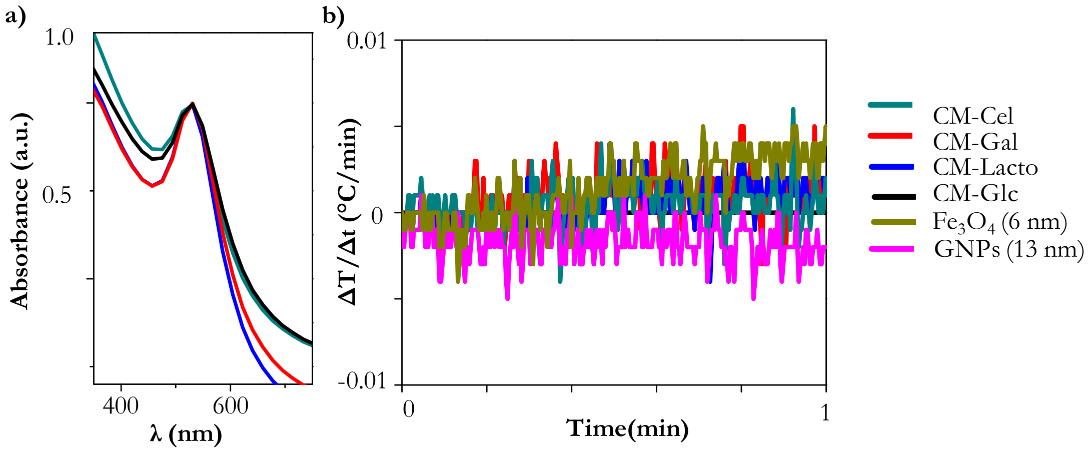

Figure 4.8. *a) UV/Vis spectra of MGNPs solutions; b) temperature increase versus time and c) overall increment of temperature per minute.*

These results show that these samples cannot be used as nanoheaters in contrast to other iron oxide NPs of *ca.* 15 nm. However, it would be possible to optimize the heating efficiency by increasing the size of the core. One of the main problems for achieving the optimum size of iron oxide NPs for hyperthermia (*ca.* 15 nm) is that the stability of these NPs in water or physiological media is very limited; in this context, the use of the gold shell and mixed-chain coatings add to iron oxide NPs a great deal of stabilization and will be object of future work.

4.4. Conclusions

In this chapter, different applications of the MGNPs were evaluated. For all the engineered NPs, toxicity was evaluated using the standard MTT colorimetric assay; results show that MGNPs do not impair the viability of HeLa cells.

MGNPs modified with tat, an internalization peptide, were used to study their internalization pathway of these MGNPs, finding that a caveolin process is the responsible. On the other hand, magnetic field effect in the internalization of tat-MGNPs was found to be negligible. Remarkably, fiber alignments were found in cells which were exposed to the magnetic field.

For sugar-modified MGNPs, their potential as hyperthermia agents was evaluated. MGNPs showed SAR values bellow current commercially available products; this is motivated the small size of the magnetic core. This is why the use of these particles was rejected and new hyperthermia agents will be exposed in the second part of this thesis.

REFERENCES

(1) Stephens, D. J.; Pepperkok, R.: The many ways to cross the plasma membrane. *Proceedings of the National Academy of Sciences* **2001**, *98*, 4295-4298.

(2) Berry, C. C.; de la Fuente, J. M.; Mullin, M.; Chu, S. W. L.; Curtis, A. S. G.: Nuclear localization of HIV-1 tat functionalized gold nanoparticles. *Ieee Transactions on Nanobioscience* **2007**, *6*, 262-269.

(3) Zhang, Y.; Yu, L. C.: Microinjection as a tool of mechanical delivery. *Current Opinion in Biotechnology* **2008**, *19*, 506-510.

(4) Aspalter, M.; Vyas, A.; Feiner, J.; Griffin, J.; Brushart, T.; Redett, R.: Modification of Schwann cell gene expression by electroporation in vivo. *Journal of Neuroscience Methods* **2009**, *176*, 96-103.

(5) Masotti, A.; Mossa, G.; Cametti, C.; Ortaggi, G.; Bianco, A.; Del Grosso, N.; Malizia, D.; Esposito, C.: Comparison of different commercially available cationic liposome-DNA lipoplexes: Parameters influencing toxicity and transfection efficiency. *Colloids and Surfaces B-Biointerfaces* **2009**, *68*, 136-144.

(6) del Pino, P.; Munoz-Javier, A.; Vlaskou, D.; Rivera Gil, P.; Plank, C.; Parak, W. J.: Gene Silencing Mediated by Magnetic Lipospheres Tagged with Small Interfering RNA. *Nano Letters* **2010**, *10*, 3914-3921.

(7) Plank, C.; Zelphati, O.; Mykhaylyk, O.: Magnetically enhanced nucleic acid delivery. Ten years of magnetofection—Progress and prospects. *Advanced Drug Delivery Reviews* **2011**, *63*, 1300-1331.

(8) Bhattarai, S. R.; Kim, S. Y.; Jang, K. Y.; Lee, K. C.; Yi, H. K.; Lee, D. Y.; Kim, H. Y.; Hwang, P. H.: Laboratory formulated magnetic nanoparticles for enhancement of viral gene expression in suspension cell line. *Journal of Virological Methods* **2008**, *147*, 213-218.

(9) Howl, J.; Nicholl, I. D.; Jones, S.: The many futures for cell-penetrating peptides: how soon is now? *Biochemical Society Transactions* **2007**, *35*, 767-769.

(10) Zhang, K.; Fang, H. F.; Chen, Z. Y.; Taylor, J. S. A.; Wooley, K. L.: Shape effects of nanoparticles conjugated with cell-penetrating peptides (HIV Tat PTD) on CHO cell uptake. *Bioconjugate Chemistry* **2008**, *19*, 1880-1887.

(11) Frankel, A. D.; Pabo, C. O.: CELLULAR UPTAKE OF THE TAT PROTEIN FROM HUMAN IMMUNODEFICIENCY VIRUS. *Cell* **1988**, *55*, 1189-1193.

(12) Green, M.; Loewenstein, P. M.: AUTONOMOUS FUNCTIONAL DOMAINS OF CHEMICALLY SYNTHESIZED HUMAN IMMUNODEFICIENCY VIRUS TAT TRANS-ACTIVATOR PROTEIN. *Cell* **1988**, *55*, 1179-1188.

(13) Josephson, L.; Tung, C.-H.; Moore, A.; Weissleder, R.: High-Efficiency Intracellular Magnetic Labeling with Novel Superparamagnetic-Tat Peptide Conjugates. *Bioconjugate Chemistry* **1999**, *10*, 186-191.

(14) Berry, C. C.; Curtis, A. S. G.: Functionalisation of magnetic nanoparticles for applications in biomedicine. *Journal of Physics D-Applied Physics* **2003**, *36*, R198-R206.

(15) Child, H. W.; Del Pino, P. A.; De La Fuente, J. M.; Hursthouse, A. S.; Stirling, D.; Mullen, M.; McPhee, G. M.; Nixon, C.; Jayawarna, V.; Berry, C. C.: Working Together: The Combined Application of a Magnetic Field and Penetratin for the Delivery of Magnetic Nanoparticles to Cells in 3D. *ACS Nano* **2011**, *5*, 7910-9.

(16) Dejardin, T.; de la Fuente, J.; del Pino, P.; Furlani, E. P.; Mullin, M.; Smith, C. A.; Berry, C. C.: Influence of both a static magnetic field and penetratin on magnetic nanoparticle delivery into fibroblasts. *Nanomedicine* **2011**, *6*, 1719-1731.

(17) Sakamoto, N.; Tanabe, Y.; Yokota, T.; Satoh, K.; Sekine-Osajima, Y.; Nakagawa, M.; Itsui, Y.; Tasaka, M.; Sakurai, Y.; Cheng-Hsin, C.; Yano, M.; Ohkoshi, S.; Aoyagi, Y.; Maekawa, S.; Enomoto, N.; Kohara, M.; Watanabe, M.: Inhibition of hepatitis C virus infection and expression in vitro and in vivo by recombinant adenovirus expressing short hairpin RNA. *Journal of Gastroenterology and Hepatology* **2008**, *23*, 1437-1447.

(18) Hamm-Alvarez, S. F.; Okamoto, C. T.: Endocytosis and sorting of macromolecules. *Advanced Drug Delivery Reviews* **2003**, *55*, 1351-1352.

(19) Bareford, L. M.; Swaan, P. W.: Endocytic mechanisms for targeted drug delivery. *Advanced Drug Delivery Reviews* **2007**, *59*, 748-758.

(20) Shi, W.; Wang, J.; Fan, X.; Gao, H.: Size and shape effects on diffusion and absorption of colloidal particles near a partially absorbing sphere: Implications for uptake of nanoparticles in animal cells. *Physical Review E - Statistical, Nonlinear, and Soft Matter Physics* **2008**, *78*.

(21) Lühmann, T.; Rimann, M.; Bittermann, A. G.; Hall, H.: Cellular uptake and intracellular pathways of PLL-g-PEG-DNA nanoparticles. *Bioconjugate Chemistry* **2008**, *19*, 1907-1916.

(22) Richard, J. P.; Melikov, K.; Vives, E.; Ramos, C.; Verbeure, B.; Gait, M. J.; Chernomordik, L. V.; Lebleu, B.: Cell-penetrating peptides: A reevaluation of the mechanism of cellular uptake. *Journal of Biological Chemistry* **2003**, *278*, 585-590.

(23) Lundberg, M.; Johansson, M.: Positively charged DNA-binding proteins cause apparent cell membrane translocation. *Biochemical and Biophysical Research Communications* **2002**, *291*, 367-371.

(24) Duchardt, F.; Fotin-Mleczek, M.; Schwarz, H.; Fischer, R.; Brock, R.: A comprehensive model for the cellular uptake of cationic cell-penetrating peptides. *Traffic* **2007**, *8*, 848-866.

(25) Sun, S. H.; Zeng, H.; Robinson, D. B.; Raoux, S.; Rice, P. M.; Wang, S. X.; Li, G. X.: Monodisperse MFe2O4 (M = Fe, Co, Mn) nanoparticles. *Journal of the American Chemical Society* **2004**, *126*, 273-279.

(26) Hillaireau, H.; Couvreur, P.: Nanocarriers' entry into the cell: Relevance to drug delivery. *Cellular and Molecular Life Sciences* **2009**, *66*, 2873-2896.

(27) Harush-Frenkel, O.; Altschuler, Y.; Benita, S.: Nanoparticle-cell interactions: Drug delivery implications. *Critical Reviews in Therapeutic Drug Carrier Systems* **2008**, *25*, 485-544.

(28) Pineiro-Redondo, Y.; Banobre-Lopez, M.; Pardinas-Blanco, I.; Goya, G.; Lopez-Quintela, M. A.; Rivas, J.: The influence of colloidal parameters on the specific power absorption of PAA-coated magnetite nanoparticles. *Nanoscale Research Letters* **2011**, *6*.

(29) Moros, M.; Pelaz, B.; Lopez-Larrubia, P.; Garcia-Martin, M. L.; Grazu, V.; de la Fuente, J. M.: Engineering biofunctional magnetic nanoparticles for biotechnological applications. *Nanoscale* **2010**, *2*, 1746-1755.

Introduction to Au NPs & their Bio-Applications

Chapter 5

As bulk materials, the novel metal gold (Au) has been for centuries a very popular subject of study in science. However, the technological development of nanoscience (nanotechnology) has revolutionized the impact of Au in the scientific community and more recently, in our society in the form of very beneficial technological applications in fields such as materials science, energy or medicine. Currently, the development of new synthetic routes to obtain Au colloids, complex multicomponent materials embedding Au colloids, and following novel applications based on these materials are the subjects of work for many scientists; consequently, reports related to gold colloids, also referred to as Au nanoparticles or nanocrystals (GNPs), have become very prolific in literature. Furthermore, the popularity of synthetic methods yielding GNPs with on demand size, shape, structure (solid or hollow), coating, etc. continues growing exponentially; as the degree of control to fabricate such structures evolves, new applications based on these materials can be explored. Photothermal therapy (PTT), photoacoustic imaging and surface enhanced resonance spectroscopy (SERS) are examples of applications where NPs such as nanorods, hollow nanospheres and nanostars, among others, can act as transducers.

Among material scientists, the interesting optical features of GNPs are their key to success; in general, photons can couple to the plasma resonance of the conduction electrons at the surface of metallic NPs to produce their collective oscillation, in a phenomenon usually refereed as localized surface plasmon resonance (LSPR). Indeed, the optical properties of metallic NPs are mainly dictated by surface plasmons. For NPs made of Au (noble metals in general), the LSPR band lies in the visible-NIR part of the spectrum; the position of the LSPR band is determined by a combination of NP attributes such as composition, size and shape, and also by the dielectric environment. The interaction of light with surface plasmons at very confined volumes like that of Au colloids is currently being explored in fields such as optics and energy.[1-3]

The ability for tuning the color of colloidal solutions of GNPs by changing their size has been known for long time. However, in the last decade, a consistent body of work has highlighted the fact that shape plays also a crucial role in determining the optical properties of nanomaterials. Ultimately, the energy confinement of electrons, holes, excitons, phonons, and plasmons with respect to the NPs shape is the reason for this observation. Colors can be attributed to changes surface plasmon resonance, energy at which light couples to the surface plasmons of NPs (Figure 5.1).

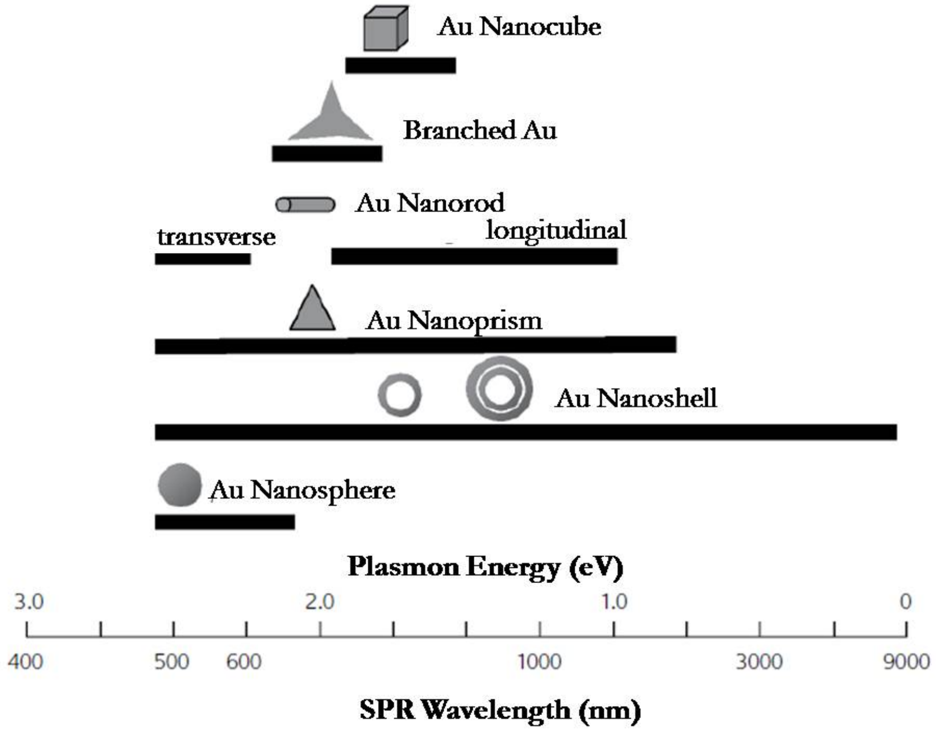

Figure 5.1. *Range of surface plasmon resonances of GNPs as a function of their shape (reproduced from Treguer-Delapierre).*[4]

In the context of biology and medicine, in addition to the widely explored optical properties, GNPs exhibit two extra value properties which make them the "stars" among a wide variety of NPs for bioapplications, *i.e.* biocompatibility and ease of surface modification by a wide range of thiolated molecules. In summary, GNPs represent an ideal platform for many applications in very different areas. The interest on Au is reflected by the increasing number of publications related to GNPs in the last years (Figure 5.1a); the most recent interest on anisotropic GNPs such as nanorods, nanoplates, branched nanostructures, nanoprisms or nanoshells can be also seen in Figure 5.1b.

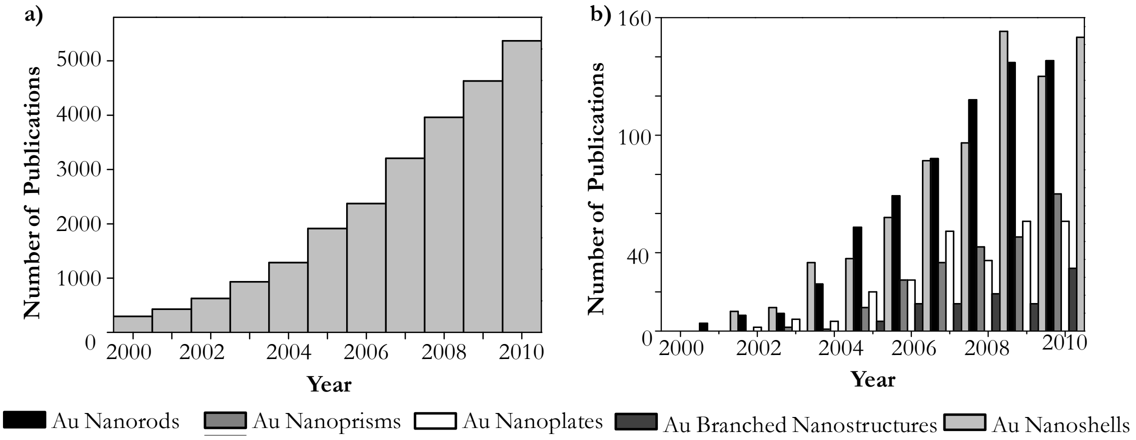

Figure 5.2. *Publication during the last decade related to a) GNPs and b) different types of anisotropic GNPs (Source Isi Web of Knowledge, June 2011).*

5.1. Ancient Uses of GNPs

During the Stone Age, gold was valued among mankind for its beauty and for its resistivity against corrosion; also, it was hammered into articles of jewelry. Gold extraction started in the 5th millennium B.C. However, in contrast to the long history of gold, the development of its chemistry was delayed because of its noble character. Gold can be only dissolved in oxidizing media such aqua regia or by complexing species such as cyanides under air.[5] Long before the development of modern gold chemistry the unique "golden" appearance of gold was highly appreciated. Probably, "soluble" gold appeared around the 5th or 4th century B.C. in Egypt and China; colloidal gold was used then to make ruby glass and for coloring ceramics, applications which continue nowadays. In the Middle Ages, gold was greatly valued due the belief of its curative powers for various diseases. All these aspects were compiled in which is considered the first book on colloidal gold wrote by F. Antonii in 1618.[6] Communications regarding the curative properties and optical features of "soluble gold" continued steadily during the 17th and 18th centuries. In 1857, M. Faraday reported on the synthesis of gold colloids by the reduction of a gold (III) salt, in a vastly cited work which may be well considered the pioneering work on the synthesis of GNPs by wet-chemistry methods.[7] However, a definitive breakthrough in the synthesis of GNPs (among other NPs) had to wait until the '90s with a series of works by Schifrin and coworkers.[8-11] It is worth mentioning that, as for GNPs, during the '90s definitive and substantial advances were achieved in the field of nanoscience.[12-14]

5.2. Synthesis of GNPs

In literature, one can find a great diversity of synthetic methods, both bottom-up and top-down approaches, to obtain GNPs with different size and shape; however, most of these synthetic routes have been reported for the synthesis of "spherical" GNPs (polyhedral). Although there are physical methods to obtain GNPs, [15-17] wet-chemical methods have been proven so far more efficient to yield NPs with controlled size, shape and coating; these are based on solution-phase colloidal chemistry. For GNPs, these methods rely on the chemical reduction of a gold salt into its metallic form which can grow then to form nanocrystals. To control the growth of the initially formed seeds and to prevent nanoparticle aggregation, donor ligands, polymers and surfactants, to name a few, are used as stabilizers. Once anchored onto NPs, these molecules can provide NPs with colloidal stability by electrostatic repulsion (*e.g.* citrate) or steric stabilization (*e.g.* polymers).

A variety of redox reactions, by using reducing agents such as sodium borohydride, hydrogen and alcohols, have been used to synthesize metal nanoparticles. As previously stated, as early as in 1857, Faraday reported the preparation of a colloidal gold sol (NPs) from the reduction of $HAuCl_4$ with phosphorous ligands as stabilizers.[7] In 1951, Turkevich and coworkers synthesized a stable deep-red dispersion of uniform 20-nm gold nanoparticles by using sodium citrate as both a reductant and a stabilizer.[18] Typically, molecules containing phosphanes and thiols are used as stabilizers by means of Au-P and Au-S bonds. Water-soluble phosphanes have been successfully used to shield GNPs,[16] however, thiolated chains appear to have been established as the prevalent stabilizer for GNPs of any size and shape. The stabilization of GNPs with alkanethiols was first reported by Mulvaney and Giersig;[19] shortly after, this group described the use of a silica coating for stabilization of GNPs.[20]

In 1994, Schiffrin and coworkers reported on a novel method (since then, normally referred to as the Brust-Schiffrin method) for the synthesis and stabilization of GNPs;[10] this method has had a tremendous impact because it allows the facile synthesis of thermally and air-stable monodispersed GNPs with controlled size. This technique is based on the Faraday's two-phase system and uses thiolated chains that strongly bind to GNPs. Shortly after, Brust and coworkers also described a single-phase system by which the synthesis and stabilization of GNPs can be extended to a variety of thiolated chains. [9,10,21] Alternative methods make use of the "alcohol reduction process" developed by Hirai and Toshima;[22] this approach is widely used for preparation of NPs stabilized by organic polymers such as poly(vinylpyrrolidone) (PVP), poly(vinyl alcohol) (PVA) and poly(methylvinyl ether).[23]

Regarding the synthesis of anisotropic GNPs, a number of synthetic approaches have been described including photochemical and electrochemical methods,[24-26] and others based on the chemical reduction of the gold precursor.[27] The most relevant synthetic methods for the synthesis of anisotropic GNPs in high yield are briefly discussed in the following:

(i) **The seed-mediated method** is nowadays the most extended aqueous synthetic approach to produce a variety of Au anisotropic NPs such as nanorods and nanoprisms. This method was developed in basis of the Zsigmondy´s "nuclear" method, which involves a two-step process for making NPs.[28] First of all, seed NPs are formed by a reduction process in which the metal salt is reduced in the presence of stabilizing agents. Typically this step involves the use of a strong reductant agent like sodium borohydride. After this, seeds are grown using a growth solution which contains the gold precursor, surfactants and a mild reducing agent. In this step, the newly formed metal atoms bind onto seed surfaces. The surfactant molecules can form suitable templates that facilitate the growth process to yield nanoparticles of desired morphology. The size of the nanoparticles can be typically tuned by adjusting the amount of growth solution. External agents such as molecules or ions can alter the growth direction of GNPs to yield NPs with very different shapes.[29-31] For instance, with the addition of a small amount of iodide ion into the growth solution to obtain nanorods, the shape of the resultant NPs can be changed to be triangular nanoprisms instead.[32]

(ii) **Polyol synthesis or thermal decomposition** is a simple and versatile route, developed in 1989 by Fievet and coworkers.[33] Probably, the most successful reaction for producing noble metal colloids with controlled shape has been the polyol process by using poly(vinyl pyrrolidone) (PVP) as a surface-capping agent. The metal precursor is dissolved in a polyol solution that is brought to near-reflux temperatures. Typical choices of polyols include ethylene glycol, 1,2-propylene glycol, and 1,5- pentanediol. Because viscosity (h) is largely determined by the length of the hydrocarbon chain of the polyol (for the solvents listed, h = 16.1, 40.4, and 140 mPa.s, respectively), the solvent of choice can greatly impact the diffusion and growth processes associated with metal nanocrystal formation. In addition, the polyol acts as the reducing agent for metal reduction and, at the relatively high temperatures for the reactions described herein, is likely oxidized to various aldehyde and ketone species.

(iii) **Template-mediated synthesis** represents a straightforward route to non-spherical GNPs. In this approach, the template serves as a scaffold within (or around) which gold is generated in situ and shaped into a morphology complementary to that of the template. A wealth of templates have been successfully developed and utilized, including channels within porous materials, mesoscale structures self-assembled from organic surfactants or block copolymers, biological macromolecules such as DNA strains or viruses, and existing nanostructures synthesized using other approaches. When the template is only physically involved, it is often necessary to remove it selectively using a post-synthesis treatment in order to harvest the resulting gold nanoparticles. It is widely accepted that template-directed synthesis is a simple and cost-effective procedure that also allows a complex topology present on the surface of a template to be duplicated. As a major drawback, the nanoparticles synthesized by this route are often polycrystalline and the quantity that can be produced in each run is relatively limited.

(iv) **Galvanic replacement reactions ("electroless deposition")** is a method introduced by Brenner and Riddell to describe the spontaneous reduction of metal ions to metallic particles and films in the absence of an external electric field.[34] Recently, this method has attracted attention due to its simplicity of operation and cost effectiveness. Xia and coworkers have prepared a number of anisotropic GNPs (*e.g.*, nanorings, prism-shaped nanoboxes, nanotubes, and multiple-walled nanoshells or nanotubes) using the galvanic replacement reaction between solutions containing Au precursor salts and Ag nanostructures prepared through polyol reduction. The electrochemical potential difference between the two species drives the reduction reaction; concurrently, metallic gold can deposit epitaxially on the surface of the AgNPs which act as anisotropic templates. In parallel to the gold deposition, the inner part made of Ag is oxidized and ultimately removed to produce hollow and, eventually, porous structures. Moreover, using Pt and Pd precursor salts instead of gold salt allows for the preparation of Pt- and Pd-containing hollow nanostructures, respectively. [35]

5.3. Common Anisotropic GNPs for Bioapplications

Among a great variety of anisotropic GNPs, those which can be prepared in a controlled way, high yield, reproducibility, etc. and are currently in use for bioapplications are discussed in the following; they are presented in order of structural complexity, *i.e.* (A) nanorods, (B) nanoprisms which will be discussed in detail as they are the main focus of Chapter 6-8, (C) nanoshells, (D) nanocages and hollow nanostructures, and (E) nanostars (also called branched nanostructures, nanoflowers, etc.).

(A) Nanorods

The first reported synthesis of gold nanorods (GNRs) was performed by using the hard-template method (electrochemical deposition in a porous membrane).[36,37] In a pioneering work, Wang and coworkers introduced a combination of surfactant additives and an electrochemical oxidation/reduction procedure to prepare colloidal GNRs with tunable aspect ratio.[38] However, the most extended methodology to generate GNRs was described independently by the groups of Murphy and El-Sayed in 2001 and 2003 respectively.[29,39] This methodology provides an excellent degree of control over the size, shape and monodispersity of the resulting NPs. The method is a two-step seed-mediated protocol which requires the use of the surfactant cetyltrimethylammonium bromide (CTAB) (Figure 5.3).

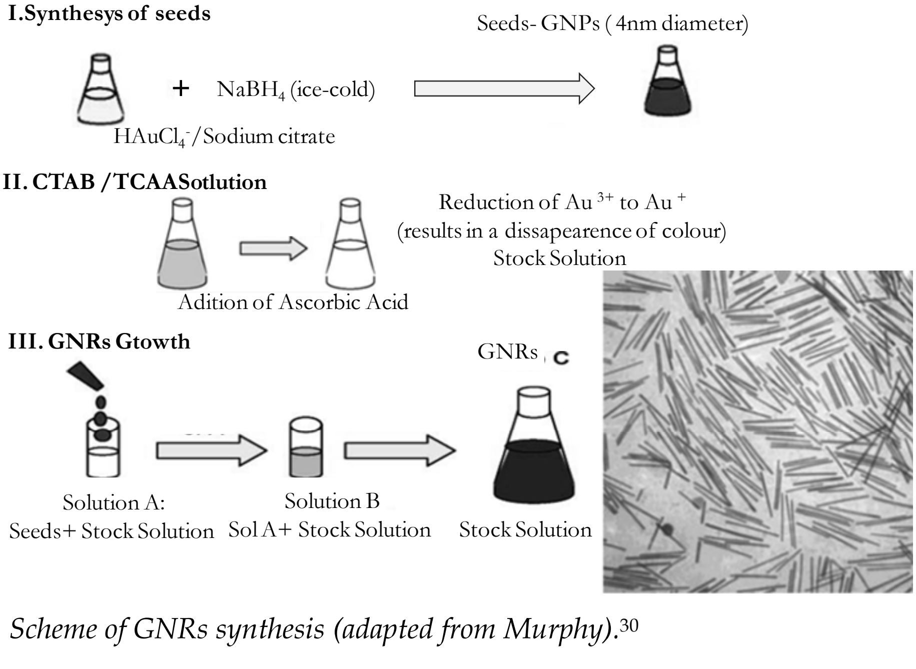

Figure 5.3. *Scheme of GNRs synthesis (adapted from Murphy).*[30]

In the first step, "seeds" (small GNPs of *ca.* 4 nm) are formed by adding aqueous sodium borohydride to a solution of CTAB and the gold (III) salt. In the second step, GNRs are grown by adding the gold seeds to a growth solution containing CTAB, silver nitrate, gold salt and ascorbic acid. Usually GNRs are allowed to growth overnight without stirring. In this methodology, silver nitrate is found to be necessary due to its effect on the final shape and crystallinity of the resulting GNRs.[39,40] Besides the seeding methodology, single-crystal GNRs (also nanowires) can be synthesized by electrochemical and photochemical methods.[38,41] Interestingly, in all cases bromide is required. This fact highlights the importance of the presence of bromide to which it might be given a more critical role in the formation of GNRs than that of CTAB.

(B) Nanoplates.

In the last decade, there have been described several methodologies to produce gold nano- and microplates. One strategy involves the use of light (photoinduced methods); although this kind of light-triggered reactions is usually used for AgNPs, it is possible to find some examples of Au nanoplates.[26,42]. A representative example is shown in Figure 5.4 where one can see a scheme of the synthetic route developed by Zhang and coworkers to produce giant Au microplates.

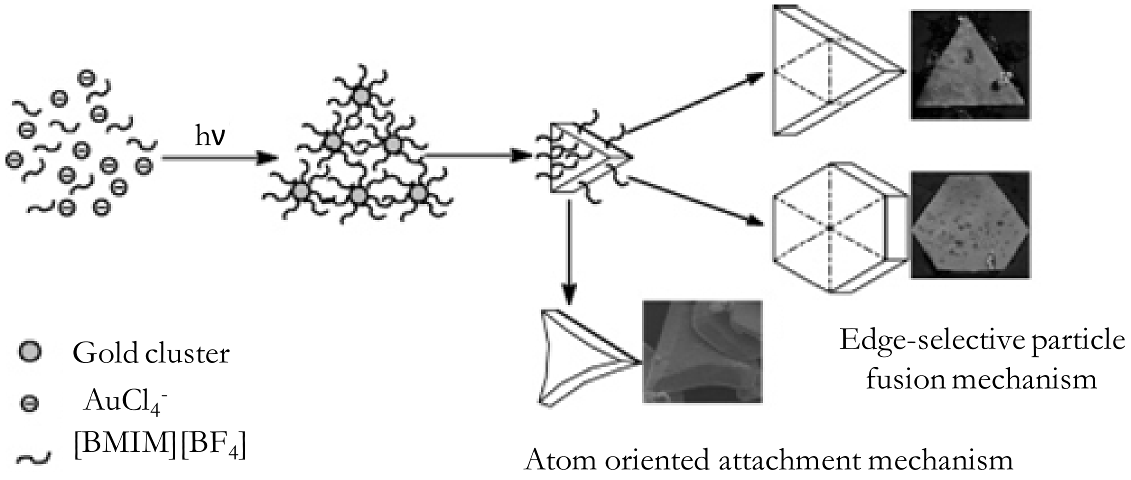

***Figure* 5.4**. *Formation of nanoplates using the photoinduced method (adapted from Zhang).*[26]

In aqueous solution, the formation of a specific shape is usually restricted to a specific choice of the reaction parameters. For instance, Sau and coworkers showed that either hexahedra (cubes) or octahedral shapes can be obtained through variations of the silver nitrate mediated synthesis of gold nanorods.[40,43,44] The seed-mediated growth of gold nanorods is frequently modified to obtain gold nanoplates. Some parameters such as an increase in the pH or surfactant concentration, and the addition of halide ions have been studied to promote the formation planar nanostructures. Unfortunately, all current procedures still result in rather low yields (40–65%) compared to those for GNRs (ca. 95–99%) and a purification step is required in order to eliminate isotropic structures.

To date, the most relevant approach to synthesize gold nanoprisms appears to be that developed in Mirkin´s lab (Figure 5.5); trigonal nanoprisms were synthesized by the group of Mirkin using a procedure adapted from the seed-mediated method to produce GNRs where the use of silver nitrate is prevented.[45,46] Citrate capped Au NPs (*ca.* 5 nm) were used as templates to grow into nanoprisms in a three-step protocol (Figure 5.5); the growing solution consisted here in a saturated CTAB solution containing the gold precursor, ascorbic acid and NaOH. Nanoprisms of average edge-length and thickness of 144 and 8 nm, respectively, were obtained with yields up to 65%. Larger prisms, with edge lengths up to 220 nm were also grown using smaller prisms as seeds.[47]

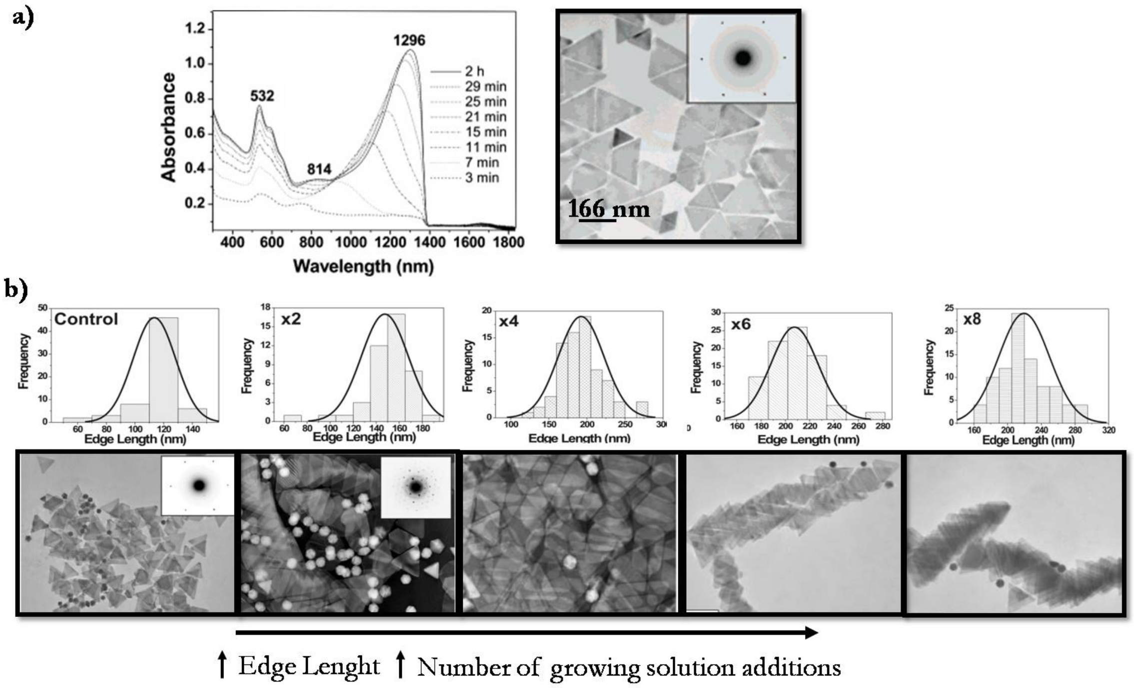

Figure 5.5. a) Growth process of gold nanoplates followed by Vis-NIR (left), and TEM images from the nanoplates obtained (right) (Adapted from Mirkin);[45] b) Effect on the edge length of nanoprisms of the addition of different amounts of the growing solution.[47]

Other useful variations to the seed-mediated method include the addition of salts or polymers to the growth solution. Ha and coworkers showed that the addition of KI at pH 4 to the CTAB based growth solution increases the yield of gold nanoprisms up to 45% (Figure 5.6).[32] Based on a series of control experiments the authors proposed a possible growth mechanism for nanoprisms involving growth inhibition of the {111} facets by strongly bonded halide ions (see growth mechanism section). In principle, the addition of traces of iodine is enough to change the morphology of the particles to nanoprisms.[48] Nanoprisms formation in the presence of iodide ions has been also demonstrated to be dependent on the pH of the growth solution and the temperature. Nevertheless, a relatively residual population of polyhedral NPs is always observed. In 2008, Mirkin´s lab also reported on the iodine effect; they found that using no iodine at all, the reaction products were exclusively polyhedral NPs whereas as the iodine concentration was increased, the shape passed through GNRs (2.5 - 5 μM I^-, 45% yield), mixture of shapes (10 μM I^-), nanoprisms (50 μM I^-,65% yield) and plate like structures for higher iodine concentrations (Figure 5.6c).[48]

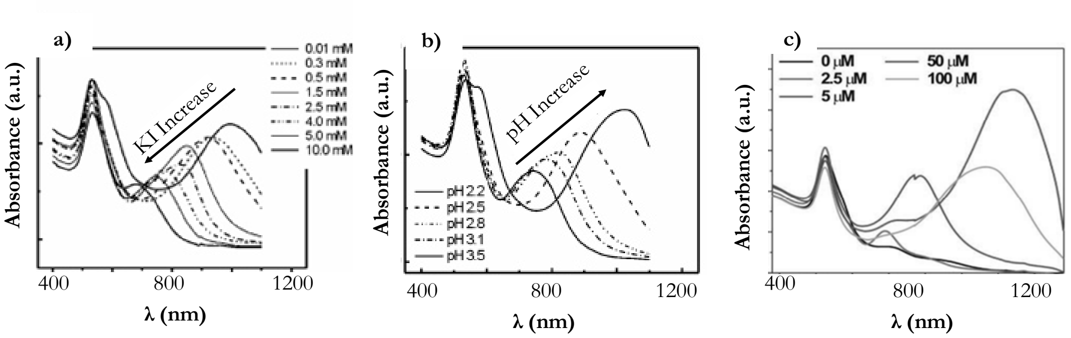

Figure 5.6. *a) Nanoprisms formation dependence with iodine concentration and b) shows pH contribution to nanoprisms formation (both adapted from Ha).*[32] *c) Different products spectra obtained changing iodine concentration (adapted from Millstone)*[48]

Fan and coworkers highlighted the importance of the crystalline structure of the seeds to produce stacking faults which ultimately, are responsible for nanoprisms generation.[49] Other work studied the effect of temperature and the presence of traces of silver ions in the shape-generation process (Figure 5.7);[50] their results showed that temperature is critical in order to generate kinetic controlled products, by changing the yield of different shapes. They also proposed an effect of the silver concentration on the shape of the seeds which ultimately determine the shape of the final product.

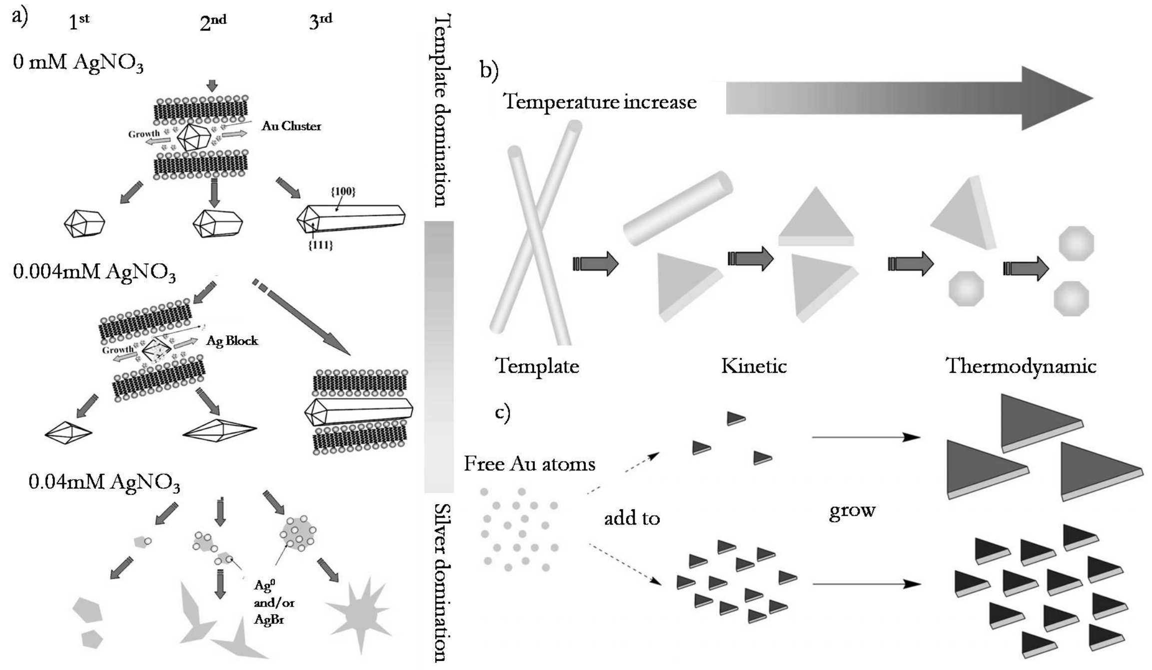

Figure 5.7. *a) Influence of silver ions on seeds and the final shape and b) influence of temperature (adapted from Chen et al.);*[50] *and c) scheme showing the influence of the concentration of seeds on the size of nanoplates (adapted from Fan et al.).*[49]

The influence of CTAB in the nucleation step to form NPs was studied by Zhang and coworkers using the see-mediated approach.[51] They were able to modulate the shape of the seeds by varying the CTAB concentration; these "controlled seeds" evolved into different products (Figure 5.8).

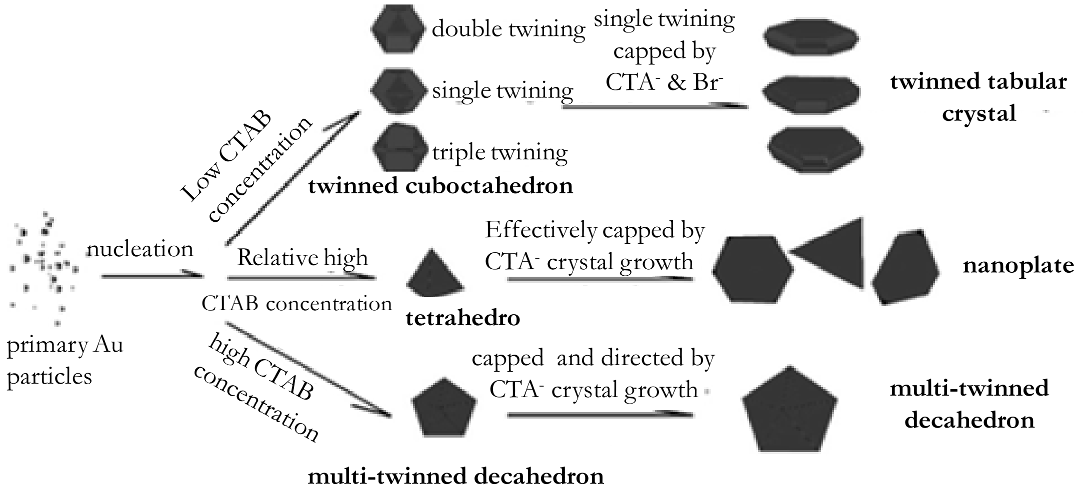

Figure 5.8. *Scheme of the CTAB directed synthesis of gold particles.(Adapted from Zhang)*[51]

Chu and coworkers published a work where in a single step, avoiding preformed seeds, and using the thermal decomposition method in the presence of CTAB, they were able to produce three different sizes of nanoplates.[52]

The use of polymers as surfactants to help plate formation during the metal salt reduction has been also studied. Polyvinylpyrrolidone (PVP) is the most popular polymer in the chemical synthesis of a wide variety of metal nanocrystals. Typically, PVP acts as capping agent, although it has been demonstrated that it may also act as a mild reducing agent.[53] Also, PVP has often been claimed to play a key role in determining the final particle morphology, through stronger adsorption onto certain crystalline facets. In the gold case, the use of PVP is linked to the use of ethylene glycol as solvent, using temperatures above 100ºC. Size-controlled gold nanoplates were synthesized with high purity by the reduction of the gold precursor by sodium citrate (in an unusual low concentration) in the presence of PVP (Figure 5.9).[54]

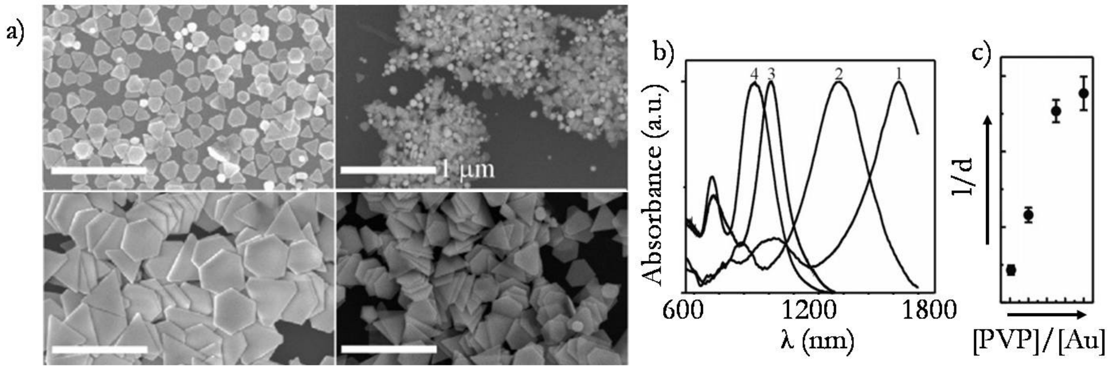

Figure 5.9. *a) SEM images, b) absorption spectra from the resultant plates with different ratios of PVP/Au and c) aspect ratio for these products which is increase meanwhile increase the ratio PVP/Au (adapted from Ah).*[54]

With the insufficient addition of the reductant, the molar ratio of sodium citrate and PVP relative to the gold salt played an important role in determining the geometric shape and size of the product. These nanoplates were single crystals edge-length in the range of 80-500 nm and thickness of 10-40 nm; these exhibited remarkable plasmon bands in the range of the EM spectrum of 700-2000 nm. Surprisingly, this methodology has not been further explored in the context of bioapplications, maybe due to the presence of PVP or irreproducibility in terms of high yield of nanoplates.

Shortly after, in 2006, Xia and coworkers proved this method to be applicable for different metals such as Ag, Pd and Pt, in addition to Au. They also studied the effect of the molecular weight of PVP, the ratio of the reagents, a negative role of the light and more importantly, they assessed to PVP the role of mild reductant in addition to its role as surfactant. Also surprisingly, the yield of the Au nanoplates was only a 30%,[23] far from the previously obtained by Ah and coworkers.[54] Micrometer triangular plates (Au nanosheets) have been also synthesized using this PVP-based methodology. Li and coworkers studied the effect of changing parameters such as temperature, PVP or gold salt concentration;[55] recently, the effect of ions in the final shape of the sheets has been reported.[56] Micrometer nanoplates have been also produced using linear polyethylenimine (LPEI) instead of PVP with an relatively good yield.[57]

In 2008, Lavarta and coworkers used amphiphilic polyethylene oxide-polystyrene oxide block copolymers as both reductant and stabilizing agents in water solution to form NPs; the production of spherical or pseudospherical nanoparticles was shown to depend on parameters such as the copolymer block length, and copolymer and gold salt concentrations. By moderate increasing the temperature up to 65 °C, they observed a progressive formation of single-crystalline gold nanoplates in good yields (up to 70%) without further addition of any reactants or growing solutions. These nanoplates are characterized by edge-length values in the range of 0.1-1.2 μm depending on copolymer concentration and reaction temperature.[58]

In the context of green chemistry, another kind of chemical reduction of gold can be achieved by using natural extracts from different organisms in approaches normally referred to as biological synthesis. For the production of Au nanoplates, the yields obtained with the reported methodologies are so far relatively low; this fact can be inferred from the optical features in the NIR range from different biological synthesis (Figure 5.10). The pioneer work in this area was published in 2004 by Sastry and coworkers; they used the extract of lemongrass plant (*cymbopogon flexuosus*) to produce gold triangular nanoplates.[59] In other work, these authors also studied the combined effect of a halide ions and the extract of lemongrass; surprisingly, it was founded that chloride ions promote nanoplate formation whereas iodine promoted pseudospherical NPs.[60] A variety of other extracts such as those from brown seaweed (*Sargassum sp.*),[61] aloe vera,[62] a green alga (*Chlorella vulgaris*),[63] and more recently an extract of pear fruit, have been used to produce gold nanoplates.[64]

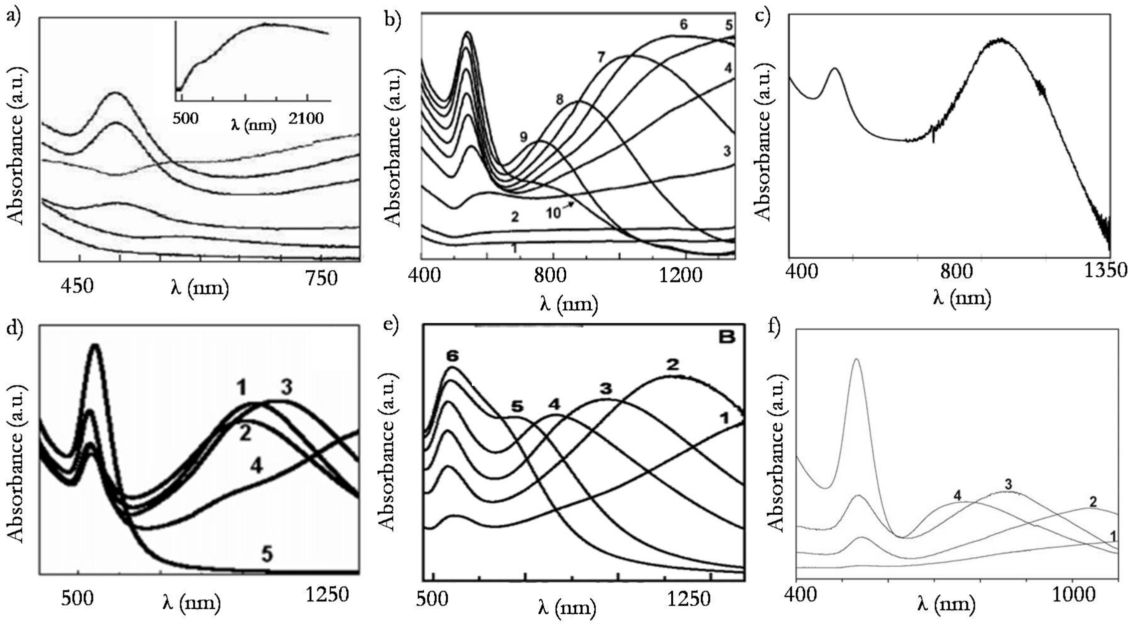

Figure 5.10. *Spectra of biological synthesized gold nanoplates using extracts from (a, b and d) lemongrass plant, (c) brown seaweed, (e) aloe vera plant and (f) a green alga. Reproduced from different works.*[59-63,65]

Also in the context of methods based on green chemistry, there have been further successful attempts to produce nanoplates; in one-pot synthesis and based on the biomineralization ability of BSA in aqueous solutions, Lee and coworkers reported the synthesis of different plate-like (triangular and hexagonal shapes) Au microstructures and the influence of temperature, pH and Ag^+ in the shape and size of the resulting NPs.[66] Malikova and coworkers found that a gold (III) salt can be reduced by salicylic acid to yield a mixture of triangular, hexagonal and polyhedral NPs.[67] In other work, by using green chemistry as well, the gold salt was reduced at room temperature by L-aspartate to produce plates whereas using L-tryptophan instead resulted in spherical NPs.[68]

(C) Gold nanoshells (GNSs)

These are spherical nanoparticles consisting of a dielectric core (*e.g.* silica, polystyrene or sodium sulfide) covered by a thin layer of gold (Figure 5.11). Typically, the optical features of these structures characterized by a tunable plasmon band that gives rise to intense optical absorption and scattering.[69] The modulation of the plasmon band can be reached controlling the thickness of the Au shell relative to the diameter of the core; thus, the plasmon band of nanoshells can be tuned in the range of 700-1300 nm.[70]

Gold nanoshells based on a silica core were originally developed by Halas and coworkers.[71] Typically, the scaffolds (silica cores) are prepared by the Stöber method and later on, small GNPs are grown onto the silica to form a relative uniform thin shell.[70-73] Due to their biocompatibility and on demand plasmon band, these structures have been widely applied in photothermal therapy by NIR light.[74-80] Moreover, the commercial product AuroLase® Therapy uses AuroShell® particles (nanoshells) with a near infrared laser source to thermally destroy cancer tissue without significant damage to surrounding healthy tissue; these particles are already in advanced stages of FDA clinical trials.

Using similar techniques Halas and coworkers have developed different of anisotropic structures;[81] *e.g.* nanorices contain elongated hematite cores as scaffolds and the thin gold shell in nanocomposites.[82] In other works, nanoshells were based on a gold sulfide core;[83,84] this nanostructure has been widely studied and applied although its core-shell nature is still very controversial.[85-89] In chapter 5, the nature of the optical features of these will be further discussed. Recently, Halas and coworkers have discussed a variety of gold coated semiconductor-cores.[90]

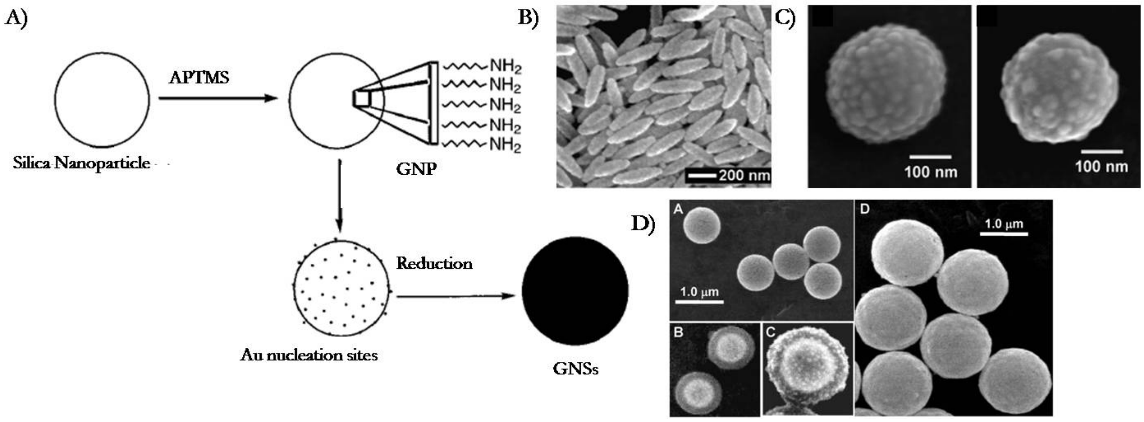

Figure 5.11. *A) Scheme of GNSs synthesis [73] B) Image of nanorice ;[82] C) Images of GNSs with different roughness ;[91] and D) Images of the sequence of synthesis of concentric GNSs.[92]*

(D) Nanocages and hollow nanostructures

These nanostructures have attracted a great deal of attention due their high surface to volume ratio and large pore volume. The most successful synthetic route to obtain these is based on the galvanic replacement method. The group of Y. Xia has used this method extensively to obtain hollow nanostructures made of different metals, *i.e.* nanocages (hollow nanocubes), nanorings, prism-shaped nanoboxes, nanotubes, and multiple-walled nanoshells or nanotubes.[93]

Galvanic replacement is based in the different electrochemical potential between two metals which drives the redox reaction. Regarding gold nanocages, Ag nanocubes serves as "reducing agents" and templates where Au^0 deposits; the reduction potential of $AuCl_4^-/Au$ (0.99 V) is more positive than AgCl/Ag (0.22 V). Redox reaction is the following: (Equation 5.1):

$$3Ag_{(s)} + HAuCl_4 \longrightarrow Au_{(s)} + 3AgCl_{(s)} + HCl_{(aq)} \tag{4.3}$$

Xia and coworkers have been able to control the reaction to obtain completely hollow gold cages, or non-complete hollow cages without corners or with holes in their faces (Figure 5.12). To obtain holes in the faces they used wet etching of silver with $Fe(NO_3)_3$ and/or NH_4OH.[35]

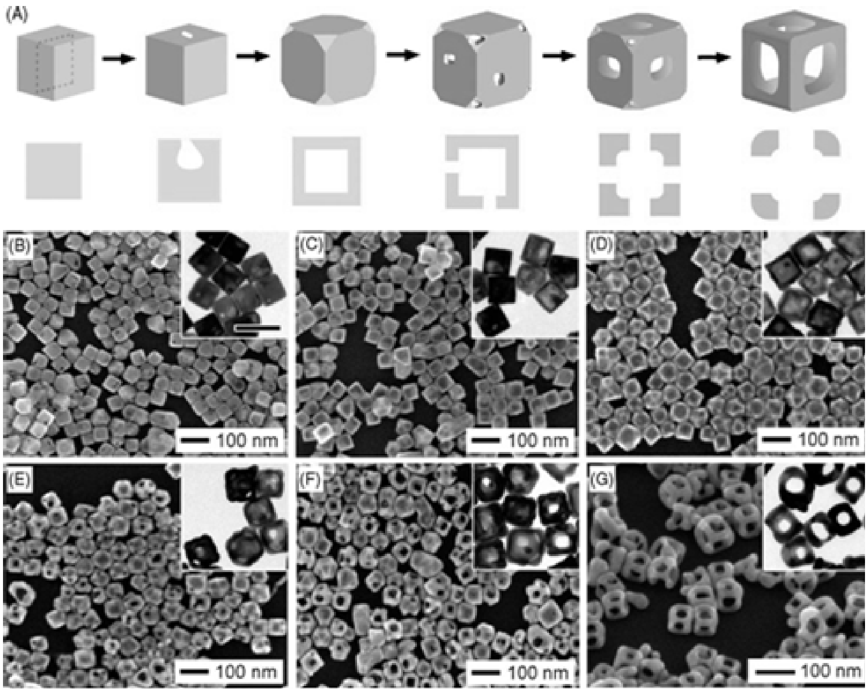

Figure 5.12. *Scheme of galvanic replacement gold nanocages formation(A)and SEM micrographs showing different structures (B-G). Adapted from Cobley.*[93]

(E) Branched nanostructures, nanostars or nanoflowers

These structurally complex structures represent an important subcategory of anisotropic structures which show remarkable optical features; sharp edges and tips exhibit large enhancements of the electric field (hot spots) which are very sensitive to local changes in the dielectric environment; these structures can be used as SERS platforms of enhanced sensitivity.[94,95] These gold nanostructures represent excellent "light confiners".[96]

The synthesis of branched nanostructures represents a complex scenario where the control of nucleation and growth processes is crucial. A highly branched structure with the same volume of a polyhedral nanocrystal has a larger surface area and thus higher surface energy. Due this high energy structure, their synthesis must be done under kinetics conditions.[95] A great diversity of parameters have been shown to play an important role in the formation of this NPs, *i.e.* the reactivity of the metal precursor,[97] the effect of the surface stabilization through a capping agent, the solvent of choice, the nature (strong, mild or soft) of the reducing agent, the reaction temperature or the effect of the additives. [95,98]

In literature, one can find two main wet-chemical approaches to produce Au-branched nanostructures, *i.e.* one-pot methods and those based on the two-step seed-growth method (Figure 5.13).

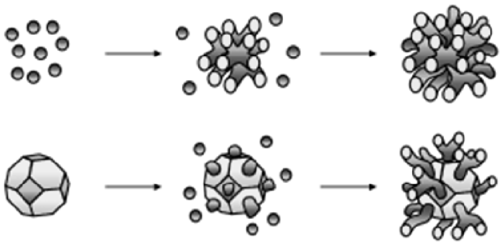

Figure 5.13. *Scheme of highly branched structures. (Adapted from Lim)*[99]

The seed-growth method used for branched nanostructures is a variant of that used to produce nanorods.[39] In the simplest approach, preformed seeds work as scaffolds to support the growth of a number of "fingers" or tips.[100,101] Variables such as the concentration of bromide and/or silver ions,[44,102] addition steps, order of reactant mixing, amount and/or type of capping agent have been shown to greatly influence in the successful generation of multi-tips. [41,99]

As previously stated, branched Au NPs can be made in one-pot synthesis where the gold precursor is reduced in the presence of an appropriate capping agent which eventually can be also act as reductant.[103-105]

5.4. Derivatization of GNPs

The colloidal stability of NPs is an important issue in the context of any application in which the organic coating is the key to success. For bioapplications, avoid aggregation and provide NPs with a load of molecules with biological relevance is of the most importance; materials scientists have to ask themselves how hybrid nanomaterials made of nanocrystals (plasmonics, superparamagnetic, semiconductors, etc.) and their constituents (surfactants, precursors, macromolecules or organic polymers, etc.) behave in a physiological environment that normally is far from the environment where the synthesis of the nanomaterials took place, *i.e.* polar or non-polar solvents with very particular attributes such as ionic strength, pH or presence of multivalent ions, salts or polymers, to name a few.

The most straightforward approach to derivatize NPs is attaching molecules onto the surface. Many synthetic routes of NPs use surfactants or molecules that can act as ligands. These molecules can avoid the aggregation by ionic stabilization (*e.g.* citrate) or by steric hindrance (*e.g.* CTAB, PVP, PEG, etc). Typically, ligand molecules must be bound onto the NPs surface by some attractive interaction such as chemisorption, electrostatic attraction or hydrophobicity.[5,106] Different groups (thiol, phosfine, amine, carboxy, etc) present in a molecule of interest can be used to promote the derivatization of NPs.[107] As previously discussed, in the case of GNPs, one of the features that make GNPs so attractive for bioapplications is the easy of functionalisation with thiolated chains. Thiol groups are considered to show the highest affinity to novel metals, principally with gold.[108]

To stabilize gold NP in organic phase solutions, thiolated hydrocarbon chains are the most popular choice. On the other hand, for GNPs in aqueous solution, the common approach is the use of bifunctional chains bearing a thiol group in one end and a hydrophilic group in the outermost end, facing the aqueous solvent. In order to create organics monolayers onto the NPs surface, amphiphilic chains are commonly used to promote the correct packaging; once stabilized, the organic layer can be exchanged by other made of molecules with higher affinity for Au^0. The group of Murray is pioneering on ligand exchange strategies.[109]

Techniques of ligand exchange have been also used for water-to-organic phase transfer of GNPs originally coated with CTAB;[77] CTAB chains strongly attached to

Au nanorods in the aqueous phase can be exchanged by using dodecanethiol to promote its transfer to organic phase whereas thiolated PEG chains can be used to organic phase-to-water re-transfer.

Other protocols reported on the use of amphiphilic molecules to provide GNPs with colloidal stability in polar and non-polar conditions. Small molecules are able to change their orientation depending on the solvent, or polymers that can be ionic or non ionic depending on surrounding conditions. (*e.g.* PEI, [110] poly(acrylic acid)[110,111]

In another approach developed by Parak and coworkers, amphiphilic polymers are intercalated in the aliphatic shell of the NPs in the organic phase; this method is usually referred to as the polymer coating method.[112,113] This strategy solves the drawbacks of some ligand exchange protocols where it is required a huge excess of the new ligand and furthermore, it provides with a general route to water soluble nanocrystals which can be then further derivatized for biological applications.[113]

Growing a glass shell around the GNPs, also referred to as the silanization method developed by Liz-Marzan and coworkers, is another approach widely used to stabilized NPs.[114]

Once achieved stabilization in physiological environments by one of the aforementioned methods, GNPs can be engineered into complex functional materials for a particular bioapplication. Nowadays, there is a wide variety of chemical methods to anchor molecules of biological relevance onto GNPs, *i.e.* fluorescence tags, PEG chains, proteins, carbohydrates, DNA, peptides, siRNA, enzymes, antibodies, cyclodextrins, biotin, etc.[13,115-119]

In all these cases, heterogeneity in surface coverage can result in patches on the surface, or in ligand conformational changes depending of the surrounding conditions which will determine their behavior in physiological media.[120,121] This difference in the surface coverage will drive protein absorption to form the known protein corona, or even the nanoparticles fate in biological systems.[122,123]

Purity of the final derivatized NPs is a really crucial aspect for many bioapplications; the physical properties of nanocrystals as well as the biofunctional coating should be as controlled as possible; in many cases, both the physical properties (plasmon bands, superparamagnetism, fluorescence, etc.) and the biological activity depends on the homogeneity of the sample. Therefore, a variety of methods are currently used for separation of functional NPs with different size, charge, shape, number of biomolecules, etc.[124]

5.5. Bioapplications of GNPs

The most outstanding property of GNPs is the presence of surface plasmons; these determine the optical properties of GNPs (in general, of metallic NPs) and open a wide range of potential applications.[125] Relative to the use of the surface plasmons of GNPs, the different applications can be categorized in different areas, *i.e.* energy; environment, information technologies and bioapplications, to name a few.

Recently, the application of GNPs in energy has become very popular due the energy problem associated with the ending of fossil fuels; GNPs are currently investigated to rise the efficiency in photovoltaic devices -[1] The use of Ag and Au NPs have increased the efficiency of photovoltaic cells by an order of 10-15%.[126]

The catalytic nature of some metallic NPs,[127,128] including GNPs, have made them very suitable candidates to be applied in the industry associated with the elimination of hazardous side-products; the products derived from industrial processes represent a problem for humans and the environment. The catalytic properties of some metallic NPs can be fostered by the excitation on their SPR; thus, GNPs can be used in photocatalysis in processes that can use solar light and mimics other biological processes. Moreover, GNPs are involved in the oxidation of CO into CO_2.[129] and can be used in homogeneous catalysis showing different catalytic behavior related with crystal structure differences.[130]

In the area of information technology, the use of metallic NPs has allowed for new methods for light manipulation, reading and writing information in sizes significantly smaller than light wavelengths, while the huge absorption and scattering cross section allows detection of very small signals .[131] Nowadays, these materials can be used to design antennas, lenses and resonators.[132,133]

Although the application of GNPs has extended to very different areas, GNPs have found a remarkable variety of applications specially in biomedicine; this has been motivated by their optical properties, biocompatibility, ease of production of multi-task nanosystems and the ability for tuning the Plasmon band in the NIR biological window. Applications in diagnosis and in therapy have been widely developed. Some bioapplications for in vivo systems of GNPs are summarized in Table 5.1.

	Modality	Nanoparticle/agent
Imaging	Optical Scattering/OCT	Au Nanoshells, GNRs, nanocages, NPs
	PET, SPECT	Radioisotope 198Au
	CT	GNPs[134]
Therapeutic actuation	Photothermal	Au nanoshells, GNRs, nanocages
	Photoacoustic	NIR absorbing GNPs
	Chemotherapy	GNPs loaded with anticancer drugs (doxorubicin, paclitaxel,etc.)
	Gene Therapy	GNPs loaded with siRNA, DNA

Table 5.1. *Imaging and Therapeutic capabilities of NPs: OCT, optical coherence tomography, MRI, magnetic imaging resonance; PET, positron electron tomography; SPECT, single photon emission computed tomography; CT, computed tomography.*[74]

Optical properties of GNPs can be complemented by its modification with molecules bearing a variety of biofunctions such as peptides, genetic material, antibodies, proteins, enzymes, fluorophores, carbohydrates, etc. In general, a correct derivatization is the key of success of these applications. In the following Table 5.2, imaging techniques related to GNPs are summarized.

The application of GNPs in imaging includes dark field imaging which uses light scattering of GNPs; this technique has been widely used for imaging of GNPs in tumoral cells.[79] For instance, this technique has been used to image gold nanorods while they were being used to treat and diagnose head and neck cancer.[135]

Optical coherence tomography (OTC) can be used to produce 3D images with micrometer resolution by analysis of a cross-section of tissues under a short coherence light source. The potential of nanoshells as OTC agents to detect tumors have been demonstrated by Halas and coworkers.[75] Also, other gold nanostructures such as rods, spheres, or nanocages have been successfully applied in this direction.[136]

Imaging Principle	Imaging Technique	Description
Scattering	Coherent optical tomography (OTC)	GNPs embedded in the medium change the backscattering properties
	Reflectance spectroscopy	Similar to above
Emission	Fluorescence	Emission of light with wavelength longer than excitation laser
	Two.photon luminiscence	Non-linear fluorescence
Absorption	Photothermal imaging	The absorption of laser energy by GNPs induces local increment of temperature that results in changes in the optical path length
	Photothermal OTC	The above effect measured by phase sensitive OCT
	Photoacoustic tomography	The absorption of laser energy by GNPs generate acoustic waves

Table 5.2. *Imaging principle, imaging technique and description of application of GNPs.*[74]

Two-photon luminescence (TPL) has been identified as a serial process involving sequential absorption of photons and emission from the recombination of electrons in the sp-band and holes in the d-band. [137] This effect is enhanced in GNPs, especially in NIR absorbing GNPs. TPL present some advantages with respect to confocal microscopy such as higher spatial resolution and reduced background signal. GNRs has been used in TPL imaging *in vitro*[137] and *in vivo*.[138]

Gold nanorods exhibit 2-fold higher contrast than clinical iodine contrast agents for X-ray computed tomography (CT);[134] this is motivated by the high atomic weight of gold. The use of GNPs has lead this imaging technique in a diagnosis tool since GNPs can be derivatized for specific purposes

Photothermal (PT) and photoacoustic (PA) imaging techniques make use of the interaction of laser-induced heating of materials, measuring directly the heat generated in the former, and detecting acoustic waves in the latter.[117] Due the strong light absorption of GNPs, showing extinction coefficients around 10^9 $M^{-1}\times cm^{-1}$, GNPs are very suitable agents for both techniques. NIR absorbing GNPs are ideal for these applications because NIR light can be used in deeper tissue-imaging applications; the penetration of NIR light is optimal for this. For instance, NIR-irradiation of NIR absorbing NPs provokes heat generation in the illuminated place. The heat dissipation to the adjacent tissue undergoes with a thermoplastic expansion creating an acoustic wave that propagates through the tissue and can be mechanically detected .[139] Gold nanorods have been applied in tumor imaging[140] and in PT flow cytometry .[117,141] In other study, 40 nm gold nanocages have been applied to imaging blood vessels by PT,[142] and they have been used also as contrast agents for photoacoustic tomography (PAT).[143,144] Gold nanostars also demonstrated their potential as PA agents.[145]

PT imaging can be combined with photothermal therapy (PTT) which use the generated heat to produce localized hyperthermia to destroy cancer cells, bacteria or virus. GNPS exposed to laser irradiation can act as therapeutic agents as themselves. NIR absorbing particles are the most appropriate agents for this therapy. In literature it is possible to find examples of PTT at molecular level, cellular lever, tumor level and in vivo. Most employed particles are GNRs, gold nanoshells and gold nanocages. Currently, Aurolase, a product based on gold nanoshells, is being commercialized by Nanospectra® Bioscience and it is currently in the process of FDA-sanctioned human pilot studies.[78] A similar PTT in clinical trials are also being designed using gold nanocages (Nanocages LLC). PTT will be discussed in detail in Chapter 7.

The ease to attach tumoral markers or drugs to GNPs has been also used to add specificity to multitask GNPs based nanosystems. El-Sayed and coworkers have carried out extensive work in this direction; for instance, they proved the ability of GNPs functionalized with a monoclonal antibody against epidermal growth factor receptor (anti-EGRF) to target only malignant epithelial cells.[146] Different labeling molecules such as platinum prodrugs, tamoxifen, folic acid, transcription necrosis factor (α-TNF) have been used to functionalize GNPs to target different cancer cells such as lung and colon, breast,[141] KB, MC-38 colon carcinoma, respectively.[147]

Since the original work of Mirkin,[13] GNPs functionalized with genetic material, DNA or siRNA, have been widely used in sensing and genetic therapy;[148-155] in a very general definition, gene therapy is the medical process by which inserting a small DNA or RNA sequence allows to modify the expression of certain specific proteins associated with a disease. GNPs functionalized with the genetic material of interest can be used to shuttle the genetic payload into cells to be repaired. Moreover, GNSs and Au nanorods loaded with DNA have been recently proven as efficient drug delivery carriers. In two studies, Halas and coworkers have shown the ability of GNPs to generate heat upon laser illumination which can be used to release genetic materials into cells.[77,156]

Others important applications of GNPs in drug delivery involve the use of laser irradiation, pH change, ionic concentration change, etc. to trigger a drug release. For instance, Xia and coworkers have achieved controlled drug release of gold nanocages upon laser irradiation.[157] Also, Parak and coworkers have used the heat capacity of GNPs upon laser illumination to release cargo from polyelectrolyte capsules.[89]

The plasmon band of GNPs is very sensitive to changes in the environment; a variety of sensors based on this sensitivity has been developed. Most popular are the based on GNPs aggregation which provoke a visible color change. Different kinds of interactions capable of producing aggregation of GNPs have been used, *e.g.* monoclonal antibodies to detect various antigenic sites or lectin-carbohydrate interactions. GNPs aggregation was also used to detect chorionic gonadotropin in the urine of pregnancy women, or to detect immunoglobulins in the blood serum of HIV patients.[158]

In 2003 Mirkin develop a single-analyte bio-bar code assay [159] It is carried out in a disposable chip through basic steps. When the sensing surface will be illuminated with light of the same frequency of the Plasmon surface of GNP could be detect target DNA sequences.

Other sensors to visualize specific interaction are based on the dot assay; this is a very useful assay due to the small volume required. Recently, the sensitivity of this assay was improved using Ag and GNPs..[160] Most important kind of assays are the enzyme-linked immunosorbent assay (ELISA) due its simple methodology,specificity and sensibility. In this kind of assays the recognition is amplified by the use of an enzyme-marked reagent which will recognize the analyte and will reveal its presence by a simple colorimetric enzymatic reaction. Result reading is performed in a plate-reader, using changes in absorbance. Previously describe strategies have been adapted to be used in this assays which amplified the method sensibility.[158]

SERS spectroscopy is one of the most powerful analytical techniques for identification of molecular species, providing complete vibrational information of the molecular system under study. This spectroscopy technique is based on the enhancement of Raman-active vibrations associated with proximity to surface plasmons; the enhancement of the Raman signal has been attributed to electromagnetic enhancement derived from the proximity to surface plasmons in on theory; (others has attributed the Raman enhancement to chemical contributions.[161]Gold nanostars are excellent SERS agents; sharp edges and tips exhibit large enhancements of the electric field (hot spots) which are very sensitive to local changes in the dielectric environment; these structures are used as SERS platforms of enhanced sensitivity.[94,95,162] (. In the last decade, SERS based on GNPs has been widely used to detect biomarkers in cancer[163]and other diseases[164], bacteria[165] or viral agents[166,167]. [162,163] Recently, SERS have been revealed as a promising technique to detect cancer cell in circulation. The advantage of this tool compared to fluorescence detection is based on the reduction of biological background interactions.[117]

5.6. NIR Absorbing GNPs

As previously stated, the optical properties (scattering and absorption of light) of GNPs come determined by their size, shape and structure (solid or hollow) as well as the nature of the surrounding medium. For anisotropic GNPs, such as nanorods, nanoprisms or nanodisks, the absorption of light, *i.e.* LSPR, is largely affected by the symmetry and aspect ratio (AR). The aspect ratio of a shape is typically defined as the length of the major axis divided by the width of the minor axis. Thus, spheres have an aspect ratio of 1. For core-shell GNPs such as Silica-Au or hollow GNPs, the optical properties depends mainly on the thickness of the Au shell (t) relative to the radius (R) of the NPs; here the aspect ratio, AR=R/t, deviates of the aforementioned definition. Figure 5.14 displays the geometry of the most common Au-based nanostructures which LSPR bands lay within the NIR window.

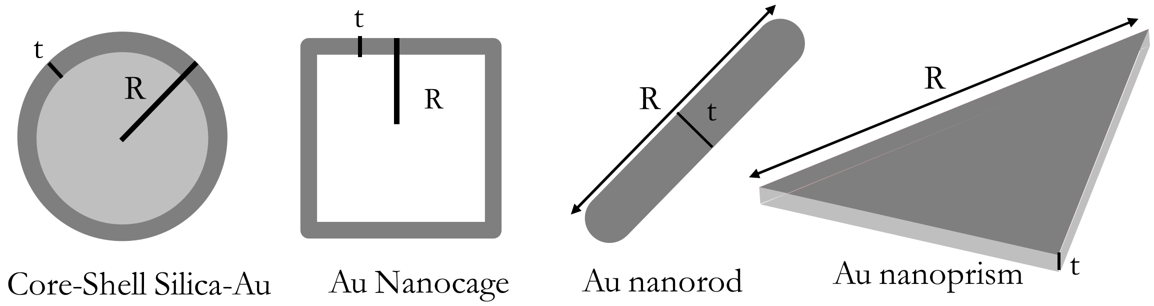

Figure 5.14. *NIR absorbing GNPs structures.*

The following table lists the parameters that define the aspect ratio for a number of NIR absorbing NPs (Table 5.3).

Nanoparticle	AR=R/t (nm/nm)	Typical AR values
Nanorods (GNRs)	(40; 50; 60; 70; 80; 90)/20	2; 2.5; 3; 3.5; 4; 4.5;[168,169] 1.61; 1.89; 2.5; 3.38; 4.23;[170]
Nanocages	(36.7/3.3);[136] (50/10);[171]	11.12;[136] 10;[171]
Nanoprisms	144/7.8;[45] (140-30)/8;[49] (310/28), (158/18), (94/14) [172]	18.5;[45] (17.5-3.75);[49] (11, 8.7, 6.7) [172]
Core-Shell Silica/Au (GNSs)	60/(2-15) [8,9]	30-4 [173,174]

Table 5.3. *Table of typical reported aspect ratios for NIR absorbing GNPs.*

For nanorods and nanoprisms, due to their anisotropy, LSPR bands appear depending on the orientation of the NP with respect to the incoming radiation. In the case of nanorods, transverse and longitudinal modes are present. As for triangular nanoprisms, four LSPR modes have been confirmed both theoretically and experimentally, namely in-plane and out-of-plane modes, both which in turn can be dipolar and quadrupolar modes (Figure 5.15); the major contribution to the UV-Vis-NIR spectrum corresponds to the in-plane dipolar mode laying in the NIR range.

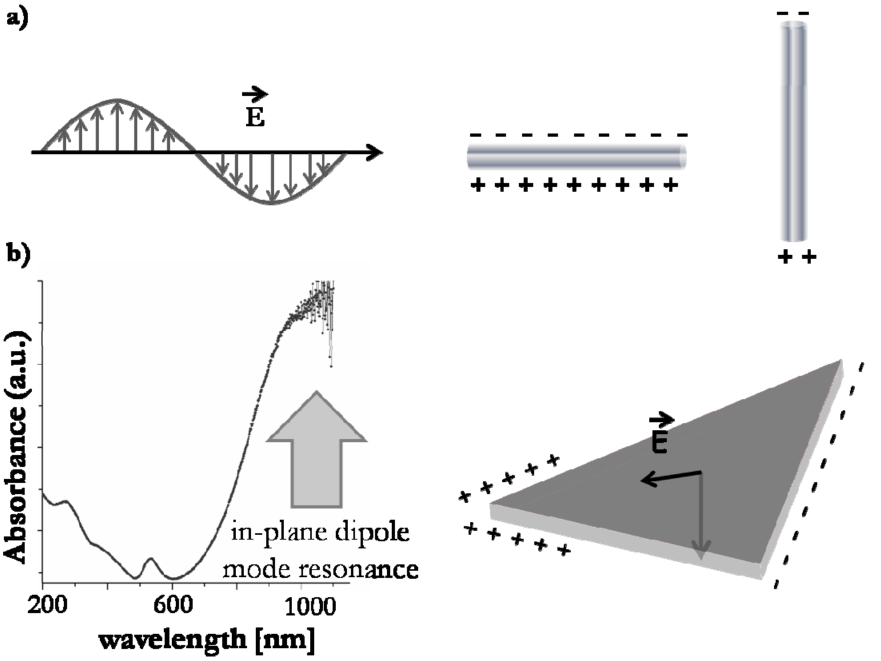

Figure 5.15. a) GNRs longitudinal and transversal modes and b) Left, dipolar and quadrupolar modes representation in gold nanoprisms; and right, absorption spectra of gold nanoprisms show in in-plane mode resonance contribution.

Since the pioneering work of the group of Halas,[173] the popularity of NIR absorbing GNPs in the field of nanomedicine has dramatically increased.[117,175] This has been motivated by two complementary facts:

(i) GNPs can produce heat when they are exposed to light matching their LSPR band.

(ii) NIR light has the most suitable penetration depth in physiological tissue.

Importantly, the NIR band of GNPs can be excited to produce heat very efficiently.[176] NIR excitation of NPs is the most favorable scenario for biomedical applications;[74,177] this is motivated for the suitable penetration depth that NIR radiation has in biological tissues (Figure 5.16). The light penetration depends on the different absorption coefficients of the major components in tissue such as blood, fat or water. This range is limited by blood, hemoglobin (Hb) and oxyhemoglobin (HbO_2), at low wavelengths and by water absorption at high wavelengths.

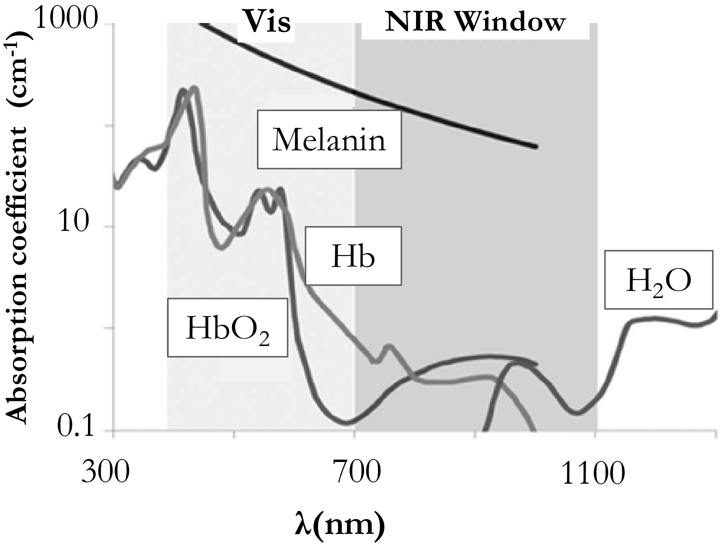

Figure 5.16. *Range of the biological window or NIR window remarked over the absorption spectra of components of tissues (adapted from Qin et al.).*[178]

Light-to-heat conversion can be used to design applications, such as hyperthermia[135,179] and drug release[77,89,156] where anisotropic GNPs act as nanoheaters which can be remotely triggered by NIR radiation. In fact, Au nanorods[180] and nanocages[181] (i.e. hollow Au nanocubes) have been successfully used for remote ablation of tumors in mice. Nevertheless many of the methods to produce NIR absorbing GNPs rely on challenging syntheses with several steps[35,136] and/or seed-mediated approaches involving the cationic surfactant cetyltrimethylammonium bromide (CTAB).[30,39,44,131,182] Table 5.4 summarizes the most relevant methods to produce NIR-absorbing GNPs in high yield with control over their architectural parameters.

Nanoparticle	Synthetic method/coating	Group
Nanorods	Seed-mediated/CTAB	Murphy [29]
Nanocages	Galvanic replacement/PVP	Xia [35]
Nanoprisms	Seed-mediated/CTAB	Mirkin [45]
Core-Shell Silica/Au	Silica NP (Stöber method) and gold coating	Halas [173]

Table 5.4. *Most widely used method to obtain asymmetric GNPs.*

5.7. Introduction to GNPs surface modification

Regarding bioapplications of GNPs, chemical derivatization of the NPs surface is of the most importance to impart biocompatibility and functionality to GNPs. For instance, the widely used surfactant CTAB is very cytotoxic at micromolar concentration and still, so far it has been proven crucial in most of synthetic methods to prepare anisotropic GNPs, very popular in bioapplications in recent years; therefore, extensive work has been done to exchange CTAB by other more biocompatible stabilizers. Nowadays, a great diversity of functional molecular linkers and passivating agents are used in the derivatization of GNPs used in bioapplications. In contrast, a limited library of chemical groups can be used for attachment of these molecules to the gold surface. Ultimately, the choice of an anchoring group is determined by the application of interest; applications where it is required a long-lasting functionalization employ commonly thiolated molecules whereas other applications, less demanding in terms of surface coating, prefer amine or carboxylate surface anchors.

Gold nanoprisms, previously referred to as NanoNachos (NNs) in Chapter 6, represent a versatile alternative to other anisotropic GNPs; the suitability of NNs for bioapplications is motivated mainly for two reason: (i) ease of synthesis in high yield and (ii) since CTAB is not required, the surface can be readily derivatized with thiolated chains. As it will be discussed in Chapters 7 & 8, the main application of NNs follows their use as nanoheaters in applications like photothermal therapy (PTT). Thus, NNs will be drained into physiological environments and harsh heating conditions which require improved stability and specificity provided by the coating of NNs. This chapter addresses the controlled functionalization of NNs with PEG brushes and other molecules of biological relevance such as CPPs, carbohydrates or proteins.

In general, the first requirement of any kind of NPs aimed for bioapplications is that they must be physically and chemically stable in aqueous conditions and thus, they should not aggregate, dissociate, or suffer any chemical reaction with the surrounding media. In the case of GNPs, aggregation is the main problem since due to their noble character dissociation and reactivity are not troubling issues. Water transfer can be achieved normally by derivatization of NPs with hydrophilic ligands; NPs nature determines which stabilization and functionalization processes should be followed into the path to qualify NPs for bioapplications (Figure 5.17).

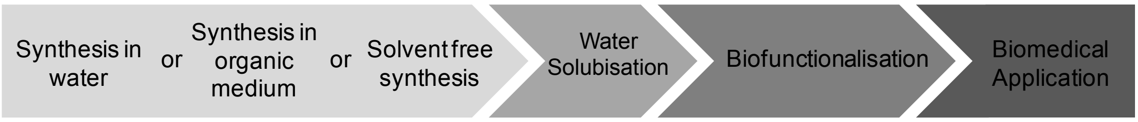

Figure 5.17. *Schematic representation of the steps required to get NPs suited for bioapplications (adapted from Green et al).*[183]

Typically, ionic stabilization is not enough for avoiding NPs aggregation in biological media or high ionic strengths or pH values differing from that where the synthesis took place. Another approach is steric stabilization which is achieved by coating NPs with a ligand shell or embedding NPs into an inorganic or polymeric matrix. Polymers are a good choice because they form a physical barrier preventing the core NPs from coming into contact. The use of small-molecule ligands provides NPs with a smaller hydrodynamic radius; however, a too thin shell can lead to NPs aggregation in demanding high ionic strengths media like physiological media.

For GNPs in the context of bioapplications, the most extended alternative is the use of thiolated chains. Thiolated molecules confer GNPs with stable coatings for up to 35 days under physiologic conditions;[184] this fact adds extra value to thiolated molecules for biofunctionalization of GNPs. For most bioapplications, it is required a solid long-term stabilization in biological environments which contain high serum concentrations and high ionic strengths. In this context, thiolated poly(ethylene glycol) chains (HS-PEGs) are by far the most widely used stabilizer;[117] the hydrophilicity conferred by PEG brushes conjugated to GNPs allows for complex bio-derivatizations and prevents unspecific absorption of serum proteins and opsonins which facilitate uptake and clearance by the reticuloendothelial system (RES). Moreover, bifunctional PEG chains containing a thiol group and another chemical group for further derivatization can be used to generate complex derivatizations onto GNPs.

The attachment of molecules with biological activity onto NNs surface will confer NNs with functionality in bioapplications. Classical cross coupling reagents can be used for the derivatization of NPs with a wide variety of biofunctional targeting, therapeutic, and imaging contrast agents. Commonly attached molecules include nucleic acids, proteins, peptides, phospholipids and carbohydrates. There are different approaches depending on the chemical groups present on the NPs and the molecule of interest. For instance, conjugation of NPs bearing carboxylates with amine-containing molecules/proteins can be achieved by classical carbodiimide cross coupling approaches; linkage to sulfhydryl groups can be similarly achieved by way of maleimide-terminal ligands, widely commercially available. Huisgen cycloaddition (click, or azide–alkyne coupling) has been similarly employed in a number of gold nanoparticle conjugation strategies.[185]

Carbodiimides are the most popular approach to activate carboxilic acids. These compounds are zero-length crosslinking agents which are used to mediate in the linkage between and amine or a phosphate and a carboxylic group with the formation of an amide or phosphoramidate, respectively;[186] zero-length reagents are named so because no additional chemical structure is introduced between the conjugating molecules. Reaction between a carboxylic group and an N-substituted carbodiimides evolves with the formation of an extremely reactive short time-life intermediate, *o*-acylisourea derivatives; this reactive species can react with nucleophiles like primary amines to form an amide bond.[187] Sulfhydryl groups are also susceptible to react with the active species to form thioester linkages; however, the linkage is not as stable as the bond formed with an amine.[188] Carboxylate activation occurs most effectively with EDC (1-Ethyl-3-[3-dimethylaminopropyl]carbodiimide hydrochloride) at pH 3.5 – 4.5, while amide bond formation occurs with highest yield in the range of pH 4 – 6. However, EDC hydrolysis speeds up at acidic pH values; the stability of the carbodiimide (aq.) increases at or above pH 6.5.[189] When working with proteins and peptides, experience indicates that EDC-mediated amide bond formation effectively occurs between pH 4.5 and 7.5. Beyond this pH range, however, the coupling reaction occurs more slowly with lower yields. The activation protocol may be modified by changing the pH, buffer salts, and ratios of reactants to obtain the desired product.

When a molecule bearing carboxylates and amines is conjugated by EDC chemistry, it may result in self-polymerization. Although the optimal pH for the use of EDC is from 4.7 to 6.0, the carbodiimide reaction occurs effectively under mildly alkaline pH conditions (e.g., pH 8.5). The use of this higher pH also can limit the polymerization of proteins, while still facilitating the coupling. Also, a good alternative to avoid polymerization is use the two-step method, which eliminates excess EDC before the addition of ligand.

To prolong the lifetime of the intermediate activated carboxylate, NHS (N-hydroxysuccinimide) or sulfo-NHS (N-hydroxysulfosuccinimide) can be used. The use of these compounds increases the EDC-coupling efficiency. Staros *et al.* (1986) showed that the addition of sulfo-NHS to the EDC coupling of glycine to hemocyanin increased the yield of derivatization about 20-fold as compared to using EDC alone.[190]

Protocols developed for carboxylic activation from proteins, and other molecules can be also applied in carboxylated nanoparticles. Figure5.18 illustrates some of the reactions that can be used for coupling amine-containing molecules to carboxylated NPs. For NPs conjugation, maintaining repulsive force between NPs to stabilize the colloidal suspension is critical, even during the activation and coupling reactions. For this reason, sometimes the use of sulfo-NHS is preferred against NHS because its reaction results in an intermediate ester which is strongly negatively charged. The sulfonates on the sulfo-NHS esters actually are more effective at keeping particles from aggregating than the original carboxylates. Anyway, previous protocols for coupling amine-containing molecules to carboxylated NPs represent viable starting points for optimizing a method that works best for the particular molecule or protein being immobilized.

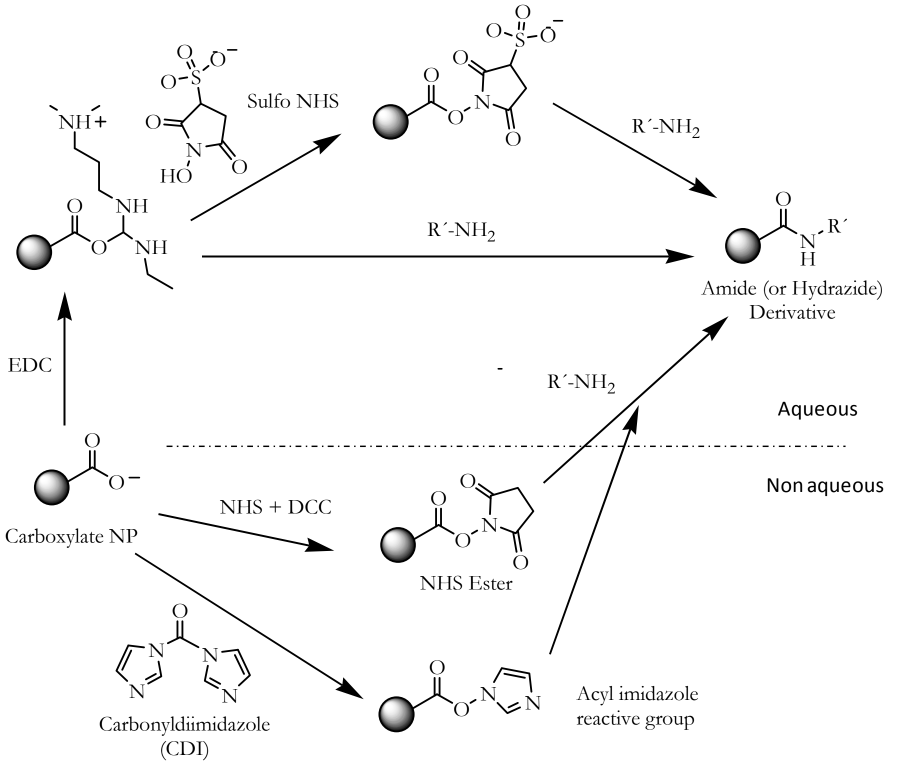

Figure 5.18. *Cabodiimine strategies for attaching amine containing ligand onto carboxylated nanoparticles surface (adapted from Bioconjugate Techniques).*[188]

REFERENCES

(1) Atwater, H. A.; Polman, A.: Plasmonics for improved photovoltaic devices. *Nature Materials* **2010**, *9*, 205-213.

(2) Lal, S.; Link, S.; Halas, N. J.: Nano-optics from sensing to waveguiding. *Nature Photonics* **2007**, *1*, 641-648.

(3) Ozbay, E.: Plasmonics: Merging photonics and electronics at nanoscale dimensions. *Science* **2006**, *311*, 189-193.

(4) Treguer-Delapierre, M.; Majimel, J.; Mornet, S.; Duguet, E.; Ravaine, S.: Synthesis of non-spherical gold nanoparticles. *Gold Bulletin* **2008**, *41*, 195-207.

(5) Schmid, G.; Corain, B.: Nanoparticulated Gold: Syntheses, Structures, Electronics, and Reactivities. *European Journal of Inorganic Chemistry* **2003**, *2003*, 3081-3098.

(6) Antonii, F.: Panacea Aurea-Auro Potabile. 1618.

(7) Faraday, M.: The Bakerian Lecture: Experimental Relations of Gold (and Other Metals) to Light. *Philosophical Transactions of the Royal Society of London* **1857**, *147*, 145-181.

(8) Brust, M.; Bethell, D.; Schiffrin, D. J.; Kiely, C. J.: NOVEL GOLD-DITHIOL NANO-NETWORKS WITH NONMETALLIC ELECTRONIC-PROPERTIES. *Advanced Materials* **1995**, *7*, 795-&.

(9) Brust, M.; Fink, J.; Bethell, D.; Schiffrin, D. J.; Kiely, C.: Synthesis and reactions of functionalised gold nanoparticles. *Journal of the Chemical Society, Chemical Communications* **1995**, 1655-1656.

(10) Brust, M.; Walker, M.; Bethell, D.; Schiffrin, D. J.; Whyman, R.: Synthesis of thiol-derivatised gold nanoparticles in a two-phase Liquid-Liquid system. *Journal of the Chemical Society, Chemical Communications* **1994**, 801-802.

(11) Kiely, C. J.; Fink, J.; Brust, M.; Bethell, D.; Schiffrin, D. J.: Spontaneous ordering of bimodal ensembles of nanoscopic gold clusters. *Nature* **1998**, *396*, 444-446.

(12) Bruchez, M.; Moronne, M.; Gin, P.; Weiss, S.; Alivisatos, A. P.: Semiconductor Nanocrystals as Fluorescent Biological Labels. *Science* **1998**, *281*, 2013-2016.

(13) Mirkin, C. A.; Letsinger, R. L.; Mucic, R. C.; Storhoff, J. J.: A DNA-based method for rationally assembling nanoparticles into macroscopic materials. *Nature* **1996**, *382*, 607-609.

(14) Caruso, F.; Caruso, R. A.; Mohwald, H.: Nanoengineering of inorganic and hybrid hollow spheres by colloidal templating. *Science* **1998**, *282*, 1111-1114.

(15) Stoeva, S.; Klabunde, K. J.; Sorensen, C. M.; Dragieva, I.: Gram-scale synthesis of monodisperse gold colloids by the solvated metal atom dispersion method and digestive ripening and their organization into two- and three-dimensional structures. *Journal of the American Chemical Society* **2002**, *124*, 2305-2311.

(16) Bonnemann, H.; Richards, R. M.: Nanoscopic metal particles - Synthetic methods and potential applications. *European Journal of Inorganic Chemistry* **2001**, 2455-2480.

(17) Uccello-Barretta, G.; Evangelisti, C.; Balzano, F.; Vanni, L.; Aiello, F.; Jicsinszky, L.: Water soluble heptakis(6-deoxy-6-thio)cyclomaltoheptaose capped gold nanoparticles via metal vapour synthesis: NMR structural characterization and complexation properties. *Carbohydrate Research* **2011**, *346*, 753-758.

(18) Turkevich, J.; Stevenson, P. C.; Hillier, J.: A study of the nucleation and growth processes in the synthesis of colloidal gold. *Discussions of the Faraday Society* **1951**, *11*, 55-75.

(19) Giersig, M.; Mulvaney, P.: PREPARATION OF ORDERED COLLOID MONOLAYERS BY ELECTROPHORETIC DEPOSITION. *Langmuir* **1993**, *9*, 3408-3413.

(20) Giersig, M.; Liz-Marzan, L. M.; Ung, T.; Su, D. S.; Mulvaney, P.: Chemistry of nanosized silica-coated metal particles EM-study. *Berichte Der Bunsen-Gesellschaft-Physical Chemistry Chemical Physics* **1997**, *101*, 1617-1620.

(21) Chen, S. W.: 4-hydroxythiophenol-protected gold nanoclusters in aqueous media. *Langmuir* **1999**, *15*, 7551-7557.

(22) Toshima, N.; Yonezawa, T.: Bimetallic nanoparticles-novel materials for chemical and physical applications. *New Journal of Chemistry* **1998**, *22*, 1179-1201.

(23) Xiong, Y.; Washio, I.; Chen, J.; Cai, H.; Li, Z.-Y.; Xia, Y.: Poly(vinyl pyrrolidone): A Dual Functional Reductant and Stabilizer for the Facile Synthesis of Noble Metal Nanoplates in Aqueous Solutions. *Langmuir* **2006**, *22*, 8563-8570.

(24) Pastoriza-Santos, I.; Alvarez-Puebla, R. A.; Liz-Marzán, L. M.: Synthetic Routes and Plasmonic Properties of Noble Metal Nanoplates. *European Journal of Inorganic Chemistry* **2010**, *2010*, 4288-4297.

(25) Furuya, K.; Hirowatari, Y.; Ishioka, T.; Harata, A.: Protective Agent-free Preparation of Gold Nanoplates and Nanorods in Aqueous HAuCl4 Solutions Using Gas–Liquid Interface Discharge. *Chemistry Letters* **2007**, *36*, 1088-1089.

(26) Zhu, J.; Shen, Y.; Xie, A.; Qiu, L.; Zhang, Q.; Zhang, S.: Photoinduced Synthesis of Anisotropic Gold Nanoparticles in Room-Temperature Ionic Liquid. *The Journal of Physical Chemistry C* **2007**, *111*, 7629-7633.

(27) Park, J.; Joo, J.; Kwon, S. G.; Jang, Y.; Hyeon, T.: Synthesis of Monodisperse Spherical Nanocrystals. *Angewandte Chemie International Edition* **2007**, *46*, 4630-4660.

(28) *the chemistry of colloids*; Zsigmondi, R., Ed., 1917.

(29) Jana, N. R.; Gearheart, L.; Murphy, C. J.: Wet chemical synthesis of high aspect ratio cylindrical gold nanorods. *Journal of Physical Chemistry B* **2001**, *105*, 4065-4067.

(30) Murphy, C. J.; Sau, T. K.; Gole, A. M.; Orendorff, C. J.; Gao, J.; Gou, L.; Hunyadi, S. E.; Li, T.: Anisotropic Metal Nanoparticles:â€‰ Synthesis, Assembly, and Optical Applications. *The Journal of Physical Chemistry B* **2005**, *109*, 13857-13870.

(31) Orendorff, C. J.; Murphy, C. J.: Quantitation of Metal Content in the Silver-Assisted Growth of Gold Nanorods. *The Journal of Physical Chemistry B* **2006**, *110*, 3990-3994.

(32) Ha, T. H.; Koo, H. J.; Chung, B. H.: Shape-controlled syntheses of gold nanoprisms and nanorods influenced by specific adsorption of halide ions. *J. Phys. Chem. C* **2007**, *111*, 1123-1130.

(33) Fievet, F.: Preparing monodisperse metal powders in micrometer and submicrometer sizes by the polyol process. *MRS Bulletin* **1989**, *14*, 29-34.

(34) Brenner, A.; Riddell, G. E.: NICKEL PLATING ON STEEL BY CHEMICAL REDUCTION. *Journal of Research of the National Bureau of Standards* **1946**, *37*, 31-34.

(35) Skrabalak, S. E.; Chen, J.; Sun, Y.; Lu, X.; Au, L.; Cobley, C. M.; Xia, Y.: Gold Nanocages: Synthesis, Properties, and Applications. *Accounts of Chemical Research* **2008**, *41*, 1587-1595.

(36) Martin, C. R.: Nanomaterials: A Membrane-Based Synthetic Approach. *Science* **1994**, *266*, 1961-1966.

(37) Khlebtsov, N.; Dykman, L.: Biodistribution and toxicity of engineered gold nanoparticles: a review of in vitro and in vivo studies. *Chemical Society Reviews* **2011**, *40*, 1647.

(38) Yu; Chang, S.-S.; Lee, C.-L.; Wang, C. R. C.: Gold Nanorods: Electrochemical Synthesis and Optical Properties. *The Journal of Physical Chemistry B* **1997**, *101*, 6661-6664.

(39) Nikoobakht, B.; El-Sayed, M. A.: Preparation and Growth Mechanism of Gold Nanorods (NRs) Using Seed-Mediated Growth Method. *Chemistry of Materials* **2003**, *15*, 1957-1962.

(40) Grzelczak, M.; Pérez-Juste, J.; Mulvaney, P.; Liz-Marzán, L. M.: Shape control in gold nanoparticle synthesis. *Chemical Society Reviews* **2008**, *37*, 1783.

(41) Tao, A. R.; Habas, S.; Yang, P.: Shape Control of Colloidal Metal Nanocrystals. *Small* **2008**, *4*, 310-325.

(42) Ibano, D.; Yokota, Y.; Tominaga, T.: Preparation of Gold Nanoplates Protected by an Anionic Phospholipid. *Chemistry Letters* **2003**, *32*, 574-575.

(43) Jain, P. K.; Huang, X. H.; El-Sayed, I. H.; El-Sayed, M. A.: Noble Metals on the Nanoscale: Optical and Photothermal Properties and Some Applications in Imaging, Sensing, Biology, and Medicine. *Accounts of Chemical Research* **2008**, *41*, 1578-1586.

(44) Sau, T. K.; Murphy, C. J.: Room Temperature, High-Yield Synthesis of Multiple Shapes of Gold Nanoparticles in Aqueous Solution. *Journal of the American Chemical Society* **2004**, *126*, 8648-8649.

(45) Millstone, J. E.; Park, S.; Shuford, K. L.; Qin, L.; Schatz, G. C.; Mirkin, C. A.: Observation of a Quadrupole Plasmon Mode for a Colloidal Solution of Gold Nanoprisms. *Journal of the American Chemical Society* **2005**, *127*, 5312-5313.

(46) Busbee, B. D.; Obare, S. O.; Murphy, C. J.: An Improved Synthesis of High-Aspect-Ratio Gold Nanorods. *Advanced Materials* **2003**, *15*, 414-416.

(47) Millstone, J. E.; Métraux, G. S.; Mirkin, C. A.: Controlling the Edge Length of Gold Nanoprisms via a Seed-Mediated Approach. *Advanced Functional Materials* **2006**, *16*, 1209-1214.

(48) Millstone, J. E.; Wei, W.; Jones, M. R.; Yoo, H.; Mirkin, C. A.: Iodide Ions Control Seed-Mediated Growth of Anisotropic Gold Nanoparticles. *Nano Letters* **2008**, *8*, 2526-2529.

(49) Fan, X.; Guo, Z. R.; Hong, J. M.; Zhang, Y.; Zhang, J. N.; Gu, N.: Size-controlled growth of colloidal gold nanoplates and their high-purity acquisition. *Nanotechnology* **2010**, *21*, 105602.

(50) Chen, H. M.; Liu, R.-S.; Tsai, D. P.: A Versatile Route to the Controlled Synthesis of Gold Nanostructures. *Crystal Growth & Design* **2009**, *9*, 2079-2087.

(51) Zhang, L.; Huang, C. Z.; Li, Y. F.; Li, Q.: Morphology Control and Structural Characterization of Au Crystals: From Twinned Tabular Crystals and Single-Crystalline Nanoplates to Multitwinned Decahedra. *Crystal Growth & Design* **2009**, *9*, 3211-3217.

(52) Chu, H.-C.; Kuo, C.-H.; Huang, M. H.: Thermal Aqueous Solution Approach for the Synthesis of Triangular and Hexagonal Gold Nanoplates with Three Different Size Ranges. *Inorganic Chemistry* **2005**, *45*, 808-813.

(53) Washio, I.; Xiong, Y.; Yin, Y.; Xia, Y.: Reduction by the End Groups of Poly(vinyl pyrrolidone): A New and Versatile Route to the Kinetically Controlled Synthesis of Ag Triangular Nanoplates. *Advanced Materials* **2006**, *18*, 1745-1749.

(54) Ah, C. S.; Yun, Y. J.; Park, H. J.; Kim, W. J.; Ha, D. H.; Yun, W. S.: Size-controlled synthesis of machinable single crystalline gold nanoplates. *Chemistry of Materials* **2005**, *17*, 5558-5561.

(55) Li, C. C.; Cai, W. P.; Cao, B. Q.; Sun, F. Q.; Li, Y.; Kan, C. X.; Zhang, L. D.: Mass Synthesis of Large, Single-Crystal Au Nanosheets Based on a Polyol Process. *Advanced Functional Materials* **2006**, *16*, 83-90.

(56) Jiu, J.; Suganuma, K.; Nogi, M.: Effect of additives on the morphology of single-crystal Au nanosheet synthesized using the polyol process. *Journal of Materials Science* **2011**, *46*, 4964-4970.

(57) Sun, X.; Dong, S.; Wang, E.: High-Yield Synthesis of Large Single-Crystalline Gold Nanoplates through a Polyamine Process. *Langmuir* **2005**, *21*, 4710-4712.

(58) Goy-Lopez, S.; Castro, E.; Taboada, P.; Mosquera, V. c.: Block Copolymer-Mediated Synthesis of Size-Tunable Gold Nanospheres and Nanoplates. *Langmuir* **2008**, *24*, 13186-13196.

(59) Shankar, S. S.; Rai, A.; Ankamwar, B.; Singh, A.; Ahmad, A.; Sastry, M.: Biological synthesis of triangular gold nanoprisms. *Nat Mater* **2004**, *3*, 482-488.

(60) Rai, A.; Singh, A.; Ahmad, A.; Sastry, M.: Role of Halide Ions and Temperature on the Morphology of Biologically Synthesized Gold Nanotriangles. *Langmuir* **2005**, *22*, 736-741.

(61) Liu, B.; Xie, J.; Lee, J. Y.; Ting, Y. P.; Chen, J. P.: Optimization of High-Yield Biological Synthesis of Single-Crystalline Gold Nanoplates. *The Journal of Physical Chemistry B* **2005**, *109*, 15256-15263.

(62) Chandran, S. P.; Chaudhary, M.; Pasricha, R.; Ahmad, A.; Sastry, M.: Synthesis of gold nanotriangles and silver nanoparticles using Aloe vera plant extract. *Biotechnology Progress* **2006**, *22*, 577-583.

(63) Xie, J.; Lee, J. Y.; Wang, D. I. C.; Ting, Y. P.: Identification of Active Biomolecules in the High-Yield Synthesis of Single-Crystalline Gold Nanoplates in Algal Solutions. *Small* **2007**, *3*, 672-682.

(64) Ghodake, G. S.; Deshpande, N. G.; Lee, Y. P.; Jin, E. S.: Pear fruit extract-assisted room-temperature biosynthesis of gold nanoplates. *Colloids and Surfaces B: Biointerfaces* **2010**, *75*, 584-589.

(65) Shankar, S. S.; Rai, A.; Ahmad, A.; Sastry, M.: Controlling the Optical Properties of Lemongrass Extract Synthesized Gold Nanotriangles and Potential Application in Infrared-Absorbing Optical Coatings. *Chemistry of Materials* **2005**, *17*, 566-572.

(66) Xie, J.; Lee, J. Y.; Wang, D. I. C.: Synthesis of Single-Crystalline Gold Nanoplates in Aqueous Solutions through Biomineralization by Serum Albumin Protein. *The Journal of Physical Chemistry C* **2007**, *111*, 10226-10232.

(67) Malikova, N.; Pastoriza-Santos, I.; Schierhorn, M.; Kotov, N. A.; Liz-MarzÃ¡n, L. M.: Layer-by-Layer Assembled Mixed Spherical and Planar Gold Nanoparticles:â€‰ Control of Interparticle Interactions. *Langmuir* **2002**, *18*, 3694-3697.

(68) Shao, Y.; Jin, Y.; Dong, S.: Synthesis of gold nanoplates by aspartate reduction of gold chlorideElectronic supplementary information (ESI) available: Fig. S1. UV/Visible-NIR extinction spectra of an aqueous dispersion of gold nanoparticles synthesized by tyrosine (a), phenylalanine (b), lysine (c), aspartate (d) and tryptophan (e). See http://www.rsc.org/suppdata/cc/b3/b315732f. *Chemical Communications* **2004**, 1104.

(69) Nehl, C. L.; Grady, N. K.; Goodrich, G. P.; Tam, F.; Halas, N. J.; Hafner, J. H.: Scattering Spectra of Single Gold Nanoshells. *Nano Letters* **2004**, *4*, 2355-2359.

(70) Radloff, C.; Halas, N. J.: Plasmonic properties of concentric nanoshells. *Nano Letters* **2004**, *4*, 1323-1327.

(71) Oldenburg, S. J.; Jackson, J. B.; Westcott, S. L.; Halas, N. J.: Infrared extinction properties of gold nanoshells. *Applied Physics Letters* **1999**, *75*, 2897-2899.

(72) Averitt, R. D.; Westcott, S. L.; Halas, N. J.: Linear optical properties of gold nanoshells. *Journal of the Optical Society of America B-Optical Physics* **1999**, *16*, 1824-1832.

(73) Pham, T.; Jackson, J. B.; Halas, N. J.; Lee, T. R.: Preparation and characterization of gold nanoshells coated with self-assembled monolayers. *Langmuir* **2002**, *18*, 4915-4920.

(74) Bardhan, R.; Lal, S.; Joshi, A.; Halas, N. J.: Theranostic Nanoshells: From Probe Design to Imaging and Treatment of Cancer. *Accounts of Chemical Research* **2011**, *44*, 936-946.

(75) Gobin, A. M.; Lee, M. H.; Halas, N. J.; James, W. D.; Drezek, R. A.; West, J. L.: Near-infrared resonant nanoshells for combined optical imaging and photothermal cancer therapy. *Nano Letters* **2007**, *7*, 1929-1934.

(76) Hirsch, L. R.; Stafford, R. J.; Bankson, J. A.; Sershen, S. R.; Rivera, B.; Price, R. E.; Hazle, J. D.; Halas, N. J.; West, J. L.: Nanoshell-mediated near-infrared thermal therapy of tumors under magnetic resonance guidance. *Proceedings of the National Academy of Sciences of the United States of America* **2003**, *100*, 13549-13554.

(77) Huschka, R.; Zuloaga, J.; Knight, M. W.; Brown, L. V.; Nordlander, P.; Halas, N. J.: Light-Induced Release of DNA from Gold Nanoparticles: Nanoshells and Nanorods. *Journal of the American Chemical Society* **2011**, *133*, 12247-12255.

(78) Lal, S.; Clare, S. E.; Halas, N. J.: Nanoshell-Enabled Photothermal Cancer Therapy: Impending Clinical Impact. *Accounts of Chemical Research* **2008**, *41*, 1842-1851.

(79) Loo, C.; Lowery, A.; Halas, N. J.; West, J.; Drezek, R.: Immunotargeted nanoshells for integrated cancer imaging and therapy. *Nano Letters* **2005**, *5*, 709-711.

(80) O'Neal, D. P.; Hirsch, L. R.; Halas, N. J.; Payne, J. D.; West, J. L.: Photo-thermal tumor ablation in mice using near infrared-absorbing nanoparticles. *Cancer Letters* **2004**, *209*, 171-176.

(81) Knight, M. W.; Halas, N. J.: Nanoshells to nanoeggs to nanocups: optical properties of reduced symmetry core-shell nanoparticles beyond the quasistatic limit. *New Journal of Physics* **2008**, *10*.

(82) Wang, H.; Brandl, D. W.; Le, F.; Nordlander, P.; Halas, N. J.: Nanorice: A hybrid plasmonic nanostructure. *Nano Letters* **2006**, *6*, 827-832.

(83) Zhou, H. S.; Honma, I.; Komiyama, H.; Haus, J. W.: CONTROLLED SYNTHESIS AND QUANTUM-SIZE EFFECT IN GOLD-COATED NANOPARTICLES. *Physical Review B* **1994**, *50*, 12052-12056.

(84) Averitt, R. D.; Sarkar, D.; Halas, N. J.: Plasmon resonance shifts of Au-coated Au2S nanoshells: Insight into multicomponent nanoparticle growth. *Physical Review Letters* **1997**, *78*, 4217-4220.

(85) Raschke, G.; Brogl, S.; Susha, A. S.; Rogach, A. L.; Klar, T. A.; Feldmann, J.; Fieres, B.; Petkov, N.; Bein, T.; Nichtl, A.; Kürzinger, K.: Gold Nanoshells Improve Single Nanoparticle Molecular Sensors. *Nano Letters* **2004**, *4*, 1853-1857.

(86) Schwartzberg, A. M.; Grant, C. D.; van Buuren, T.; Zhang, J. Z.: Reduction of HAuCl(4) by Na(2)S revisited: The case for Au nanoparticle aggregates and against Au(2)S/Au Core/Shell particles. *J. Phys. Chem. C* **2007**, *111*, 8892-8901.

(87) Mikhlin, Y.; Likhatski, M.; Karacharov, A.; Zaikovski, V.; Krylov, A.: Formation of gold and gold sulfide nanoparticles and mesoscale intermediate structures in the reactions of aqueous HAuCl4 with sulfide and citrate ions. *Physical Chemistry Chemical Physics* **2009**, *11*, 5445-5454.

(88) Skirtach, A. G.; Dejugnat, C.; Braun, D.; Susha, A. S.; Rogach, A. L.; Parak, W. J.; Möhwald, H.; Sukhorukov, G. B.: The Role of Metal Nanoparticles in Remote Release of Encapsulated Materials. *Nano Letters* **2005**, *5*, 1371-1377.

(89) Munoz Javier, A.; del Pino, P.; Bedard, M. F.; Ho, D.; Skirtach, A. G.; Sukhorukov, G. B.; Plank, C.; Parak, W. J.: Photoactivated Release of Cargo from the Cavity of Polyelectrolyte Capsules to the Cytosol of Cells. *Langmuir* **2008**, *24*, 12517-12520.

(90) Bardhan, R.; Grady, N. K.; Ali, T.; Halas, N. J.: Metallic Nanoshells with Semiconductor Cores: Optical Characteristics Modified by Core Medium Properties. *ACS Nano* **2010**, *4*, 6169-6179.

(91) Wang, H.; Goodrich, G. P.; Tam, F.; Oubre, C.; Nordlander, P.; Halas, N. J.: Controlled Texturing Modifies the Surface Topography and Plasmonic Properties of Au Nanoshells. *The Journal of Physical Chemistry B* **2005**, *109*, 11083-11087.

(92) Prodan, E.: A Hybridization Model for the Plasmon Response of Complex Nanostructures. *Science* **2003**, *302*, 419-422.

(93) Cobley, C. M.; Xia, Y.: Engineering the properties of metal nanostructures via galvanic replacement reactions. *Materials Science and Engineering: R: Reports* **2010**, *70*, 44-62.

(94) Kumar, P. S.; Pastoriza-Santos, I.; Rodriguez-Gonzalez, B.; Garcia de Abajo, F. J.; Liz-Marzan, L. M.: High-yield synthesis and optical response of gold nanostars. *Nanotechnology* **2008**, *19*.

(95) Guerrero-Martínez, A.; Barbosa, S.; Pastoriza-Santos, I.; Liz-Marzán, L. M.: Nanostars shine bright for you: Colloidal synthesis, properties and applications of branched metallic nanoparticles. *Current Opinion in Colloid & Interface Science* **2011**, *16*, 118-127.

(96) Alvarez-Puebla, R. n.; Liz-Marzán, L. M.; García de Abajo, F. J.: Light Concentration at the Nanometer Scale. *The Journal of Physical Chemistry Letters* **2010**, *1*, 2428-2434.

(97) Henglein, A.: Small-particle research: physicochemical properties of extremely small colloidal metal and semiconductor particles. *Chemical Reviews* **1989**, *89*, 1861-1873.

(98) Gasser, U.; Weeks, E. R.; Schofield, A.; Pusey, P. N.; Weitz, D. A.: Real-Space Imaging of Nucleation and Growth in Colloidal Crystallization. *Science* **2001**, *292*, 258-262.

(99) Lim, B.; Xia, Y.: Metal Nanocrystals with Highly Branched Morphologies. *Angewandte Chemie International Edition* **2011**, *50*, 76-85.

(100) Nehl, C. L.; Liao, H.; Hafner, J. H.: Optical Properties of Star-Shaped Gold Nanoparticles. *Nano Letters* **2006**, *6*, 683-688.

(101) Wu, H.-L.; Chen, C.-H.; Huang, M. H.: Seed-Mediated Synthesis of Branched Gold Nanocrystals Derived from the Side Growth of Pentagonal Bipyramids and the Formation of Gold Nanostars. *Chemistry of Materials* **2008**, *21*, 110-114.

(102) Wu, H. L.; Chen, C. H.; Huang, M. H.: Seed-Mediated Synthesis of Branched Gold Nanocrystals Derived from the Side Growth of Pentagonal Bipyramids and the Formation of Gold Nanostars. *Chemistry of Materials* **2009**, *21*, 110-114.

(103) Xie, J.; Lee, J. Y.; Wang, D. I. C.: Seedless, Surfactantless, High-Yield Synthesis of Branched Gold Nanocrystals in HEPES Buffer Solution. *Chemistry of Materials* **2007**, *19*, 2823-2830.

(104) Liao, H.-G.; Jiang, Y.-X.; Zhou, Z.-Y.; Chen, S.-P.; Sun, S.-G.: Shape-Controlled Synthesis of Gold Nanoparticles in Deep Eutectic Solvents for Studies of Structure–Functionality Relationships in Electrocatalysis. *Angewandte Chemie International Edition* **2008**, *47*, 9100-9103.

(105) Burt, J. L.; Elechiguerra, J. L.; Reyes-Gasga, J.; Martin Montejano-Carrizales, J.; Jose-Yacaman, M.: Beyond Archimedean solids: Star polyhedral gold nanocrystals. *Journal of Crystal Growth* **2005**, *285*, 681-691.

(106) Sperling, R. A.; Parak, W. J.: Surface modification, functionalization and bioconjugation of colloidal inorganic nanoparticles. *Philosophical Transactions of the Royal Society a-Mathematical Physical and Engineering Sciences* **2010**, *368*, 1333-1383.

(107) Khlebtsov, N. G.; Dykman, L. A.: Optical properties and biomedical applications of plasmonic nanoparticles. *Journal of Quantitative Spectroscopy and Radiative Transfer* **2010**, *111*, 1-35.

(108) Love, J. C.; Estroff, L. A.; Kriebel, J. K.; Nuzzo, R. G.; Whitesides, G. M.: Self-assembled monolayers of thiolates on metals as a form of nanotechnology. *Chemical Reviews* **2005**, *105*, 1103-1169.

(109) Ackerson, C. J.; Jadzinsky, P. D.; Kornberg, R. D.: Thiolate ligands for synthesis of water-soluble gold clusters. *Journal of the American Chemical Society* **2005**, *127*, 6550-6551.

(110) Song, H. T.; Choi, J. S.; Huh, Y. M.; Kim, S.; Jun, Y. W.; Suh, J. S.; Cheon, J.: Surface modulation of magnetic nanocrystals in the development of highly efficient magnetic resonance probes for intracellular labeling. *Journal of the American Chemical Society* **2005**, *127*, 9992-9993.

(111) Jans, H.; Jans, K.; Lagae, L.; Borghs, G.; Maes, G.; Huo, Q.: Poly(acrylic acid)-stabilized colloidal gold nanoparticles: synthesis and properties. *Nanotechnology* **2010**, *21*.

(112) Pellegrino, T.; Manna, L.; Kudera, S.; Liedl, T.; Koktysh, D.; Rogach, A. L.; Keller, S.; Radler, J.; Natile, G.; Parak, W. J.: Hydrophobic nanocrystals coated with an amphiphilic polymer shell: A general route to water soluble nanocrystals. *Nano Letters* **2004**, *4*, 703-707.

(113) Moros, M.; Pelaz, B.; Lopez-Larrubia, P.; Garcia-Martin, M. L.; Grazu, V.; de la Fuente, J. M.: Engineering biofunctional magnetic nanoparticles for biotechnological applications. *Nanoscale* **2010**, *2*, 1746-1755.

(114) Liz-Marzan, L. M.; Giersig, M.; Mulvaney, P.: Synthesis of nanosized gold-silica core-shell particles. *Langmuir* **1996**, *12*, 4329-4335.

(115) de la Fuente, J. M.; Berry, C. C.; Riehle, M. O.; Curtis, A. S. G.: Nanoparticle targeting at cells. *Langmuir* **2006**, *22*, 3286-3293.

(116) Rojo, J.; Diaz, V.; de la Fuente, J. M.; Segura, I.; Barrientos, A. G.; Riese, H. H.; Bernade, A.; Penades, S.: Gold glyconanoparticles as new tools in antiadhesive therapy. *Chembiochem* **2004**, *5*, 291-297.

(117) Dreaden, E. C.; Alkilany, A. M.; Huang, X.; Murphy, C. J.; El-Sayed, M. A.: The golden age: gold nanoparticles for biomedicine. *Chemical Society Reviews* **2012**.

(118) Sokolov, K.; Follen, M.; Aaron, J.; Pavlova, I.; Malpica, A.; Lotan, R.; Richards-Kortum, R.: Real-time vital optical imaging of precancer using anti-epidermal growth factor receptor antibodies conjugated to gold nanoparticles. *Cancer Research* **2003**, *63*, 1999-2004.

(119) El-Sayed, I. H.; Huang, X. H.; El-Sayed, M. A.: Surface plasmon resonance scattering and absorption of anti-EGFR antibody conjugated gold nanoparticles in cancer diagnostics: Applications in oral cancer. *Nano Letters* **2005**, *5*, 829-834.

(120) Verma, A.; Uzun, O.; Hu, Y.; Hu, Y.; Han, H.-S.; Watson, N.; Chen, S.; Irvine, D. J.; Stellacci, F.: Surface-structure-regulated cell-membrane penetration by monolayer-protected nanoparticles. *Nat Mater* **2008**, *7*, 588-595.

(121) Nel, A. E.; Madler, L.; Velegol, D.; Xia, T.; Hoek, E. M. V.; Somasundaran, P.; Klaessig, F.; Castranova, V.; Thompson, M.: Understanding biophysicochemical interactions at the nano-bio interface. *Nat Mater* **2009**, *8*, 543-557.

(122) Gref, R.; Lück, M.; Quellec, P.; Marchand, M.; Dellacherie, E.; Harnisch, S.; Blunk, T.; Müller, R. H.: 'Stealth' corona-core nanoparticles surface modified by polyethylene glycol (PEG): influences of the corona (PEG chain length and surface density) and of the core composition on phagocytic uptake and plasma protein adsorption. *Colloids and Surfaces B: Biointerfaces* **2000**, *18*, 301-313.

(123) Monopoli, M. P.; Walczyk, D.; Campbell, A.; Elia, G.; Lynch, I.; Baldelli Bombelli, F.; Dawson, K. A.: Physical−Chemical Aspects of Protein Corona: Relevance to in Vitro and in Vivo Biological Impacts of Nanoparticles. *Journal of the American Chemical Society* **2011**, *133*, 2525-2534.

(124) Kowalczyk, B.; Lagzi, I.; Grzybowski, B. A.: Nanoseparations: Strategies for size and/or shape-selective purification of nanoparticles. *Current Opinion in Colloid & Interface Science* **2011**, *16*, 135-148.

(125) Garcia, M. A.: Surface plasmons in metallic nanoparticles: fundamentals and applications. *Journal of Physics D-Applied Physics* **2011**, *44*.

(126) Sundararajan, S. P.; Grady, N. K.; Mirin, N.; Halas, N. J.: Nanoparticle-Induced Enhancement and Suppression of Photocurrent in a Silicon Photodiode. *Nano Letters* **2008**, *8*, 624-630.

(127) Zhou, S.; Varughese, B.; Eichhorn, B.; Jackson, G.; McIlwrath, K.: Pt–Cu Core–Shell and Alloy Nanoparticles for Heterogeneous NOx Reduction: Anomalous Stability and Reactivity of a Core–Shell Nanostructure. *Angewandte Chemie International Edition* **2005**, *44*, 4539-4543.

(128) Wang, D. S.; Li, Y. D.: Bimetallic Nanocrystals: Liquid-Phase Synthesis and Catalytic Applications. *Advanced Materials* **2011**, *23*, 1044-1060.

(129) Hashmi, A. S. K.; Rudolph, M.: Gold catalysis in total synthesis. *Chemical Society Reviews* **2008**, *37*, 1766-1775.

(130) Burda, C.; Chen, X. B.; Narayanan, R.; El-Sayed, M. A.: Chemistry and properties of nanocrystals of different shapes. *Chemical Reviews* **2005**, *105*, 1025-1102.

(131) Sau, T. K.; Rogach, A. L.: Nonspherical Noble Metal Nanoparticles: Colloid-Chemical Synthesis and Morphology Control. *Advanced Materials* **2010**, *22*, 1781-1804.

(132) Martin, O. J. F.; Hecht, B.; Pohl, D. W.: Resonant Optical Antennas. *Science* **2005**, *308*, 1607-9.

(133) Barnes, W. L.; Dereux, A.; Ebbesen, T. W.: Surface plasmon subwavelength optics. *Nature* **2003**, *424*, 824-830.

(134) von Maltzahn, G.; Park, J. H.; Agrawal, A.; Bandaru, N. K.; Das, S. K.; Sailor, M. J.; Bhatia, S. N.: Computationally Guided Photothermal Tumor Therapy Using Long-Circulating Gold Nanorod Antennas. *Cancer Research* **2009**, *69*, 3892-3900.

(135) Huang, X.; El-Sayed, I. H.; Qian, W.; El-Sayed, M. A.: Cancer Cell Imaging and Photothermal Therapy in the Near-Infrared Region by Using Gold Nanorods. *Journal of the American Chemical Society* **2006**, *128*, 2115-2120.

(136) Chen, J.; Saeki, F.; Wiley, B. J.; Cang, H.; Cobb, M. J.; Li, Z.-Y.; Au, L.; Zhang, H.; Kimmey, M. B.; Li; Xia, Y.: Gold Nanocages: Bioconjugation and Their Potential Use as Optical Imaging Contrast Agents. *Nano Letters* **2005**, *5*, 473-477.

(137) Durr, N. J.; Larson, T.; Smith, D. K.; Korgel, B. A.; Sokolov, K.; Ben-Yakar, A.: Two-Photon Luminescence Imaging of Cancer Cells Using Molecularly Targeted Gold Nanorods. *Nano Letters* **2007**, *7*, 941-945.

(138) Tong, L.; Zhao, Y.; Huff, T. B.; Hansen, M. N.; Wei, A.; Cheng, J. X.: Gold Nanorods Mediate Tumor Cell Death by Compromising Membrane Integrity. *Advanced Materials* **2007**, *19*, 3136-3141.

(139) Eghtedari, M.; Oraevsky, A.; Copland, J. A.; Kotov, N. A.; Conjusteau, A.; Motamedi, M.: High Sensitivity of In Vivo Detection of Gold Nanorods Using a Laser Optoacoustic Imaging System. *Nano Letters* **2007**, *7*, 1914-1918.

(140) Agarwal, A.; Huang, S. W.; O'Donnell, M.; Day, K. C.; Day, M.; Kotov, N.; Ashkenazi, S.: Targeted gold nanorod contrast agent for prostate cancer detection by photoacoustic imaging. *Journal of Applied Physics* **2007**, *102*.

(141) Dreaden, E. C.; Mackey, M. A.; Huang, X.; Kang, B.; El-Sayed, M. A.: Beating cancer in multiple ways using nanogold. *Chemical Society Reviews* **2011**, *40*, 3391.

(142) Lu, W.; Huang, Q.; Geng, K. B.; Wen, X. X.; Zhou, M.; Guzatov, D.; Brecht, P.; Su, R.; Oraevsky, A.; Wang, L. V.; Li, C.: Photoacoustic imaging of living mouse brain vasculature using hollow gold nanospheres. *Biomaterials* **2010**, *31*, 2617-2626.

(143) Wang, Y.; Xie, X.; Wang, X.; Ku, G.; Gill, K. L.; O'Neal, D. P.; Stoica, G.; Wang, L. V.: Photoacoustic Tomography of a Nanoshell Contrast Agent in the in Vivo Rat Brain. *Nano Letters* **2004**, *4*, 1689-1692.

(144) Yang, X.; Skrabalak, S. E.; Li, Z.-Y.; Xia, Y.; Wang, L. V.: Photoacoustic Tomography of a Rat Cerebral Cortex in vivo with Au Nanocages as an Optical Contrast Agent. *Nano Letters* **2007**, *7*, 3798-3802.

(145) Kim, C.; Song, H. M.; Cai, X.; Yao, J. J.; Wei, A.; Wang, L. H. V.: In vivo photoacoustic mapping of lymphatic systems with plasmon-resonant nanostars. *Journal of Materials Chemistry* **2011**, *21*, 2841-2844.

(146) El-Sayed, I. H.; Huang, X. H.; El-Sayed, M. A.: Selective laser photo-thermal therapy of epithelial carcinoma using anti-EGFR antibody conjugated gold nanoparticles. *Cancer Letters* **2006**, *239*, 129-135.

(147) De, M.; Ghosh, P. S.; Rotello, V. M.: Applications of Nanoparticles in Biology. *Advanced Materials* **2008**, *20*, 4225-4241.

(148) Cao, Y. W. C.; Jin, R. C.; Mirkin, C. A.: Nanoparticles with Raman spectroscopic fingerprints for DNA and RNA detection. *Science* **2002**, *297*, 1536-1540.

(149) Han, M. S.; Lytton-Jean, A. K. R.; Oh, B. K.; Heo, J.; Mirkin, C. A.: Colorimetric screening of DNA-binding molecules with gold nanoparticle probes. *Angewandte Chemie-International Edition* **2006**, *45*, 1807-1810.

(150) Lee, J. S.; Han, M. S.; Mirkin, C. A.: Colorimetric detection of mercuric ion (Hg2+) in aqueous media using DNA-functionalized gold nanoparticles. *Angewandte Chemie-International Edition* **2007**, *46*, 4093-4096.

(151) Park, S. J.; Taton, T. A.; Mirkin, C. A.: Array-based electrical detection of DNA with nanoparticle probes. *Science* **2002**, *295*, 1503-1506.

(152) Rosi, N. L.; Giljohann, D. A.; Thaxton, C. S.; Lytton-Jean, A. K. R.; Han, M. S.; Mirkin, C. A.: Oligonucleotide-modified gold nanoparticles for intracellular gene regulation. *Science* **2006**, *312*, 1027-1030.

(153) Rosi, N. L.; Mirkin, C. A.: Nanostructures in biodiagnostics. *Chemical Reviews* **2005**, *105*, 1547-1562.

(154) Stoeva, S. I.; Lee, J. S.; Thaxton, C. S.; Mirkin, C. A.: Multiplexed DNA detection with biobarcoded nanoparticle probes. *Angewandte Chemie-International Edition* **2006**, *45*, 3303-3306.

(155) Storhoff, J. J.; Elghanian, R.; Mucic, R. C.; Mirkin, C. A.; Letsinger, R. L.: One-pot colorimetric differentiation of polynucleotides with single base imperfections using gold nanoparticle probes. *Journal of the American Chemical Society* **1998**, *120*, 1959-1964.

(156) Huschka, R.; Neumann, O.; Barhoumi, A.; Halas, N. J.: Visualizing Light-Triggered Release of Molecules Inside Living Cells. *Nano Letters*, *10*, 4117-4122.

(157) Rai, P.; Mallidi, S.; Zheng, X.; Rahmanzadeh, R.; Mir, Y.; Elrington, S.; Khurshid, A.; Hasan, T.: Development and applications of photo-triggered theranostic agents. *Advanced Drug Delivery Reviews* **2010**, *62*, 1094-1124.

(158) Cao, X.; Ye, Y.; Liu, S.: Gold nanoparticle-based signal amplification for biosensing. *Analytical Biochemistry* **2011**, *417*, 1-16.

(159) Nam, J.-M.; Thaxton, C. S.; Mirkin, C. A.: Nanoparticle-Based Bio-Bar Codes for the Ultrasensitive Detection of Proteins. *Science* **2003**, *301*, 1884-1886.

(160) Gupta, S.; Huda, S.; Kilpatrick, P. K.; Velev, O. D.: Characterization and Optimization of Gold Nanoparticle-Based Silver-Enhanced Immunoassays. *Analytical Chemistry* **2007**, *79*, 3810-3820.

(161) Garcia, M. A.: Surface plasmons in metallic nanoparticles: fundamentals and applications. *Journal of Physics D: Applied Physics* **2011**, *44*, 283001.

(162) Rodriguez-Lorenzo, L.; Alvarez-Puebla, R. A.; de Abajo, F. J. G.; Liz-Marzan, L. M.: Surface Enhanced Raman Scattering Using Star-Shaped Gold Colloidal Nanoparticles. *J. Phys. Chem. C*, *114*, 7336-7340.

(163) Qian, X.; Peng, X.-H.; Ansari, D. O.; Yin-Goen, Q.; Chen, G. Z.; Shin, D. M.; Yang, L.; Young, A. N.; Wang, M. D.; Nie, S.: In vivo tumor targeting and spectroscopic detection with surface-enhanced Raman nanoparticle tags. *Nature Biotechnology* **2008**, *26*, 83-90.

(164) Dufek, E. J.; Ehlert, B.; Granger, M. C.; Sandrock, T. M.; Legge, S. L.; Herrmann, M. G.; Meikle, A. W.; Porter, M. D.: Competitive surface-enhanced Raman scattering assay for the 1,25-dihydroxy metabolite of vitamin D3. *Analyst* **2010**, *135*, 2811-2817.

(165) Stasko, N. A.; Johnson, C. B.; Schoenfisch, M. H.; Johnson, T. A.; Holmuhamedov, E. L.: Cytotoxicity of Polypropylenimine Dendrimer Conjugates on Cultured Endothelial Cells. *Biomacromolecules* **2007**, *8*, 3853-3859.

(166) Zhang, R.; Khalizov, A.; Wang, L.; Hu, M.; Xu, W.: Nucleation and Growth of Nanoparticles in the Atmosphere. *Chemical Reviews* **2011**, 111101135938003.

(167) Zhang, H.; Harpster, M. H.; Park, H. J.; Johnson, P. A.; Wilson, W. C.: Surface-Enhanced Raman Scattering Detection of DNA Derived from the West Nile Virus Genome Using Magnetic Capture of Raman-Active Gold Nanoparticles. *Analytical Chemistry* **2010**, *83*, 254-260.

(168) Hu, M.; Chen, J. Y.; Li, Z. Y.; Au, L.; Hartland, G. V.; Li, X. D.; Marquez, M.; Xia, Y. N.: Gold nanostructures: engineering their plasmonic properties for biomedical applications. *Chemical Society Reviews* **2006**, *35*, 1084-1094.

(169) Perez-Juste, J.; Liz-Marzan, L. M.; Carnie, S.; Chan, D. Y. C.; Mulvaney, P.: Electric-field-directed growth of gold nanorods in aqueous surfactant solutions. *Advanced Functional Materials* **2004**, *14*, 571-579.

(170) Harris, N.; Ford, M.; Mulvaney, P.; Cortie, M.: Tunable infrared absorption by metal nanoparticles: The case for gold rods and shells. *Gold Bulletin* **2008**, *41*, 5-14.

(171) Lu, X.; Au, L.; McLellan, J.; Li, Z.-Y.; Marquez, M.; Xia, Y.: Fabrication of Cubic Nanocages and Nanoframes by Dealloying Au/Ag Alloy Nanoboxes with an Aqueous Etchant Based on Fe(NO3)3 or NH4OH. *Nano Letters* **2007**, *7*, 1764-1769.

(172) Ah, C. S.; Yun, Y. J.; Park, H. J.; Kim, W.-J.; Ha, D. H.; Yun, W. S.: Size-Controlled Synthesis of Machinable Single Crystalline Gold Nanoplates. *Chemistry of Materials* **2005**, *17*, 5558-5561.

(173) Oldenburg, S. J.; Averitt, R. D.; Westcott, S. L.; Halas, N. J.: Nanoengineering of optical resonances. *Chemical Physics Letters* **1998**, *288*, 243-247.

(174) Averitt, R. D.; Westcott, S. L.; Halas, N. J.: Ultrafast optical properties of gold nanoshells. *Journal of the Optical Society of America B-Optical Physics* **1999**, *16*, 1814-1823.

(175) Huang, X.; El-Sayed, M. A.: Gold nanoparticles: Optical properties and implementations in cancer diagnosis and photothermal therapy. *Journal of Advanced Research* **2010**, *1*, 13-28.

(176) Govorov, A. O.; Richardson, H. H.: Generating heat with metal nanoparticles. *Nano Today* **2007**, *2*, 30-38.

(177) Dreaden, E. C.; Mackey, M. A.; Huang, X.; Kang, B.; El-Sayed, M. A.: Beating cancer in multiple ways using nanogold. *Chemical Society Reviews*, *40*, 3391-3404.

(178) Qin, Z.; Bischof, J. C.: Thermophysical and biological responses of gold nanoparticle laser heating. *Chemical Society Reviews* **2012**.

(179) Krpetić, Z. e.; Nativo, P.; Sée, V.; Prior, I. A.; Brust, M.; Volk, M.: Inflicting Controlled Nonthermal Damage to Subcellular Structures by Laser-Activated Gold Nanoparticles. *Nano Letters* **2010**, *10*, 4549-4554.

(180) Dickerson, E. B.; Dreaden, E. C.; Huang, X.; El-Sayed, I. H.; Chu, H.; Pushpanketh, S.; McDonald, J. F.; El-Sayed, M. A.: Gold nanorod assisted near-infrared plasmonic photothermal therapy (PPTT) of squamous cell carcinoma in mice. *Cancer Letters* **2008**, *269*, 57-66.

(181) Chen, J.; Glaus, C.; Laforest, R.; Zhang, Q.; Yang, M.; Gidding, M.; Welch, M. J.; Xia, Y.: Gold Nanocages as Photothermal Transducers for Cancer Treatment. *Small*, *6*, 811-817.

(182) Jana, N. R.; Gearheart, L.; Murphy, C. J.: Seed-Mediated Growth Approach for Shape-Controlled Synthesis of Spheroidal and Rod-like Gold Nanoparticles Using a Surfactant Template. *Advanced Materials* **2001**, *13*, 1389-1393.

(183) Thanh, N. T. K.; Green, L. A. W.: Functionalisation of nanoparticles for biomedical applications. *Nano Today* **2010**, *5*, 213-230.

(184) Flynn, N. T.; Tran, T. N. T.; Cima, M. J.; Langer, R.: Long-Term Stability of Self-Assembled Monolayers in Biological Media. *Langmuir* **2003**, *19*, 10909-10915.

(185) Gole, A.; Murphy, C. J.: Azide-Derivatized Gold Nanorods: Functional Materials for "Click" Chemistry. *Langmuir* **2007**, *24*, 266-272.

(186) Hoare, D. G.; Koshland, D. E.: A PROCEDURE FOR SELECTIVE MODIFICATION OF CARBOXYL GROUPS IN PROTEINS. *Journal of the American Chemical Society* **1966**, *88*, 2057-&.

(187) Williams, A.; Ibrahim, I. T.: CARBODIIMIDE CHEMISTRY - RECENT ADVANCES. *Chemical Reviews* **1981**, *81*, 589-636.

(188) *Bioconjugate Techniques*: 2nd edition ed.; Hermanson, G. T., Ed.; Elsevier, 2008, pp 1233.

(189) Nakajima, N.; Ikada, Y.: MECHANISM OF AMIDE FORMATION BY CARBODIIMIDE FOR BIOCONJUGATION IN AQUEOUS-MEDIA. *Bioconjugate Chemistry* **1995**, *6*, 123-130.

(190) Staros, J. V.; Wright, R. W.; Swingle, D. M.: Enhancement by N-hydroxysulfosuccinimide of water-soluble carbodiimide-mediated coupling reactions. *Analytical Biochemistry* **1986**, *156*, 220-222.

Tailoring the Synthesis of NanoNachos

Chapter 6

CTAB is the most widely used and convenient surfactant for high-yielding syntheses of Au nanorods[1,2] and nanoprisms[3,4] even though it is a well-known highly toxic component.[5,6] Free CTAB molecules are cytotoxic, reducing cell viability to 50% after 200nM exposure for four days. Methods to exchange CTAB for other less cytotoxic surfactants have been extensively reported.[7-11] However, an alternative method to produce NIR absorbing GNPs without CTAB is of the most importance, as recently highlighted by Murphy and co-workers,[5] pioneering author of the seed-mediated approach involving CTAB. Moreover, in order to establish photothermal therapy based on GNP nanoheaters as a feasible and widely extended treatment against cancer, the development of straightforward and scalable synthesis and biofunctionalisation methods to produce non-cytotoxic Au nanoheaters are crucial issues.

This chapter describes a novel and straightforward wet-chemical synthesis route to produce single-crystalline gold tabular NPs, called here NanoNachos (NNs) due to their characteristic shape. The synthesis proceeds in water at room temperature at pH 5.5. While the thickness of NNs remained constant (*ca.* 9 nm), the edge can be tuned in the range of *ca.* 100 – 170 nm by adjusting the final concentration/molar ratio of gold salt and reducing agent (thiosulfate). This allows tuning the surface plasmon band of NNs along the NIR range, in the so-called biological window. In contrast to most of the previously reported methods to produce Au nanoprisms in high yield, CTAB, a well-known toxic cationic surfactant, is not required in the method here proposed.

6.1. Precedents: Synthesis of Gold@Gold Sulfide Nanoshells

A number of structures including gold nanorods, core-shell silica gold NPs or Au nanoprisms have been described to exhibit LSPR bands in the NIR range.[4,12,13] Furthermore, most of the methods to produce these NPs allow for tuning the LSPR along the NIR range which allow for matching the energy of different NIR sources.[3,14] In order to find a straightforward, reproducible and a high yield synthesis method, an extensive bibliographic research was made. Finally, the chosen system was a core-shell Au-Au_2S NP.

The method to produce these NPs was originally described by the group of Zhou in 1994.[15] In this original work, they claimed that the product of reduction of $HAuCl_4$ by 24 h aged Na_2S was a core of Au_2S (dielectric) coated by thin shell of metallic Au. The UV-Vis-NIR spectrum resulting from this synthesis method displayed two major peaks; the major one was centered at 530 nm and the minor one was shifted to NIR wavelengths.

In 1997, Halas and co-workers reported theoretical calculations (based on generalized Mie scattering calculations for the nanoshell geometry) in order to assess the optical features of the core-shell Au-Au_2S system.[16] During a decade, many papers studied this synthesis method trying to add some light about the nature of the products obtained in this synthesis; in the mean while, others made use of these NPs and exploited their LSPR band laying in the NIR for applications where these NPs act as nanoheaters.

For the first time in 2006, J.J. Diao & H. Chen suggested that the products responsible for the NIR peak were tabular nanostructures instead of the core-shell Au-Au_2S system.[17] Following this work, the group of Zhang made many experiments to conclude that the NIR peak was consequence of aggregates of GNPs instead of the core-shell NPs or nanoplates.[18] They also studied the products resulting from Na_2S aging which seems to be crucial in the formation of the NIR peak. They concluded that the major product was sodium thiosulfate and suggested that this could be the reductant responsible to produce aggregates of gold NPs with NIR features.

To our knowledge, the last paper in regards to the reaction of sodium sulfide with chloroauric acid and the controversy over the structure of the resulting product date 2009; there, Mikhlin & coworkers refused the possibility of gold NPs aggregates as responsible for the NIR band and pointed at tabular GNPs as the answer.[19]

Taking into consideration all of the aforementioned body of experimental work, we attempted to reproduce and optimize the method to produce NIR absorbing GNPs. The main reasons to choose this system were (i) apparently ease of production and (ii) avoiding CTAB neither as precursor nor as capping agent.

6.2. Synthetic Method to Produce NIR Absorbing NanoNachos

Aiming for NIR absorbing NPs, in the present work, the methodology described by Zhou and co-workers was chosen to avoid the use of CTAB. [15]As for a first attempt, the reaction conditions reported by Zhou & co-workers were used. The synthesis starts by mixing 10 mL of 2 mM gold salt solution and a first addition of 12 mL of 24 h aged 1 mM sodium sulfide solution (reducing solution). The reaction goes for 12 minutes prior to a second addition of 0.5 mL of reducing solution. In the original work, the time separation between additions is not well defined and in the present work, 12 minutes were used as result of an optimization of the NIR band (Figure 6.1). The synthesis evolves under moderate stirring conditions at room temperature and pH 5.5. The fate of the reaction was monitored in real-time by UV-Vis-NIR spectroscopy as shown in Figure 6.2. Under these conditions, once the reaction is finished, an absorption peak centred at *ca.* 800 nm was apparent; however, the spectral weight of this peak relative to the peak at 530 nm is relatively low, although in accordance with values in literature.

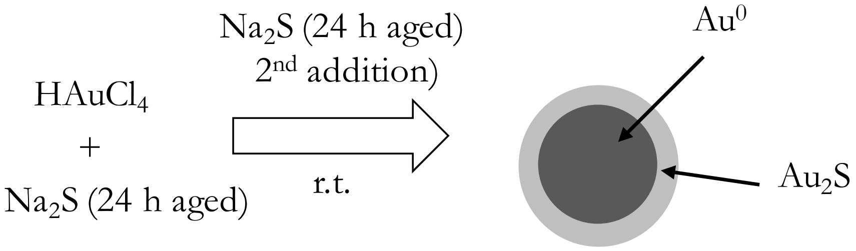

Figure 6.1. *Reaction scheme to produce core@shell Au-Na_2S nanoparticles.*

In order to maximize the spectral ratio between the peaks at 800 nm and 530 nm, attempts of optimization were carried out by trying out different concentrations/aging times of the reducing solution and time intervals between additions of the reduction solution. A peak centered in 900 nm appeared when Na_2S solution was aged during 48h; in contrast, using freshly prepared reducing solution prevented the NIR feature; this also happened when using concentrations of 0.5 mM or 2 mM (instead of 1 mM) of the reducing solution. With these reaction conditions, absorption features were observed mainly at 530 nm (Figure 6.2). Furthermore, at 220 nm it is still discernible the gold (III) peak (non reduced gold); this result allow us to speculate that the content of the reducing solution is insufficient to reduce all the gold salt into metallic gold.

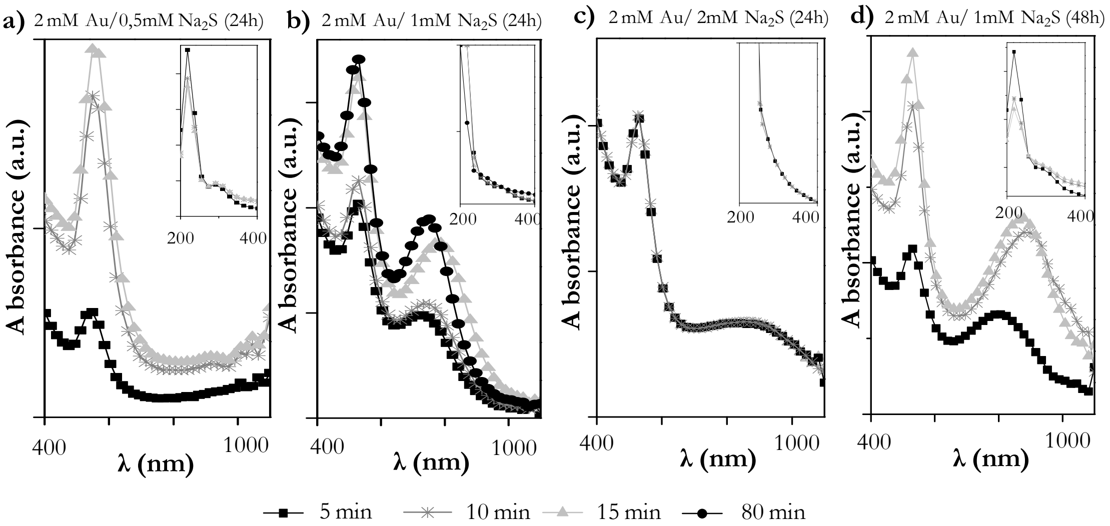

Figure 6.2. *UV/Vis spectra using different sodium disulfide ratio, aged 24 h a) 0,5 mM Na_2S; b) 1 mM Na_2S; c) 2 mM Na_2S and d) Na_2S aged 48h and 1mM. Different symbols indicate different reaction times, i.e. black squares, gray stars, gray triangles and black circles represent 5, 15, 25 and 80 minutes, respectively.*

The redox reaction goes for *ca.* 80 minutes and then,[16] since the UV-Vis-NIR features remain unaltered, we can conclude the reaction and corresponding products are finished. The solution remains stable for *ca.* 2 days; however, the products precipitate ultimately if further stabilization is not done.

The synthesis products were characterized by TEM (Figure 6.3). TEM micrographs show a broad mixture of quasi-spherical NPs (53±15 nm) mixed with a minor amount of triangular nanoplates (125±37 nm). The contrast of the NPs obtained and considerations on the context of this reaction seems to indicate that these NPs are made of gold.

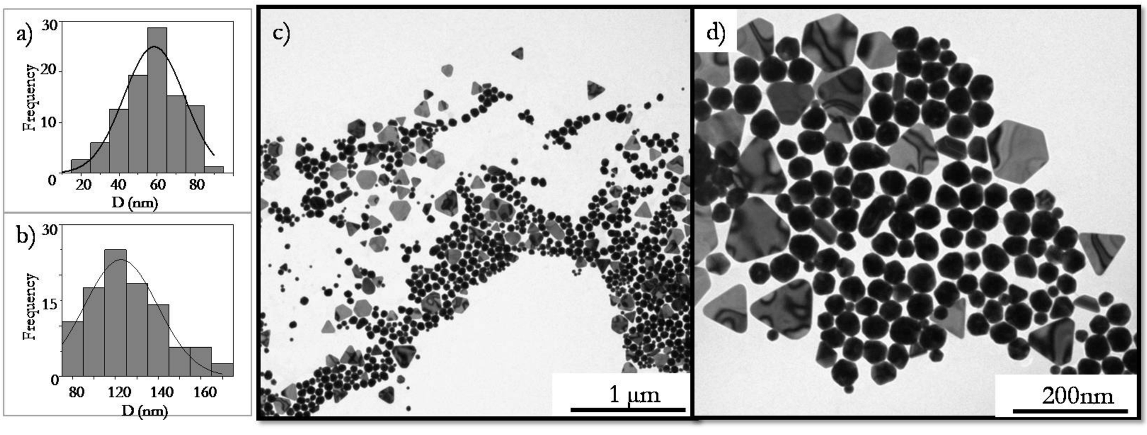

Figure 6.3. *a) Sphere histogram; (b) nanoplates histogram; c) and d) view of the synthesis products using different magnifications.*

The principal drawback of the original method, based on the aging of Na_2S, is the low reproducibility. This is motivated by the reaction conditions which under slight changes including small temperature changes, slight deviation on the concentration of the reagents or different sodium sulfide aging times yield different outcomes. Therefore, the challenges here were to control the reproducibility, to improve the homogeneity of the products and to maximize the spectral ratio between the peaks in the NIR (*i.e.* 800 nm) and that in the visible (*i.e.* 530 nm). The increment of reduction reaction increases as long as Na_2S aging time. This indicates that an oxidize product from Na_2S is the real responsible of the redox reaction. Zhang and co-workers suggested that sodium thiosulfate could be the reductant agent.[18] So, sodium sulphate was substituted by sodium thiosulfate as reducing agent. Comparing the reaction product absorption spectra obtained using 24 h aged Na_2S and fresh thiosulfate at the same concentration is clear that major NIR absorbing structures are produce using sodium thiosulfate (Figure 6.4. a and b).In the course of the optimization process to produce NIR absorbing NPs, we found that the spectral ratio between the NIR and Vis peaks is correlated with the molar ratio between tabular and pseudo-spherical NPs (Figure 6.4); *i.e.* the greater the spectral ratio is, the larger the population of tabular NPs relative to the pseudo-spherical NPs is. This observation lead us to agree with the arguments of previous works which claim tabular NPs, instead of the core-shell Au-Au_2S, as responsible for the NIR features in the context of this synthesis method.

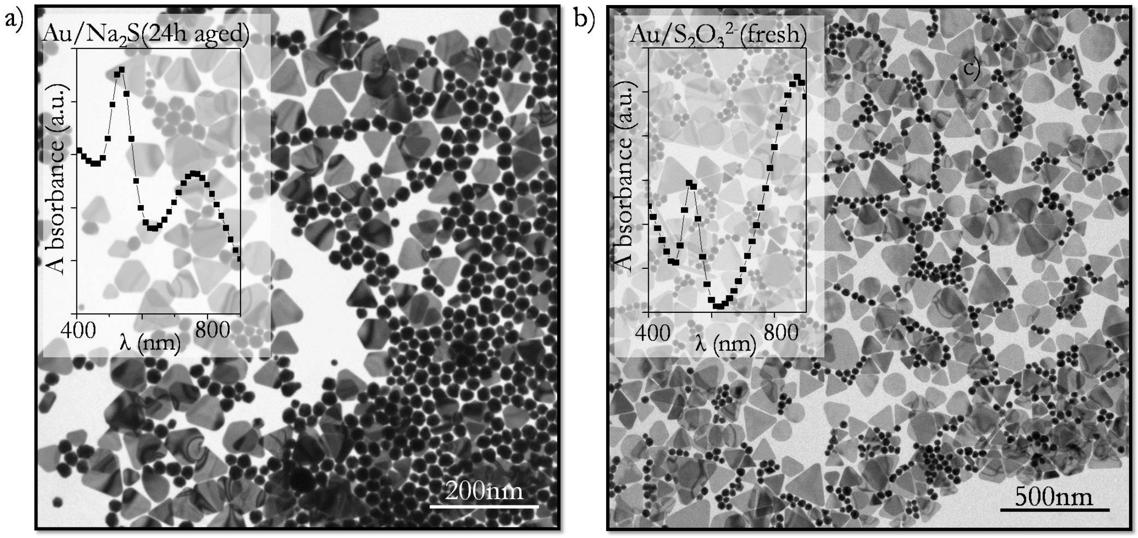

Figure 6.4. *Comparison of reaction products using a)* Na_2S *or b)* NaS_2O_3 *as reductant agent, and its effect on the Plasmon band.*

6.3. Optimization of the Synthetic Method

Based on the findings aforementioned, we therefore sought to synthesize Au tabular NPs by means of the reduction of $HAuCl_4$ using thiosulfate. Indeed, the main aim was to optimize the synthesis towards improved reproducibility, homogeneous size distribution and high yield of tabular nanostructures over other unwanted by products such polyhedral GNPs. Over the last decade, there have been great efforts to control the shape of Au nanocrystals, among other materials such as Ag, Pt, Pd, Cu, Fe, Co or Ni.[20-22] Thus, a vast diversity of methods has been proposed for controlling the shape of Au nanocrystals, and as for Pd and Ag nanocrystals, the selection of reductant, reaction conditions, and stabilizer are all critical to yield a particular shape. There have been described many methods to produce Au tabular nanostructures by wet-chemical synthetic routes; based on previous works, reducing the reduction rate seems to be the crucial factor to promote this shape (see (B) Nanoplates in section 5.3. Common Anisotropic GNPs for Bioapplications of Chapter 5). As an alternative to the seeded-mediated method, proven so far to give the best yield/control to produce Au nanoplates, we propose to use thiosulphate as a reducing agent; it is therefore very important to adjust the reduction rate by controlling the reaction conditions, *i.e.* concentration of the gold salt/reducing agent, temperature and time interval between additions of the reductant. In the following we discuss these "adjustments":

Thiosulfate as reductant agent; concentration of the reducing solution

Following the experimental evidences made by Schwartzberg *et al.*,[18] the first "obvious" change to introduce in the reaction was replacing Na_2S by sodium thiosulfate ($Na_2S_2O_3$); this step should prevent the required aging of the reducing solution. A number of concentrations (0.12 – 2.5 mM) of sodium thiosulfate were checked. Based on the spectral ratio (the greater the better) between the peaks in the NIR and Vis (Figure 6.5), the most suitable concentration was 0.5 mM ($Na_2S_2O_3$) instead of 1 mM (Na_2S as used by Zhou). Figure 6.7 also indicates that when using 0.25 mM reducing solution, some gold salt remains (non-reduced), whereas using 1 mM reducing solution, the 220 nm peak of the gold salt disappears rapidly; this indicates that the amount of reductant is enough to reduce all the gold (III) into gold (0), metallic gold. However, there seems to be an excess of reductant that speeds up the reaction to yield pseudo-nanospheres (53 nm; peak at 530 nm) as the major product.

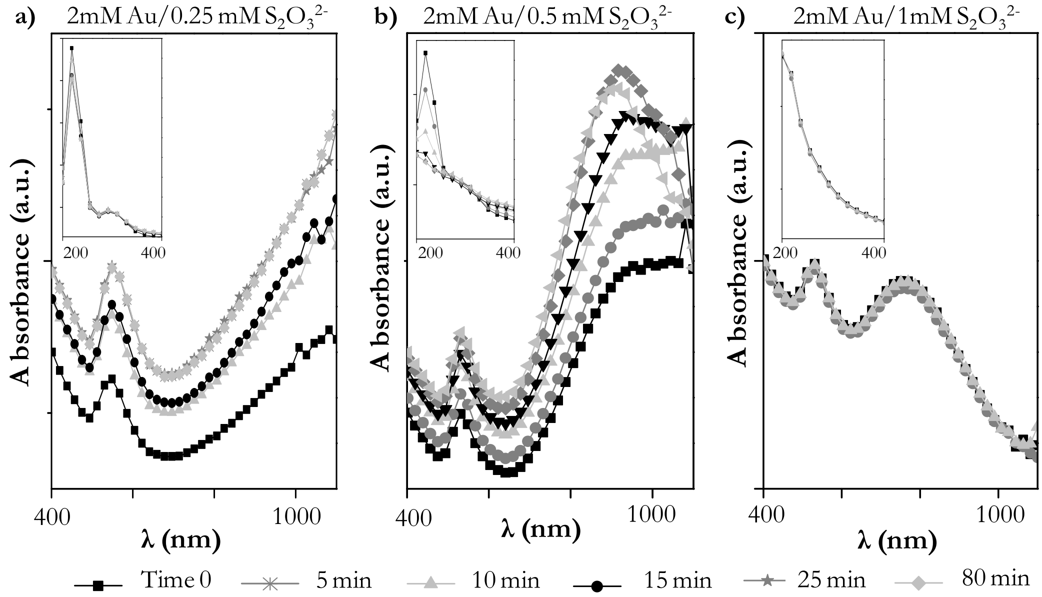

Figure 6.5. UV/Vis spectra of Au^{3+} reduction with a) 0.25 mM; b) 0.5 mM and c) 1 mM solutions of $S_2O_3^{2-}$ evolving in time, comparing the formation of NIR structures.

Concentration of the gold salt

Figure 6.6 demonstrates that the best NIR features are obtained using the original molar ratio [2mM $HAuCl_4$: 0.5mM $Na_2S_2O_3$]. Using higher concentrations of salt gold, the reductant amount is not enough to complete the redox process as is observed in the 220 nm peak.

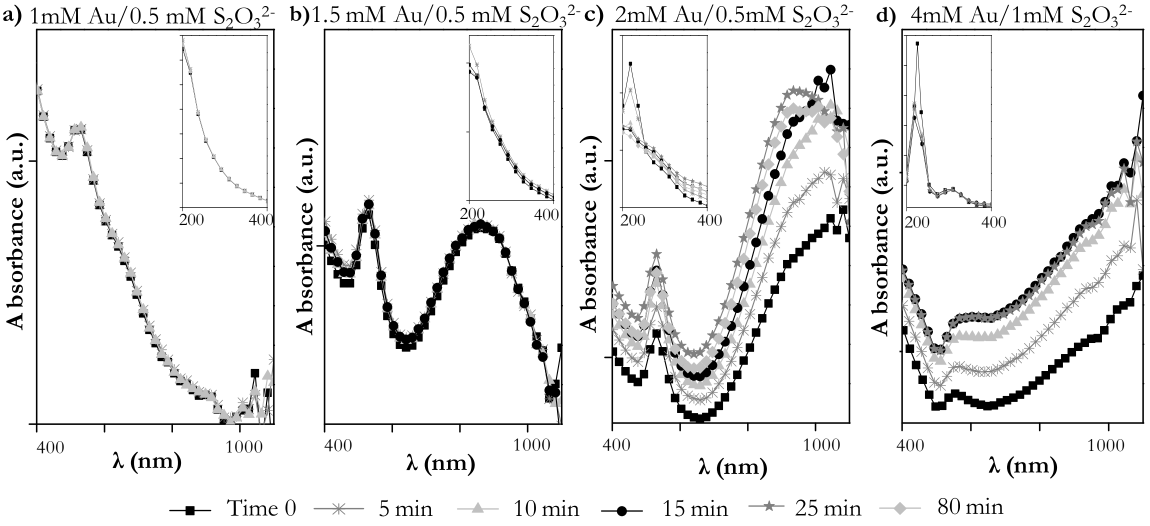

Figure 6.6. UV/Vis spectra of Au^{3+} reduction evaluation with a constant solution of $S_2O_3^{2-}$ and varying the Au salt concentration a) 1 mM; b) 1.5 mM; c) 2 mM and d) 4 mM at different times.

Time interval between additions of thiosulfate

Another important parameter evaluated is the time between the two additions of the reducing solution. At first, experimental data indicated that the second addition was required to guaranty the formation/stability of NPs. However, following experiments showed that the most important parameter here is the final amount of sodium thiosulfate added to the reaction, and the concentration ratio [Au^{3+} : $S_2O_3^{2-}$] during nucleation and growth of the NPs. Thus, the role of the second addition is providing the necessary amount of reductant to determine the final products.

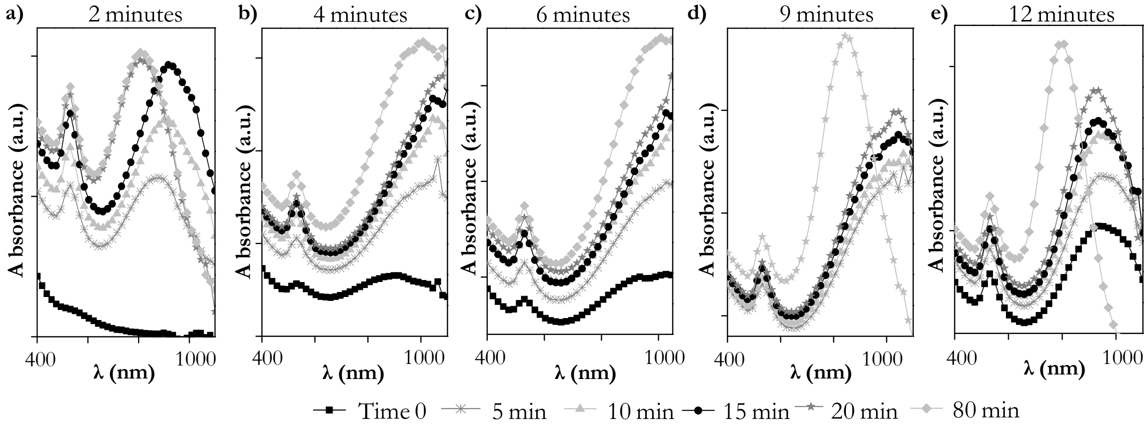

Figure 6.7. UV/Vis spectra of the reduction reaction of constant solution Au^{3+} by a constant amount of $S_2O_3^{2-}$ and varying the time between additions a) 2 minutes; b) 4 minutes; c) 6 minutes, d) 9 minutes and e) 12 minutes. Spectra were recorded at different times present in the legend.

Best results were achieved using time intervals between additions in the range of 9–12 minutes, as shown in Figure 6.7 (d and e); for 9 and 12 minutes between additions, the NIR peaks are narrower and higher relative to the 530 nm peak than for other times. Shorter and larger time intervals yielded poorer results in terms of NIR features.

Volume of the second addition of reductant

The role of this addition is to supplement the amount of reductant towards defining the final position of the NIR peak. The NIR peak red-shifted as the volume of the addition increased from 0.1 to 10 mL (Figure 6.8); a volume larger than 7.5 mL did not cause any significant improvement (Figure 6.10(e)). On the other hand, the spectral ratio between NIR and Vis peaks remain very similar independently of the volume of the 2nd addition.

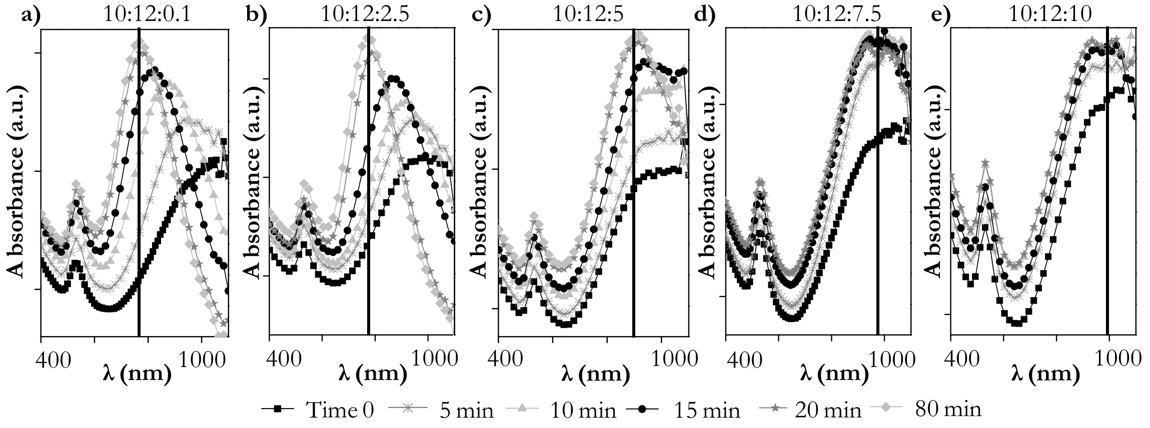

Figure 6.8. *UV/Vis spectra of the reaction of an aqueous solution of Au^{3+}(10mL) maintaining constant the volume of the first addition of reductant (12 mL) and varying the volume of the 2nd addition of $S_2O_3^{2-}$; a) 0.1mL; b) 2.5 mL; c) 5 mL, d) 7.5 mL minutes and e) 10 mL. Spectra were recorded at different times intervals from 0 to 60 minutes.*

There are reports which highlight the importance of temperature and illumination.[23,24] Therefore, these were evaluated to check their influence in the fate of the reaction. UV light was found to play no role at all in the formation of nanoplates. On the other hand, as expected, temperature is an important factor. If the reaction goes at temperatures lower that RT, *i.e.* 4 °C, the reduction rate slows down although the final products remain the same. In contrast, at high temperatures, *i.e.* 50 °C, the reduction rate speeds up and the final product ultimately consists on polyhedral GNPs which LSPR band lays centered at about 530 nm.

Analysis of the Redox Reaction

Next challenge in line was to figure out the redox reaction involved in the synthesis of NNs using thiosulfate. As thiosulfate is used as reductant, it has to be oxidized. Typically, thiosulfate is oxidized tetrathionate ($S_4O_6^{2-}$) or sulfate (SO_4^{2-}) depending on the redox conditions. For mild conditions, thiosulfate is transformed into tetrationate; as for strong conditions, thiosulfate is typically oxidized into sulfate.

The generation of NNs, metallic NPs made of Au^0, evolves through gold (III) reduction triggered by thiosulfate addition. In order to clarify which reaction mechanism applies here, the oxidation state of gold and sulphur were analyzed by X-ray photoelectron spectroscopy (XPS). The binding energies of the doublet for Au $4f_{7/2}$ (84.5 eV) and Au $4f_{5/2}$ (88.1 eV) clearly indicate the presence of just metallic Au (Figure 6.9). Besides gold, the most informative element in the context of this synthesis is sulphur. The spectrum shown in Figure 6.11(B) revealed a major peak (90% of intensity) centered at 168.7 eV which may be attributed to the binding energy of sulphate (S^{+6}). As controls, sulphate and thiosulphate XPS spectra were also analyzed. Experimentally, we found that the binding energy of sulphate is 168.4 eV. On the other hand, thiosulphate S $2p_{3/2}$ spectrum shows two double peaks (binding energies at 161.1 and at 168.2 eV) which contribute to the overall spectrum similarly. XPS results confirm that during the synthesis, Au^{3+} is fully reduced into Au^0 and that at least an 80% of the added thiosulfate is oxidized into sulphate.

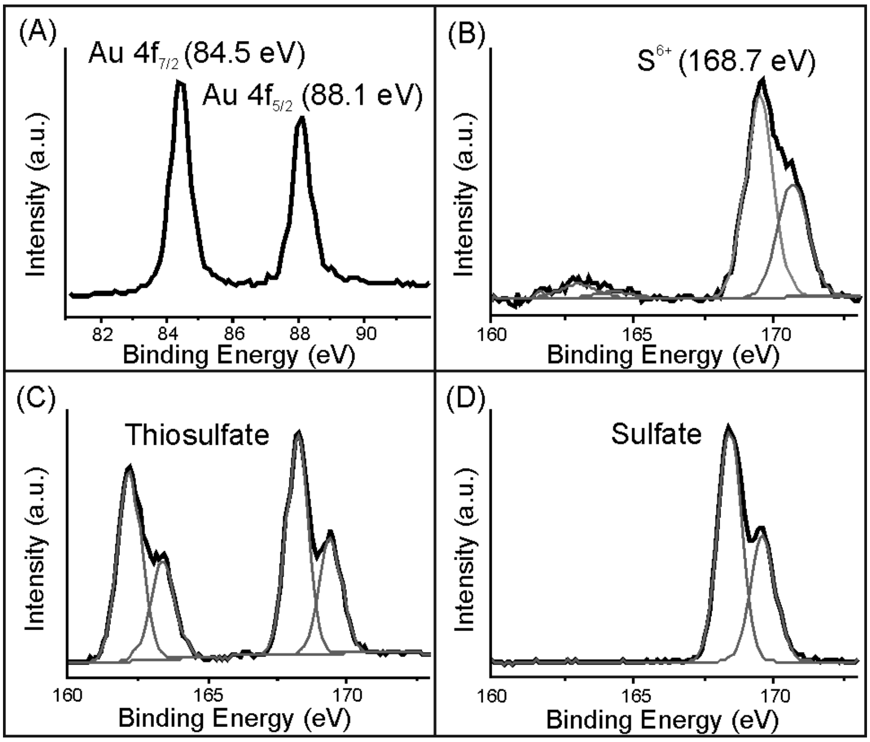

Figure 6.9. *XPS spectra in regions of Au 4f (A) and S 2p (B) for the synthesis of NNs. XPS spectra in the region S 2p for sulphate (C) and thiosulfate (D).*

Based on the molar ratio [Au^{3+}: $Na_2S_2O_3$] required for the reaction to success, we speculate that thiosulfate should be oxidized into sulphate which will be in agreement with XPS results. If thiosulphate would be oxidized into tetrathionate, the amount of reductant would not be enough (non sufficient number of electrons) to reduce all the gold salt; this would be in contradiction with our observations. In contrast, if sulphate is the product of the oxidation, the redox equations can be easily balanced and more importantly, this supports our experimental observations concerning the molar ratio [Au^{3+}: $Na_2S_2O_3$] required for the reaction to success and XPS data. This and simple electrochemical considerations allow us to propose the following redox reaction leading to the growth of NNs:

Reduction $\mathrm{Au^{III}} + 3\mathrm{e^-} \leftrightarrow \mathrm{Au^0}$

Oxidation $\mathrm{S_2O_3^{2-}} + 3\mathrm{e^-} \leftrightarrow 2\mathrm{SO_4^{2-}} + 10\mathrm{H^+} + 8\mathrm{e^-}$

Overall Reaction $8\mathrm{Au^{III}} + 3\mathrm{S_2O_3^{2-}} + 15\mathrm{H_2O} \leftrightarrow 8\mathrm{Au^0} + 6\mathrm{SO_4^{2-}} + 30\mathrm{H^+}$

Summarizing, the most suitable reaction conditions in order to obtain NNs are the following: mix aqueous solutions of x mL of 2 mM $\mathrm{HAuCl_4}$ and *1.2*x mL of 0.5 mM $\mathrm{Na_2S_2O_3}$ under mild stirring conditions at RT, followed by a second reductant addition (elapsed by 9 – 12 minutes) of reductant in the range of 0.2x – 0.5x mL; the volume of the second addition will ultimately determine the position of the NIR peak. The redox reaction goes for *ca.* 70 minutes until done.

6.4. Tuning the LSPR band of NNs along the NIR range

As previously stated, the most convenient method to synthesize Au nanoprisms is based on the seed-growth method which requieres CTAB, a surfactant that is highly cytotoxic and should be avoided if possible. Besides the undesirable use of CTAB, this method allows for tuning the LSPR of nanoprisms along the NIR range. To match this great deal of control represented a challenge in the context of the synthetic method proposed here. In the following, we describe the method to produce NNs with different aspect ratios (edge length, L, over thickness, t).

As previously discussed, the synthesis starts by mixing x mL of 2 mM chloroauric acid and 1.2x mL of 0.5 mM reducing solution at room temperature, where x comes determined by the initial volume of the gold salt solution. Within the initial 5 minutes of the reaction the color of the solution changed from yellow (gold salt) to brownish. This change of color indicates the formation of GNPs (“seeds”). To prevent aggregation and further increase the colloidal stability of the products, the resulting NPs were derivatized with heterobifunctional (-SH and –COOH groups) polyethylene glycol chains (HS-PEG-COOH, M.W. 5000 g/mol) (Figure 6.10). The thiol group (-SH) can form a pseudo-covalent bond with gold atoms on the surface of the NPs whereas the carboxylic group (-COOH) should give negative charge to the NPs above *ca.* pH 5.[25] PEG is often used as capping ligand for NPs as it reduces nonspecific adsorption of molecules to the particle surface and it provides colloidal stability because particles with PEG brushes on their surface repel each other for steric reasons; here the outermost ends of the polymer are carboxylic groups which also improve colloidal stability by charge repulsion. Moreover, the carboxylic groups of the PEG also provide NPs with a potential reactivity for further chemical modifications. By adding this polymer the reaction can be stopped at any time as the UV-Vis-NIR features get "frozen";10 mg of PEG per 10 mL of original synthesis solution were added while the pH of the solution was adjusted to 12 by adding NaOH; thus, the reactivity of the thiol group was increased.

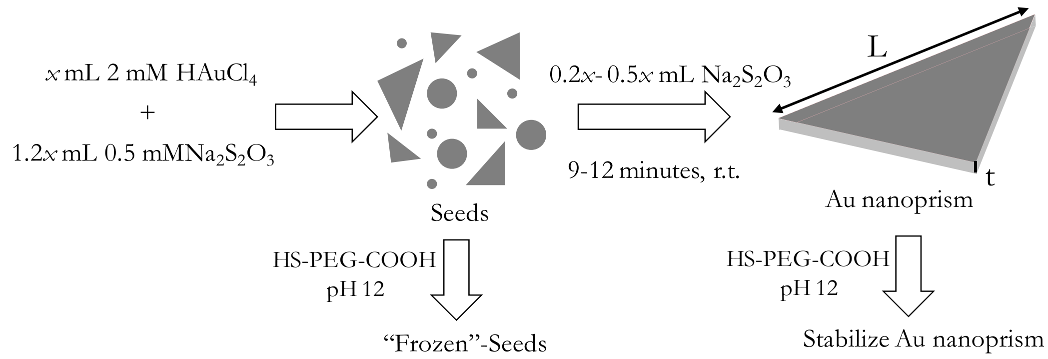

Figure 6.10. *NNs reaction scheme and stabilization with thiolated PEG chains of seeds (1st addition) and final nanoprisms.*

At this early stage of the reaction, 1 mg of HS-PEG-COOH was added to 1 mL of the initial mixture. Such an excess of thiolated polymer prevents further growth of NPs. Figure 6.11(a) shows a representative TEM image of the "frozen" products obtained within the initial stage of the reaction. This image revealed the presence of small NPs (diameter less than 3 nm), polyhedral GNPs (diameter less than 15 nm) and mainly, Au nanoprisms (edge length less than 35 nm). These initial NPs are called "seeds" because the final products of the synthesis route proposed leaded to "grown seeds", *i.e.* polyhedral GNPs (diameter of 30 nm) and NNs (edge length of 100-200 nm).

The fate of the "seeds" was monitored in real-time by UV-Vis-NIR spectroscopy for a selected sample where the volume of the second addition of reducing solution was 0.2x (Figure 6.11(b)). The reduction of the gold salt can be followed in the inset in Figure 6.11(b) at the sharp peak centered at 221 nm which is "consumed" as metallic gold (Au^0) is formed and used for further growth of NPs; after *ca.* 90 minutes, this peak remains stable and the reaction is considered to be finished as the spectrum remains the same over time.

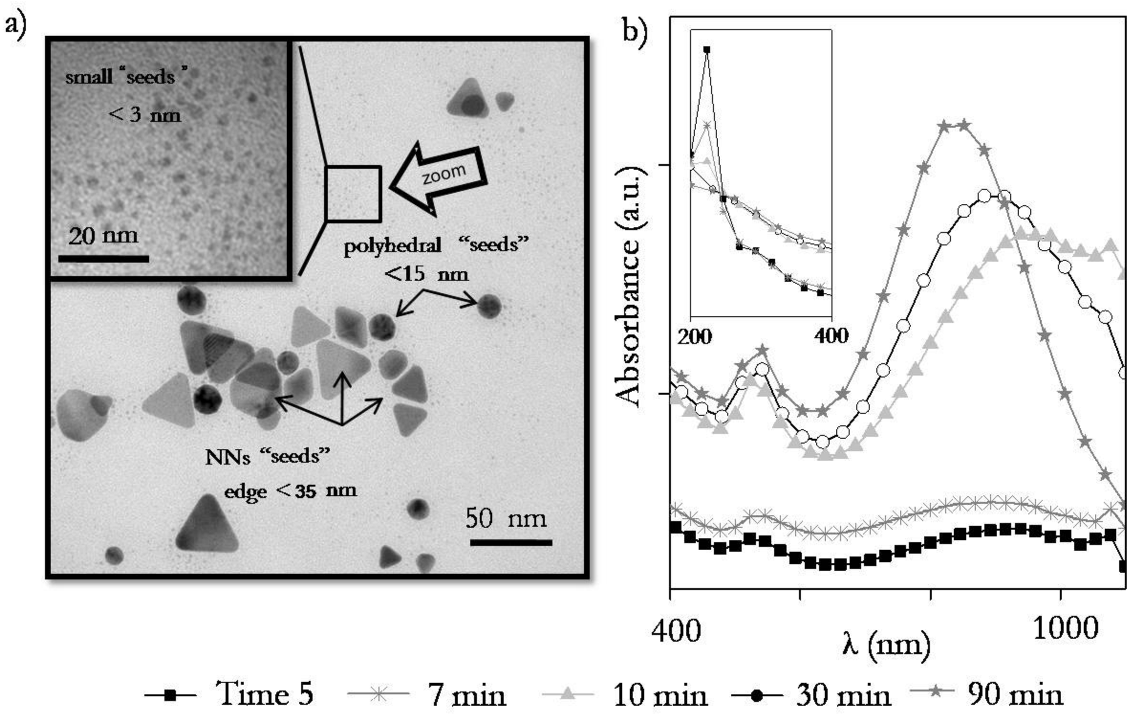

Figure 6.11. *TEM image of the "frozen" products obtained within the first 5 minutes of the reaction. Arrows point at different NPs, i.e. NNs "seeds", polyhedral "seeds" and small "seeds". Inset shows a magnification of a region of the TEM-grid containing small "seeds". (A) In situ UV-Vis-NIR spectroscopy of the reaction following the formation of NPs where the volume of the second addition of reducing solution was 0.2x.*

Figure 6.11(b) shows two classes of peaks, which can be linked to the LSPR of GNPs. First, a band in the visible remains fixed at 530 nm although its intensity increases over time. The second band moves along the NIR range as the reaction proceeds. After the second addition of reducing solution (9 minutes), this band increased in intensity drastically (compared to the 530 nm band). This indicates that the second addition of the reductant is used to grow NNs mainly. Other synthesis methods based on the seed-mediated approach showed that the NIR band red-shifts as the reaction evolves;[3,4] this is linked to the increase of the edge length of nanoprisms while the thickness remains constant and almost of the same value as the diameter of the precursor seeds. In contrast, we found that after the second addition of reducing solution, the NIR band blue-shifts. This is an indication for the decrease of the aspect ratio of NNs (edge over thickness, *l/t*) of nanoprisms.

The reaction was stirred at room temperature for 9 minutes prior to a second addition of reducing solution. The volume of the second addition ultimately determined where the NIR band is centered; this can be tuned from 750 nm to

1050 nm as the volume of the second addition of reductant increased from 0.2*x* to 0.5*x* mL, respectively (Figure 6.12(a)).

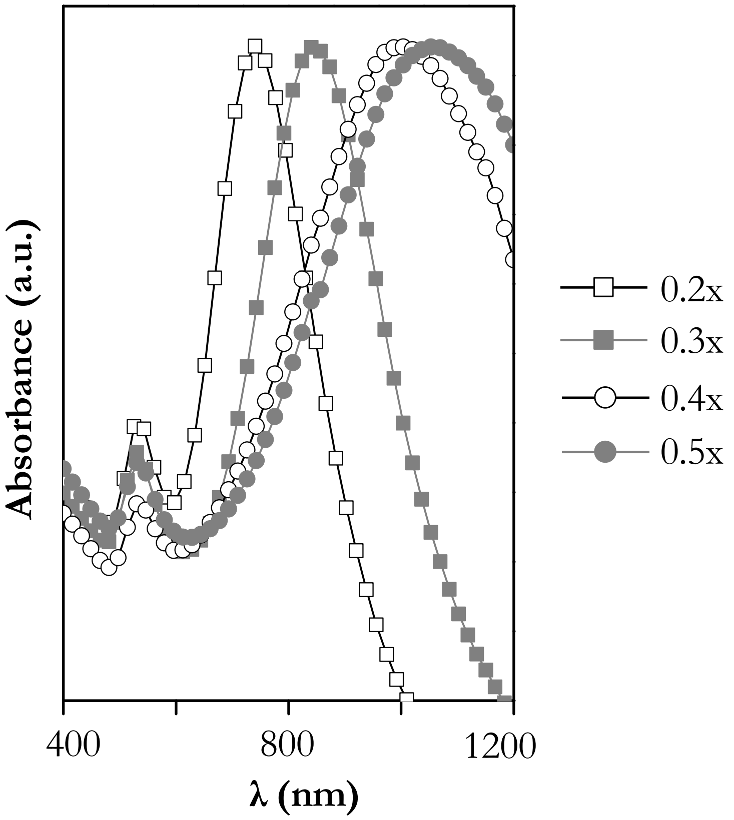

Figure 6.12. *UV-Vis-NIR spectra of the resulting preparations as the volume of the second addition of reductant increases, i.e. 0.2x, 0.3x, 0.4x and 0.5x.*

The spectra shown in Figure 6.12(a) clearly reveal two distinct LSPR bands for each synthesis. They exhibit a common LSPR band at 530 nm which is typically attributed to polyhedral GNPs. However, the major contribution to the spectra comes from distinctive NIR bands which are characteristic of anisotropic GNPs, *e.g.* Au nanorods or nanoprisms.

6.5. PEGylation of the Resulting NNs

In general, a dense well-packed coating is an extra value for NPs. This coating provides NPs with a crucial stability in aqueous media against pH variations, ionic strength, protein concentration, etc. In the long run, to build a consistent coating will be a determinant factor to success or not in a given bioapplication. If the system is unstable in the experimental environment, this coating must be discarded because the results will not be reproducible.

In the case of NNs, after the required optimization to yield as few as possible by-products, the next step was to provide NNs with the best stability properties. NNs as result from the synthesis are constituted by metallic gold stabilized by sulphate anions; thus, the most suitable choice here is to employ the well-known thiol-gold chemistry. In this case, a coordination bond is formed; the Au-S bond is sufficiently strong to resist oxidative conditions such as those applying in an aqueous solution during extended periods of time. The tricky part here is to find the proper moiety which is able to stabilize NNs.(Figure 6.13)

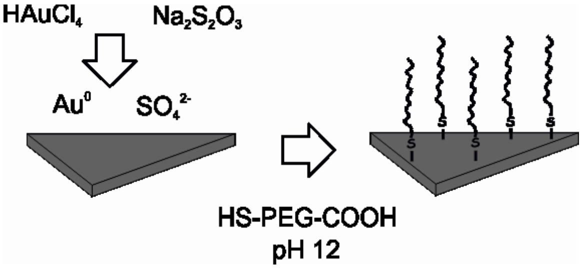

Figure 6.13. *NNs scheme of reaction and stabilization with thiolated PEG chains.*

Different molecules were tested such as tiopronin (N-(2-mercaptopropionyl)-glycine), MUA (11-mercaptoundecanoic acid), short chains of PEG terminated by a thiol group and methoxy or a carboxylic group (HS-PEG-OMe or HS-PEG-CO_2H), and long chains of heterobifunctional PEG. In attempts with small molecules, it was found that even when using a large excess of ligands and long incubation times, they were not able to stabilize such large surface NPs and ultimately leading to aggregation. Best stabilizers were found to be thiolated poly(ethylene glycols) with sizes between 2-5 KDa.

Typically, solutions of NNs were supplemented with thiolated PEG chains. The pH of the solution was adjusted to 12.0 with a concentrated solution of NaOH. Samples were left overnight to react (ligand-exchange) under mild stirring conditions. The use of these heterobifunctional PEG chains provided NNs with a solid stability and also, it was feasible to modulate the global negative charge of NNs by using different combinations of PEGs terminated by carboxylic and methoxy groups. Different attempts to optimize the global charge of the NNs were made with the aim of maximizing the number of chains attached. Different reaction conditions were evaluated. The effect of rising the pH to 12 to promote deprotonation of thiol group and the presence of a surfactant, 0.01% of SDS (Sodium Dodecyl Sulfate), to avoid NN agglomeration during the exchange were also studied. The ligand exchange conditions are summarized in Table 6.1.

Knowing that the selected solutions of NNs exhibited 1 OD at the maximum of their plasmon band, yields (efficiency) were calculated comparing the initial absorption of non-functionalized NN solution (1 OD) against final functionalized NN (Figure 6.14). Final solutions were washed out of excess of reagents by consecutive centrifugation steps at 9000 rpm.

Sample	SH-PEG-CO_2H (% ; M.W(KDa))	SH-PEG-OMe (%; M.W.(KDa))	Conditions	Yield (%)
A	70% (5 KDa)	30% (5 KDa)	Water	61.8
B	30% (5 KDa)	70% (5 KDa)	Water	56.1
C	70% (5 KDa)	30% (5 KDa)	pH 12, 0.01%SDS	92.4
D	30% (5 KDa)	70% (5 KDa)	pH 12, 0.01%SDS	89
E	70% (5 KDa)	30% (2 KDa)	pH 12, 0.01%SDS	87.8
F	30% (5 KDa)	70% (2 KDa)	pH 12, 0.01%SDS	93.9
G	100% (5 KDa)	-	pH 12, 0.01%SDS	100
H	70% (5 KDa)	30% (2 KDa)	Water	42.7
I	30% (5 KDa)	70% (2 KDa)	Water	62

Table 6.1. *PEGylation conditions for each sample.*

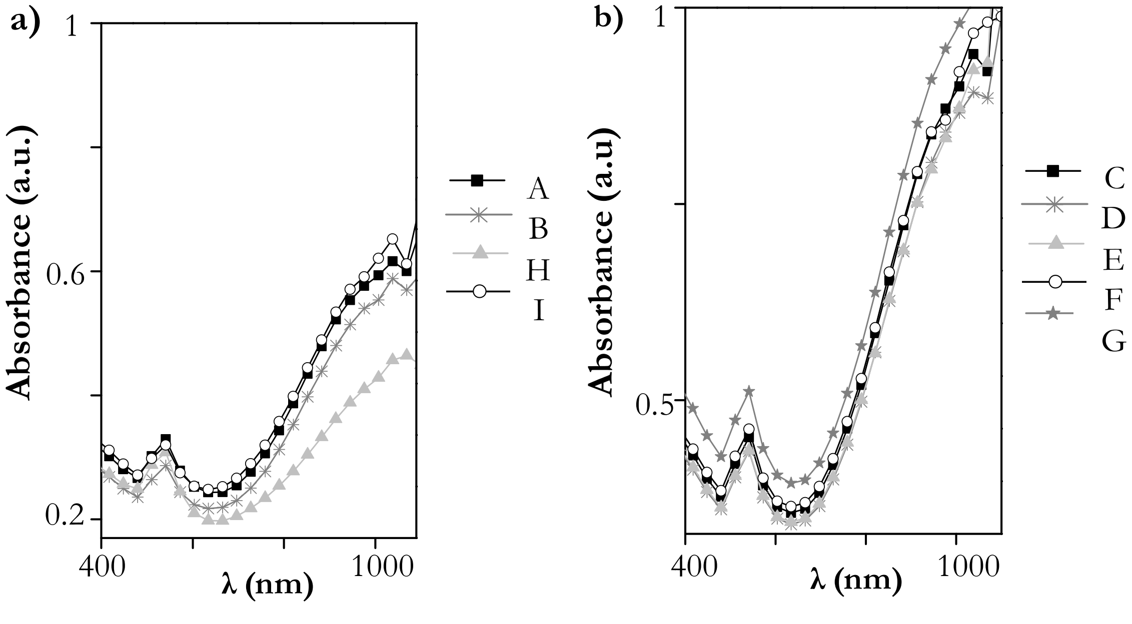

Figure 6.14. *UV/Vis spectra of (a) NNs PEGylated in water and (b) NNs PEGylated at pH 12 and 0.01% SDS.*

The differences shown in Figure 6.14 can be ascribable to different efficiencies in the functionalization. Especially important is the low absorbance in sample H where ca. 60% of NNs were lost in this step. Best conditions were achieved using 100% carboxylic PEG, basic pH and SDS. PEG mixes using basic pH and SDS works acceptably in all the cases.

To elucidate whether functionalization works better because of deprotonation of the thiol group at basic pH and/or SDS stabilization, NN were functionalized with a 100% of carboxylic PEG (5 KDa) modifying the functionalization conditions as shown in Table 6.2.

Sample	Conditions (PEG CO_2H, 5KDa)
J	pH 12
K	pH 12/ 0.01% SDS
L	pH 3

Table 6.2. *PEGylation conditions to prove the pH influence in NNs functionalization.*

In view of the spectra end and the agarose gel, it is clear that the thiol "activation" is a remarkable advantage (Figure 6.15). On the other hand, the role of the SDS does not seem really crucial. Therefore, in the following NN were functionalized with 5 kDa HS-PEG-CO_2H in basic conditions without SDS to prevent possible undesirable interactions.

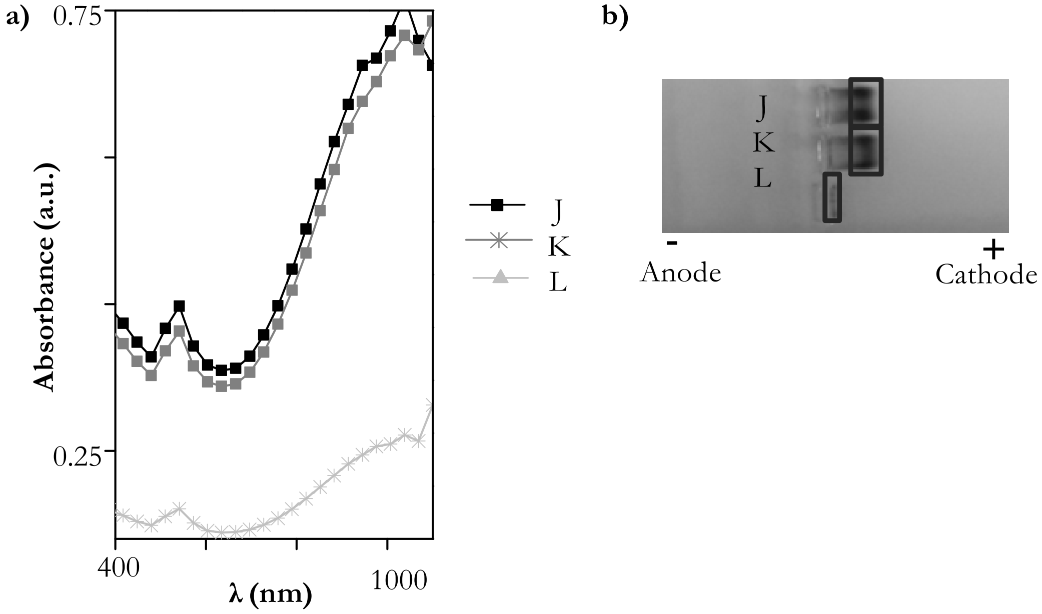

Figure 6.15. *(a) UV/Vis of the NNs PEGylated at different conditions and (b) electrophoretic mobility evaluation of the resultant NNs (agarose gel (0.6%), 50V, 2h 30 min, TBE 0.5x).*

The net charge of NNs with different coatings was analyzed with the following protocol: samples C, D, E, F and G (all samples where PEGylation worked properly) were separated by centrifugation in 3 fractions as shown schematically in Figure 6.15. Samples were first centrifugated at 6000 rpm during 20 minutes; supernatants were then pipetted out (Fraction 1). Precipitates were resuspended and then centrifugated during 20 minutes at 2000 rpm, supernatant (Fraction 2) and precipitated (Fraction 3) were separated. (Figure 6.15)

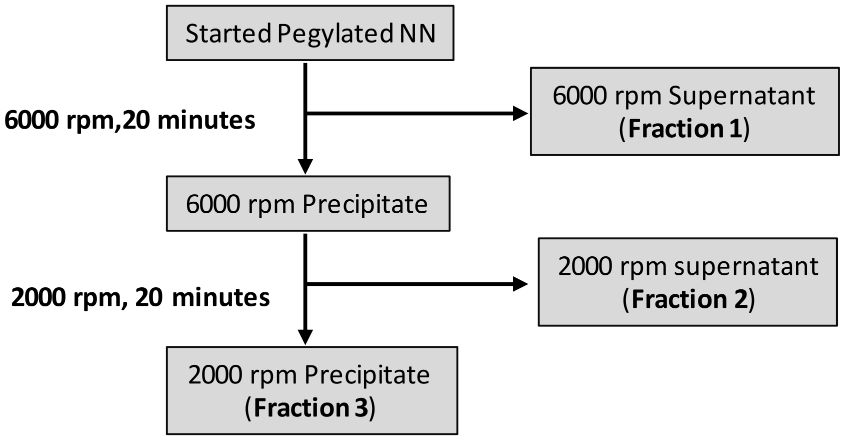

Figure 6.16. Scheme of separation process and the final fractions (in bold) obtained for an individual study.

NPs charge from all the fractions were evaluated by electrophoresis in agarose gels as shown in Figure 6.17; the dashed line indicates the position of the loading wells.

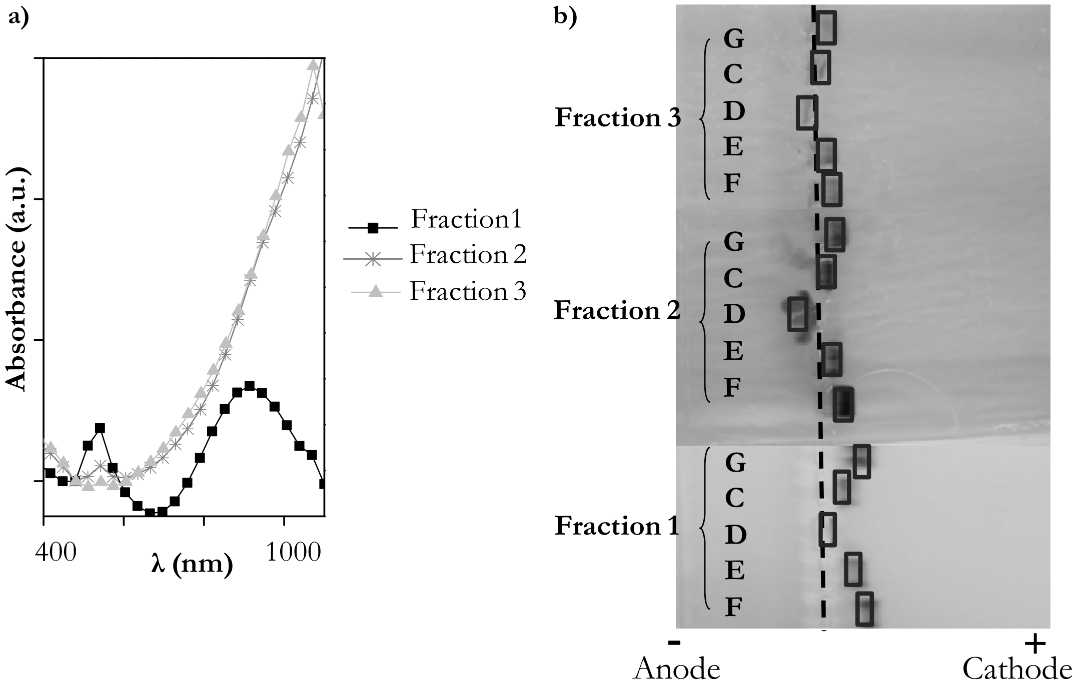

Figure 6.17. *(a) UV/Vis of the different fractions obtained by fractionated centrifugation and (b) corresponding electrophoretic mobility evaluation of the resultant NNs (0.6% agarose gel, 50V, 2.5 h, TBE 0.5x).*

As it was expected, small pseudo-spherical NPs (Fraction 1) exhibit a higher electrophoretic mobility due their smaller size; it is followed by Fraction 2 and Fraction 3 in terms of electrophoretic mobility. This effect could be also ascribable to a competitive effect of both charge and size; spherical NPs and small plates run free inside the gel whereas larges NNs experiment a major delay because of retention in the gel pores. Regarding differences between syntheses, sample D, where carboxylated PEG chains represent the minor coating component, is the most delayed whereas sample G (100% of carboxylated PEG) is the sample with major mobility.

Thermogravimetric analysis (TGA) was used to determine the amount of inorganic material that NNs bear before and after PEGylation (Figure 6.17 (a) and (b) respectively). Non PEGylated NNs were centrifugated for 5 hours (1000 rpm) to remove excess of thiosulphate and other reagents from the synthesis (labelled NNs from synthesis in Figure 6.18(a)); washed non PEGylated NNs were centrifugated for 10 minutes (8000 rpm); precipitate and supernatant were separated and lyophilized (labeled as precipitate and supernatant in Figure 6.18(a)). Equivalently, washed PEGylated NNs were separated (Figure 6.18 (b)).

Results shows that samples of large NNs (precipitate samples) contain a higher content of inorganic content as expected from their lower surface to volume ratio than that of quasi-spheres and small nanoplates. Also as expected, PEGylated NNs contain a higher organic content than non PEGylated NNs. These results confirm that PEGylation worked properly.

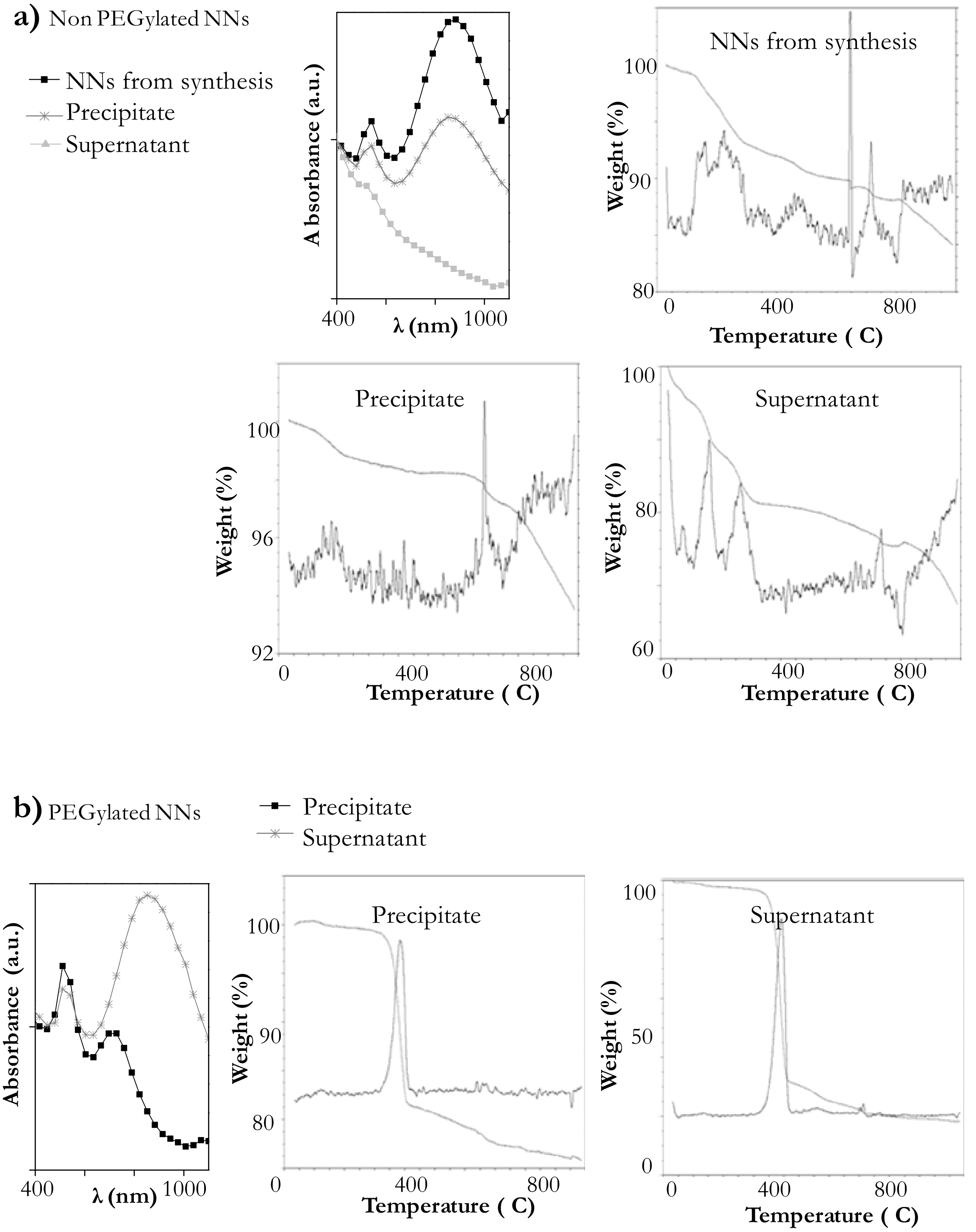

Figure 6.18. *UV/Vis of the different fractions obtained by fractionated centrifugation and thermogravimetric analysis (TGA) results for each fraction of a) non PEGylated NNs and b) PEGylated NN.*

6.6. Purification of NNs@PEG

Purification of NNs by centrifugation

An exhaustive centrifugation was done to try to separate and identify different NNs fractions. The increased colloidal stability allowed us to separate NNs derivatized with HS-PEG-COOH (NN@PEG) from other by products by selective centrifugal precipitation (Figure 6.19). PEG derivatization prevents irreversible aggregation of NPs, which otherwise is inevitable, while centrifuging for separation. Centrifugations at a number of increasing rotation frequencies (8000 – 2000 rpm) were used to precipitate heavier NPs from their lighter partners which remain in the supernatants; these were analyzed by UV-Vis-NIR spectroscopy and electron microscopy with the aim of assessing the relation between shape and optical features. Thus, the NIR bands of Figure 6.13 can be univocally linked to the presence of NN@PEG with different aspect ratios (edge length over thickness). The selective separation experiment was done with a sample which did not present any relevant "good" quality in terms of the spectral ratio between NIR and Vis optical features.

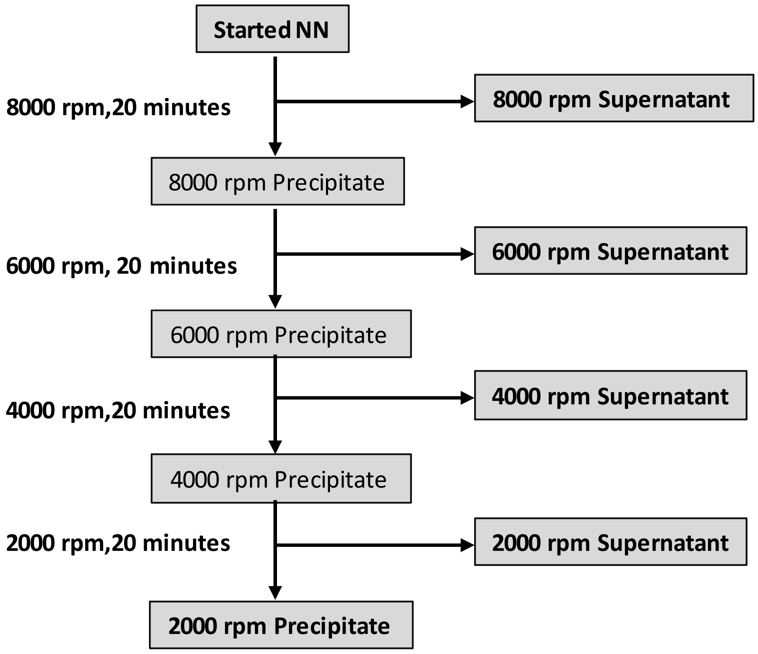

Figure 6.19. *Scheme of separation process to evaluated the nature of the different NNs fractions. Bold letter containing boxes indicate which samples were analyzed.*

Figure 6.20 shows the link between the optical features and shape/size of the NPs (electron microscopy images and corresponding histograms) resulting from the previously described separation. The original synthesis yielded a mixture of tabular and polyhedral GNPs; although the NIR peak is actually more prominent than the Vis peak, the histogram indicates that the presence of polyhedral NPs is notable (*ca.* 16 % w/w or *ca.* 46 % molar ratio relative to NNs). As expected, using the fastest rotation frequency, *i.e.* 8000 rpm, the major component of the supernatant were polyhedral NPs (*ca.* 40 nm) and small tabular NPs (*ca.* 50 nm edge length). As the rotation frequency decreases, larger NPs can be found in the supernatants. We find polyhedral NPs at even 2000 rpm which is surprising since these NPs should not precipitate at this frequency; we speculate that larger tabular NPs (*ca.* 160 nm) can drag these polyhedral NPs to precipitate. The size of NNs present in the supernatants was increasing as the speed of centrifugation was decreased. As 6000rpm size of plates was around 70 nm, whereas at 4000 rpm size was *ca.* 110 nm, and the 130 nm for the plates founded in the 2000 rpm supernatant. Summarizing, lighter NPs (majorly polyhedral NPs) show Vis optical absorption whereas heavier NPs (majorly NNs) have distinctive NIR features. This result irrefutably confirms that the NIR peak is caused by tabular NPs instead of the controversial core-shell Au-Au_2S system.

To estimate the concentration of NNs in solution, selected samples of NN@PEG were:

(i) Observed by UV-Vis-NIR spectroscopy to give them a NIR signature (OD units at a given frequency).

(ii) Analyzed by electron microscopy to assess their geometry.

(iii) Lyophilized for linking optical features and dry weight.

Using this approach, optical "signatures" can be assigned to a known concentration of NNs with a given geometry. For instance, for a sample displaying the LSPR peak at 1000 nm, 1 OD unit in a 1 mL, 1 cm path length cuvette, the concentration is 0.04 $mg \cdot mL^{-1}$ of NN@PEG with an average edge length of *ca.* 120 nm. This data led to a molar extinction coefficient of *ca.* 1.9×10^{10} $M^{-1} \times cm^{-1}$.

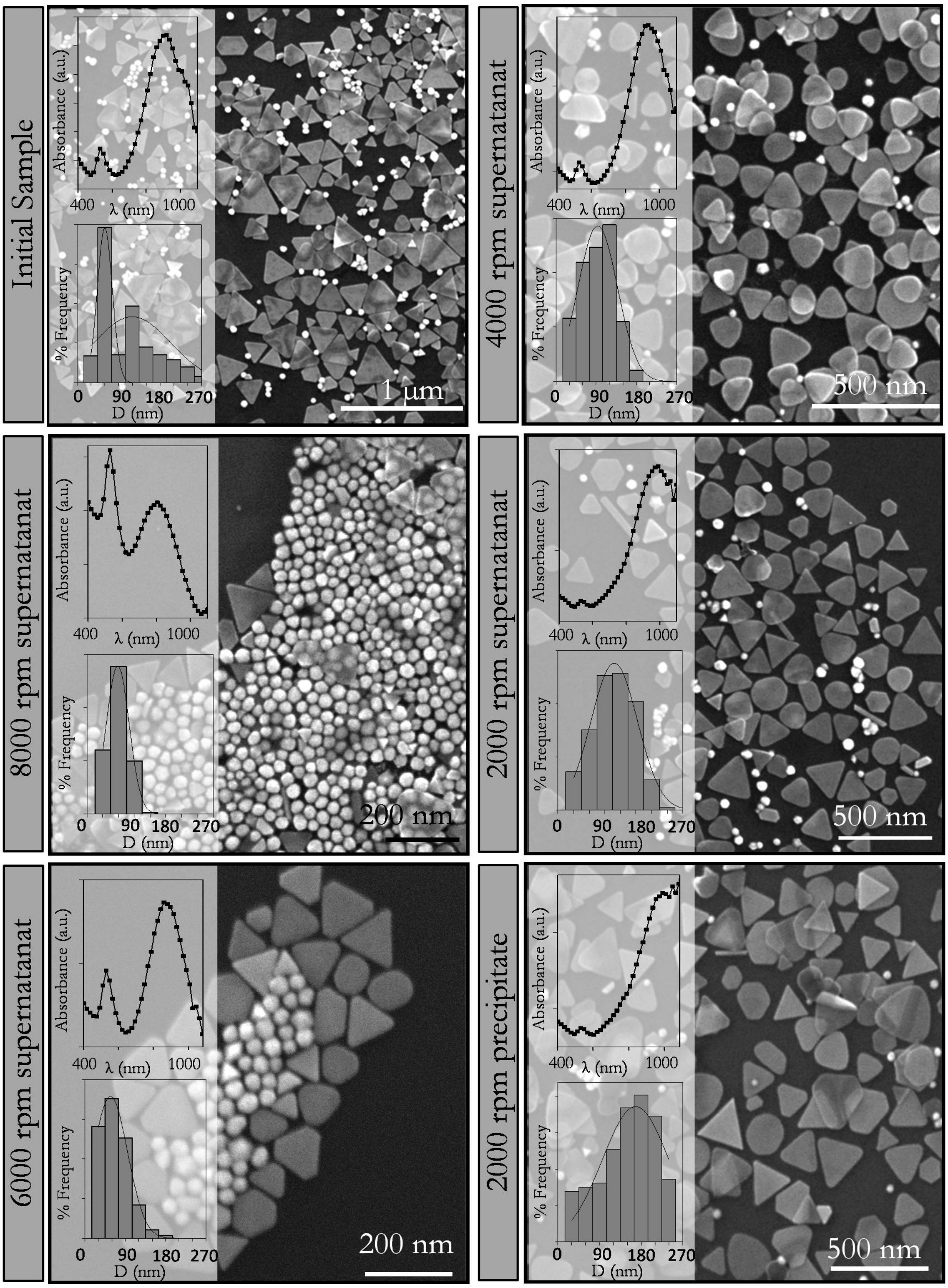

Figure 6.20. *UV/Vis spectra, SEM images and size distribution of different fractions of NNs separated by fractionated precipitation.*

Purification of NNs by electrophoresis

As centrifugation process did not avoid the presence of polyhedral nanoparticles, using the previously increased colloidal stability allows separating NNs from other by products by electrophoresis. Briefly, 10 mL of each sample (0.2*x* - 0.5*x*) was supplemented with 1 mg of thiolated PEG. The pH of the solution was adjusted to 12.0 with a concentrated solution of NaOH. Samples were left overnight to react (ligand-exchange) under mild stirring conditions. The increased colloidal stability allowed washing the NPs by centrifugation (centrifuged twice for 15 min at 10000 rpm and resuspending pellets in MilliQ water); prior to PEG-derivatization, centrifugation aggregated the NPs irreversibly. Furthermore, PEG-derivatized NNs were stable in tris-borate-EDTA (1x TBE) buffer, among other buffers, which is used in gel-electrophoresis generally. Samples were loaded (mixed with loading buffer, *i.e.* 1x TBE, 10% glycerol) then in wells within an agarose gel (0.6x) immersed in an electrophoresis cuvette filled with TBE 1x. Electrophoresis separation was run at 100 V for 15 minutes.

Due to the increased electrophoretical mobility of NPs other than NNs, i.e. polyhedral Au-NPs, two bands were resolved in the gel (Figure 6.21(a)). UV-Vis-NIR spectra of the original products are shown in Figure 6.21(b). The band corresponding to the NNs were cut and introduced in TBE-filled dialysis membranes (cut-off 10 KDa). They were immersed in the electrophoresis cuvette. NNs were extracted from the gel-cut segments by application of 100 V for 2 hours. The purification products were analyzed by UV-Vis-NIR spectroscopy and gave the optical features shown in Figure 6.21 (c). Thus, the NIR bands of Figure 6.21(c) can be univocally linked to the presence of NNs with different aspect ratios (edge length over thickness) and therefore different NIR “signatures”.

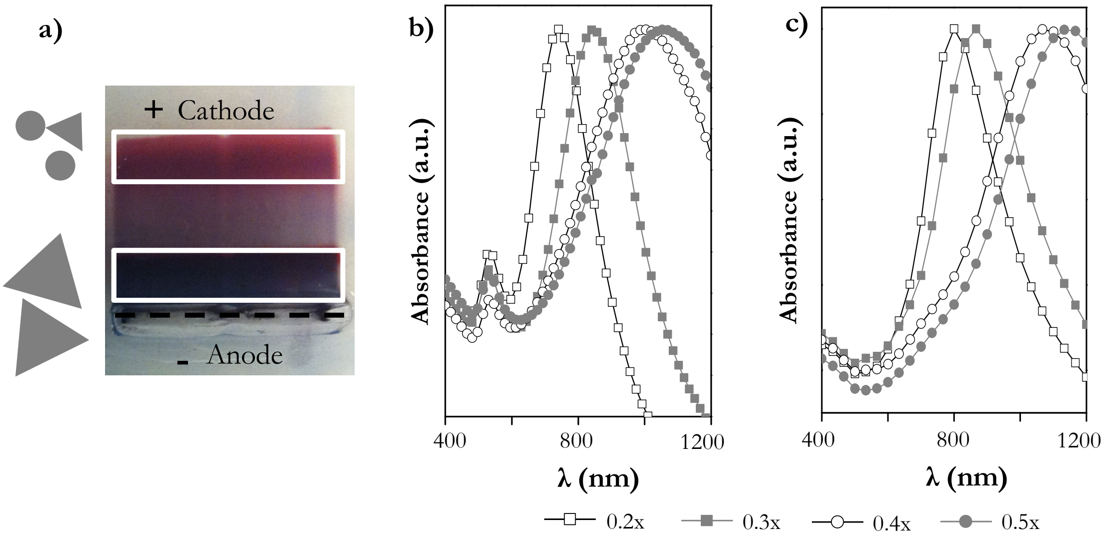

Figure 6.21. *(a) Image of the electrophoresis gel where two band were resolved; (b) and (c) are the UV-Vis-NIR spectra of the original and purified products, respectively.*

6.7. Electron transmission characterization of purified NNs

The purification products were extensively characterized by electron microscopy (Figure 6.22). When the products lie flat on a substrate, the NNs appear to have a triangular-like morphology which exhibit congruent edge lengths which vary among the four different preparations. The average edge lengths were 104.5 ± 32 nm (*l* 1), 127.6 ± 40 nm (*l* 2), 146.9 ± 35 nm (*l* 3) and 165.3 ± 42 nm (*l* 4) corresponding to NIR bands of Figure 6.5-x (b) centered at 800 nm, 865 nm, 1078 nm and 1148 nm respectively. Most colloidal syntheses of triangular nanoprisms tend to yield some small percentage of tip-truncated nanoprisms or nanodisks.[3] Indeed, Figure 6.16 corroborated the presence of NPs deviating from an ideal triangular nanoprism to a lesser or greater extent depending on the sample. The significance of this effect increases as the edge length of NNs decreases. Figure 6.5-3 also shows the residual presence of pseudo-spherical NPs (average diameter of 30 ± 6 nm). Pseudo-spherical NPs are a common product of wet- chemical synthesis methods to produce triangular nanoprisms.[3,4,26] Our synthesis approach gives a very high yield of NNs over other residual products (*ca.* 70% molar ratio or *ca.* 96% w/w); even before the purification step, the contribution of pseudo-spherical NPs (LSPR at 532 nm) is significantly low compared to that of the NIR band attributed to NNs (Figure 6.15(a)).

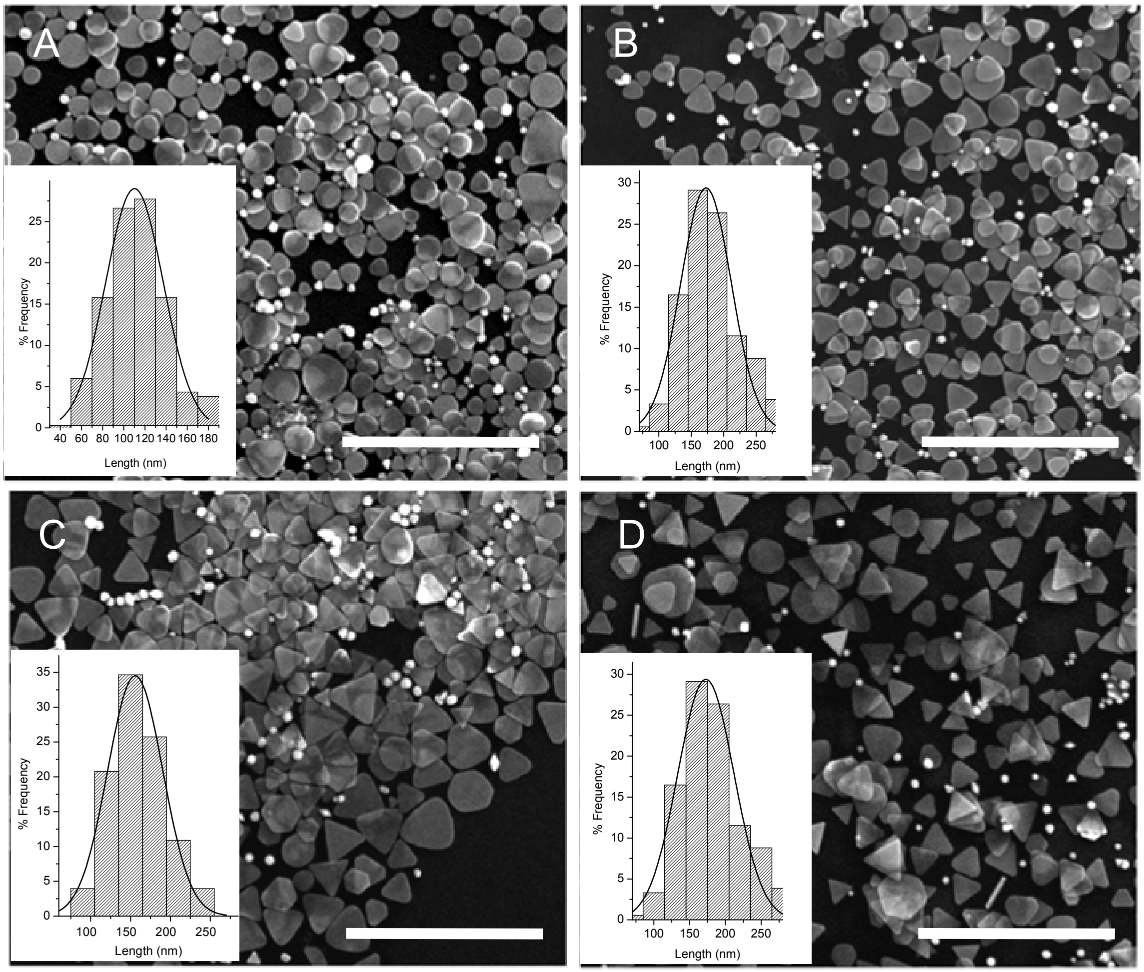

Figure 6.22. *SEM images of each reported NNs@PEG, i.e. A) 0.2x, B) 0.3x, C) 0.4x and D) 0.5x. Insets show the corresponding histograms (over more than 300 NPs) representing the size distribution of different NNs. Scale bars are 1 μm in all cases.*

The crystal structure of NNs (top and edge facets) was also studied by aberration corrected HR-TEM (Figure 6.23). The analysis of the digital diffractogram of a single NN showed a hexagonal-shaped pattern that is characteristic of the [111] orientation of a *fcc* Au structure (Figure 6.23(A), inset, boxed spot corresponding to the lattice spacing of 1.44 Å). In addition, the diffraction pattern exhibit a set of weak spots indexed as 1/3 {422} (circled spot with a lattice spacing of 2.48 Å); these reflections have been linked to the combination of twin planes and [111] stacking faults.[27,28]

The flat morphology of a single NN with a thickness of 9 nm can be inferred from the TEM side-view of the NN (Figure 6.23(B)). The corresponding diffraction pattern (Figure 6.23 (B), inset) revealed a rectangular pattern consistent with a [-1-12] orientation on a *fcc* crystal.

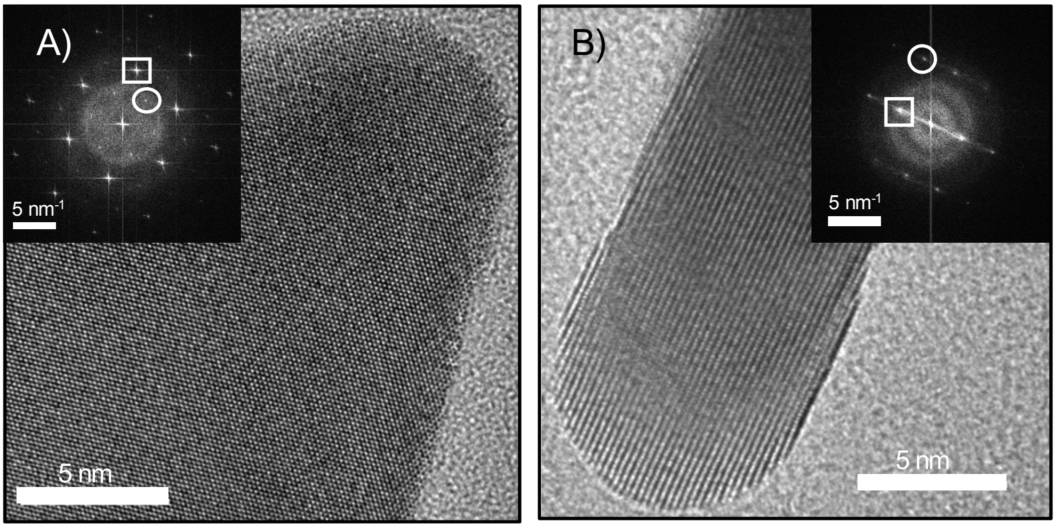

Figure 6.23. *(A) Aberration corrected high resolution (HR) TEM image of the top-facet of a NN. The inset shows the corresponding diffraction pattern where the boxed spot belongs to the hexagonal-shaped pattern which indicates the [111] fcc surface facet; the circled spot has been linked to the combination of twin planes and [111] stacking faults. (B) Aberration corrected HR-TEM image of the side-facet of a NN. The inset shows the corresponding diffraction pattern; the boxed and circled spots were indexed as [111] and [-131] reflections, respectively.*

As we previously discussed, all synthesis methods to produce gold nanoprisms tend to yield some small percentage of tip-truncated nanoprisms or nanodisks. High magnification of selected STEM images highlight this fact which becomes more apparent as the edge length of NNs decreases (Figure 6.18); here, panel (A) shows the predominant disk-like morphology of NNs with an average edge length of 104.5 ± 32 nm (note that this length can be measured from tip to tip of the NP because the triangular shape still is discernible); the NNs in panel (B) with edge length 127.6 ± 40 nm still show disk-like shape although to a lesser extent than NPs in panel (A); in panel (C), for NNs with average edge length 146.9 ± 35 nm, the rounded-tips and edges are still discernible; finally, NNs in panel (D) with average edge length 165.3 ± 42 nm show regular edges even though due to tip-truncation some NPs appear to have hexagonal top/bottom faces.

The flat morphology of NNs was studied by TEM tilt series. Figure 6.24 (E) shows the side view of a NN (surrounded by polyhedral NPs) which apparently resembles the shape of a rod. However, a TEM image of the same group of NPs with the specimen tilted about 30° revealed the prismatic nature of the NN (Figure 6.24 (F)). Indeed, STEM images shown in Figure 6.24 (G, G, and I) exhibit the presence of apparently rod-like NPs with constant thickness (9 nm) which correspond to the side view of NNs.

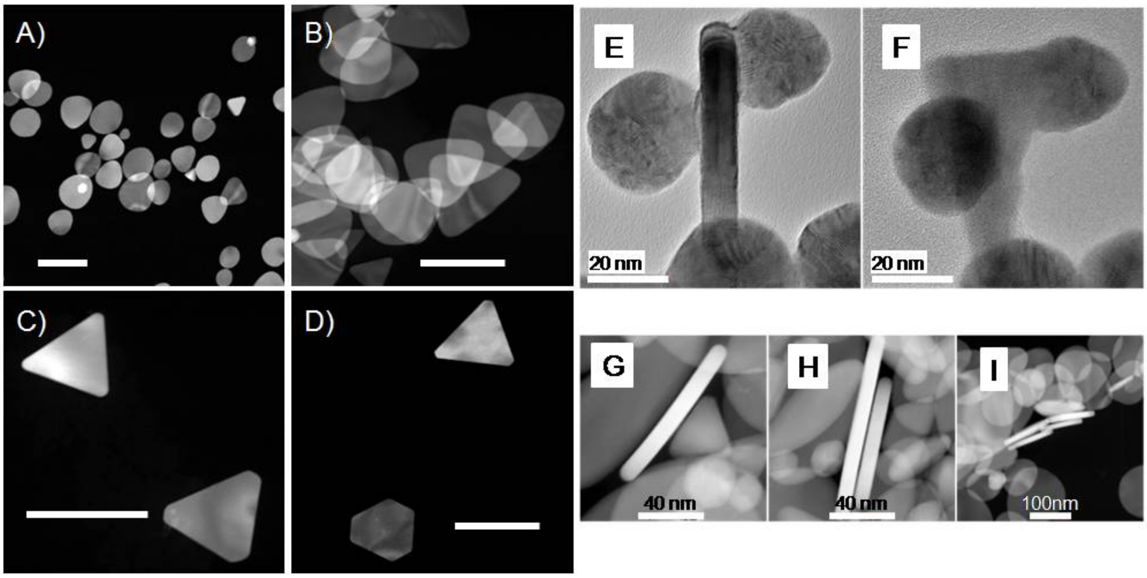

Figure 6.24. *Selected STEM images of each reported NN, i.e. A) 0.2x, B) 0.3x, C) 0.4x and D) 0.5x. Scale bars are 200 nm in all panels. HR-TEM images of (E) the side view of a NN and (F) the corresponding image of the tilted specimen showing the prismatic morphology of the NP. HR-STEM images of selected samples (G, H and I) where the flat shape and constant thickness of NNs is apparent.*

Furthermore, EELS thickness analysis indicated that a uniform thickness of approximately 9 nm is conserved among different preparations. This is supported by the STEM-HAADF images, where contrast uniformity in flat NNs indicates the same thickness. Different EELS thickness maps (Figure 6.25) measure the sample thickness homogeneity in the reported samples.

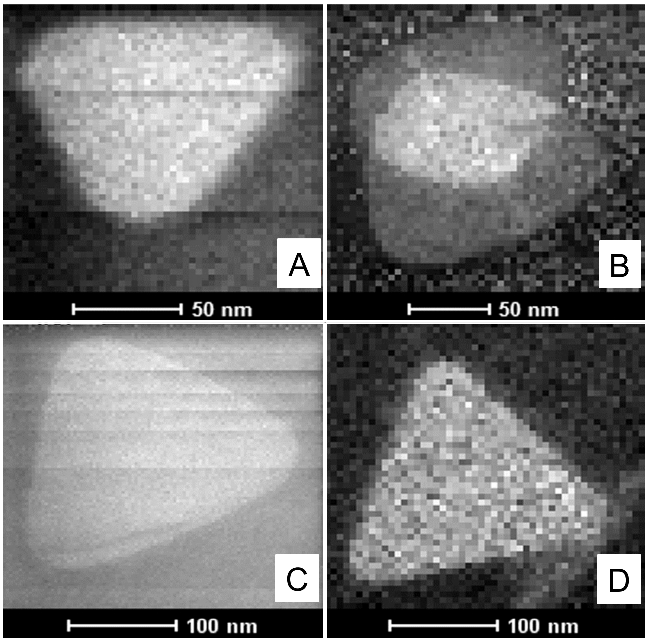

Figure 6.25. *EELS thickness map of each reported NN, i.e. A) 0.2x, B) 0.3x, C) 0.4x and D) 0.5x.*

Figure 6.26 show a tomographic reconstruction of a series of group of NPs where the flat morphology of NNs is further corroborated.

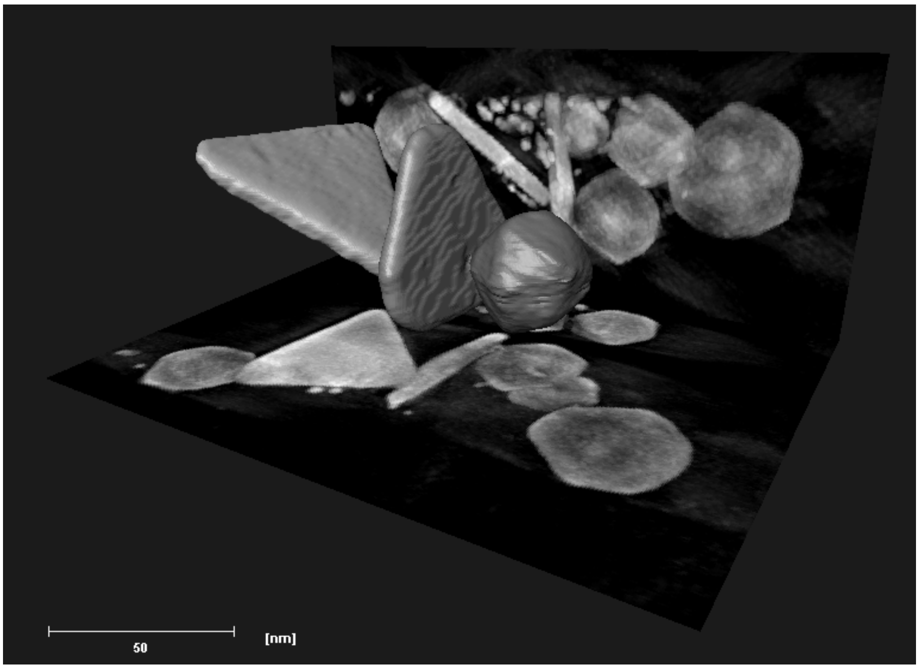

Figure 6.26. *Tomographic reconstruction of NNs sample.*

6.8. Conclusions

This work provided a straightforward and novel method to produce single crystal Au nanoprisms (NanoNachos (NNs)), in water at room temperature. The edge length and LSPR band of NNs can be tuned along the NIR range by simply adjusting the concentration/molar ratio of gold salt and reducing agent, meaning that a variety of NNs sizes can be accessed synthetically enabling tailoring for specific purposes. The synthetic method to produce NIR NNs was built upon the original work of Zhou *et al.*; over the past two decades, many independent groups have claimed that the nature of the NIR absorption band is related to the core@shell structure of Au_2S@Au nanoshells. However, the results presented here, such as XPS analysis, UV-Vis-NIR spectroscopy and electron microscopy, demonstrate that the NIR band which display the NPs produced by the method of Zhou *et al.* is due to the anisotropic structure of Au nanoprisms (or NNs). Importantly, this synthetic method avoids the use of toxic surfactants such as CTAB, the most widely used surfactant for the synthesis of gold nanorods and nanoprisms. Avoiding the use of toxic surfactants greatly simplifies the functionalization and application of NPs for bio-purposes since extensive purification or complex ligand exchange methods are not required.

The NPs produced by the synthetic method proposed here were derivatized with HS-PEG-COOH to increase their colloidal stability (NPs@PEG) over time and harsh chemical environments (such as those required for derivatization with other molecules). The increased colloidal stability allowed washing the NPs by centrifugation (centrifuged twice for 15 min at 10000 rpm and resuspending pellets in MilliQ water); prior to PEGylation, centrifugation aggregated the NPs irreversibly. Furthermore, NNs@PEG could be separated from other by-products by gel electrophoresis. Due to the increased electrophoretical mobility of NPs other than NNs, *i.e.* polyhedral Au-NPs, two bands were resolved in the gel.

The purified products were characterized extensively by electron microscopy (SEM, TEM, STEM and EELS); results demonstrated conclusively the flat morphology of NNs (*ca.* 9 nm thick) which is conserved among different samples. The crystal structure of NNs (top and edge facets) was also studied by aberration corrected HRTEM. The analysis of the digital diffractogram of a single NN showed a hexagonal–shaped pattern that is characteristic of the [1 1 1] orientation of a *fcc* Au single crystal; in addition, the diffraction pattern exhibited a set of weak spots indexed as 1/3 {4 2 2} which have been linked to the combination of twin planes and [1 1 1] stacking faults.

REFERENCES

(1) Nikoobakht, B.; El-Sayed, M. A.: Preparation and Growth Mechanism of Gold Nanorods (NRs) Using Seed-Mediated Growth Method. *Chemistry of Materials* **2003**, *15*, 1957-1962.

(2) Sau, T. K.; Murphy, C. J.: Room Temperature, High-Yield Synthesis of Multiple Shapes of Gold Nanoparticles in Aqueous Solution. *Journal of the American Chemical Society* **2004**, *126*, 8648-8649.

(3) Millstone, J. E.; Métraux, G. S.; Mirkin, C. A.: Controlling the Edge Length of Gold Nanoprisms via a Seed-Mediated Approach. *Advanced Functional Materials* **2006**, *16*, 1209-1214.

(4) Millstone, J. E.; Park, S.; Shuford, K. L.; Qin, L.; Schatz, G. C.; Mirkin, C. A.: Observation of a Quadrupole Plasmon Mode for a Colloidal Solution of Gold Nanoprisms. *Journal of the American Chemical Society* **2005**, *127*, 5312-5313.

(5) Alkilany, A.; Murphy, C.: Toxicity and cellular uptake of gold nanoparticles: what we have learned so far? *Journal of Nanoparticle Research* **2010**, *12*, 2313-2333.

(6) Alkilany, A. M.; Nagaria, P. K.; Hexel, C. R.; Shaw, T. J.; Murphy, C. J.; Wyatt, M. D.: Cellular Uptake and Cytotoxicity of Gold Nanorods: Molecular Origin of Cytotoxicity and Surface Effects. *Small* **2009**, *5*, 701-708.

(7) Takahashi, H.; Niidome, Y.; Niidome, T.; Kaneko, K.; Kawasaki, H.; Yamada, S.: Modification of Gold Nanorods Using Phosphatidylcholine to Reduce Cytotoxicity. *Langmuir* **2005**, *22*, 2-5.

(8) Yu, C.; Varghese, L.; Irudayaraj, J.: Surface Modification of Cetyltrimethylammonium Bromide-Capped Gold Nanorods to Make Molecular Probes. *Langmuir* **2007**, *23*, 9114-9119.

(9) Leonov, A. P.; Zheng, J.; Clogston, J. D.; Stern, S. T.; Patri, A. K.; Wei, A.: Detoxification of Gold Nanorods by Treatment with Polystyrenesulfonate. *ACS Nano* **2008**, *2*, 2481-2488.

(10) Huschka, R.; Neumann, O.; Barhoumi, A.; Halas, N. J.: Visualizing Light-Triggered Release of Molecules Inside Living Cells. *Nano Letters*, *10*, 4117-4122.

(11) Huschka, R.; Zuloaga, J.; Knight, M. W.; Brown, L. V.; Nordlander, P.; Halas, N. J.: Light-Induced Release of DNA from Gold Nanoparticles: Nanoshells and Nanorods. *Journal of the American Chemical Society* **2011**, *133*, 12247-12255.

(12) Jana, N. R.; Gearheart, L.; Murphy, C. J.: Wet chemical synthesis of high aspect ratio cylindrical gold nanorods. *Journal of Physical Chemistry B* **2001**, *105*, 4065-4067.

(13) Oldenburg, S. J.; Averitt, R. D.; Westcott, S. L.; Halas, N. J.: Nanoengineering of optical resonances. *Chemical Physics Letters* **1998**, *288*, 243-247.

(14) Jana, N. R.; Gearheart, L.; Murphy, C. J.: Seed-Mediated Growth Approach for Shape-Controlled Synthesis of Spheroidal and Rod-like Gold Nanoparticles Using a Surfactant Template. *Advanced Materials* **2001**, *13*, 1389-1393.

(15) Zhou, H. S.; Honma, I.; Komiyama, H.; Haus, J. W.: CONTROLLED SYNTHESIS AND QUANTUM-SIZE EFFECT IN GOLD-COATED NANOPARTICLES. *Physical Review B* **1994**, *50*, 12052-12056.

(16) Averitt, R. D.; Sarkar, D.; Halas, N. J.: Plasmon resonance shifts of Au-coated Au2S nanoshells: Insight into multicomponent nanoparticle growth. *Physical Review Letters* **1997**, *78*, 4217-4220.

(17) Diao, J. J.; Chen, H.: Near infrared surface plasmon resonance of gold tabular nanostructures in the HAuCl4-Na2S reaction. *Journal of Chemical Physics* **2006**, *124*.

(18) Schwartzberg, A. M.; Grant, C. D.; van Buuren, T.; Zhang, J. Z.: Reduction of HAuCl(4) by Na(2)S revisited: The case for Au nanoparticle aggregates and against Au(2)S/Au Core/Shell particles. *J. Phys. Chem. C* **2007**, *111*, 8892-8901.

(19) Mikhlin, Y.; Likhatski, M.; Karacharov, A.; Zaikovski, V.; Krylov, A.: Formation of gold and gold sulfide nanoparticles and mesoscale intermediate structures in the reactions of aqueous HAuCl(4) with sulfide and citrate ions. *Physical Chemistry Chemical Physics* **2009**, *11*, 5445-5454.

(20) Xia, Y. N.; Xiong, Y. J.; Lim, B.; Skrabalak, S. E.: Shape-Controlled Synthesis of Metal Nanocrystals: Simple Chemistry Meets Complex Physics? *Angewandte Chemie-International Edition* **2009**, *48*, 60-103.

(21) Tao, A. R.; Habas, S.; Yang, P.: Shape Control of Colloidal Metal Nanocrystals. *Small* **2008**, *4*, 310-325.

(22) Sajanlal, P. R.; Sreeprasad, T. S.; Samal, A. K.; Pradeep, T.: Anisotropic nanomaterials: structure, growth, assembly, and functions. *Nano Reviews* **2011**, *2*.

(23) Chen, H. M.; Liu, R.-S.; Tsai, D. P.: A Versatile Route to the Controlled Synthesis of Gold Nanostructures. *Crystal Growth & Design* **2009**, *9*, 2079-2087.

(24) Sun, Y. G.; Mayers, B.; Xia, Y. N.: Transformation of silver nanospheres into nanobelts and triangular nanoplates through a thermal process. *Nano Letters* **2003**, *3*, 675-679.

(25) Love, J. C.; Estroff, L. A.; Kriebel, J. K.; Nuzzo, R. G.; Whitesides, G. M.: Self-assembled monolayers of thiolates on metals as a form of nanotechnology. *Chemical Reviews* **2005**, *105*, 1103-1169.

(26) Malikova, N.; Pastoriza-Santos, I.; Schierhorn, M.; Kotov, N. A.; Liz-MarzÃ¡n, L. M.: Layer-by-Layer Assembled Mixed Spherical and Planar Gold Nanoparticles:â€‰ Control of Interparticle Interactions. *Langmuir* **2002**, *18*, 3694-3697.

(27) Germain, V.; Li, J.; Ingert, D.; Wang, Z. L.; Pileni, M. P.: Stacking Faults in Formation of Silver Nanodisks. *The Journal of Physical Chemistry B* **2003**, *107*, 8717-8720.

(28) Lofton, C.; Sigmund, W.: Mechanisms Controlling Crystal Habits of Gold and Silver Colloids. *Advanced Functional Materials* **2005**, *15*, 1197-1208.

NanoNachos as NanoHeaters

Chapter 7

In this chapter the conceptual bases of optical hyperthermia (NIR-light driven heating of anisotropic GNPs) and their bioapplications will be discussed. Due its high NIR-absorption band, NNs under NIR illumination matching their plasmon band are expected to behave as excellent nanoheaters. The potential of NNs as photon-to-heat transducers will be evaluated both at macroscopic and molecular level. Concerning the morphologies changes following laser illumination, as reported for other anisotropic GNPs,[1-5] reshaping of NNs under laser irradiation will be also addressed in the following.

7.1. Optical hyperthermia and photothermal therapy (PTT)

Optical properties of GNPs have been studied over the past centuries intensively; recently, the ability of plasmonic NPs to drive photon-to-heat conversion has attracted much attention, in bioapplications specially. In this context, the therapeutic application of heat generated following light absorption of NPs (typically anisotropic GNPs) is usually referred to as optical hyperthermia; the most relevant application is photothermal therapy (PTT) for cancer treatment.[6] The potential of this application resides in the transparency of biological tissues in the so called NIR-biological window where NIR light exhibits suitable penetration depths (Figure 7.1.).

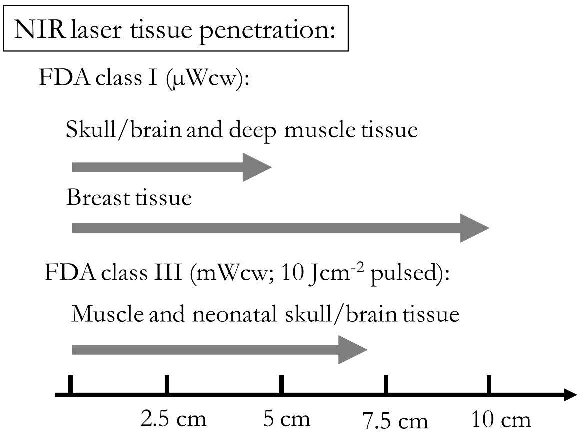

Figure 7.1. *NIR-laser irradiation depth penetrability for medical uses in different tissues. (Adapted from El-Sayed).*[7]

In general, metallic nanoparticles exhibit very low optical quantum yield and high absorption coefficients.[8] Parameters such as fluence of the light source, GNPs type and the nature of the surrounding media can greatly modulate the thermophysical response of GNPs under illumination. During GNPs laser irradiation, energy is transferred from the light source (photons) to GNPs; this energy (photons) can be absorbed or scattered. In general, light can be (i) absorbed by GNPs and/or (ii) re-emitted by the particle at same frequency (Rayleigh scattering, an elastic process) or at shifted frequency (Raman scattering, inelastic process).[9] When light interacts with metallic particles, the incoming electromagnetic field induces oscillations in the electronic cloud (mobile electrons) of the particle. If the frequency of the incident light is close to that of the collective resonance (LSPR) of the mobile electrons of the NP, this interaction will ultimately lead to heating. At the nano-scale, heat generation involves a cascade of processes as shown in Figure 7.2.[10,11] When photons from the light source excite mobile electrons from GNPs, these electrons jump to an excited energy state. As the energy of excited electrons is higher than that of the lattice energy (or temperature), electron-phonon interaction processes drives an energy transfer. This process is known as electron-phonon relaxation which is in the time scale of picoseconds. Ultimately, the energy of phonons is dissipated with the surrounding media by phonon-phonon scattering. This process strongly depends on the size and shape of GNPs.[12]

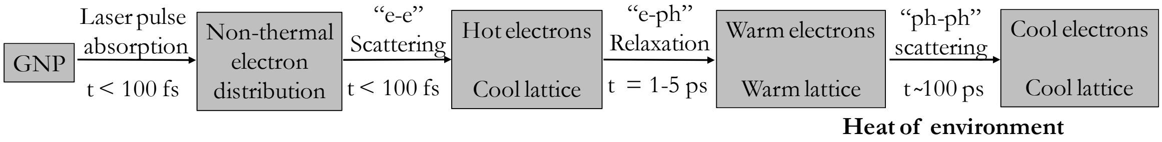

Figure 7.2. *Scheme of process and time of each produce when a laser interact with the LSRP of a GNP to produce heating; e and ph stand for electron and phonon, respectively (adapted from Pelton).*[13]

Analogously as for magnetic nanoparticles but in the context of optical hyperthermia, the evaluation of the heating ability of GNPs can be also defined by a parameter typically referred to as specific absorption rate (SAR). The experimental expression of SAR is given by equation 7.1,

$$\mathrm{SAR} = \mathrm{C}\rho_{\mathrm{medium}}\left(\frac{\Delta \mathrm{T}}{\Delta \mathrm{t}}\right)_{\mathrm{initial}} \qquad (7.1)$$

where the experimental value of $(\Delta \mathrm{T}/\Delta \mathrm{t})_{\mathrm{initial}}$ is calculated by performing a linear fit of the hyperthermia data (temperature versus time) in the initial time interval, t

= [1-10] s; C and ρ_{medium} are the NPs concentration and the density of the surrounding media, respectively.[9]

On the other hand, the theoretically SAR value can be defined as given in the following expression (equation 7.2):

$$\mathrm{SAR} = \mathrm{N}.\,\mathrm{Q_{nano}} = \mathrm{N}.\,\mathrm{C_{abs}}.\,\mathrm{I} = \mu_a.\,\mathrm{I} \qquad (7.2)$$

where N is defined as the number of nanoparticles per m^3 and Q_{nano} is the heat generated by each nanoparticle under laser light; Q_{nano} can be expressed as the product of the absorption cross-section area of each NP (C_{abs}) and the power density (I given in W/m^2); μ_a represents the simultaneous absorption of light of a group N of NPs under laser irradiation.

In this equation (7.2), there are factors which are difficult to estimate experimentally; first, the actual absorption and scattering of light by each NP depends on the shape and size of the particle; second, the local laser fluence is a complex function of the laser and the composition of the media where NPs are embedded. Additionally, this can be greatly complicated when working media is a cell or tissue.[9]

The heating profile of one particle and its temperature decay with distance, have been evaluated using different models.[14-16] The temperature of a NP decays quickly from the NP surface (Figure 7.3.).[17]

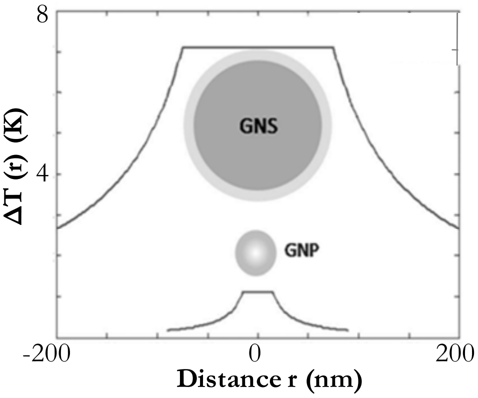

Figure 7.3. *Calculation of temperature profile of two different types of NPs, i.e. gold nanoshells of 150 nm (GNS) and a GNP of 30 nm (adapted from Bischof).*[9,17]

Some theoretical studies have shown that heat generation depends strongly on the NP shape which ultimately is related to the magnitude of the surface plasmon band of NPs. For instance, for systems (of the same material) occupying the same volume, the sphere was founded to be the less effective heating shape.[12,18] Shapes exhibiting red-shifted plasmon bands are more efficient to produce heat; for instance, nanorods are 60% more efficient nanoheaters than spherical NPs (Figure 7.4-a).

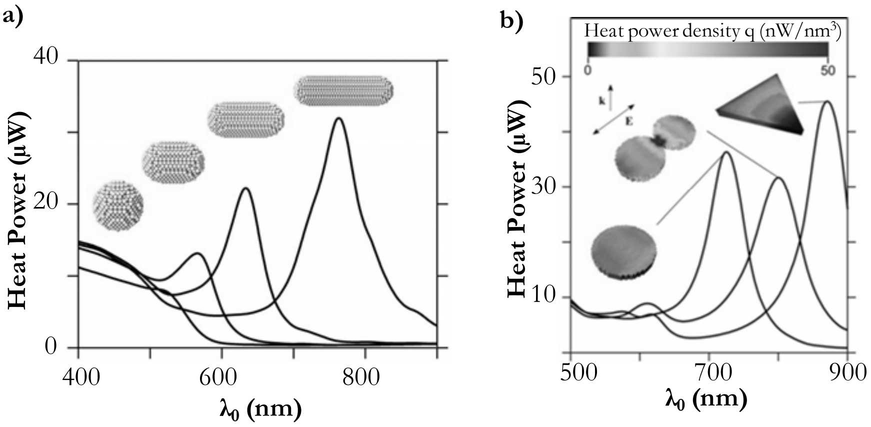

Figure 7.4. Theoretical calculation of heating power from different structures with the same volume; (a) comparison of a sphere and different-length rods; (b) comparison of a disk, two adjacent disks and a tabular nanoprisms. (adapted from Baffou).[12]

Another theoretical work compares different planar structures with same volume (Figure7.4-b); they found that the presence of sharp and edges promote heat generation, although nanoparticle temperature is equal in all its surface due the good gold conductivity.[12] This profile of heat generation indicates that NNs (tabular nanoprisms) are very suitable candidates to photothermal therapy and reveal that for instance, two small adjacent nanodisks instead one (of the same volume) is not an advantage in terms of heat production although their plasmon band is red-shifted relative to that of the two adjacent nanodisks.

Recently, Bartczak *et al.* reported on a theoretical/experimental work where they evaluated the effect of laser irradiation on a single NP and compared it to the cumulative heating of a group of cells containing different kinds of GNPs (Figure 7.5);[19] they studied the heating ability of a gold sphere of 15 nm (SP), a core@shell silica@gold NP (CR) of 43 nm (core) and 7 nm (shell), a nanorod (NR) of 47 nm (length) × 17 nm (thickness), and a hollow sphere of 91 nm and a shell of 9 nm (HG). The laser power density selected in this work was 30 W/cm^2, which correspond with mild hyperthermia conditions typically used in this kind of experiment.[20]

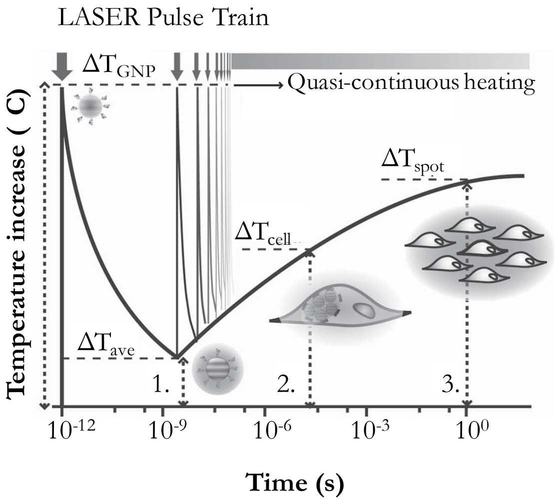

Figure 7.5. *Representation of time scales in nanoparticle heating (1), single-cell heating (2) and an area of illumination containing several cells (3) (adapted from Bartczak).*[19]

Bartczak *et al.* argued that the temperature in a single-particle irradiated by a laser pulse train decays rapidly, only a low average temperature remains (ΔT_{ave}); the average temperature is several orders of magnitude smaller than the peak of heat generated by only one laser pulse train (Figure 7.6(a) and (b)).

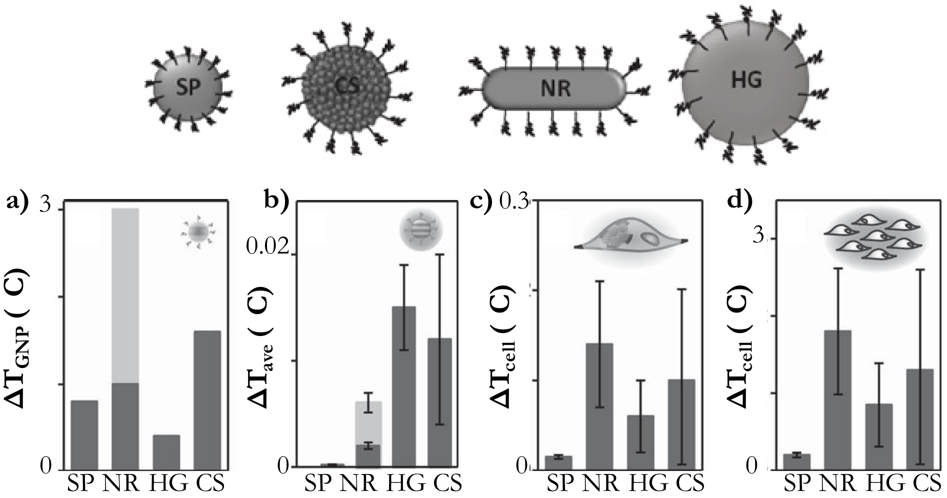

Figure 7.6. *Representation of temperature increment in different types of GNPs in a) single-NP irradiated by a laser pulse train; b) residual temperature after single NPs laser-pulse irradiation; c) temperature increment under a quasi-continuous laser irradiation of a cell filled with GNPs; and d) temperature increment in a group of cells containing NPs after quasi-continuous irradiation. For the gold NRs, two temperatures are shown corresponding to random polarization of the incident light (dark grey bar) and polarization parallel to the NR long-axis (light gray bar) (adapted from Bartczak).*[19]

Their results showed that the heating ability, as previously explained, depends of the NP absorption cross-section; in the case of cells, the laser pulse train excitation is replaced by a quasi-continue irradiation as it happens in a larger time-length scale. Based on their theoretical predictions, the authors claim that temperature generated in one cell containing NPs could only rises up to a small fraction of degree which is not enough to explain their experimental results. However, they predict increments of few degrees when the irradiated area includes a group of NP-containing cells; this increment would be enough to damage cells (Figure 7.6 (c) and (d)).[19]

Other works have studied the behavior of GNPs solutions under laser irradiation. This experiments used different approaches such as drops[17] or cuvettes with magnetic stirring in a vacuum chamber,[21] or not.[22] In general, an energy balance is proposed in these studies; the system has to reach the steady state under laser illumination in order to evaluate the photothermal conversion process and determine the photothermal conversion efficiency.[23] This energy balance is expressed in Equation 7.3 as follows,

$$\left(m_s c_{p,s} + m_c c_{p,c}\right)\frac{d\Delta T}{dt} = Q_{laser} - Q_{loss} \tag{7.3}$$

where m_s is the mass of the solution; $c_{p,s}$ is the constant-pressure heat capacity of the solution (of value 4.187 J $g^{-1}K^{-1}$ for aqueous solutions); m_c is the mass of the recipient; $c_{p,c}$ corresponds to the heat capacity of the recipient material (in the case of a quartz cuvette, it is 0.839 Jg^{-1} K^{-1}); ΔT is the increment of temperature obtained in a time t; Q_{laser} is the energy from the laser, and Q_{loss} is the energy dissipated to the surrounding environment. Chen *et al.* used this expression to predict temperature increments of solutions of GNRs under illumination at their longitudinal plasmon band. Experimentally, they found that a solution of GNRs under illumination can reach temperatures up to ca. 75 °C in 30 minutes at the selected concentration where the solution exhibited an absorbance peak of 2 OD at their plasmon band. Their theoretical calculations confirmed this result.[22] They also calculated theoretical curves of heating over time and compared them with experimental results using GNRs with different longitudinal plasmon bands. Equilibrium temperatures reached by solutions of GNRs with different longitudinal plasmon bands in the range of 760-860 nm differed less than 5 °C when illuminated by a 809 nm laser.[22] In this very same work, the aggregation state of GNPs was also proven to influence in the process of heat generation; this can be easily correlated with the plasmon band change expected when aggregation occurs. Spherical and rods were aggregated selectively and irradiated by a 809 nm laser; spherical GNPs aggregation leaded to an enhancement on heat generation due to the plasmon band shift towards the wavelength of the laser. On the other hand, GNRs aggregation translated into a decrease on the absorption at 809 nm and consequently, a decrease of heat generation was observed.[22]

Works addressing the heating ability of GNPs agree on the exponential tendency of temperature variation over time when solutions are irradiated; the cooling behavior has been also found to present a tendency typical of an exponential decay.[21-23]

Due to the different length-scale of different systems (single NP, group of NPs, NPs contained in a cell, etc.), it is possible to make a classification of the bioapplications of GNPs concerning their heating ability (Table 7.1.).

Scale	Interacting bio-system	Example applications
Nano	Biomolecules	Nanoscale membrane melting[24-26]
		Ultrafast DNA melting assay[27]
		Drug release from GNP[27-29]
		Selective protein denaturation[30]
		Sub-wave-length molecular surgery[31]
Micro	Cells	Transmembrane drug delivery[32]
		Liposome/endosomal release[33]
		Single cell ablation[34,35]
Macro	Organs/Tissues	Photothermal Therapy (PTT)[36]
		Photothermal enhancement of drug targeting[37]
		Photothermal enhancement of drug release[38,39]
		Photothermal enhancement of radiation therapy[40]
		GNP preconditioning for enhanced thermal therapy

***Table 7.1.** Bioapplications of laser-GNPs interactions (adapted from Bischof)*[9]

The major goal of this chapter is to study the efficiency as light-to-heat transducers of NNs. For such proposal, different PEGylated NNs will be irradiated with two different light sources (809 nm and 1064 nm). The ability of different solutions of NNs to produce macroscopic heating will be addressed. In addition, the heating of NNs at the biomolecular level will be evaluated indirectly through conformational changes experienced by a temperature-sensitive molecule, an enzyme. Changes on the enzymatic activity will be related to the temperature on NNs surface. Finally, the potential reshaping of NNs after irradiation will be studied; this effect have been widely reported for other anisotropic GNPs such as GNRs and GNSs.[4,41]

7.2. Global heating of NNs solutions

Two DPSSL (Diode-pump solid-state laser) systems (809 nm and 1064 nm sources) were used to irradiate samples (Figure 7.7).Two systems were used due the equipment availability. 809 nm will be the same laser wavelength that will be use at single-cell experiments exposed in chapter 7, the source available at Philipps-University of Marburg (Prof. Parak). 1064 nm-laser corresponds with the source available in our investigation group (Dr. de la Fuente). Evaluation of macroscopic heating of NNs was carried out using different solutions of PEGylated NNs; these solutions exhibited plasmon bands at 850 nm (sample NNs^{850}, *ca.* 120 nm) and 1050 nm (sample NNs^{1050}, *ca.* 150 nm) ,as shown in Figure 7.8 (a) and (b) respectively, to maximized the light absorption for each system.

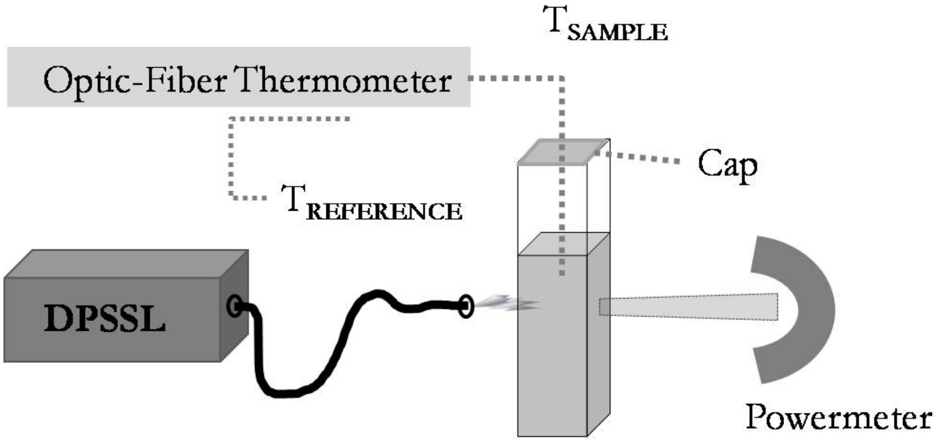

Figure 7.7. *Scheme of the setup used for the irradiation experiments.*

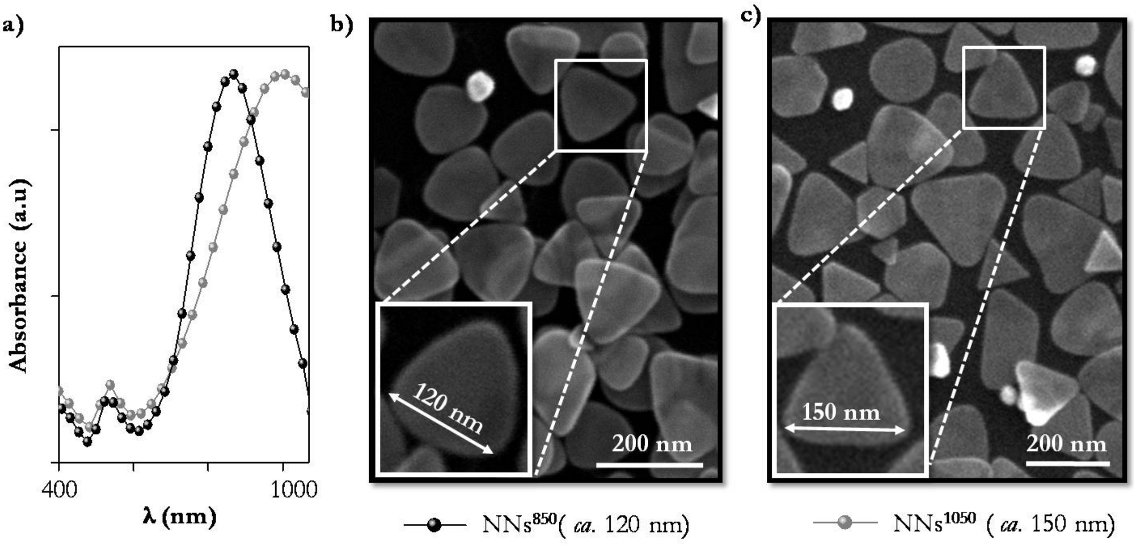

Figure 7.8. *a) UV-Vis absorption spectra of NNs^{850} and NNs^{1050}; SEM images from b) NNs^{850} and c) NNs^{1050}.*

809nm DPSSL system

Solutions of NNs (0.5 mL) were irradiated during 2 minutes with an 809 nm laser coupled to an optic fiber (multimode) using 1.3 W to yield a power density of *ca.* 10 W×cm^{-2} (illumination spot of *ca.* 0.4 cm). Temperature was monitored in real time by a thermocouple immersed in the solution and placed at *ca.* 0.4 cm away from the beam spot. As control, a sample containing just water was measured in similar conditions showing a residual heating; this was subtracted in all the following temperature over time plots. As expected based on theoretical premises, sample NNs^{850} heated more efficiently than NNs^{1050}; Figure 7.9 (c) and (d) show plots of temperature over time at various concentrations of samples NNs^{850}and NNs^{1050}, respectively. These values confirm that NNs have a great potential as light-to-heat converters. For sample NNs^{850}, temperature rises up to ca. 70°C when using 0.1 mg/ml (2.5 O.D. of absorbance, *ca.* 36 pM); this increment occurs in 2 minutes which translates into a temperature rate of about 22°C/min; analogously, NNs^{1050} rises up to 55°C at a concentration is 0.1 mg/mL (2.5 O.D., *ca.* 31 pM) and the temperature rate is 14°C/min in this case (Figure 7.9(b)).

The differences in terms of heating efficiency observed between samples are consistent with the different amount of energy expected to be absorbed by the two samples. Best NNs in terms of heating are those which LSPR maximum is closer to the laser wavelength;[22] therefore, NNs^{850} are more appropriate for the light source (809 nm) used since it almost matched the maximum of the plasmon band of sample NNs^{850}. Also as it was expected, the heat generation rate grows as the concentration does; at low values of concentration, the heating behavior of NNs^{1050} and NNs^{850} were very similar; this is most probably motivated by the very low absorption rate at these conditions. (Figure 7.9(b)).

In all the temperature curves, the exponential tendency is apparent (Figure 7.9(c) and (d)); saturation temperature was not reached in any case since the laser was turned off before reaching the equilibrium.

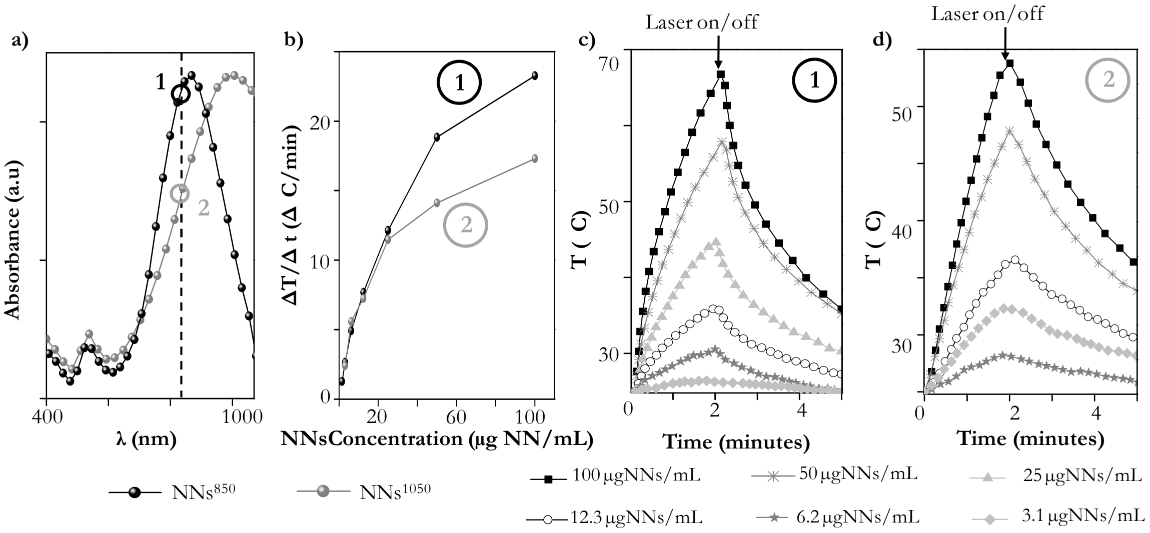

Figure 7.9. a)Absorption Spectra of NNs, NNs^{850}& NNs^{1050}, solutions where the dotted line indicates the laser wavelength (809 nm). b) Heating rate during laser irradiation. Heating and cooling curves for different concentrations for c) NNs^{850}and d) NNs^{1050}.

1064 nm DPSSL system

Solutions of NNs^{1050} were also heated with a 1064 nm source coupled to an optic fiber (monomode TE$_{00}$) using a power density of 50 W×cm^{-2} (illumination spot of ca. 0.2 cm). In this case a 1 mL cuvette was used and NNs solutions were heated during 10 minutes which allows for reaching saturation, *i.e.* steady state where temperature is close to a temperature plateau (ca. thermal equilibrium). In the first seconds of irradiation, the temperature increases rapidly; after approximately for 2 minutes, temperature increased more slowly indicating that the thermal equilibrium was closer (Figure 7.10).

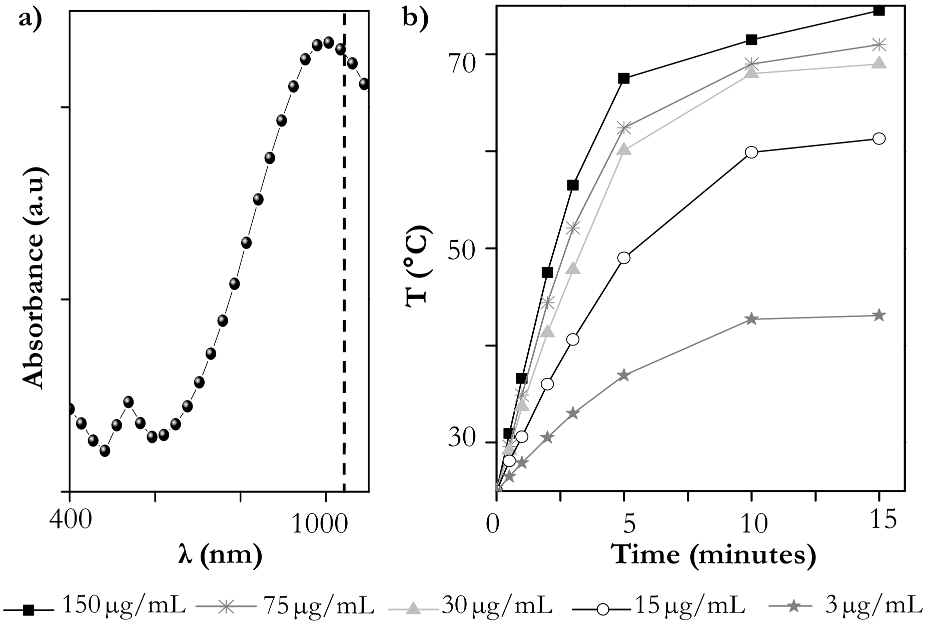

Figure 7.10. *NNs^{1050} solution: a) absorption spectra with a dot line indicating laser irradiation wavelength. b) Heat generation curves of different concentration of NNs^{1050}.*

The evaluation and comparison of the heating ability of NNs as well as other NPs such GNRs or GNSs are very challenging tasks as there are many variable parameters playing a role, *i.e.* the setup used, stability of NPs, the laser source, etc. For instance, taken together the data concerning to the heating ability of NNs^{1050} under illumination with the 809 nm (Figure 7.9 (d)) and 1064 nm (Figure 7.10 (b)) DPSSL systems indicates that both results are not easily comparable; for equal concentrations of NNs^{1050}, the global heating observed is not the same (Figure 7.11).

Dashed lines in Figure 7.11 (a) indicate the irradiation wavelengths for both systems (overlapped with the spectra of NNs^{1050}); NNs^{1050} should heat more efficiently since their plasmon band is closer to 1064 nm than 809 nm. However, the heating rate of both systems seem to indicate the contrary (Figure 7.11 (b); this is probably due to the different heat losses which are dependent on the set up and more importantly, the fibers used irradiation are different; for the 809 nm system, the irradiation spot had a diameter of *ca.* 0.4 cm whereas for the 1064 nm system, it was *ca.* 0.2 cm which resulted in a greater power density (50 W×cm^{-2} compared to 10 W×cm^{-2}) with the cost of irradiating less NNs simultaneously (Figure 7.11 (b)) and consequently, less number of NNs were producing heat simultaneously.

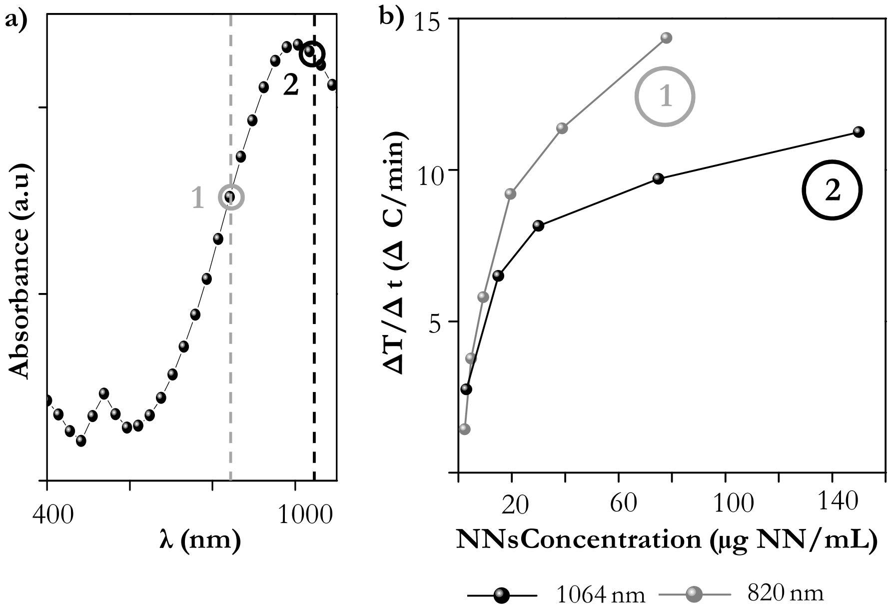

Figure 7.11. *a) NNs^{1050} solution spectra with a call for laser irrradiation region (1) 809 nm laser and (2) 1064 nm laser; b) Comparison of heating speed of different concentration of NNs^{1050} with both lasers.*

In literature, one can find some equivalent works where GNPs solutions were evaluated in terms of heating ability following laser irradiation. Chen and coworkers observed a temperature increase up to 76°C (equivalent to ours) following 30 minutes irradiation of a GNRs solution (peak of 2 OD in the longitudinal resonance). The temperature plateau (steady-state) was reached after 15 minutes irradiation; they used a CW (continuous wave) diode laser of 809 nm (8.75 W/cm^2).[22] Similar experiments where the solution was kept under high vacuum (to minimize heat losses) has been reported;[21,23] Roper *et al.* measured the temperature increment in an isolated micro-volume (≤10 μL) containing spherical GNPs (190 pM) following laser irradiation; they used a 514 nm laser modulated by a 6000 rpm chopper) to deliver a power density of 2.4 W/cm^2; the maximum temperature increment observed was of 2.2°C in 320 s which translates into a temperature increment rate of ca. 0.41 °C/min. In another similar work, Halas and coworkers evaluated the heating ability of solutions of GNRs, gold silica nanoshells and gold@gold-sulfide nanoshells. It should be noticed that the gold@gold-sulfide nanoshells were obtained using an experimental protocol ($HAuCl_4$ reduced by $Na_2S_2O_3$) very similar to the one used, and previously described in Chapter 6, to obtain NNs; therefore, it is mandatory to compare the heating efficiency they report with ours since actually, we present conclusive results that supports that the product of the reduction of $HAuCl_4$ by $Na_2S_2O_3$ are

NNs instead of nanoshells. Halas and coworkers used a 815 nm light source (incident power of ca. 160 mW but sadly, unknown power density) to irradiate sample solutions (2.5 mL) with equivalent absorption features at 815 nm; to get equivalent absorptions the GNPs concentrations were dilute accordingly, *i.e.* 3 pM for SiO_2@Au, 100 pM for Au@Au_2S and 300 pM for gold nanorods.[21] After 40 minutes illumination, solutions of SiO_2@Au, Au@Au_2S and gold nanorods experienced a increment of temperature of 2ºC, 3.5ºC and 3°C, respectively. In principle, the 300 pM solution of Au@Au_2S is "equivalent" to the 125 μg/mL solution of NNs; however, the temperature of NNs (NNs^{850}) experienced a increment of *ca.* 20ºC following 2 minutes irradiation (*ca.* 10 W/cm^2); this notable difference in terms of heating ability can be partly explained by the different power densities used (note that for Cole et al., this data is missing). Nevertheless, the absorption spectra of NNs present a NIR band much higher than the Au/Au_2S structures which seems to present a great content of spherical GNPs (this is speculative argument based on the spectra they reported).

Summarizing, the feasibility of NNs as nanoheaters under NIR illumination was proven in solution. Comparison between the heating ability of NNs and other nanoheaters indicates that NNs may represent an improved structure which definitely should be add to the pool of nanoheaters as a versatile alternative which do not require challenging synthetic methods or laborious extensive ligand exchange to remove the highly toxic CTAB surfactant.

Morphology analysis of NNs following laser illumination

In literature since 1999,[1] several studies have been reported regarding the reshaping or fragmentation of GNRs in solution, in solid or embedded in a PVP film following laser irradiation.[5] Reshaping processes were studied by changes in absorption spectra of the particles and by TEM analysis. GNRs can be transformed into spheres with the same volume that the initial GNRs if the energy absorbed following irradiation is sufficiently high (above a certain energy threshold); in contrast, if the energy is below this threshold, GNRs achieve a transition state where one can find wider and shorter rods relative to the original ones.[1,42] GNRs disruption was also described;[2] this phenomena was been also observed in the case of gold spheres.[43,44] Silica and gold GNSs are susceptible also to suffer disruptions of their core-shell structure. As function of the regime or the laser power density, different levels of morphology transformation can be observed, reaching even the silica core deformation. As in the GNRs case, this changes were observable by absorption spectra and under TEM observation.[4]

Therefore, it is mandatory to evaluate possible morphology changes following laser irradiation. Spectra of NNs (sample NNs^{850} & 1050-NNs) remained the same before and after irradiation in all the cases presented so far; Figure 7.12 (a) & (b) shows these spectra where aqueous solutions (1 mg/ml) containing samples of NNs^{850} & NNs^{1050} were irradiated for 15 minutes with the 810 nm & 1064 nm laser sources, respectively. These results indicated that neither dramatic morphology changes nor aggregation issues are driven by laser irradiation in the conditions used in the present work.

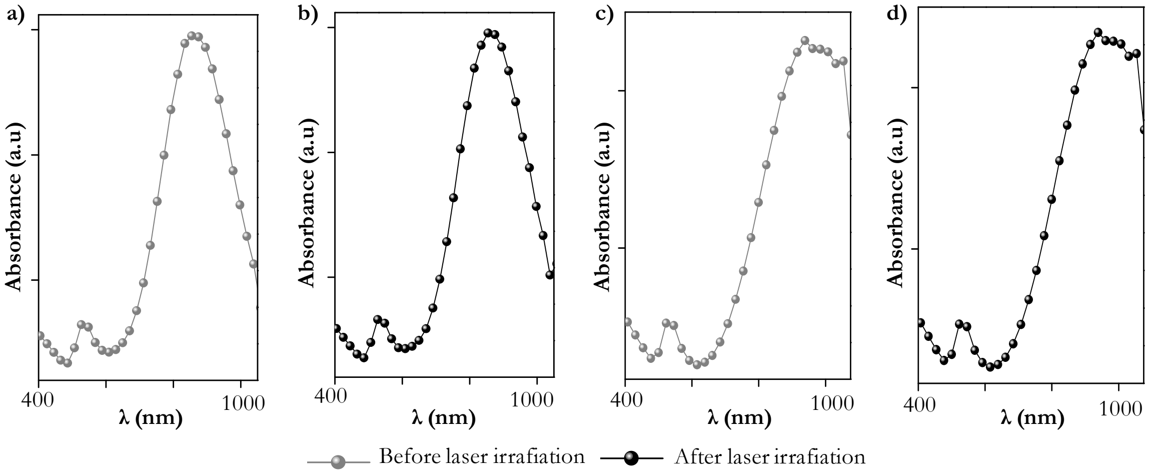

Figure 7.12. *a) and b) NNs^{850} absorption spectra after and before laser irradiation,respectively and c) and d) for NNs^{1050}.*

SEM analysis following laser irradiation was used in selected samples to confirm the absence of morphology changes driven by laser irradiation. The SEM sample was inspected in its totally looking after apparent morphology changes; as shown in Figure 7.13 (b), the morphology and size of NNs (sample NNs^{1050}) remained intact after laser irradiation with the 1064 nm laser system.

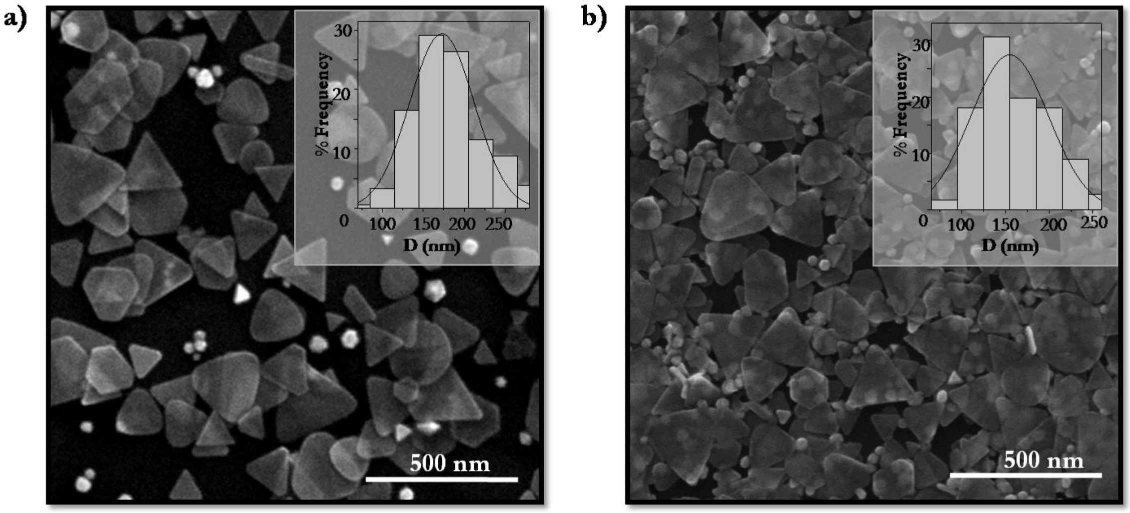

Figure 7.13. *SEM images from a) NNs before laser exposure and b) NNs after laser exposure.*

Nevertheless, morphology changes could appear due to a dramatic increase of temperature which can be the case in very concentrated samples or even dried samples. To study the effect of laser illumination in very concentrated samples, a drop of sample 1050-NNs (10 µL of a aqueous solution 1 mg/mL) was left to dry onto a piece of silicon wafer (SEM sample holder); then, the dry product was shortly illuminated (<5 seconds) with the 1064 nm laser system. Interestingly, NNs following illumination presented a number of darker spots on their surface that could be related to hole formation (Figure 7.14); this is a speculative argument and future work should be done in this direction; nevertheless, this effect can be very important since inside cells NNs will be found mostly in cellular compartments where they are in close proximity with each other and collective effects are surely of the most importance. Independently of whether there is or not formation of holes or thinning of some regions on the surface of NNs, apparently, there are neither dramatic morphology changes such as a collective transformation into other structures like spheres, rods or disks, nor extreme tip deformation. It should be clarify that this does not mean that dramatic morphology changes can occur for NNs following laser irradiation with higher power densities.

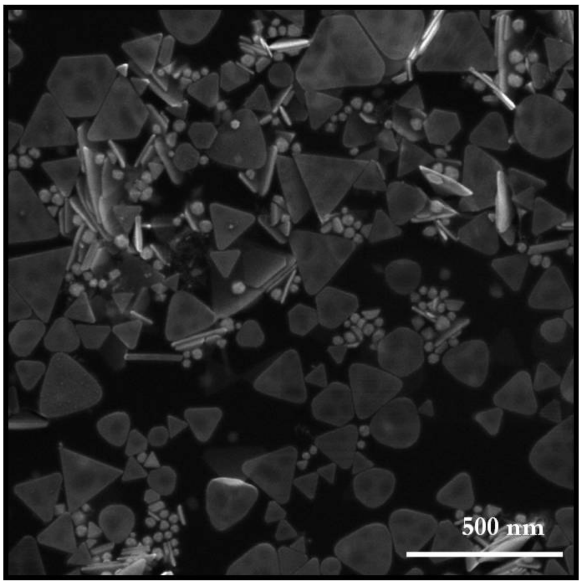

Figure 7.14. *Morphology of NNs-dried irradiated where the holes are detectable.*

7.3. Local heating

As it was previously described, NPs present a rapid temperature decay from their surfaces;[17] also, the NP temperature can be considered homogeneous in the time scale of ps following laser irradiation.[45] Several works based on theoretical calculations have pointed out that the heat produced by a single GNP can increase the equilibrium temperature of the NP only in a few degrees, even when it is irradiated with extremely high power densities (*i.e.* 10^6 W/cm^2).[12,18,46,47] However, it has been extensively proven, here and in other works, that even very diluted (pM range) solutions of anisotropic NPs can achieve high temperatures following laser irradiation; this can be explained as a collective heating produced by many nanoheaters.

In this section, the concept of molecular heating is explored; the temperature in the most immediate vicinity of NNs can be indirectly assessed by evaluating the enzymatic activity of enzymes (*i.e.* GOx) conjugated onto PEGylated NNs.

Attachment of enzymes

Proteins represent another important group of biomolecules; among them, enzymes are very interesting because of their catalytic activity. To provide PEGylated NNs with catalytic activity, these were modified with two different enzymes, *i.e.* HRP (horseradish peroxidase) and GOx (glucose oxidase).

First attempt was conjugating HRP molecules to EDC-activated NNs@PEG-CO_2H (activated as previously described); for HRP derivatization, 32 µg of HRP (44 KDa, isoelectric point of 7.2) were added to activated NNs; incubation and purification steps were carried out as previously described. Comparison of the UV-Vis-NIR spectra of NNs before and after HRP conjugation remains very similar and therefore, aggregation can be ruled out (Figure 7.15(a)). To evaluate whether conjugation of HRP was successful, a colorimetric assay based on the catalytic activity of HRP was used; this reaction is widely used in ELISA tests because of its high sensitivity and ease of execution. Briefly, HRP is able to oxidize hydrogen peroxide into water resulting in the production of electrons; then, these can oxidize ABTS (2, 2′-azino-bis (3-ethylbenzothiazoline-6-sulphonic acid) into its oxidized form, turning from yellow to green the solution (Figure 7.15(b)).

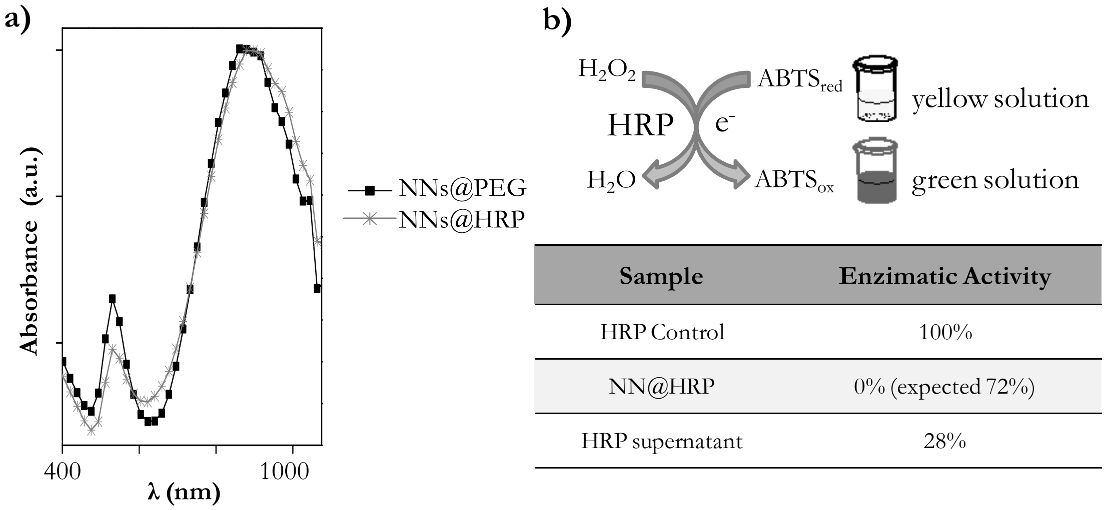

Sample	Enzimatic Activity
HRP Control	100%
NN@HRP	0% (expected 72%)
HRP supernatant	28%

Figure 7.15. *a) Absorption spectra of NNs before and after HRP attachment; b) upper part, HRP colorimetric activity assay where reduced ABTS present a light green color whereas the oxidized species presents a dark green color; bottom part, table shows the resulting activity values.*

Results showed that the conjugation of NNs with HRP was successful since the catalytic activity of the supernatants (uncoupled HRP) decreased drastically (dropped to 28% activity). Surprisingly, although NNs derivatized with HRP (NNs@HRP) should have kept the remaining 72% of activity, they showed none. This effect can be ascribable to the catalytic nature of Au NPs themselves; recently, the GOx-like activity of Au NPs has been reported in different works.[48,49] Here, we speculate that the redox nature of the gold surface of NNs could inactivate the colorimetric assay by capturing the electrons and preventing the oxidation of ABTS.

Protein determination analysis was performed (Bradford assay, see annex A) in sample NNs@HRP; results indicated that the rest of HRP (78%) was actually onto NNs. To further probe the effective conjugation of HRP onto NNs, NNs@HRP were supplemented with an antibody against HRP (anti-HRP modified with rhodamine isothiocianate; see annex A). Anti-HRP is a polyclonal antibody which can bind to multiple sites on the HRP structure; non-captured anti-HRP was washed out by three centrifugation steps. The absorption spectrum of NNs@HRP-anti-HRP exhibits bands at 280 nm and 555 nm which correspond to the absorption bands of anti-HRP and the modified rhodamine, respectively. Figure 7.16(b) shows an image of a drop containing the sample taken by fluorescence microscopy that further demonstrates the presence of the fluorescence antibody.

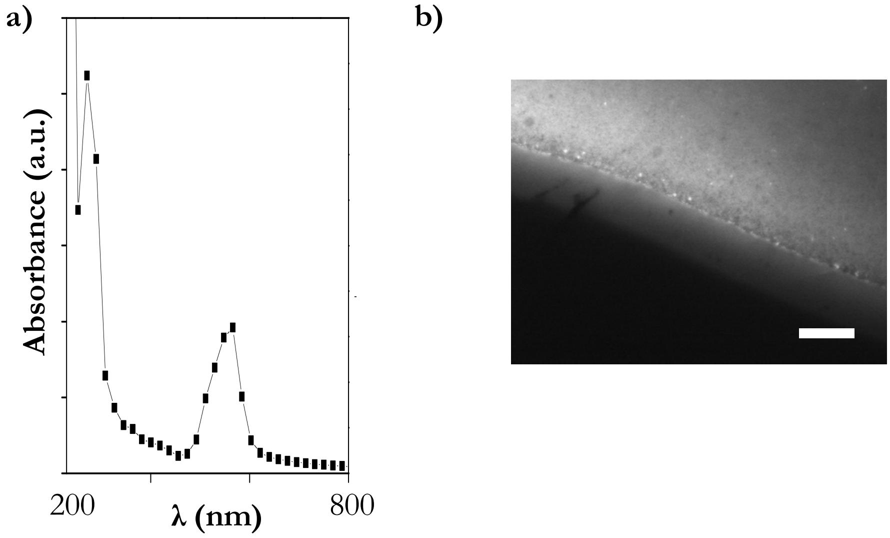

Figure 7.16. *a) Absorption spectra of the Ab-HRP-rhodamine; b) fluorescence image from the drop containing NN-HRP incubated with fluorescent anti-HRP.*

Since HRP onto NNs was problematic to detect by the colorimetric assay based on the reduction of ABTS, another enzyme was tried out, *i.e.* GOx (A. Niger, 360kDa, EC 1.1.3.4, pI= 4.2). This enzyme was modified to present a region rich in amine groups that could be used for coupling to carboxylic groups present on NNs@PEG; details on the protocol to modify the sugars present on the enzyme can be found in Annex X. This amination produces a rise in the isoelectric point (pI) of the enzyme allowing its interaction with EDC-activated NNs at pH 6. Moreover, this modification produces a preferential orientation of the enzyme onto NNs; presumably, the coupling should occur far from the active center of the enzyme which should be attached onto NNs by its more positive region, *i.e.* the aminated sugar region.[50] This strategy has been proven very efficient to conjugate antibodies onto NPs surface in a controlled way.[51] The derivatization of NNs with the modified GOx was carried out equivalently to the conjugation with HRP.

GOx is an enzyme of the redox family enzyme, as HRP is. However, the activity of GOx is based on its ability to oxidize glucose (oxidizing agent) whereas in the case of HRP, it enzymatic activity remains in its ability as reducing agent (water into peroxide). Other differences compared to HRP are that GOx is considerably larger in size (360 vs. 44 KDa) and the activation center of GOx is presumably further away from the gold surface. However, the method to detect GOx is also a colorimetric assay which involves ABTS, in addition to glucose and HRP. In this case, GOx acts as an oxidizing agent that catalyzes the oxidation of glucose to hydrogen peroxide and D-glucono-δ-lactone; hydrogen peroxide can be then oxidized by HRP and the assay follows as previously explained (Figure 7.17(a)). Spectra of unmodified NNs and GOx-derivatized NNs are very similar and therefore, aggregation during conjugations can be ruled out (Figure 7.17(b)).

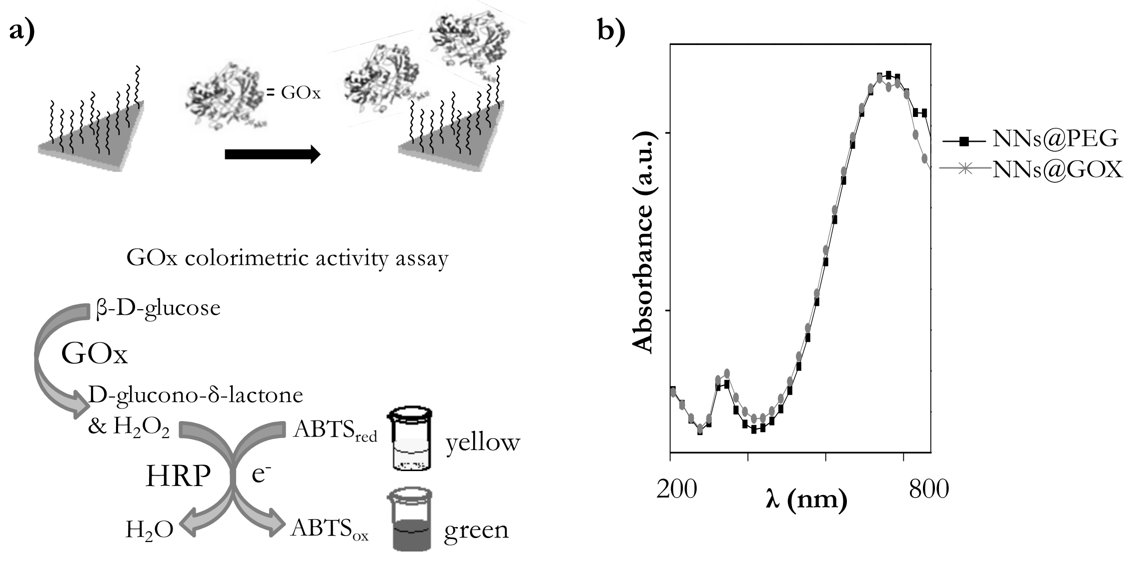

Figure 7.17. *a) Scheme of derivatization of NNs with GOx and the corresponding colorimetric assay to determine the enzymatic activity of GOx; b) absorption spectra of unmodified NNs and NNs derivatized with GOx.*

In contrast to the case of HRP, GOx-derivatized NNs kept the enzymatic activity expected; as it can be noticed in Table 7.2, the activity of NN@GOx is close to the difference between the amount of GOx added and unbound GOx present in the supernatant (Sb NNs@GOx) after purification of NNs (Table 7.2).

Sample	Enzymatic Activity
Contol GOx	100%
Sb NNs@GOx	38%
NNs@ GOx	54% (expected 62%)

Table 7.2. *Enzymatic activity percentages obtained in the enzymatic assay for GOx added, unbound GOx and GOx attached to NNs.*

It should be highlighted here that the enzymatic activity of GOx conjugated to NNs is temperature dependent; above 55ºC, *ca.* 50% of the enzymatic activity is irreversibly lost (denaturation temperature) as shown in Figure 7.18. This in agreement with reports addressing on the denaturation temperature of free GOx;[52] this is the temperature at which at least 50% of the enzymes lose their activity.[52] As previously described, the carbohydrates present on the enzyme GOx were partly aminated to improve the derivatization of NNs with the enzyme; this modification does not modify the thermal stability of the enzyme.[53]

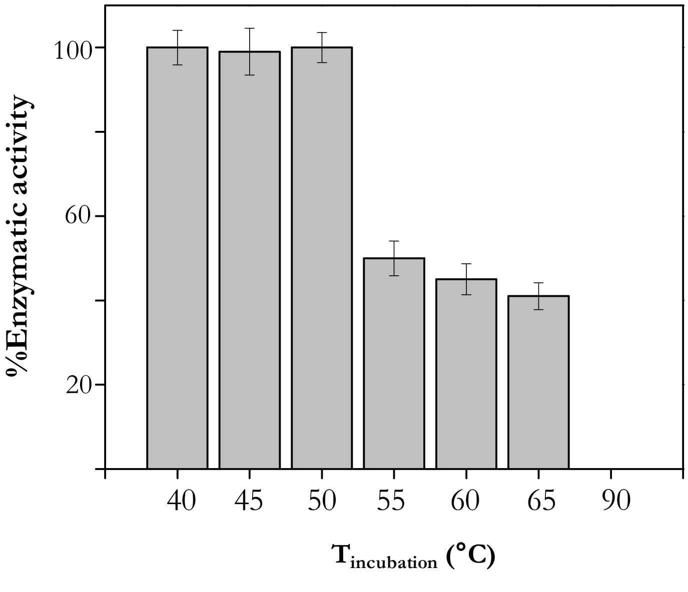

Figure 7.18. *Evaluation of temperature stability of GOx-NNs.*

NNs@Gox laser irradiation experiment

A diluted aqueous solution (1 mL, 75 µg/mL or *ca.* 20 pM) of PEGylated NNs derivatized with GOx molecules (NNs-GOx) was irradiated with the 1064 nm DPSSL system previously described (ca. 50 W/cm^2); the solution was irradiated continuously during 30 minutes under vigorous magnetic stirring which allowed for rapid temperature homogenization. The spectra of NNs-GOx before and after irradiation remained the same which points out that the colloidal stability and morphology of the NPs was unaffected (no signs of aggregation or NP reshaping at all) (Figure 7.12(a)). As shown in Figure 7.19(b), the temperature of the solution rose up to ca. 37°C very rapidly (7°C in less than 5 minutes); then, the temperature increased steadily up to *ca.* 45°C until the laser was switched off (30 minutes). In addition, the temperature of the solution was always bellow 55°C, the denaturalization temperature of GOx and therefore, one would expect that the enzyme retains its catalytic activity intact.

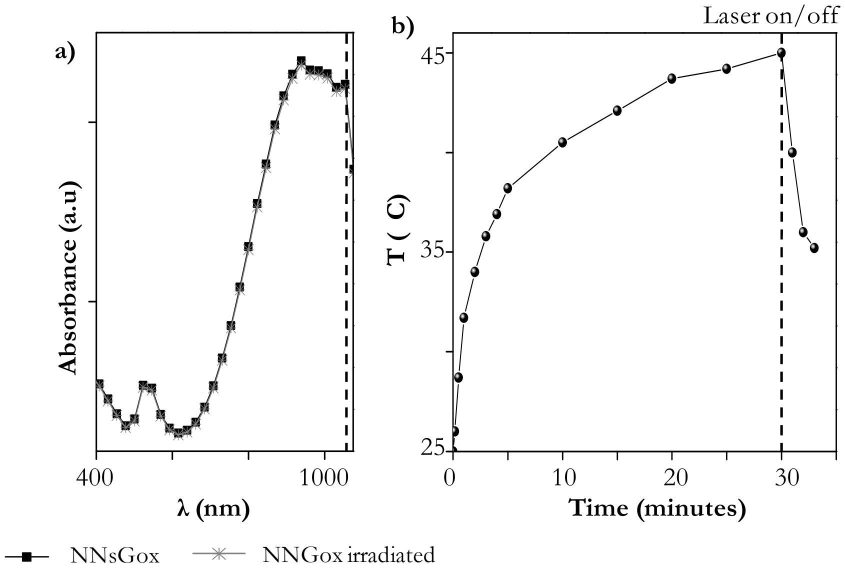

Figure 7.19. *a) Absorption spectra of GOX-NN before and after laser irradiation. b) Heating curve of NNGox during laser irradiation.*

To determine the effect of NNs heating on the enzyme (its activity, conformational change or denaturation), the enzymatic activity of GOx was measured by a facile colorimetric assay previously described. The enzymatic activity was evaluated in four different samples, *i.e.* (1) NNs-GOx, (2) NNs-GOx which were previously heated up (by a PCR-heater plate) and kept at 50°C for 30 minutes, (3) NNs-GOx which were previously heated up (by a PCR-heater plate) and kept at 65°C for 30 minutes and (4) NNs-GOx irradiated (as previously described) during 30 minutes and which temperature was always bellow 45°C (Figure 7.19(b)). Results of the enzymatic activity assay show that the enzymatic activity remains intact in Figure 7.20 (1) NNs-GOx without heating treatment and (2) those heated up and kept at 50°C for 30 minutes; this is in agreement with the enzymatic activity of free GOx. Also as expected, the enzymatic activity of (3)

NNs-GOx heated up and kept at 65ºC for 30 minutes dropped at *ca.* 40%. Finally, sample (4) of irradiated NNs@GOx exhibited *ca.* 50% of the original enzymatic activity.

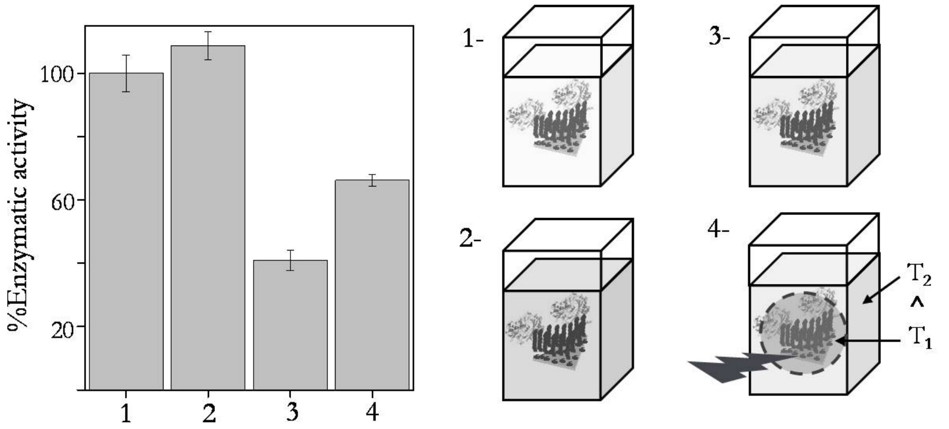

***Figure** 7.20. Enzymatic activity founded in NNs@GOX: 1- NNs@GOX untreated (r.t.); 2- NNs@GOX heated at 50°C during 30 minutes; 3- NNs-GOX heated at 65°C during 30 minutes, and 4- NNs@GOX irradiated with 1064 nm laser. In the schematic representation is indicated the possible presence of two temperatures, T_1 closer to irradiated NNs surface and T_2, which is lower, in the surroundings.*

The enzymatic activity fall in sample (4) can be only explained as an effect of the temperature increment following irradiation; however, the temperature of the solution remains below the denaturation temperature of GOx in all time during irradiation. This result points out that that the heat produced by NNs under illumination is enough to denature some bound GOx; equivalently, it is also in order to say that the temperature on the region of illumination (only 2.5% of the sample volume) is temporally above the denaturation temperature of GOx.[52,54] As previously described, most theoretical works claim that using the irradiation conditions used in this work, the temperature on the surface of NNs cannot be increased by more than few tens of degree. On the other hand, our results are conclusive in terms of achievable temperatures on the surface of NNs; being able to denature GOx conjugated to NNs represent a proof that the heat produced by NNs, even at very diluted conditions as used here, it is possible to locally increase the temperature up to important values in terms of denaturing proteins. Nevertheless, it should be emphasized that this results does not mean that the temperature of just one NN can be risen up to GOx-denaturing values, but the illumination of *ca.* 2.5% of the sample volume and following collective heating is able to release to the medium enough energy to denaturize GOx molecules (at least partly) bound to NNs; either due to the collective coupling of several NNs or the collaborative heating of several NNs it is possible to locally increase the temperature of the region under illumination by several degrees. This approach to study plasmonic heating will be further explored in the future in order to evaluate the ability of just one, a controlled group or supramolecular arrangements of NNs to produce heat.

7.4. Conclusions

NNs were evaluated as plasmonic nanoheaters under NIR laser irradiation. NNs with two different aspect ratios (and consequently, different plasmon bands) NNs were irradiated using two laser sources of different wavelengths, *i.e.* 809 nm and 1064 nm. Colloidal solutions of NN@PEG under illumination, even at very moderate NP concentrations, could reach ΔT up to 50 ºC in the vicinity of the illumination spot. This result provides fundamental evidence of the feasibility of the biofunctionalized NN system for NIR-driven heating for bioapplications and opens the possibility of using this system for local hyperthermia and drug-release applications. The heating ability of NNs under irradiation is comparable to the best result founded in literature. Therefore, NNs can be added to the pool of nanoheaters as a versatile alternative which do not require challenging synthetic methods or laborious extensive ligand exchange to remove the highly toxic CTAB surfactant.

As a proof of concept, the local heating ability of NNs under illumination was addressed. An active enzyme, GOx, was attached onto NNs surface and its activity was evaluated in different conditions, including after laser irradiation. The enzyme activity of laser-irradiated NNs@GOx decreased down to 40% whereas the activity remained 100% even after external heating (55º, half hour). This result indicates that the heat produced by NNs under illumination can irreversibly damaged the enzymatic activity of GOx in close proximity to the NNs surface. Nevertheless, considering the laser fluence used in this experiments, it is not possible to confirm theoretically that GOx denaturation is caused by the heat produced by one single NN or by a collective heating produced by several NNs in close proximity and irradiated simultaneously.

REFERENCES

(1) Chang, S. S.; Shih, C. W.; Chen, C. D.; Lai, W. C.; Wang, C. R. C.: The shape transition of gold nanorods. *Langmuir* **1999**, *15*, 701-709.

(2) Link, S.; Burda, C.; Mohamed, M. B.; Nikoobakht, B.; El-Sayed, M. A.: Laser photothermal melting and fragmentation of gold nanorods: Energy and laser pulse-width dependence. *Journal of Physical Chemistry A* **1999**, *103*, 1165-1170.

(3) Link, S.; Burda, C.; Nikoobakht, B.; El-Sayed, M. A.: How long does it take to melt a gold nanorod? A femtosecond pump-probe absorption spectroscopic study. *Chemical Physics Letters* **1999**, *315*, 12-18.

(4) Aguirre, C. M.; Moran, C. E.; Young, J. F.; Halas, N. J.: Laser-Induced Reshaping of Metallodielectric Nanoshells under Femtosecond and Nanosecond Plasmon Resonant Illumination. *The Journal of Physical Chemistry B* **2004**, *108*, 7040-7045.

(5) Pérez-Juste, J.; Rodríguez-González, B.; Mulvaney, P.; Liz-Marzán, L. M.: Optical Control and Patterning of Gold-Nanorod–Poly(vinyl alcohol) Nanocomposite Films. *Advanced Functional Materials* **2005**, *15*, 1065-1071.

(6) Huang, X.; Jain, P. K.; El-Sayed, I. H.; El-Sayed, M. A.: Plasmonic photothermal therapy (PPTT) using gold nanoparticles. *Lasers in Medical Science* **2007**, *23*, 217-228.

(7) Dreaden, E. C.; Mackey, M. A.; Huang, X.; Kang, B.; El-Sayed, M. A.: Beating cancer in multiple ways using nanogold. *Chemical Society Reviews* **2011**, *40*, 3391.

(8) Richardson, H. H.; Carlson, M. T.; Tandler, P. J.; Hernandez, P.; Govorov, A. O.: Experimental and Theoretical Studies of Light-to-Heat Conversion and Collective Heating Effects in Metal Nanoparticle Solutions. *Nano Letters* **2009**, *9*, 1139-1146.

(9) Qin, Z.; Bischof, J. C.: Thermophysical and biological responses of gold nanoparticle laser heating. *Chemical Society Reviews* **2012**.

(10) Burda, C.; Chen, X. B.; Narayanan, R.; El-Sayed, M. A.: Chemistry and properties of nanocrystals of different shapes. *Chemical Reviews* **2005**, *105*, 1025-1102.

(11) Link, S.; El-Sayed, M. A.: Shape and size dependence of radiative, non-radiative and photothermal properties of gold nanocrystals. *International Reviews in Physical Chemistry* **2000**, *19*, 409-453.

(12) Baffou, G.; Quidant, R.; Girard, C.: Heat generation in plasmonic nanostructures: Influence of morphology. *Applied Physics Letters* **2009**, *94*, 153109-3.

(13) Pelton, M.; Aizpurua, J.; Bryant, G.: Metal-nanoparticle plasmonics. *Laser & Photonics Reviews* **2008**, *2*, 136-159.

(14) Ekici, O.; Harrison, R. K.; Durr, N. J.; Eversole, D. S.; Lee, M.; Ben-Yakar, A.: Thermal analysis of gold nanorods heated with femtosecond laser pulses. *Journal of Physics D-Applied Physics* **2008**, *41*.

(15) Letfullin, R. R.; George, T. F.; Duree, G. C.; Bollinger, B. M.: Ultrashort Laser Pulse Heating of Nanoparticles: Comparison of Theoretical Approaches. *Advances in Optical Technologies* **2008**, *2008*.

(16) Merabia, S.; Shenogin, S.; Joly, L.; Keblinski, P.; Barrat, J.-L.: Heat transfer from nanoparticles: A corresponding state analysis. *Proceedings of the National Academy of Sciences* **2009**, *106*, 15113-15118.

(17) Govorov, A. O.; Richardson, H. H.: Generating heat with metal nanoparticles. *Nano Today* **2007**, *2*, 30-38.

(18) Baffou, G.; Quidant, R.; García de Abajo, F. J.: Nanoscale Control of Optical Heating in Complex Plasmonic Systems. *Acs Nano* **2010**, *4*, 709-716.

(19) Bartczak, D.; Muskens, O. L.; Nitti, S.; Sanchez-Elsner, T.; Millar, T. M.; Kanaras, A. G.: Interactions of Human Endothelial Cells with Gold Nanoparticles of Different Morphologies. *Small* **2011**, n/a-n/a.

(20) Bartczak, D.; Muskens, O. L.; Millar, T. M.; Sanchez-Elsner, T.; Kanaras, A. G.: Laser-Induced Damage and Recovery of Plasmonically Targeted Human Endothelial Cells. *Nano Letters* **2011**, *11*, 1358-1363.

(21) Cole, J. R.; Mirin, N. A.; Knight, M. W.; Goodrich, G. P.; Halas, N. J.: Photothermal Efficiencies of Nanoshells and Nanorods for Clinical Therapeutic Applications. *The Journal of Physical Chemistry C* **2009**, *113*, 12090-12094.

(22) Chen, H.; Shao, L.; Ming, T.; Sun, Z.; Zhao, C.; Yang, B.; Wang, J.: Understanding the Photothermal Conversion Efficiency of Gold Nanocrystals. *Small* **2010**, *6*, 2272-2280.

(23) Roper, D. K.; Ahn, W.; Hoepfner, M.: Microscale heat transfer transduced by surface plasmon resonant gold nanoparticles. *Journal of Physical Chemistry C* **2007**, *111*, 3636-3641.

(24) Urban, A. S.; Fedoruk, M.; Horton, M. R.; Rädler, J. O.; Stefani, F. D.; Feldmann, J.: Controlled Nanometric Phase Transitions of Phospholipid Membranes by Plasmonic Heating of Single Gold Nanoparticles. *Nano Letters* **2009**, *9*, 2903-2908.

(25) Bendix, P. M.; Nader, S.; Reihani, S.; Oddershede, L. B.: Direct Measurements of Heating by Electromagnetically Trapped Gold Nanoparticles on Supported Lipid Bilayers. *Acs Nano* **2010**, *4*, 2256-2262.

(26) Kyrsting, A.; Bendix, P. M.; Stamou, D. G.; Oddershede, L. B.: Heat Profiling of Three-Dimensionally Optically Trapped Gold Nanoparticles using Vesicle Cargo Release. *Nano Letters* **2010**, *11*, 888-892.

(27) Stehr, J.; Hrelescu, C.; Sperling, R. A.; Raschke, G.; Wunderlich, M.; Nichtl, A.; Heindl, D.; Kurzinger, K.; Parak, W. J.; Klar, T. A.; Feldmann, J.: Gold NanoStoves for Microsecond DNA Melting Analysis. *Nano Letters* **2008**, *8*, 619-623.

(28) Bakhtiari, A. B. S.; Hsiao, D.; Jin, G.; Gates, B. D.; Branda, N. R.: An Efficient Method Based on the Photothermal Effect for the Release of Molecules from Metal Nanoparticle Surfaces. *Angewandte Chemie International Edition* **2009**, *48*, 4166-4169.

(29) Jain, P. K.; Qian, W.; El-Sayed, M. A.: Ultrafast Cooling of Photoexcited Electrons in Gold Nanoparticle−Thiolated DNA Conjugates Involves the Dissociation of the Gold−Thiol Bond. *Journal of the American Chemical Society* **2006**, *128*, 2426-2433.

(30) Yan, C.; Pattani, V.; Tunnell, J. W.; Ren, P.: Temperature-induced unfolding of epidermal growth factor (EGF): Insight from molecular dynamics simulation. *Journal of Molecular Graphics and Modelling* **2010**, *29*, 2-12.

(31) Csaki, A.; Garwe, F.; Steinbruck, A.; Maubach, G.; Festag, G.; Weise, A.; Riemann, I.; Konig, K.; Fritzsche, W.: A parallel approach for subwavelength molecular surgery using gene-specific positioned metal nanoparticles as laser light antennas. *Nano Letters* **2007**, *7*, 247-253.

(32) Pitsillides, C. M.; Joe, E. K.; Wei, X. B.; Anderson, R. R.; Lin, C. P.: Selective cell targeting with light-absorbing microparticles and nanoparticles. *Biophysical Journal* **2003**, *84*, 4023-4032.

(33) Wu, G.; Mikhailovsky, A.; Khant, H. A.; Fu, C.; Chiu, W.; Zasadzinski, J. A.: Remotely Triggered Liposome Release by Near-Infrared Light Absorption via Hollow Gold Nanoshells. *Journal of the American Chemical Society* **2008**, *130*, 8175-8177.

(34) Tong, L.; Zhao, Y.; Huff, T. B.; Hansen, M. N.; Wei, A.; Cheng, J. X.: Gold Nanorods Mediate Tumor Cell Death by Compromising Membrane Integrity. *Advanced Materials* **2007**, *19*, 3136-3141.

(35) Zharov, V. P.; Letfullin, R. R.; Galitovskaya, E. N.: Microbubbles-overlapping mode for laser killing of cancer cells with absorbing nanoparticle clusters. *Journal of Physics D-Applied Physics* **2005**, *38*, 2571-2581.

(36) O'Neal, D. P.; Hirsch, L. R.; Halas, N. J.; Payne, J. D.; West, J. L.: Photo-thermal tumor ablation in mice using near infrared-absorbing nanoparticles. *Cancer Letters* **2004**, *209*, 171-176.

(37) Park, J.-H.; von Maltzahn, G.; Xu, M. J.; Fogal, V.; Kotamraju, V. R.; Ruoslahti, E.; Bhatia, S. N.; Sailor, M. J.: Cooperative nanomaterial system to sensitize, target, and treat tumors. *Proceedings of the National Academy of Sciences* **2009**.

(38) Sershen, S. R.; Westcott, S. L.; Halas, N. J.; West, J. L.: Temperature-sensitive polymer-nanoshell composites for photothermally modulated drug delivery. *J. Biomed. Mater. Res.* **2000**, *51*, 293-298.

(39) You, J.; Shao, R.; Wei, X.; Gupta, S.; Li, C.: Near-Infrared Light Triggers Release of Paclitaxel from Biodegradable Microspheres: Photothermal Effect and Enhanced Antitumor Activity. *Small* **2010**, *6*, 1022-1031.

(40) Diagaradjane, P.; Shetty, A.; Wang, J. C.; Elliott, A. M.; Schwartz, J.; Shentu, S.; Park, H. C.; Deorukhkar, A.; Stafford, R. J.; Cho, S. H.; Tunnell, J. W.; Hazle, J. D.; Krishnan, S.: Modulation of in vivo tumor radiation response via gold nanoshell-mediated vascular-focused hyperthermia: Characterizing an integrated antihypoxic and localized vascular disrupting targeting strategy. *Nano Letters* **2008**, *8*, 1492-1500.

(41) Perez-Juste, J.; Liz-Marzan, L. M.; Carnie, S.; Chan, D. Y. C.; Mulvaney, P.: Electric-field-directed growth of gold nanorods in aqueous surfactant solutions. *Advanced Functional Materials* **2004**, *14*, 571-579.

(42) Link, S.; Burda, C.; Nikoobakht, B.; El-Sayed, M. A.: Laser-induced shape changes of colloidal gold nanorods using femtosecond and nanosecond laser pulses. *Journal of Physical Chemistry B* **2000**, *104*, 6152-6163.

(43) Takami, A.; Kurita, H.; Koda, S.: Laser-induced size reduction of noble metal particles. *Journal of Physical Chemistry B* **1999**, *103*, 1226-1232.

(44) Fujiwara, H.; Yanagida, S.; Kamat, P. V.: Visible Laser Induced Fusion and Fragmentation of Thionicotinamide-Capped Gold Nanoparticles. *The Journal of Physical Chemistry B* **1999**, *103*, 2589-2591.

(45) Baffou, G.; Girard, C.; Quidant, R.: Mapping Heat Origin in Plasmonic Structures. *Physical Review Letters* **2010**, *104*, 136805.

(46) Baffou, G.; Girard, C.; Quidant, R.: Mapping Heat Origin in Plasmonic Structures. *Physical Review Letters* **2010**, *104*.

(47) Baffou, G.; Quidant, R.; Girard, C.: Thermoplasmonics modeling: A Green's function approach. *Physical Review B* **2010**, *82*.

(48) Luo, W.; Zhu, C.; Su, S.; Li, D.; He, Y.; Huang, Q.; Fan, C.: Self-Catalyzed, Self-Limiting Growth of Glucose Oxidase-Mimicking Gold Nanoparticles. *ACS Nano* **2010**, *4*, 7451-7458.

(49) Zheng, X.; Liu, Q.; Jing, C.; Li, Y.; Li, D.; Luo, W.; Wen, Y.; He, Y.; Huang, Q.; Long, Y.-T.; Fan, C.: Catalytic Gold Nanoparticles for Nanoplasmonic Detection of DNA Hybridization. *Angewandte Chemie International Edition* **2011**, *50*, 11994-11998.

(50) Fernandez-Lorente, G.; Godoy, C. A.; Mendes, A. A.; Lopez-Gallego, F.; Grazu, V.; de las Rivas, B.; Palomo, J. M.; Hermoso, J.; Fernandez-Lafuente, R.; Guisan, J. M.: Solid-phase chemical amination of a lipase from Bacillus thermocatenulatus to improve its stabilization via covalent immobilization on highly activated glyoxyl-agarose. *Biomacromolecules* **2008**, *9*, 2553-2561.

(51) Puertas, S.; Batalla, P.; Moros, M. a.; Polo, E.; del Pino, P.; Guisán, J. M.; Grazú, V.; de la Fuente, J. s. M.: Taking Advantage of Unspecific Interactions to Produce Highly Active Magnetic Nanoparticle−Antibody Conjugates. *ACS Nano* **2011**, *5*, 4521-4528.

(52) Zoldák, G.; Zubrik, A.; Musatov, A.; Stupák, M.; Sedlák, E.: Irreversible Thermal Denaturation of Glucose Oxidase from Aspergillus niger Is the Transition to the Denatured State with Residual Structure. *Journal of Biological Chemistry* **2004**, *279*, 47601-47609.

(53) Kalisz, H. M.; Hecht, H. J.; Schomburg, D.; Schmid, R. D.: EFFECTS OF CARBOHYDRATE DEPLETION ON THE STRUCTURE, STABILITY AND ACTIVITY OF GLUCOSE-OXIDASE FROM ASPERGILLUS-NIGER. *Biochimica Et Biophysica Acta* **1991**, *1080*, 138-142.

(54) Bankar, S. B.; Bule, M. V.; Singhal, R. S.; Ananthanarayan, L.: Glucose oxidase - An overview. *Biotechnology Advances* **2009**, *27*, 489-501.

NanoNachos & Cells (*in vitro* assays)

Chapter 8

Many theoretical studies have addressed the topic of light–to-heat conversion driven by GNPs as it was discussed previously in Chapter 7. However, many of these approaches are not suitable when GNPs are irradiated inside biological environments. It should be highlighted that in general, cells challenged with NPs will store them in cytosolic vesicles where both the local concentration of NPs and the interparticle couplings will be very high; plasmonic coupling of NPs can give rise to greatly enhanced heating responses following irradiation.[1] Several works have reported on the ability of NIR laser irradiation to damage cells loaded with GNPs, both *in vitro* and *in vivo*.[2-10] Upon irradiation, the mechanism responsible for damaging the cells loaded with GNPs is typically related to the thermophysical response of GNPs and the surrounding media (for detail discussion in this matter, see the recent and excellent review by Quin & Bischof);[11] the production of reactive oxidative species (ROS) has been also recently pointed as responsible for cell injury.[10,12] In any case, the thermophysical response following irradiation of GNPs inside cells is a complex process that depends on several parameters including the local distribution, concentration and type of GNPs inside cells, and the wavelength and power density of the light source. Therefore, it is very difficult to compare the results of different works addressing the heating ability of GNPs inside cells.

In a recent work, Bartczak *et al.* have combined experimental findings (most of the data from another work of the same group)[8] and theoretical models where they discuss the heating ability of different types of GNPs inside cells;[9] they used power densities on the range of 1-50 W/cm^2, typically used in many other similar studies. They claim that heat-generation at the single-particle level is insufficient to damage cells; in order to explain the widely reported cell damage upon heating following irradiation of GNPs, it is mandatory to jump into the macroscopic scale (several hundreds of micrometers) where the collective heating of several cells (thousands) loaded with GNRs can undergo cell damage. This observation is important, as it implicates that this will affect all cells in the illumination volume, limiting the possibility of targeting of individual cell types.

Recently, Qin & Bischof proposed a combination of equations to predict and compare the nano-, micro-, and macroscale plasmonic heating; based on these, they predicted the laser power density required to achieve a 10ºC temperature rise for different biological systems with increased complexity, from the single cell to 10^9 cells which typically correspond to 10 mm tumor (Table 8.1). It should be noticed here that they had to assume a uniform GNP concentration of 5 µg Au per g of the biological system (a common value that is typically achieved by systemic delivery). Although they had to take many other important assumptions to compare these systems, assuming a uniform concentration of GNPs and neglecting collective coupling of GNPs inside cells represent (in our opinion which is based on our experimental findings and other works)[1,13] a too restricting boundary condition.[1,13]

Bio-System	Size (Diameter)	Power Density (W/cm^2)
Single GNP	30 nm	8.8×10^4
Single cell	10 µm	2.1×10^6
10 cells	22 µm	4.4×10^5
100 cells	46 µm	9.5×10^4
10^3 cells	100 µm	2.5×10^4
10^6 cells	1 mm	2.1×10^2
10^9 cells	10 mm	2.1

Table 8.1. *Predicted power density required for achieving 10ºC of heating for different scaled systems at steady state (reproduced from Qin & Bischof).*[11]

In this chapter, the stability, cytotoxicity and internalization efficiency of different NNs derivatized with molecules of biological relevance are addressed in cell cultures. Finally, the effect of laser irradiation will be evaluated at the single cell level and in areas containing thousands of cells; this studies allow for evaluation of the heating ability of NNs to trigger changes in the cell-morphology.

8.1. Activation of PEGylated NNs

Carboxyl-PEGylated NNs (NNs@PEG-CO_2H) were conjugated with different amine-containing molecules using EDC/sulfo NHS chemistry. The improved stability of PEGylated NNs allows for activation conditions that otherwise would lead to aggregation of NNs.

In a typical functionalization, 1 mg NNs@PEG-CO_2H were incubated with 1:3 mg of EDC:Sulfo-NHS in 2 mL MES buffer (2-Aminoethanoland 2-(N-morpholino)ethanesulfonic acid) pH 6 for 20 minutes at 37 ºC; at this point, activated NNs@PEG (bearing a semi-stable amine-reactive ester) were centrifugated during 15 minutes (9000 rpm) to remove excess of reagents and then, amine-containing ligands were added (Table 8.2); the particular protocol followed for each functionalization with a ligand or mix of ligands had to be slightly modified upon different functionalizations. Table 8.2 summarizes the different functionalizations.

Sample	Ligands
NNs@T	dye TAMRA
NNs@T&tat	dye TAMRA/ peptide tat
NNs@T&Lacto	dye TAMRA/ Lactose
NNs@T&Glc	dye TAMRA/ Glucose

Table 8.2. *Summary of NNs nomenclature for each chemical modification.*

Attachment of the dye TAMRA, carbohydrates and the peptide tat

The immediate application of NNs is their use in cell cultures and therefore, it is very convenient to be able to follow in situ the position of NNs in cell cultures by fluorescence microscopy. The fluorescent dye 5-TAMRA-cadaverine (Tetramethylrhodamine - 5 - carboxamide cadaverine) was chosen in this case because it bears an amine group susceptible to react with an activated carboxylic group (Figure 8.1).

Another important group of biomolecules due to its biological relevance is the carbohydrate family. These biomolecules are mainly located in the outer membrane of most types of cells conjugated to sphingolipids (glycosphingolipids) or to proteins (glycoproteins). These carbohydrates are responsible for communication with other cells and with the extracellular matrix, and are involved in viruses and bacteria infections as well as in many other non pathological biorecognition processes. [14,15] Taking into account the amount of processes where carbohydrates are involved and their biocompatibility, the high potential of these biomolecules in the nanomedicine field is clear. Cells present many carbohydrates receptors and different pathways to internalize them; thus, the use of glyconanoparticles is really suitable to enhance the cellular uptake of NPs. Another important role of these molecules is to prevent unspecific absorption of proteins present in physiological media; NPs passivated with carbohydrates can avoid this undesirable effect;[16] PEG brushes are also known for avoid this kind of unspecific interactions. For this aim, NNs were derivatized with lactose (Figure 8.1 (B)); this molecule contains a small chain of two carbons with an amine terminal group. Details on the synthesis of this molecule can be found in Annex.

Alternatively, a commercial modified glucose (4-aminophenyl β-D-glucopyranoside) was also used (Figure 8.1 (C)). The glucose modified structure consists of an amine group bonded to the monosaccharide through a phenyl cycle.

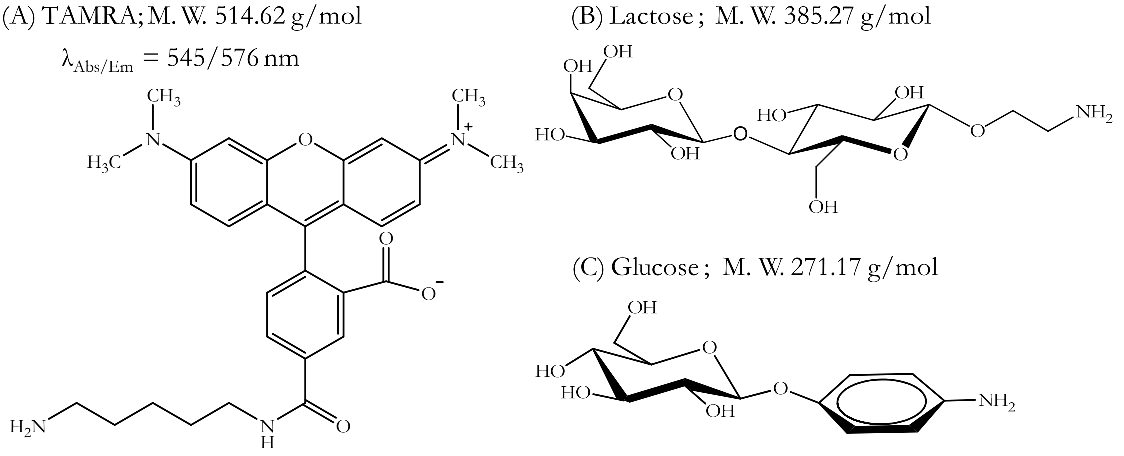
(A) TAMRA; M. W. 514.62 g/mol

$\lambda_{Abs/Em}$ = 545/576 nm

(B) Lactose ; M. W. 385.27 g/mol

(C) Glucose ; M. W. 271.17 g/mol

Figure 8.1. *(A) Structure, molecular weight and absorption/emission wavelength data of 5-TAMRA-cadaverine. (B) Chemical structure of aminoethoxylactose (C) Chemical structure of glucose (4-Aminophenyl β-D-glucopyranoside).*

Aiming to enhance the cellular uptake of the derivatives, NNs were modified with the peptide tat (GRKKRRQRRRPQ; 1621.91 g×mol^{-1}), a 12 amino acids short peptide of the family CPPs (cell penetrating peptides); these kind of molecules are useful because promote cell penetration (see chapter 4 for more details).

Different combinations of the molecules aforementioned were attached onto NNs aiming the design of a functional material with the properties of their counterparts, *i.e.* optical properties of the inorganic core and bio-functions of the attached molecules. Solutions of (i) TAMRA only or (ii) TAMRA & lactose or (iii) TAMRA & glucose or (iv) TAMRA & tat were added to EDC-activated NNs as follows: for 1 mg of activated NNs, (i) 100 µg of TAMRA or (ii) 100 µg of TAMRA & 500 µg of lactose (*ca.* 1:9 molar ratio TAMRA:lactose) or (iii) 100 µg of TAMRA and & 270 µg of glucose (*ca.* 1:5 molar ratio TAMRA:glucose) (iv) 100 µg of TAMRA & 56 µg of tat (1:0.2 molar ratio TAMRA:tat) were added to the solution; mixtures were left under mild stirring conditions at 4 ºC overnight; functional NNs were then washed out of ligand excess by centrifugal precipitation; functional NNs were centrifuged twice for 15 min at 10000 rpm and then, pellets were resuspended in MilliQ water. Finally, functional NNs were characterized by UV-Vis-NIR & fluorescence spectroscopy and gel electrophoresis (Figure 8.2).

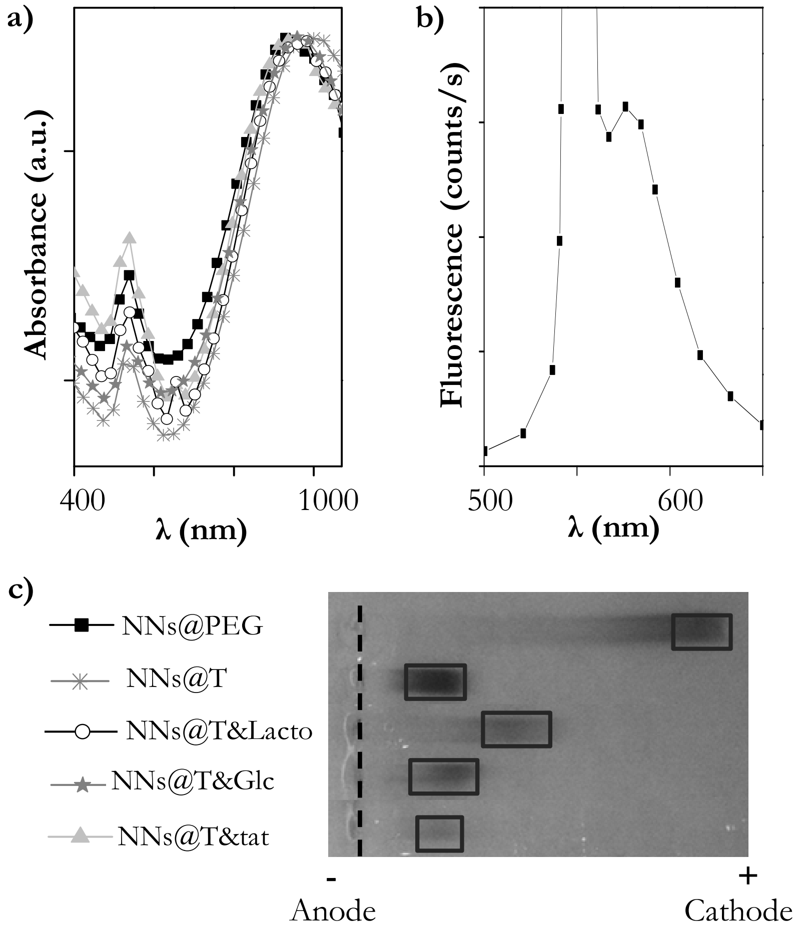

Figure 8.2. *a)UV-Vis-NIR absorption spectra of functionalized NNs; b) fluorescence emission spectra of one selected sample of NNs derivatized with TAMRA (all samples presented the same fluorescence features); c) electrophoresis gel (0,5%, 100V, 1h).*

8.2. Evaluation of the stability of modified NNs in cell cultures

The stability and of functional NNs in physiological media (Dulbecco's modified Eagle's medium (DMEM) supplemented with 10% fetal bovine serum (FBS)), as well as their biocompatibility, are critical issues before the application of these NPs in any biological application. Here, the stability in culture medium of PEGylated NNs derivatized with TAMRA (NNs@T) and another functional molecule, *i.e.* lactose (NNs@T&Lacto), tat (NNs@T&tat) or glucose (NNs@T&Glc) will be evaluated.

Prior to their used in cell cultures, functional NNs must be sterilized; filters of 0.2 μm (membrane of cellulose) were used to prevent the presence of bacteria and yeast in solutions of NNs. To evaluate the monodispersity and to confirm that NNs do not get retain in the filters, absorption spectra before and after filtration of NNs suspended in complete culture medium were collected (Figure 8.3(a)). Since no significant differences were found between spectra, it is clear that NNs are stable in the medium, *i.e.* they remain colloidally stable with no sign of aggregation and do not get retained by the filters. Thus, it is possible to sterilize NNs by filtration.

The absorption spectra of functional NNs were again compared before and after cell incubation (Figure 8.3(b)); for the sake of clarity, only samples NNs@T&Lacto are shown in Figure 8.3. After cell incubation, non-uptaken NNs were washed by three centrifugations steps (20 minutes at 8000 rpm) to remove them from the cell culture media. Again, absorption spectra do not show significant differences and therefore, it can be concluded that NNs maintain their stability even in long incubation times in complete cell culture medium, where high ionic strength conditions and the presence of serum proteins could be problematic. Nevertheless, a new band at *ca.* 280 nm is apparent (even after several washings) in the spectrum after cell medium incubation; this is indicative that there is some unspecific protein absorption (inset in Figure 8.3(b)).

In addition, Z-potential measurements were collected before and after incubation (Figure 8.3(c)); from the Z-potential evaluation, it can be also derived that the surface of NNs were modified following medium incubation. The Z-potential of NNs after cell culture is more positive than before incubation (in the pH range 6-8); this confirms the unspecific absorption of serum proteins. Despite the unspecific absorption of proteins, NNs remain stable in cell cultures for extended periods of time. Changes in the surface charge of NNs were also confirmed by an electrophoresis gel (Figure 8.3(d)); NNs after cell incubation present a lower negative charge than the original NNs.

As shown here, the charge of nanomaterials can also be greatly modified in physiological media due to the absorption of biomolecules present in the physiological milieu; absorption of proteins and following physiochemical surface changes on nanomaterials are the focus of several studies.[16-21] Thus the adsorption of serum proteins on the surface of nanomaterials can hide the synthetic organic layer and lead to unspecific uptake of nanomaterials into cells by receptor-mediated endocytosis.[22-24] Protein absorption onto nanoparticles can also adversely affect the function and structure of proteins;[25-27] for instance, disease-related fibrils made of human β2-microglobulin are formed in the surface of different nanoparticles.[19] Given that adsorption of proteins changes the nano-bio interface, it is worth noting that both the uptake and toxicity of NPs can be greatly influenced by the absorption of serum proteins.[22,23,26,28,29]

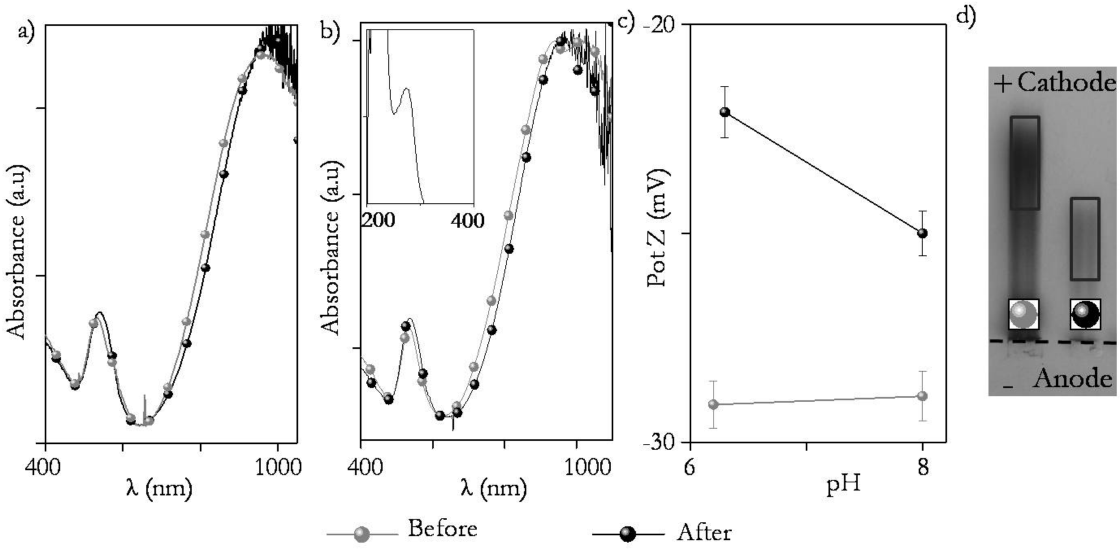

Figure 8.3. *a) Absorption spectra of NNs@T&Lacto before and after filtration; b) absorption spectra of NNs@T&Lacto before and after cell culture; c) Z-potential measurements of NNs@T&Lacto before and after cell incubation and d) electrophoresis gel of NNs@T&Lacto before and after cell incubation.*

8.3. Evaluation of cytotoxicity of NNs

Although there are no standardized protocols for assessing cytotoxicity of NPs, MTT-assays are widely used as a preliminary test to evaluate the biocompatibility of engineered NPs. In addition, the influence of NNs on cell cycle, activation of the complement system and morphology changes following NNs uptake were evaluated.

First, to account for cytotoxicity effects, the respiration activity of the cells challenged with NNs was analyzed by a MTT-based viability assay. This assay is a colorimetric method based on the metabolic reduction of MTT by the mitochondrial succinate dehydrogenase. The cell line Vero was used to evaluate the viability of different NNs in cell cultures; Vero cells were originally isolated from kidney epithelial cells extracted from an African green monkey. Six different types of modified NNs were evaluated in terms on cytotoxicity (Figure 8.5), *i.e.* (1) NNs obtained directly from the synthesis (NNs), (2) PEGlylated NNs (NNs@PEG), PEGylated NNs modified with (3) TAMRA (NNs@T), (4) TAMRA and tat (NNs@T&tat), (5) TAMRA and lactose (NNs@T&Lacto) and (6) TAMRA and glucose (NNs@T&Glc). Cells were challenged with different concentration of functional NNs (previously sterilized) for 24 hours prior to the MTT test; details on the execution of the assay itself can be found in Chapter 4. Figure 8.4 shows the MTT results.

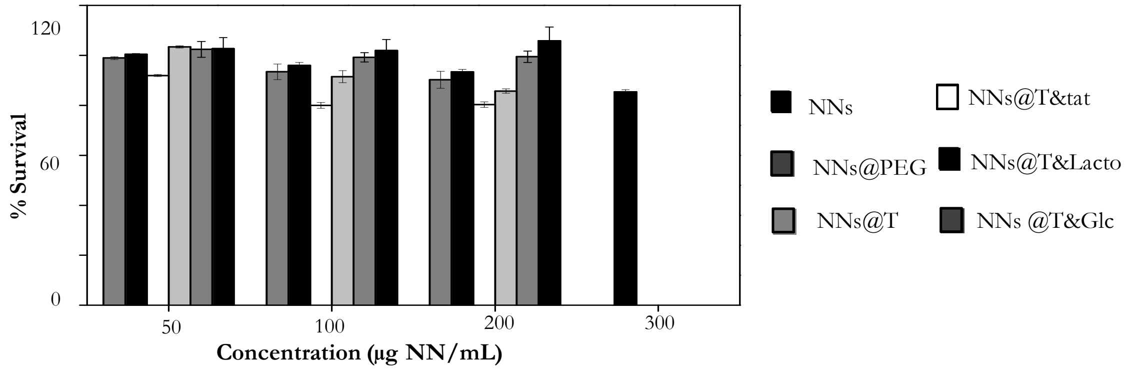

Figure 8.4. *Results of the MTT assay of Vero cells challenged with (1) NNs obtained directly from the synthesis (NNs); (2) PEGlylated NNs (NNs@PEG); PEGylated NNs modified with (3) TAMRA (NNs@T); (4) TAMRA and tat (NNs@T&tat); (5) TAMRA and lactose (NNs@T&Lacto) and (6) TAMRA and glucose (NNs@T&Glc). All types of NNs were evaluated for concentrations in the range of 50-200 µg/mL; only sample NNs@T&Lacto was evaluated additionally up to 300 µg/mL because of this sample was used this concentrated in other experiments in the following described.*

Cell viability is above 80% in all the cases, even when the concentration of NNs is as high as 300 µg/mL. In addition, cell viability appears to be very little dependent on the derivatization of NNs and concentration; only NNs@T&tat appears slightly more interfering in the test which can be speculatively connected to an improved uptake. These results indicate that these functional NNs do not impair mitochondrial respiration. As previously discussed, MTT-assays are widely used as a preliminary test to evaluate the biocompatibility of engineered NPs. Thus, functional NNs used in this work appear to be suitable candidates for bioapplications.

As a complementary test to the MTT assay, the effect of different NNs on cell cycle was also evaluated; DNA damage can be evidenced in cell cycle progression. Cell cycle study is other way to evaluate the NNs effect on cells. Cell cycle analysis provides a rapid and convenient assay to study cell cycle and cell proliferation in NNs treated cells and untreated. In normal cells, DNA density changes depending on whether the cell is growing, dividing, resting, or performing its ordinary functions. Flow cytometry can allow for determining whether the cell is in G0/G1, S, or G2/M, giving a clearer picture of how cells in different stage of cell cycle are distributed throughout the sample and the level of proliferation activity. For instance, in apoptotic cells, DNA is degraded by endogenous nucleases and diffused out of cells. During the life of cell, a cycle occurs (Figure 8.5); cell cycle is divided in interphase and M phase. Interphase is the longest stage; it includes G_1, S and G_2 phases. During the cells cycle, the DNA content and presentation is different in each phase; this DNA content is what is studied in the cell cycle assay which allows to determine the percentage of cells from a cell culture that are in each stage. Modifications in cell cycle can lead to tumor formation.[30]

For the cell cycle assay, 5×10^6 cells challenged with NNs@T&Glc (24 hours, two concentrations, *i.e.* 50 and 100 µg/mL) were trypsinized and fixed with a p-formaldehyde solution; then, cells were treated for 30 minutes with propidium iodide and RNAse prior to flow cytometry analysis. Results are summarized in Table 8.3; in all the cases, cells are in diploid stage and percentages of cells in different stages are similar to those in cells non-treated with NNs. These results show that NNs do not interfere in the cell cycle of Vero cells.

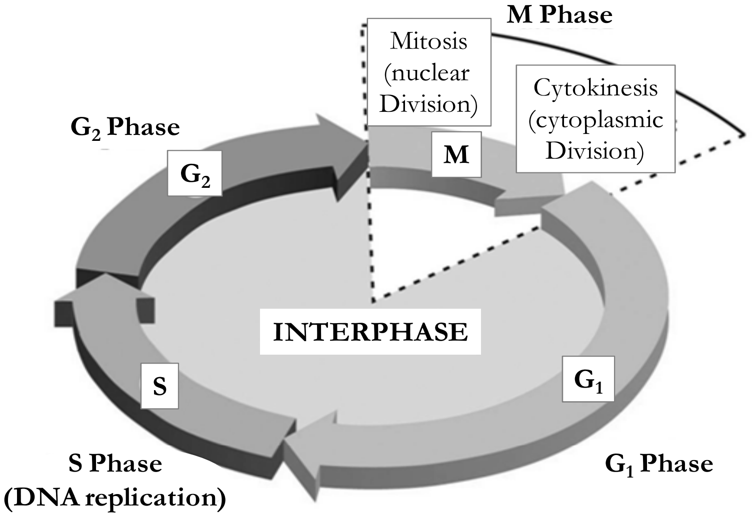

Figure 8.5. *Scheme of cell cycle and its stages according to their order and their duration.*

Sample	%Diploid	%G1	%G2	%S
Ctrol	100	68.00	9.28	22.72
50 µg NN/mL	100	68.54	8.13	23.33
100 µg NN/mL	100	69.58	9.27	21.15

Table 8.3. *Cytometer results data in VERO cells samples; control; incubated cells during 24 h with 50 µg NNs@TGlc/ mL and 100 µg NNs@TGlc /mL.*

Normally, when a strange body burst in the blood circulatory system, an inflammatory response is produced. This response is mediated by the complement system, which consists of a number of small proteins found in the blood, generally synthesized by the liver, and normally circulating as inactive precursors. When these precursors are triggered, proteases in the system cleave specific proteins to release cytokines and initiate an amplifying cascade of further cleavages (Figure 8.6). Here, the potential inflammatory reaction induced by NNs was studied by assessing the activation of the complement system. This system can be activated through three alternative pathways, *i.e.* classical, alternative or lectin-mediated.

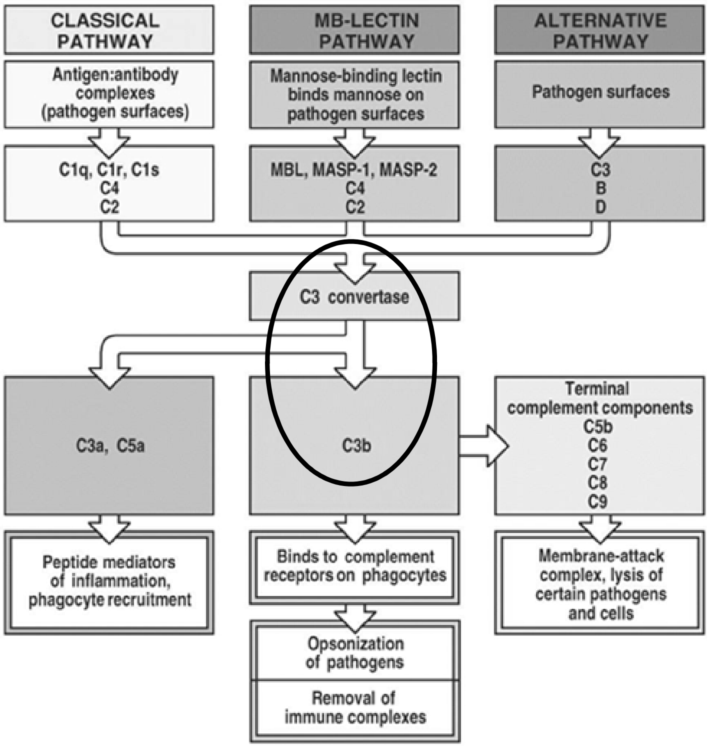

Figure 8.6. *Schematic representation of three complement pathways. In the black circle is marked the hydrolysis reaction and both proteins which are involved in complement assay.*[31]

Although the main function of the complement system is the opsonization and clearance of invading agents, the complement system also mediates inflammation, favors phagocytosis and targets cell death.[32] A critical step in the activation of this system consists of the cleavage of the complement component 3 protein (C3). Although this protein shows spontaneous and basal degradation, its cleavage is considerably increased after activation of the complement cascade by any of the three pathways.

To examine whether NNs have potential effects on the complement activation cascade, we analyzed C3 degradation by electrophoresis followed by Western blot analysis with antibodies directed against C3. None of the NNs assayed promoted C3 cleavage (Figure 8.7). While the band corresponding to C3 almost disappeared in the positive control (increasing in accordance with the intensity of the C3 split product), no major differences were found in plasma incubated with NPs compared to the negative control (plasma incubated with PBS). Similar results have been described for 30 and 50 nm citrate-capped gold NPs,[33] whereas carbon nanotubes and different different sized core shell polysaccharide NPs cause complement activation.[34,35]

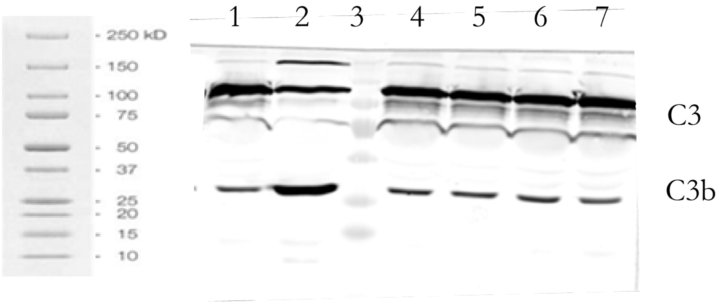

1. C -
2. C+
3. Ladder
4. NNs@T&Lacto
5. NNs@T
6. NNs@T&tat
7. NNs@PEG

Figure 8.7. *Image of revealed membrane with IgG2 C3/C3b. Well number 1 shows the pattern of a negative sample and well 2 has the positive control. NN pattern in all the cases are equal to negative control.*

To evaluate the effect of NNs on cell morphology, cells challenged for 24 hours with different concentration of NN@T&Glc (50, 100 and 200 μg/mL) for 12 hours. Then cells were fixed and observed by scanning electron microscopy (SEM). Sample preparation is described in detail in the Annex. Cells presented similar morphology independently of the concentration of NNs. There were not unusual philopodia or protusions in the texture of cytoplasm or nucleus. NNs do not seem to alter the cellular morphology following 12 hours incubation. Figure 8.8 show images taken at low and high magnifications for all concentrations and the control sample.

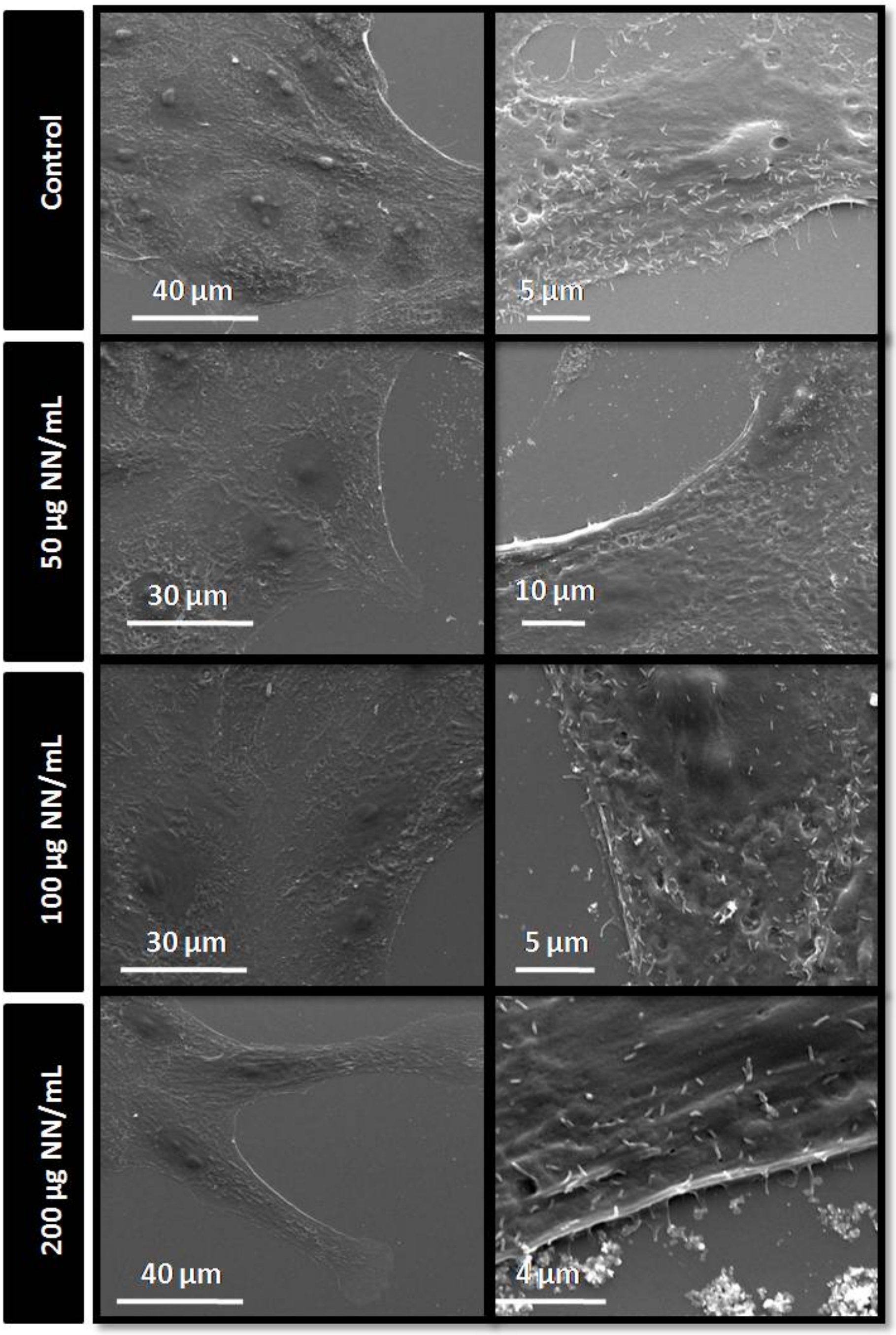

Figure 8.8. *SEM micrographs of VERO cells, control or incubated with 50, 100 and 200 µg/mL of NNs@T&Glc. Left panel images show a general view of various cells and right panel images show the corresponding high magnification images aiming the edges of the cytoplasm and philopodia.*

8.4. Uptake experiments

A number of series of uptake (internalization of NNs by cells) studies were performed to evaluate the influence of ligands attached onto NNs surface, *i.e.* PEGylated NNs modified with TAMRA (NNs@T), TAMRA and tat (NNs@T&tat) and TAMRA and lactose (NNs@T&Lacto). The sample selected (as scaffold for further derivatizations) for these studies is the previously referred to as NNs^{850} which consists on NNs which exhibit the plasmon band centered at *ca.* 850 nm (edge-length of *ca.* 120 nm). The cell line used was 3T3 cells; these cells are fibroblast from embryonic mouse. Fluorescence inside cells was evaluated over time by confocal microscopy which allows determining whether NNs are inside cells, accurately.

Under the same conditions of concentration and incubation time, the differences between these three types of functional NNs are apparent (Figure 8.9). These differences are motivated ultimately by the different functional groups which ultimately can have two effects, *i.e.* (1) introducing a receptor-mediated internalization and/or (2) changing the charge of the NPs; previously addressed characterization of these NNs clearly indicated that they bear different net charge.

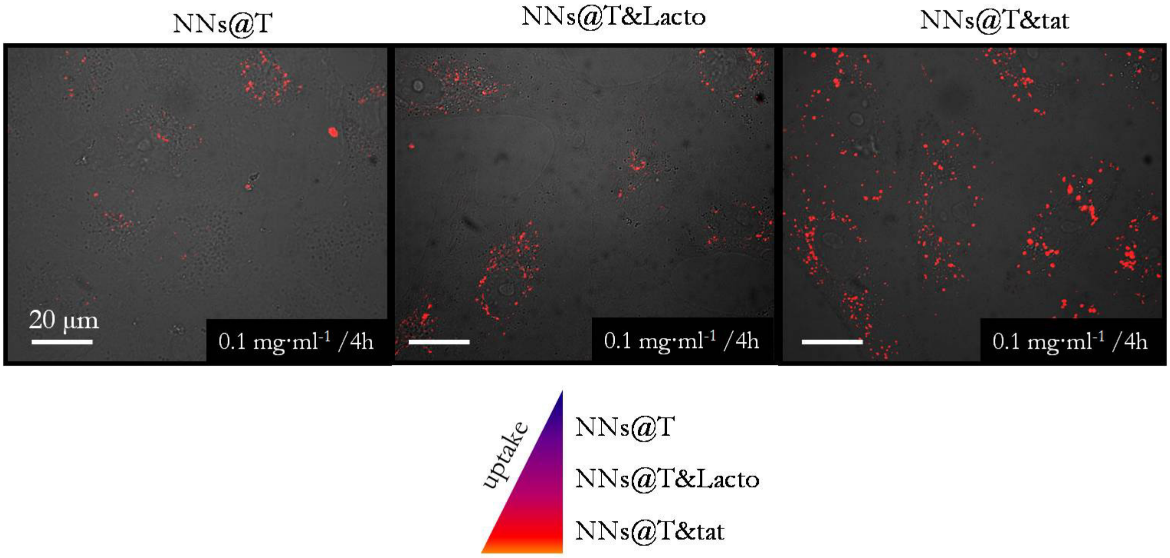

Figure 8.9. *Comparative uptake for equal concentration and incubation time of modified NNs. Scale bar is 20 µm in all cases.*

Typically, endocytic processes for internalization of NPs (or other bodies) can be broadly classified in phagocytosis and non-phagocytosis mechanisms. First one occurs mainly in specialized cells and its function is protecting the organisms from exogenous elements. Non-phagocitic pathways can occur in all cells and can be subcategorized into clathrin- and non-clathrin-dependent endocytosis; the last one can be further subdivided into three major mechanisms, *i.e.* macropinocytosis, caveolae-mediated endocytosis and clathrin- and caveolae independent endocytosis.[36] To date, pathways and rate of NPs uptake have been proven to be cell type dependent and furthermore, these vary also with NPs size, charge and other properties.[37,38]

First set of images shows the uptake of NNs@T using a concentration of 0.1 mg/mL concentration (Figure 8.10); here, it seems that the uptake of these NNs is very slow and most probably, this is due to the unspecific absorption of serum proteins after long periods of time in the medium. In fact, PEGylation itself should prevent the internalization of these NNs.[39] NNs are located in the surroundings of the nuclei in small vesicles.

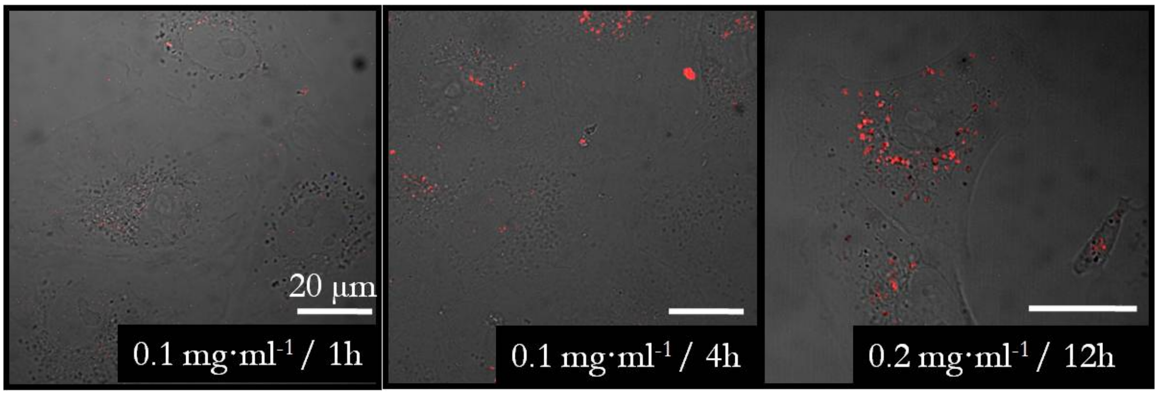

Figure 8.10. *Uptake of NNs@T versus time.*

An equivalent study was done for the sample NNs@T&Lacto (Figure 8.11); in this case, the uptake appears to be much faster and efficient. NNs were found in vesicles around nuclei as in the previous study; vesicles appear to increase in size upon use of higher concentrations or longer incubation times. It has been previously reported that NPs modified with saccharides, once internalized in cells, are stored in endocytic vesicles;[40,41] this seems to be the case here.

Finally, in the case of NNs@T&tat, the uptake is definitely faster than previous cases (Figure 8.12); this fact is supported by the effect of the vectorization with a cell penetrating peptide like tat.[42] Interestingly, NNs appeared again inside vesicles; this is in agreement with the experimental evidences (previously addressed in Chapter 4) that suggested that internalization of tat peptide derivatized NPs (Fe_3O_4@Au NPs) is mediated in a caveolin mediated pathway.[43]

In contrast to previous NNs, tat derivatized NNs also appeared attached on the cellular membrane.

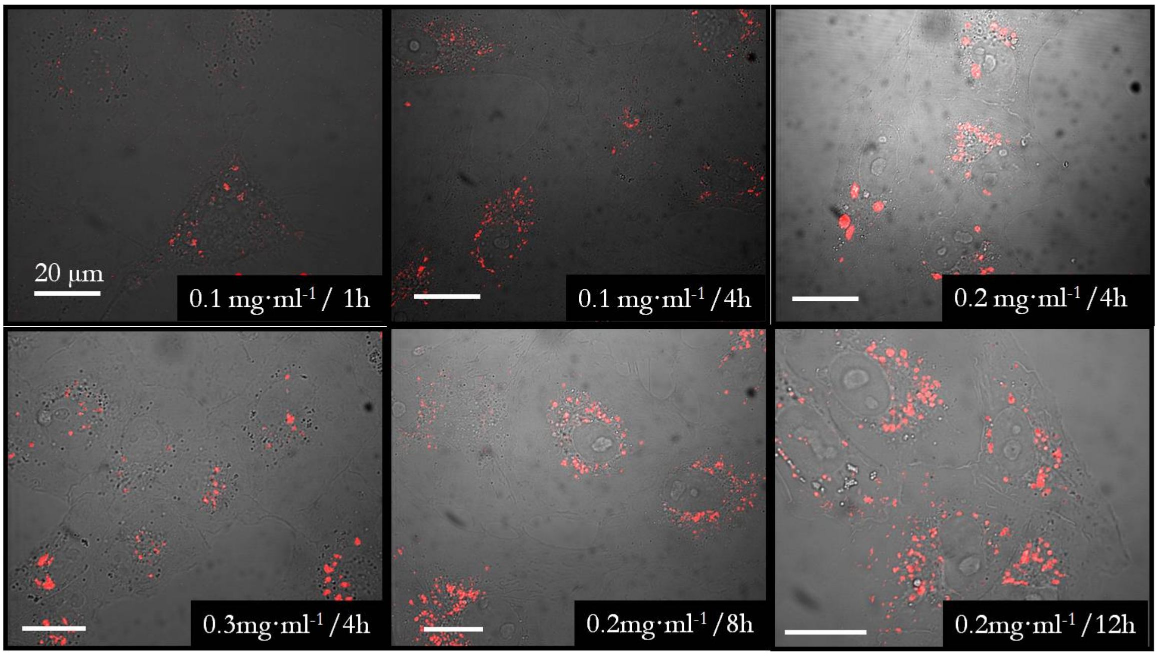

Figure 8.11. *Uptake of NNs@T&Lacto vs. time at different concentrations. Scale bar is 20 µm in all cases.*

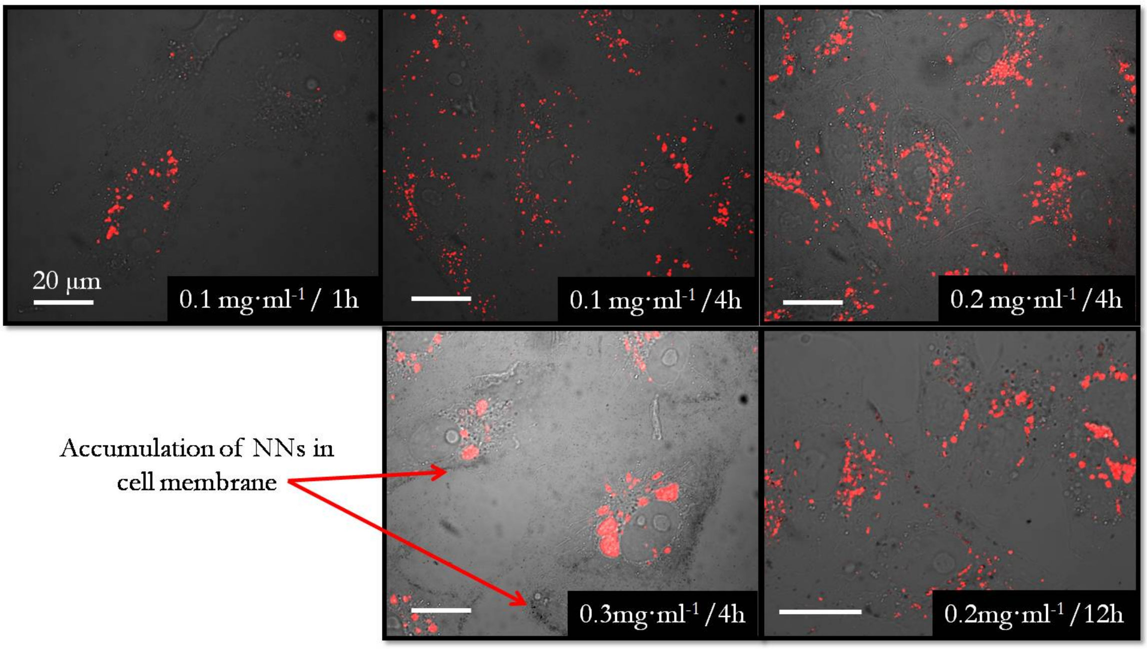

Figure 8.12. *Uptake of NN@TatT vs time. Scale bar is 20 µm in all cases.*

Ultimately, the charge can also greatly influence in the uptake of NPs. In general, more positively charged NPs present the highest degree of cell interaction and/or internalization.[29,44-48]

8.5. PTT *in vitro* studies

Irradiation experiments were also carried out using NNs which exhibit their plasmon band centered at *ca.* 1050 nm; consequently, for this experiments the 1064 nm DPSSL system previously described was used (Chapter 7); the laser system was equipped with a single-mode TE_{00} fiber which illuminates the sample with a power per unit of area of *ca.* 30 W×cm^{-2} at the sample position.

Vero cells were cultured in µ-Dishes from Ibidi (3.5 cm^2, ibiTreat coated for optimized adhesion of most cell types). Cells were grown for 24 hours prior to addition of NPs; then, cells were supplemented with previously sterilized NN@T&Glc to a final concentration of 0.1 mg×mL^{-1}. Cells were challenged with functional NNs for 8 hours; then, cells were washed out of non-internalized NNs and washed with PBS.

Figure 8.13 depicts the effect of laser irradiation on cells (with and without NNs) following laser irradiation (2 minutes, 30 W/cm^2). Dashed white circles represent the area under. The Live/Dead assay (Invitrogen, See annex A) was used to assess the viability of cells without NNs (Figure 8.13(a) and (b)) and cells loaded with functional NNs (Figure 8.13(c) and (d)) exposed to laser irradiation; this test provides a two-color fluorescence cell viability assay that is based on the simultaneous determination of live (green staining in the cytosol) and dead (red staining in the nuclei) cells with two probes, calcein AM and ethidium homodimer (EthD-1), that measure recognized parameters of cell viability, *i.e.* intracellular esterase activity and plasma membrane integrity, respectively. Immediately after irradiation, bright field (BF) images clearly indicate that cells filled with NNs and exposed to irradiation are damaged; irradiated cells were then incubated for 12 hours to assess whether cells can recover from irradiation. In the control experiment where cells were cultured in the absence of NNs (Figure 8.13(a) and (b)), cells are 100% viable since all cells are green (Calcein AM) stained and there is not sign of cell damage in the BF or fluorescence merged image. In contrast, for the cells cultured in the presence of NNs, the damage is apparent in the BF image and fluorescence merged images (Figure 8.13(c) and (d)).

For the experiment shown in Figure 8.13(e) and (f), cells were stained for the nucleus DNA with Blue Hoechst dye. Cells were observed immediately after laser exposure. In the right panel (bright field image), the effect of laser irradiation is apparent; also, in the right panel (merged image from blue and red fluorescence channels) functional NNs (red fluorescence) escaped from irradiated cells, probably, due to membrane damage, whereas cells in the non-illuminated regions kept NNs.

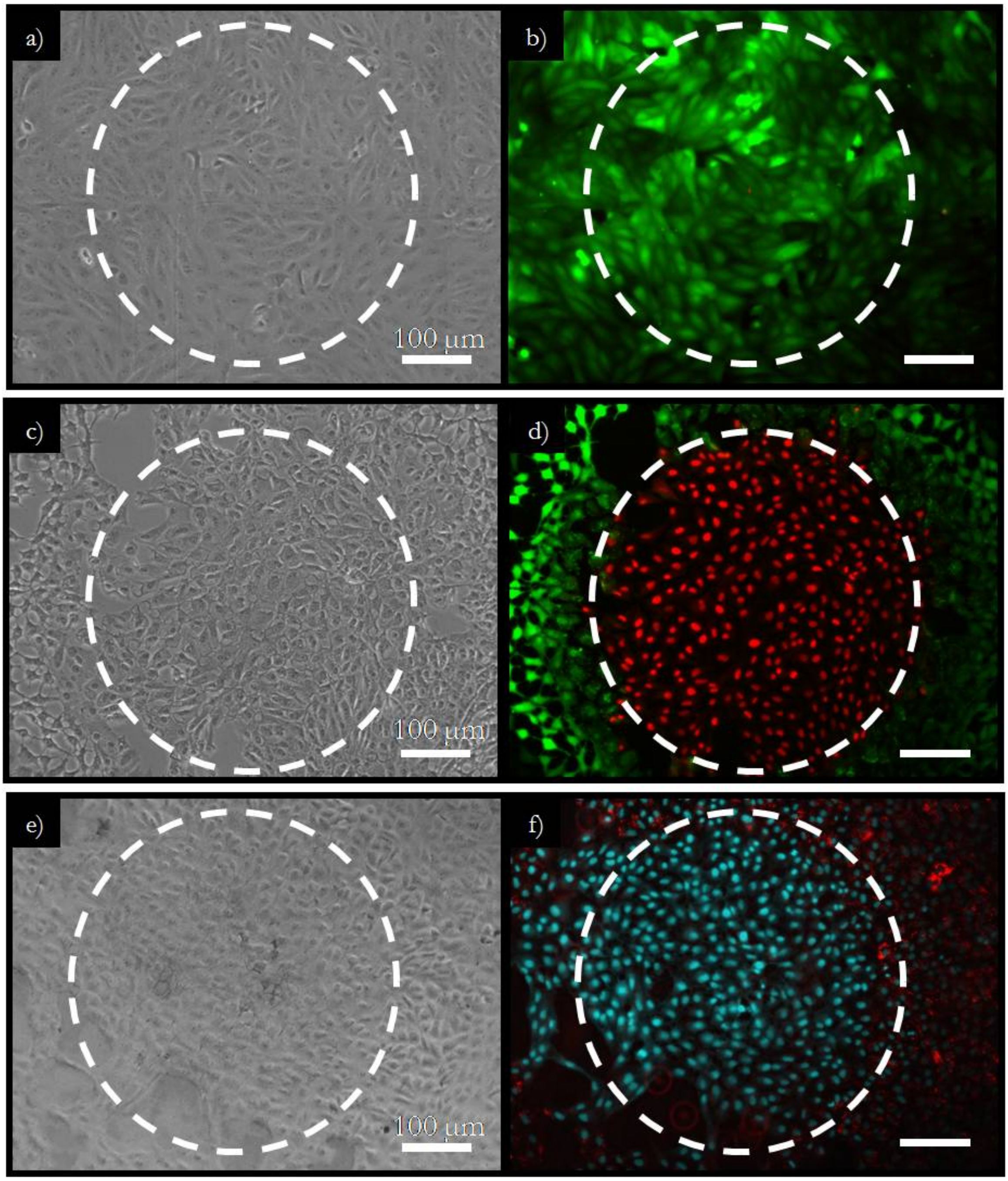

Figure 8.13. *a) and c) BF images and b) and d) corresponding fluorescence merged image of green and red channels corresponding to Calcein AM (viable cells) and EthD-1 (dead cells) of control Vero cells laser irradiated (a and b) and Vero cells filled with NNs (c and d). e) BF image of cells filled with NNs@T&Glc following laser irradiation; f) corresponding fluorescence image (red and blue fluorescence corresponding to NNs and nuclei, respectively. The white dashed circle represents the laser spot. Scale bar is 100 µm in all the cases.*

Results are conclusive in this matter; the viability of cells loaded with NNs was clearly impaired as their nuclei were stained red with EthD-1; Figure 8.14(C) shows a magnification of the irradiated region with dead cells whereas regions outside the beam spot (Figure 8.14(A)) shows viable cells (Calcein AM) containing NN@T&Glc (red fluorescence).

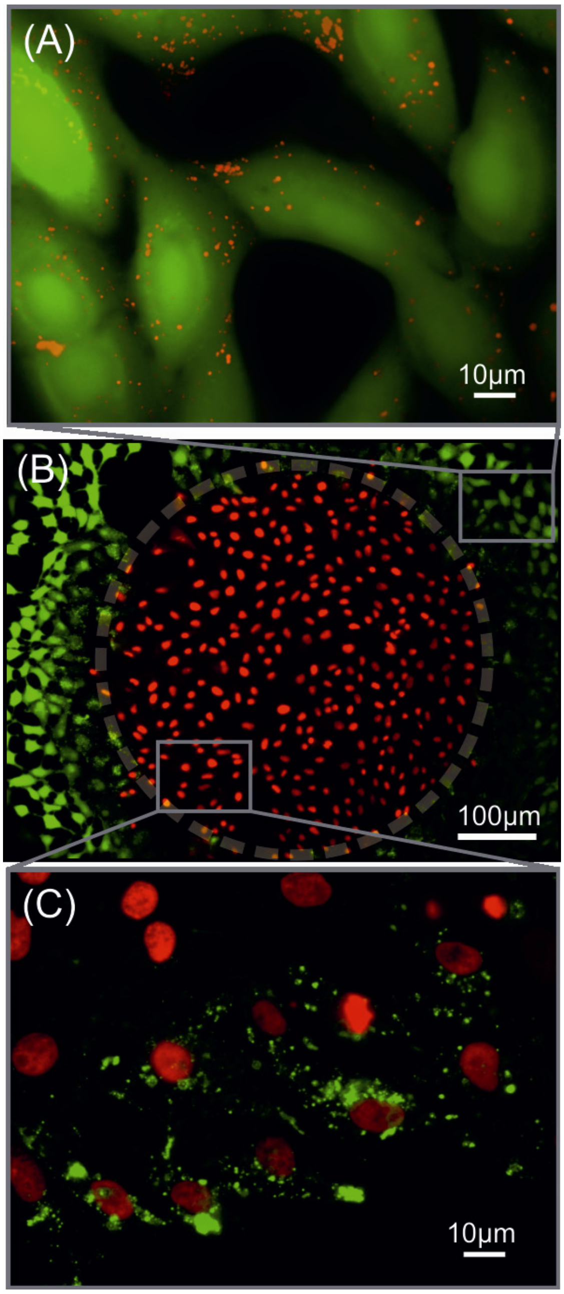

Figure 8.14. *(A) Cells outside the irradiation area remain viable (green staining) with NNs (TAMRA, red staining) in their cytosol; (B) red stained cells (EthD-1) correspond to the irradiation spot whereas cells outside the irradiation area remain viable (Calcein AM, green staining), the dashed line corresponds to the irradiation area;. CB) merged image of red and green fluorescence channels shows that the viability of irradiated cells was impaired (EthD-1 red staining).*

Immediately after fluorescence observation, cells were fixed and prepare for their observation under SEM (details on sample preparation can be found in the Annex). The effect of the laser is apparent (Figure 8.15); the damage area is clearly discernible and of the same magnitude as the red stained area in Figure 8.14 (B).

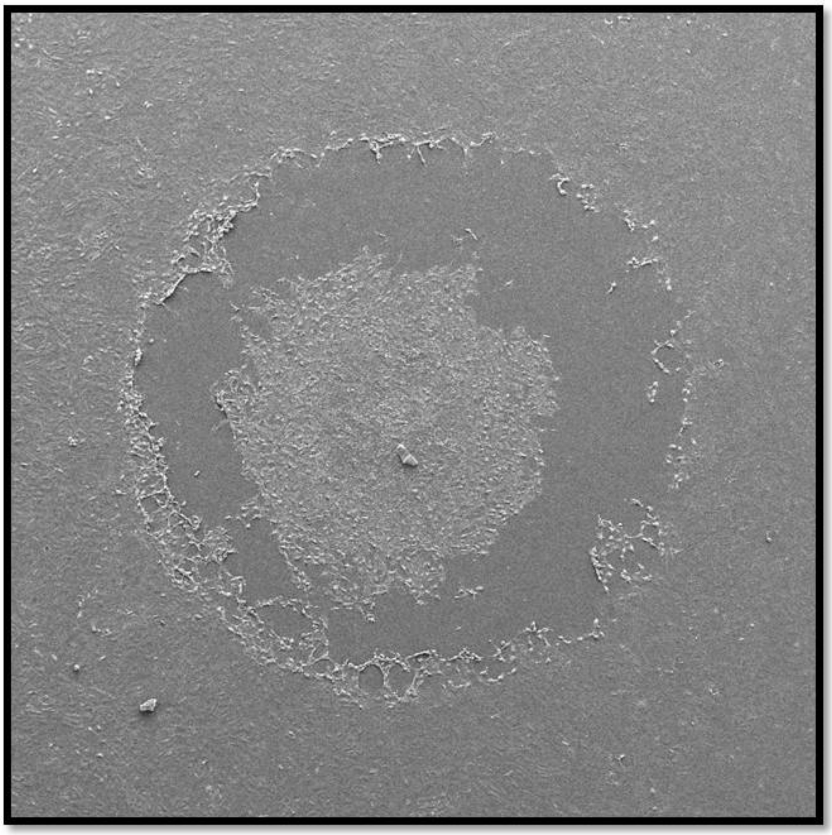

Figure 8.15. *SEM image showing the damaged area after laser irradiation.*

To account for morphology changes following laser irradiation, immunostaining of the cytoskeleton of irradiated cells was also done (Annex). Samples were observed by confocal microscopy. Nuclei were also stained with DAPI.

Actin fibers were stained using phalloidine Alexa 488. Actin is one of the principal proteins which form the cytoskeleton (Figure 8.16). Figure 8.16(a) shows the general aspect of the cytoskeleton before laser irradiation; Figure 8.16(b) clearly indicates that in the irradiated regions, actin fibers are damaged to a degree which do not allows for immunostaining. In contrast regions away of the spot center could be actin-immunostained. The white dashed circle represents the laser spot; past this line, cells present exactly the same appearance as control cells.

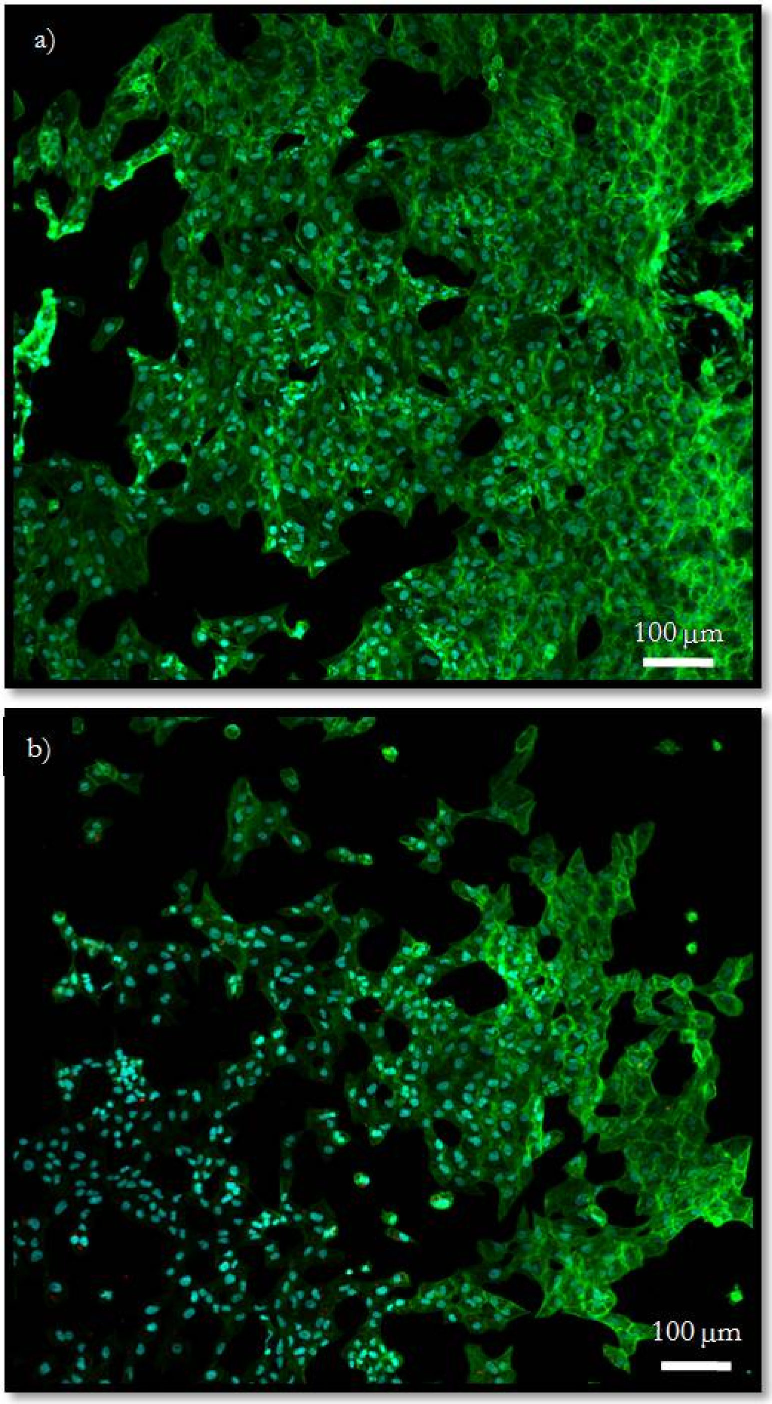

Figure 8.16. *Merged channels of Vero cells green stained (actin) and blue stained (nuclei). Cells incubated with NNs a) before and b) after laser irradiation.*

Magnifications of three different regions of Figure 8.16(b) are shown in Figure 8.17 (a, b and c). Viable cells exhibit a well-packed density of actin fibers which produced an impressive green staining (Figure 8.17(c)). The membrane of cells placed in the center of the laser spot appear to present a perforated morphology (BF image of Figure 8.17(a)) where actin staining was almost inexistent; this is indicative that cells after irradiation lost their integrity and their proteins were probably denaturized. Cells close to the border of the laser spot still show the presence of actin-staining although its appearance in the BF image clearly revealed that they were also damaged (Figure 8.17(b)), although to a lesser extent than cells at the center of the spot.

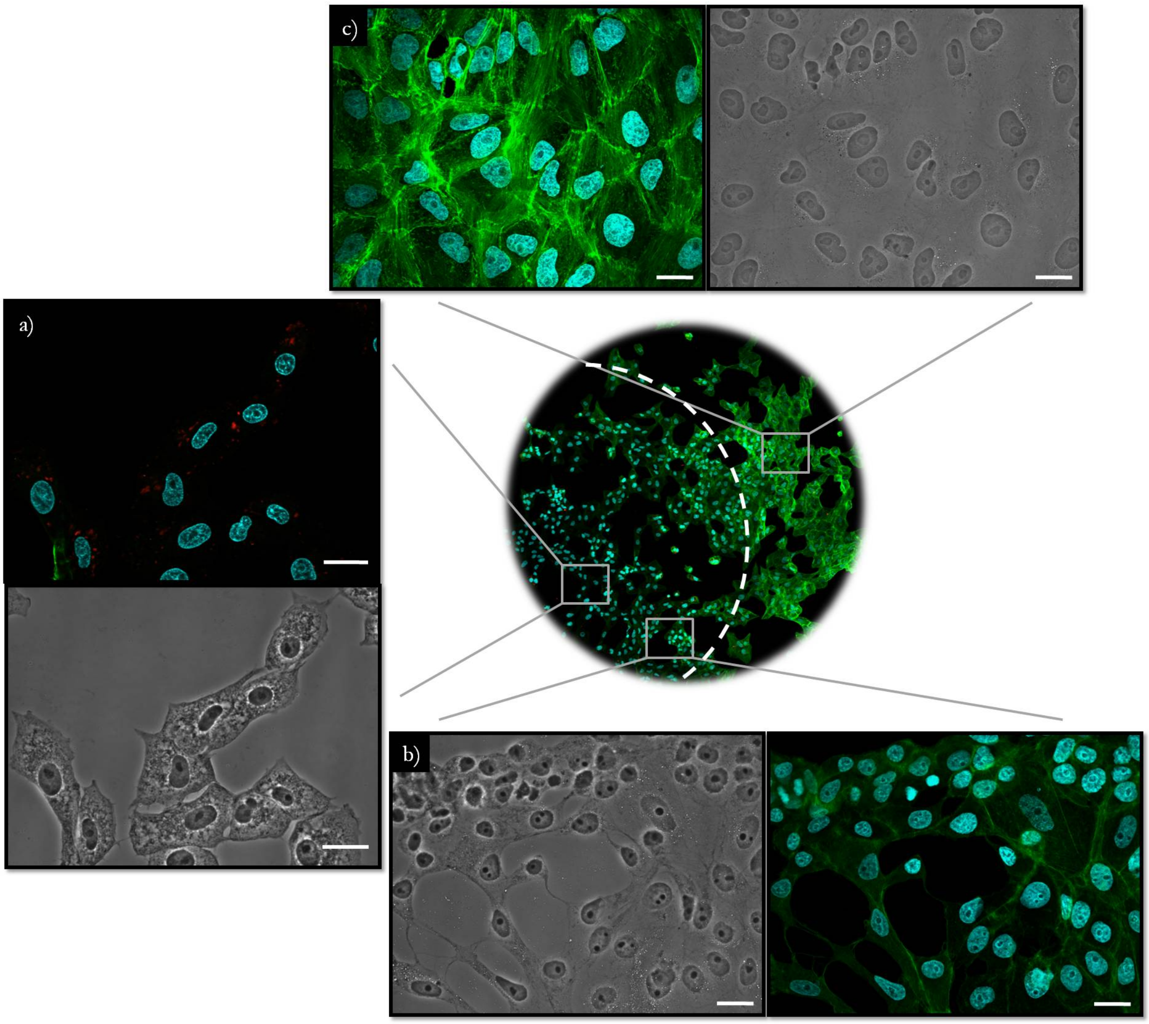

Figure 8.17. *Vero cells green (actine) and blue (nuclei) channel merged after laser irradiation (central panel). The insets show bright field and fluorescence merged channels of a) cells in the middle of laser spot; b) cells near to the edge of laser spot and c) cell out of laser spot. Scale bar is 20 µm in all the images.*

Morphology changes following laser irradiation were also evaluated by scanning electron microscopy. Sample preparation is described in the Annex. SEM images allow for easily identifying the area which was under laser influence; after sample preparation (thin film of gold by sputtering) the laser spot region appeared with a major contrast. This is probably due to damages in the cell membrane that allows for major gold deposition. Low and high magnification

SEM images of regions from the center of the beam (where the membrane of cells appear to have many holes) up to regions away from the influence of the laser (viable cells) are shown in Figure 8.18. Results are summarized in the following images.

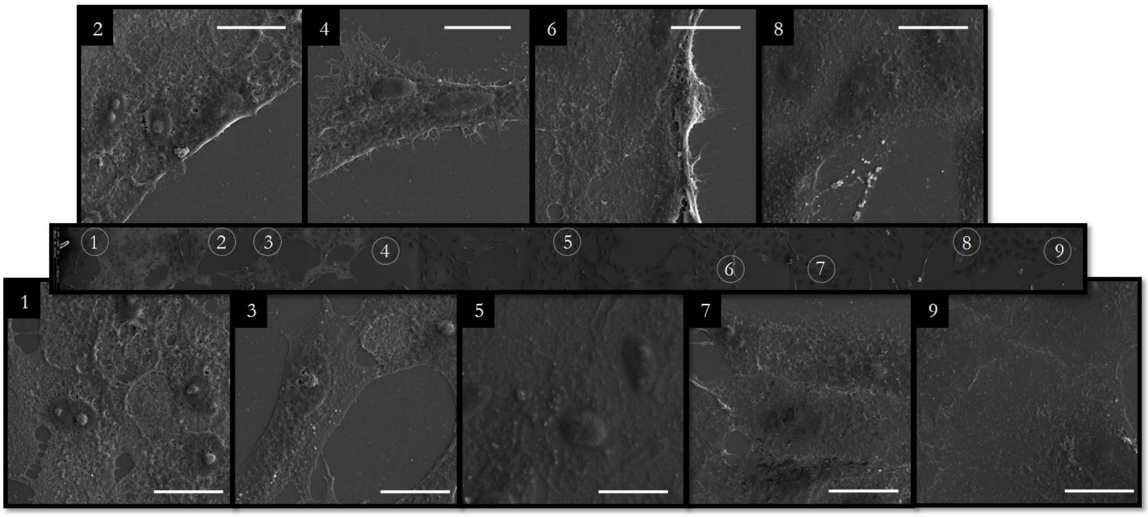

Figure 8.18. *Group of SEM micrographs where it is possible to see that the cell morphology variations depend on the distance to the center of the laser beam. White circles show the regions where high magnification images were taken; regions were selected at a number of distances from the laser spot, from left to right, at 100 µm, 320 µm, 420 µm, 550 µm, 900 µm, 1400 µm, 1850 µm, 2250 µm, and 3750 µm. Bar scale are in all the cases 20 µm.*

In Figure 8.18, it is possible to see the distance-dependence on the effect of the laser on cells. Laser damage was observed up to 2.2 mm where cells started to show their normal appearance (Figure 8.18 {8}). The area showing the most damages expands up to 1.1 mm from the center of the beam (Figure 8.18 {1, 2 ,3 and 4}). Cells close to the center of the beam appeared full of holes in the cytoplasm and rounded nucleus. These cells are placed in a radius of *ca.* 0.9 mm. From 900 µm to 1100 µm apart from the center, cells presented more protrusions than normal cells which typically is indication of cellular damage. As the distance increases, the normal cell morphology is recovered. Cells observed at 1400 µm (Figure 8.18 {9}) and 1600 µm (Figure 8.19) show no holes in the cytoplasm. Further than this distance, cell morphology appears completely normal. Apparently, they did not suffer laser damage (Figure 8.19). Clearly, NNs inside cells are responsible of cell damage. Importantly, laser damage appears to be dependent on the NIR beam profile; this should be solved in the future by coupling the laser to a suitable optical objective. Future studies will address in detail (systematically) the effect of NIR irradiation of NNs inside cells.

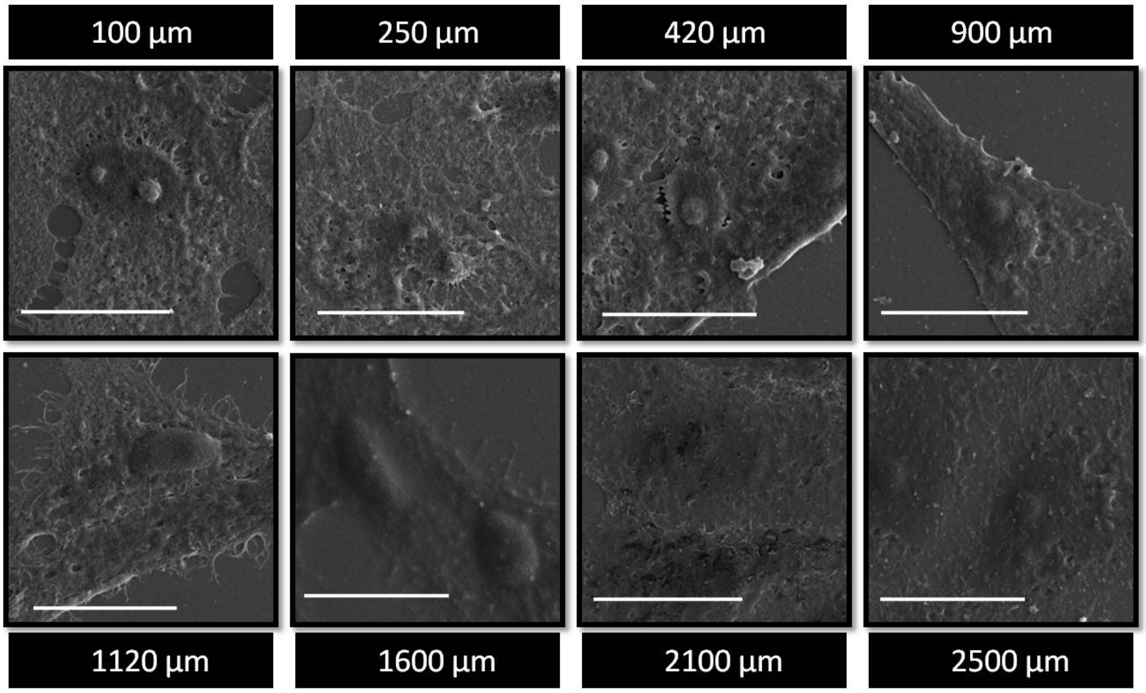

Figure 8.19. *Magnifications of SEM micrographs where it is possible to follow the distance-dependence on the effect of the laser on cells filled with NNs. Scale bar is 20 µm in all cases.*

8.6. Single cell experiments (809 nm laser system)

To evaluate the potential use of NNs as light-to heat converters at the single cell level, NIR laser irradiation experiments were performed using a light source (809 nm, 100 mW) coupled to an upright microscope (Axitotech, Zeiss, 40× objective) leading to a focused light spot of a few micrometers in diameter in the image plane; by changing the operation voltage of the laser, the resulting power of the focused light spot could be tuned in the range of 0-35 mW (power densities up to *ca.* 10^6 W/cm^2). This equipment allows for observation of cell changes following extremely high irradiation *in situ*;[49] this homemade equipment is placed in the facilities of the Philipps-University of Marburg (Prof. Parak).

The main goals of these irradiation experiments were two; first, to study the thermophysical effect on NNs and cells following laser irradiation (note that the spot is of few micrometers and therefore bellow the size range of cells) of NNs stored in vesicles within one single cell; two, to develop a controlled release methodology by adjusting the laser fluence and irradiation time. Both are important goals to achieve in the application of NNs as drug release agents, nanoscalpels in surgery or hyperthermia studies.

The scheme shown in Figure 8.20 described the protocol followed in the irradiation of NNs inside single cells; first, 3T3 cells were seeded on ibidi plates (3.5 cm^2, ibiTreat coated for optimized adhesion of most cell types) and incubated (37ºC, 5%CO_2) during 12 h with NN@T&Lacto (0.3 mg/mL). Cells were observed under confocal microscopy to evaluate and study NNs internalization. Then, cells were trypsinized and transferred to Petri plates; this step prevent the attachment of NNs to the cell membrane and assures that NNs can be only be inside cells; the transfer to Petri-dishes was motivated by experimental reason since this plates are better suited for NIR-laser-coupled microscope. After 3h on the Petri plates, laser irradiation experiments were carried out

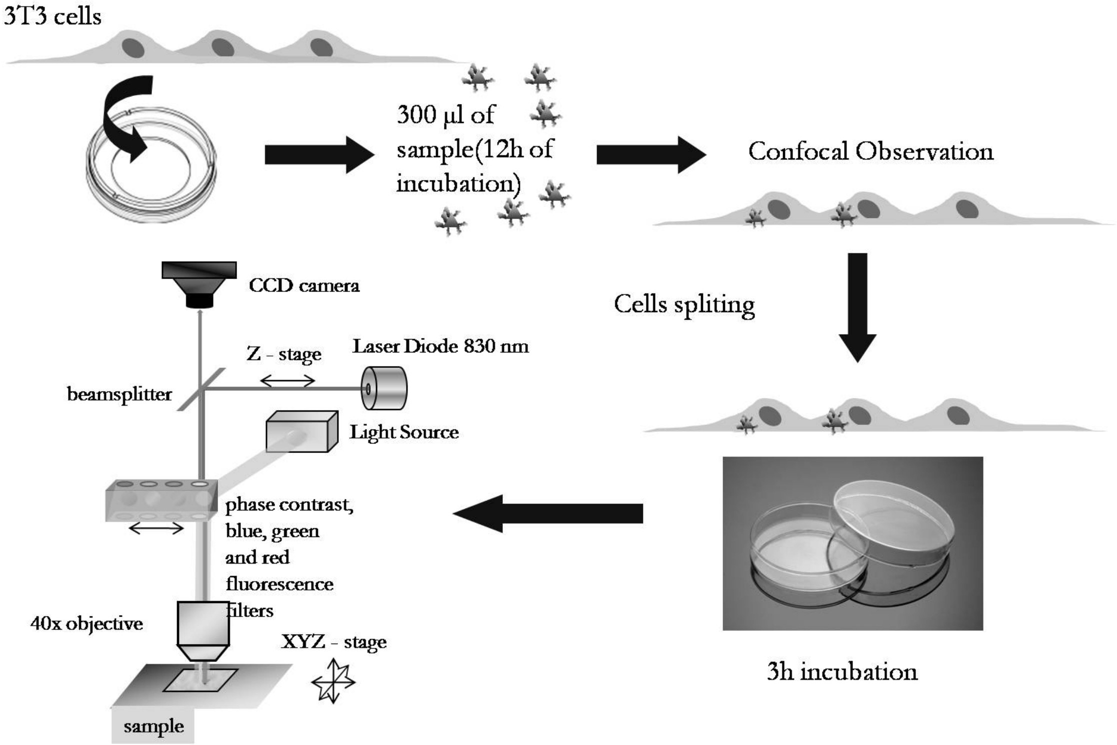

Figure 8.20. Scheme of NIR laser irradiation methodology.

As it was previously explained NN@T&tat appeared attached on the membrane, even after trypsinization. To see the potential of NNs as nanoheaters, these were irradiated. Immediately following irradiation, the formation of bubbles was apparent; see the white spot on the second panel of Figure 8.21(a). Sequences of images show the bubble formation during the laser irradiation which ultimately produced irreversible cell injury; cell retraction was also visible in real time even when the formation of bubbles was not apparent. In sequence (a) of Figure 8.21, one can notice that the nucleus lost its entity entirely; sequence (b) shows a cell irradiated in two different points. Bubble formation has widely reported as result of plasmonic heating driven by laser illumination; under high fluence laser irradiation, especially ns and fs lasers, the surface temperature of GNP can easily surpass the boiling point of water and the liquid water around GNP becomes strongly superheated (see the review by Qin & Bischof for further details).[11]

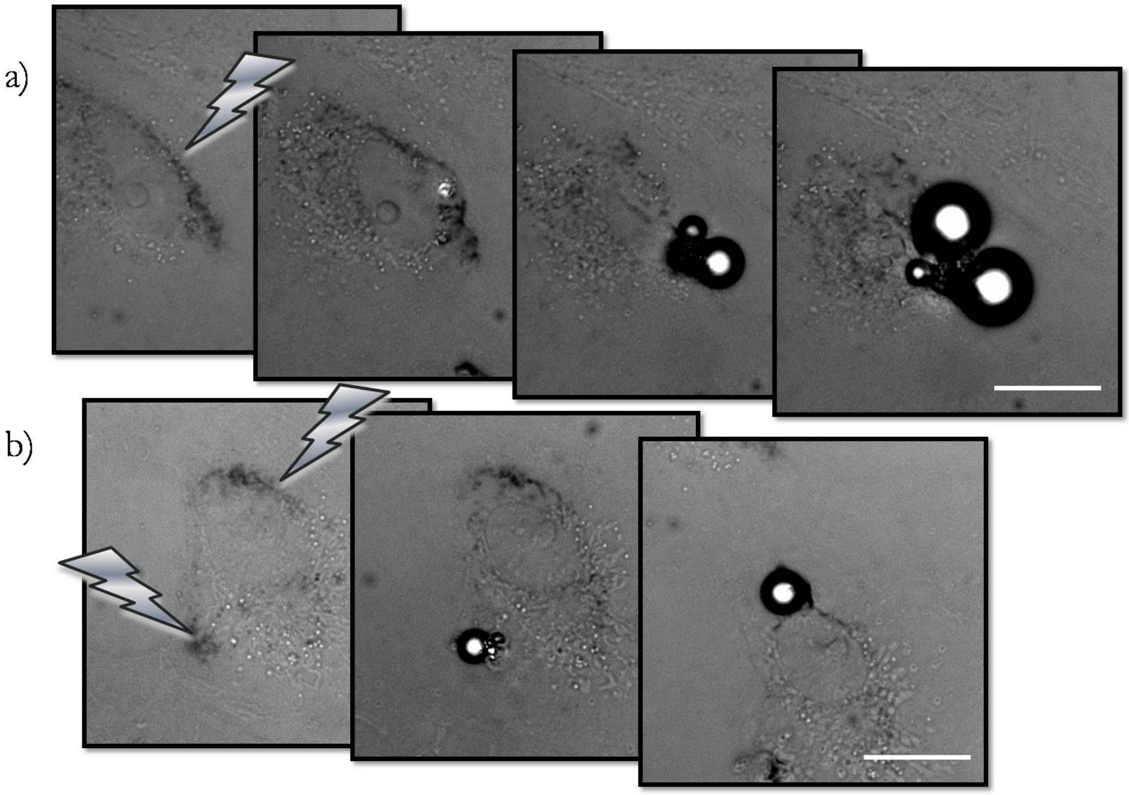

Figure 8.21. *Image sequences showing the effects of the localized laser irradiation; (a) a 3T3 cell loaded with NNs@T&tat was irradiated in one point until its complete destruction; b) a 3T3 cell was irradiated in two points. Scale bar is 10 µm.*

In another experiment, cells were challenged with NNs@T&Lacto and treated as previously discussed. Cells were in this case irradiated with lower laser fluence (*ca.* 7 mW). Interestingly, cells exposed to irradiation of their cytosolic vesicles (containing NNs) experienced a significant increase of red fluorescence (TAMRA) which was extended to the whole cytosol of cells; fluorescence images were taken with the same parameters of time exposure. Figure 8.22 (a) and (c) correspond to cells before irradiations whereas (b) and (d) correspond to irradiated cells. The fluorescence image after irradiation is even saturated due the large increase of fluorescence intensity (right panel in Figure 8.22(b) and (d)). It is also remarkable that cellular morphology remains unalterable as it can be observed in phase contrast images.

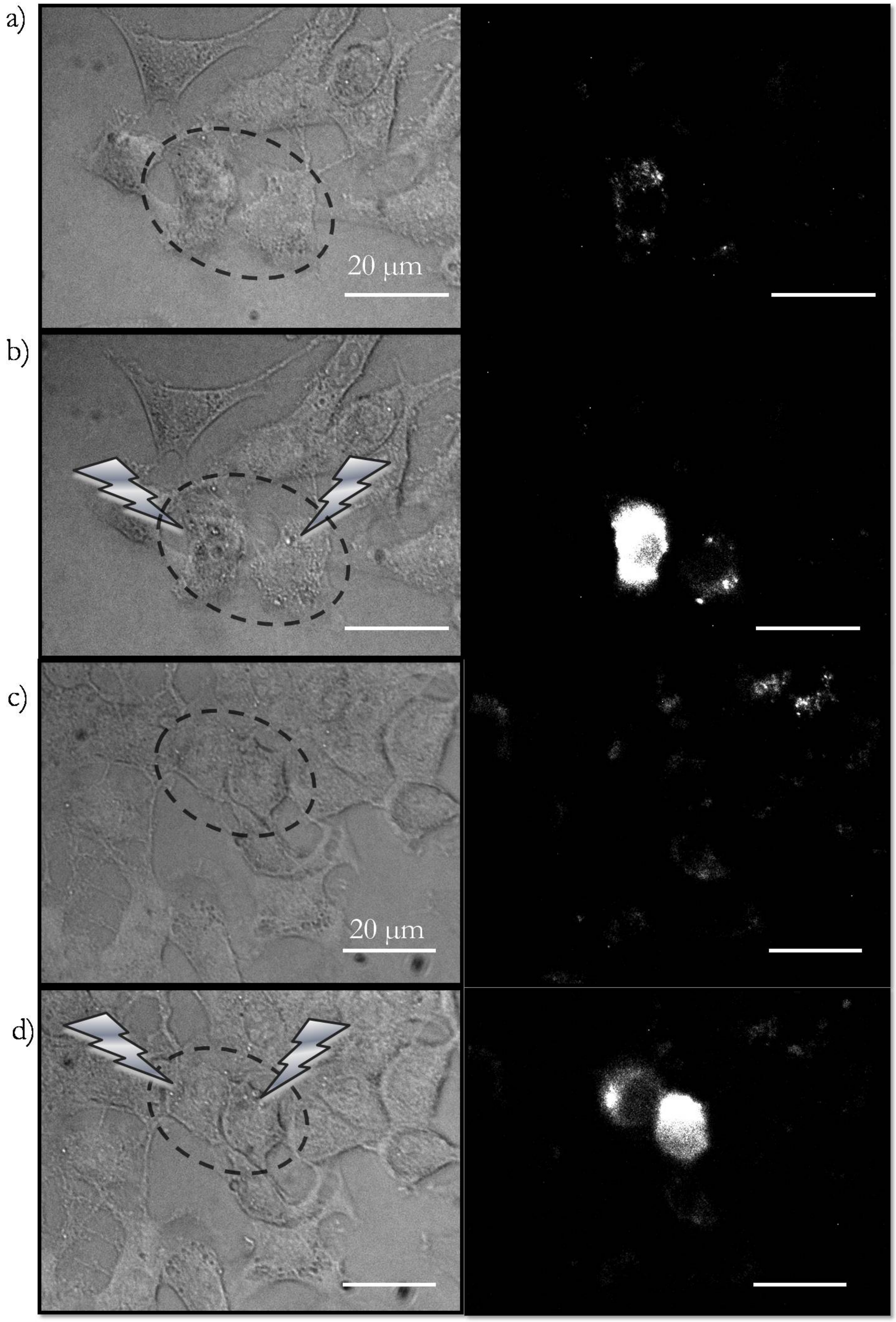

***Figure 8.22.** Phase contrast and red fluorescence images of 3T3 cells loaded with NNs@T&Lacto a) and c) before and b) and d) after laser irradiation with 7 mW in marked points.*

When the laser power was reduced to 3.6 mW this effect was still observable (Figure 8.23). However, the intensity of the increase of red fluorescence appears to be less dramatic.

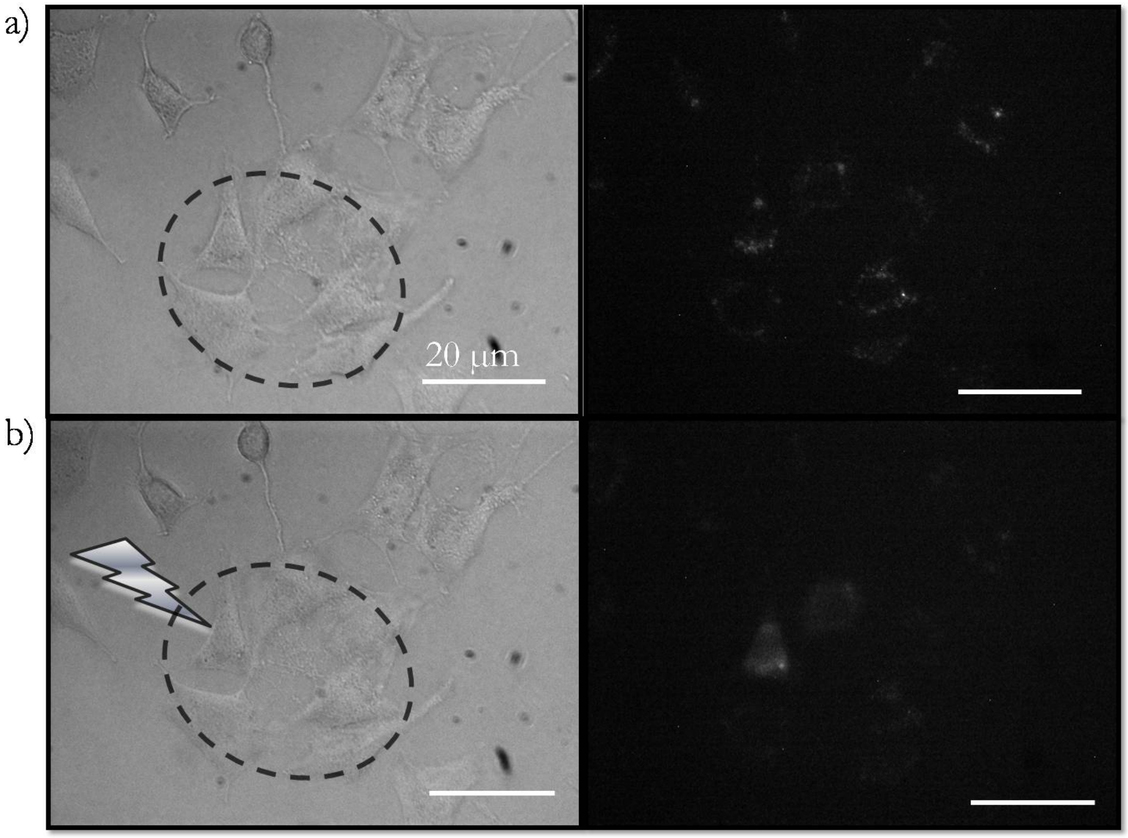

Figure 8.23. *Another example of phase contrast and fluorescence image of 3T3 cells a) before and b) after laser irradiation with 3.6 mW in marked points.*

It is well-known the ability of GNPs to produce quenching effects on fluorescence dyes. Thus, a plausible explanation for the observed fluorescence enhancement after laser irradiation can be the release of NNs from the vesicles where they were stored. The increased fluorescence filling the cytoplasm does not disappears (at least in the time scale of hours); this indicates that NNs release did not produce apparently any membrane damage which ultimately would have produced the release of NNs to the media.

These experiments at the single cell level demonstrate that, with the appropriate light source, NNs can be used to damage single cells or to drive a controlled release experiments. Further work in this direction will be the subject of ongoing studies.

8.7. Conclusions

In vitro viability of NNs was evaluated by a MTT assay, cell cycle & complement activation tests, and cellular morphology analysis; results for cells challenged with NNs corroborated the absence of cytotoxic effects, metabolism alterations or apparent morphology changes. NNs uptake was also studied for NNs derivatized differently, *i.e.* NNs@T, NNs@T&Lacto and NNs@T&tat. Under the same conditions most internalized NPs are NNs@T&tat followed by lactose modified NNs and, as expected, NNs@T presented the slowest internalization rate. These differences are motivated by the different functional groups which can have two effects, *i.e.* (i) introducing a receptor-mediated internalization and/or (ii) changing the charge of the NNs.

The use of NNs as NIR-to-heat -transducers was firstly evaluated in VERO cells challenged with NNs@T&Glc and irradiated with a 1064 nm laser system. Laser effects were evaluated in terms of cell viability. Cellular morphology changes along the laser spot were evaluated by SEM and cytoskeleton immunostaining. It was found different degrees of cellular damage as function of distance from the center of the laser spot (*ca.* 1 mm). These changes are ascribable to the beam profile. Using a different set up (809 nm laser) and a 3T3 cell line, the irradiation effect on cells loaded with NNs was evaluated at the single-cell level. Preliminary results indicated the feasibility of NNs for remote controlled release of NNs@*drugs* (complex nanosystems containing NNs) from the interior of cellular compartments.

REFERENCES

(1) Baffou, G.; Quidant, R.; de Abajo, F. J. G. *ACS Nano* **2010**, *4*, 709-716.

(2) Gobin, A. M.; Lee, M. H.; Halas, N. J.; James, W. D.; Drezek, R. A.; West, J. L. *Nano Letters* **2007**, *7*, 1929-1934.

(3) Hirsch, L. R.; Stafford, R. J.; Bankson, J. A.; Sershen, S. R.; Rivera, B.; Price, R. E.; Hazle, J. D.; Halas, N. J.; West, J. L. *Proceedings of the National Academy of Sciences of the United States of America* **2003**, *100*, 13549-13554.

(4) O'Neal, D. P.; Hirsch, L. R.; Halas, N. J.; Payne, J. D.; West, J. L. *Cancer Letters* **2004**, *209*, 171-176.

(5) Dickerson, E. B.; Dreaden, E. C.; Huang, X.; El-Sayed, I. H.; Chu, H.; Pushpanketh, S.; McDonald, J. F.; El-Sayed, M. A. *Cancer Letters* **2008**, *269*, 57-66.

(6) El-Sayed, I. H.; Huang, X.; El-Sayed, M. A. *Cancer Letters* **2006**, *239*, 129-135.

(7) Huang, X.; El-Sayed, I. H.; Qian, W.; El-Sayed, M. A. *Journal of the American Chemical Society* **2006**, *128*, 2115-2120.

(8) Bartczak, D.; Muskens, O. L.; Millar, T. M.; Sanchez-Elsner, T.; Kanaras, A. G. *Nano Letters* **2011**, *11*, 1358-1363.

(9) Bartczak, D.; Muskens, O. L.; Nitti, S.; Sanchez-Elsner, T.; Millar, T. M.; Kanaras, A. G. *Small* **2012**, *8*, 122-130.

(10) Krpetić, Z. e.; Nativo, P.; Sée, V.; Prior, I. A.; Brust, M.; Volk, M. *Nano Letters* **2010**, *10*, 4549-4554.

(11) Qin, Z.; Bischof, J. C. *Chemical Society Reviews* **2012**.

(12) Tong, L.; Cheng, J.-X. *Nanomedicine* **2009**, *4*, 265-276.

(13) Baffou, G.; Girard, C.; Quidant, R. *Physical Review Letters* **2010**, *104*.

(14) Varki, A. *Glycobiology* **1993**, *3*, 97-130.

(15) Dwek, R. A. *Chemical Reviews* **1996**, *96*, 683-720.

(16) Moros, M.; Pelaz, B.; Lopez-Larrubia, P.; Garcia-Martin, M. L.; Grazu, V.; de la Fuente, J. M. *Nanoscale* **2010**, *2*, 1746-1755.

(17) Rocker, C.; Potzl, M.; Zhang, F.; Parak, W. J.; Nienhaus, G. U. *Nat Nano* **2009**, *4*, 577-580.

(18) Gref, R.; Lück, M.; Quellec, P.; Marchand, M.; Dellacherie, E.; Harnisch, S.; Blunk, T.; Müller, R. H. *Colloids and Surfaces B: Biointerfaces* **2000**, *18*, 301-313.

(19) Linse, S.; Cabaleiro-Lago, C.; Xue, W.-F.; Lynch, I.; Lindman, S.; Thulin, E.; Radford, S. E.; Dawson, K. A. *Proceedings of the National Academy of Sciences* **2007**, *104*, 8691-8696.

(20) Walczyk, D.; Bombelli, F. B.; Monopoli, M. P.; Lynch, I.; Dawson, K. A. *Journal of the American Chemical Society* **2010**, *132*, 5761-5768.

(21) Monopoli, M. P.; Walczyk, D.; Campbell, A.; Elia, G.; Lynch, I.; Baldelli Bombelli, F.; Dawson, K. A. *Journal of the American Chemical Society* **2011**, *133*, 2525-2534.

(22) Alkilany, A. M.; Nagaria, P. K.; Hexel, C. R.; Shaw, T. J.; Murphy, C. J.; Wyatt, M. D. *Small* **2009**, *5*, 701-708.

(23) Chithrani, B. D.; Ghazani, A. A.; Chan, W. C. W. *Nano Letters* **2006**, *6*, 662-668.

(24) Zhao, F.; Zhao, Y.; Liu, Y.; Chang, X.; Chen, C.; Zhao, Y. *Small* **2011**, *7*, 1322-1337.

(25) Nel, A. E.; Madler, L.; Velegol, D.; Xia, T.; Hoek, E. M. V.; Somasundaran, P.; Klaessig, F.; Castranova, V.; Thompson, M. *Nat Mater* **2009**, *8*, 543-557.

(26) Deng, Z. J.; Liang, M.; Monteiro, M.; Toth, I.; Minchin, R. F. *Nat Nano* **2011**, *6*, 39-44.

(27) Lacerda, S. H. D. P.; Park, J. J.; Meuse, C.; Pristinski, D.; Becker, M. L.; Karim, A.; Douglas, J. F. *ACS Nano* **2009**, *4*, 365-379.

(28) Xie, J.; Xu, C.; Kohler, N.; Hou, Y.; Sun, S. *Advanced Materials* **2007**, *19*, 3163-3166.

(29) Hauck, T. S.; Ghazani, A. A.; Chan, W. C. W. *Small* **2008**, *4*, 153-159.

(30) Mahmoudi, M.; Azadmanesh, K.; Shokrgozar, M. A.; Journeay, W. S.; Laurent, S. *Chemical Reviews* **2011**, *111*, 3407-3432.

(31) *Immunobiology: The Immune System In Health and Disease*; 6th ed.; Janeway, C. A., Travers, P., Walport, M., Shlomcik, M., Ed.; Garland Science: New York, 2005.

(32) Sim, R. B.; Tsiftsoglou, S. A. *Biochemical Society Transactions* **2004**, *32*, 21-27.

(33) Dobrovolskaia, M. A.; Patri, A. K.; Zheng, J.; Clogston, J. D.; Ayub, N.; Aggarwal, P.; Neun, B. W.; Hall, J. B.; McNeil, S. E. *Nanomedicine : nanotechnology, biology, and medicine* **2009**, *5*, 106-117.

(34) Bertholon, I.; Vauthier, C.; Labarre, D. *Pharmaceutical Research* **2006**, *23*, 1313-1323.

(35) Salvador-Morales, C.; Flahaut, E.; Sim, E.; Sloan, J.; Green, M. L. H.; Sim, R. B. *Molecular Immunology* **2006**, *43*, 193-201.

(36) Sahay, G.; Alakhova, D. Y.; Kabanov, A. V. *Journal of Controlled Release* **2010**, *145*, 182-195.

(37) Hillaireau, H.; Couvreur, P. *Cellular and Molecular Life Sciences* **2009**, *66*, 2873-2896.

(38) Franca, A.; Aggarwal, P.; Barsov, E. V.; Kozlov, S. V.; Dobrovolskaia, M. A.; Gonzalez-Fernandez, A. *Nanomedicine* **2011**, *6*, 1175-1188.

(39) Storm, G.; Belliot, S. O.; Daemen, T.; Lasic, D. D. *Advanced Drug Delivery Reviews* **1995**, *17*, 31-48.

(40) Osaki, F.; Kanamori, T.; Sando, S.; Sera, T.; Aoyama, Y. *Journal of the American Chemical Society* **2004**, *126*, 6520-6521.

(41) Moros, M.; Hernáez, B.; Garet, E.; Dias, J. T.; Sáez, B.; Grazu, V.; González-Fernández, A.; Alonso, C.; De La Fuente, J. M. *ACS Nano* **2012**.

(42) Frankel, A. D.; Pabo, C. O. *Cell* **1988**, *55*, 1189-1193.

(43) Smith, C. A. M.; de la Fuente, J.; Pelaz, B.; Furlani, E. P.; Mullin, M.; Berry, C. C. *Biomaterials* **2010**, *31*, 4392-4400.

(44) Gratton, S. E. A.; Ropp, P. A.; Pohlhaus, P. D.; Luft, J. C.; Madden, V. J.; Napier, M. E.; DeSimone, J. M. *Proceedings of the National Academy of Sciences* **2008**, *105*, 11613-11618.

(45) Martin, A. L.; Bernas, L. M.; Rutt, B. K.; Foster, P. J.; Gillies, E. R. *Bioconjugate Chemistry* **2008**, *19*, 2375-2384.

(46) Cho, E. C.; Xie, J.; Wurm, P. A.; Xia, Y. *Nano Letters* **2009**, *9*, 1080-1084.

(47) Chung, T.-H.; Wu, S.-H.; Yao, M.; Lu, C.-W.; Lin, Y.-S.; Hung, Y.; Mou, C.-Y.; Chen, Y.-C.; Huang, D.-M. *Biomaterials* **2007**, *28*, 2959-2966.

(48) Arvizo, R. R.; Miranda, O. R.; Thompson, M. A.; Pabelick, C. M.; Bhattacharya, R.; Robertson, J. D.; Rotello, V. M.; Prakash, Y. S.; Mukherjee, P. *Nano Letters* **2010**, *10*, 2543-2548.

(49) Munoz Javier, A.; del Pino, P.; Bedard, M. F.; Ho, D.; Skirtach, A. G.; Sukhorukov, G. B.; Plank, C.; Parak, W. J. *Langmuir* **2008**, *24*, 12517-12520.

Conclusions

Even though specific conclusions have been addressed at the end of each chapter, the most relevant, global, conclusions of the research described in this thesis are presented herein.

Part I: Fe_3O_4@Au NPs

(1) Superparamagnetic Fe_3O_4@Au NPs were synthesized by a thermal decomposition method in organic solvent; the composite NPs presented a Fe_3O_4 core of *ca.* 4 nm of diameter and a Au outer shell of *ca.* 3 nm. Aiming for applications in physiological media, NPs were water transferred using a variety of organic molecules which provide the nanocomposites with a suitable hydrophilic coating. Among these ligands, mixed chains were designed and custom synthesized by organic chemistry in our Lab; organic compounds were fully characterized. Physical and chemical properties were evaluated for the different nanocomposites. Importantly, the NPs transferred to the aqueous phase show a good stability in aqueous solution; these can be centrifuged, precipitated and lyophilized which confirm that the phase transfer strategy work properly. Values of magnetization saturation depend on the chain used for the water transfer. ICP measurements demonstrated that monosaccharide-modified chains form an improved densely packed monolayer which translates into a greater amount of organic material onto the NPs surface. Nevertheless, the core@shell nature of these particles could not be confirmed 100%; results are not conclusive in this regards and it is possible that the gold shell does not fully cover the iron oxide core. On the other hand, the products exhibited Au-like uniform contrast in STEM measurements, surface plasmon resonance and superparamagnetic behavior.

(2) For all the engineered NPs, viability was addressed by using a standard MTT colorimetric assay; results show that these engineered nanocomposites do not impair the viability of HeLa cells. Importantly, nanocomposites modified with tat, an internalization peptide, were used to study their internalization pathway, finding that a caveolin process is the responsible. On the other hand, magnetic field effect in the internalization of tat derivatized nanocomposites was found to be

negligible. Remarkably, fiber alignments were found in cells which were exposed to the magnetic field.

(3) For sugar-modified nanocomposites, their potential as hyperthermia agents was evaluated. The SAR values of these were below current commercially available products; this is probably motivated the small size of the magnetic core. These results drove this work towards other alternative hyperthermia agents, such as those based on plasmonic heating, *i.e.* the second part of this work.

Part II: Au Nanoprisms or NanoNachos (NNs)

(4) This work provided a straightforward and novel method to produce single crystal Au nanoprisms (NanoNachos (NNs)), in water at room temperature. The edge length and LSPR band of NNs can be tuned along the NIR range by simply adjusting the concentration/molar ratio of gold salt and reducing agent, meaning that a variety of NNs sizes can be accessed synthetically enabling tailoring for specific purposes. The synthetic method to produce NIR NNs was built upon the original work of Zhou *et al.*; over the past two decades, many independent groups have claimed that the nature of the NIR absorption band is related to the core@shell structure of Au_2S@Au nanoshells. However, the results presented here, such as XPS analysis, UV-Vis-NIR spectroscopy and electron microscopy, demonstrate that the NIR band which display the NPs produced by the method of Zhou *et al.* is due to the anisotropic structure of Au nanoprisms (or NNs). Importantly, this synthetic method avoids the use of toxic surfactants such as CTAB, the most widely used surfactant for the synthesis of gold nanorods and nanoprisms. Avoiding the use of toxic surfactants greatly simplifies the functionalization and application of NPs for bio-purposes since extensive purification or complex ligand exchange methods are not required.

(5) The NPs produced by the synthetic method proposed here were derivatized with HS-PEG-COOH to increase their colloidal stability (NPs@PEG) over time and harsh chemical environments (such as those required for derivatization with other molecules). The increased colloidal stability allowed washing the NPs by centrifugation (centrifuged twice for 15 min at 10000 rpm and resuspending pellets in MilliQ water); prior to PEGylation, centrifugation aggregated the NPs irreversibly. Furthermore, NNs@PEG could be separated from other by-products by gel electrophoresis. Due to the increased electrophoretical mobility of NPs other than NNs, *i.e.* polyhedral Au-NPs, two bands were resolved in the gel.

(6) The purified products were characterized extensively by electron microscopy (SEM, TEM, STEM and EELS); results demonstrated conclusively the flat morphology of NNs (*ca.* 9 nm thick). The crystal structure of NNs (top and edge facets) was also studied by aberration corrected HRTEM. The analysis of the digital diffractogram of a single NN showed a hexagonal–shaped pattern that is characteristic of the [1 1 1] orientation of a *fcc* Au single crystal; in addition, the diffraction pattern exhibited a set of weak spots indexed as 1/3 {4 2 2} which have been linked to the combination of twin planes and [1 1 1] stacking faults.

(7) NNs were evaluated as plasmonic nanoheaters under NIR laser irradiation. NNs with two different aspect ratios (and consequently, different plasmon bands) NNs were irradiated using two laser sources of different wavelengths, *i.e.* 809 nm and 1064 nm. Colloidal solutions of NN@PEG under illumination, even at very moderate NP concentrations, could reach ΔT up to 50 ºC in the vicinity of the illumination spot. This result provides fundamental evidence of the feasibility of the biofunctionalized NN system for NIR-driven heating for bioapplications and opens the possibility of using this system for local hyperthermia and drug-release applications. The heating ability of NNs under irradiation is comparable to the best result founded in literature. Therefore, NNs can be added to the pool of nanoheaters as a versatile alternative which do not require challenging synthetic methods or laborious extensive ligand exchange to remove the highly toxic CTAB surfactant.

(8) As a proof of concept, the local heating ability of NNs under illumination was addressed. An active enzyme, GOx, was attached onto NNs surface and its activity was evaluated in different conditions, including after laser irradiation. The enzyme activity of laser-irradiated NNs@GOx decreased down to 40% whereas the activity remained 100% even after external heating (55º, half hour). This result indicates that the heat produced by NNs under illumination can irreversibly damaged the enzymatic activity of GOx in close proximity to the NNs surface. Nevertheless, considering the laser fluence used in this experiments, it is not possible to confirm theoretically that GOx denaturation is caused by the heat produced by one single NN or by a collective heating produced by several NNs in close proximity and irradiated simultaneously.

(9) *In vitro* viability of NNs was evaluated by a MTT assay, cell cycle & complement activation tests, and cellular morphology analysis; results for cells challenged with NNs corroborated the absence of cytotoxic effects, metabolism

alterations or apparent morphology changes. NNs uptake was also studied for NNs derivatized differently, *i.e.* NNs@T, NNs@T&Lacto and NNs@T&tat. Under the same conditions most internalized NPs are NNs@T&tat followed by lactose modified NNs and, as expected, NNs@T presented the slowest internalization rate. These differences are motivated by the different functional groups which can have two effects, *i.e.* (i) introducing a receptor-mediated internalization and/or (ii) changing the charge of the NNs.

(10) The use of NNs as NIR-to-heat -transducers was firstly evaluated in VERO cells challenged with NNs@T&Glc and irradiated with a 1064 nm laser system. Laser effects were evaluated in terms of cell viability. Cellular morphology changes along the laser spot were evaluated by SEM and cytoskeleton immunostaining. It was found different degrees of cellular damage as function of distance from the center of the laser spot (*ca.* 1 mm). These changes are ascribable to the beam profile. Using a different set up (809 nm laser) and a 3T3 cell line, the irradiation effect on cells loaded with NNs was evaluated at the single-cell level. Preliminary results indicated the feasibility of NNs for remote controlled release of NNs@*drugs* (complex nanosystems containing NNs) from the interior of cellular compartments.

Materials & Methods

Annex

A1. Synthetic procedures to produce organic compounds & NPs

(A1.1) Mixed chain synthesis:[1]

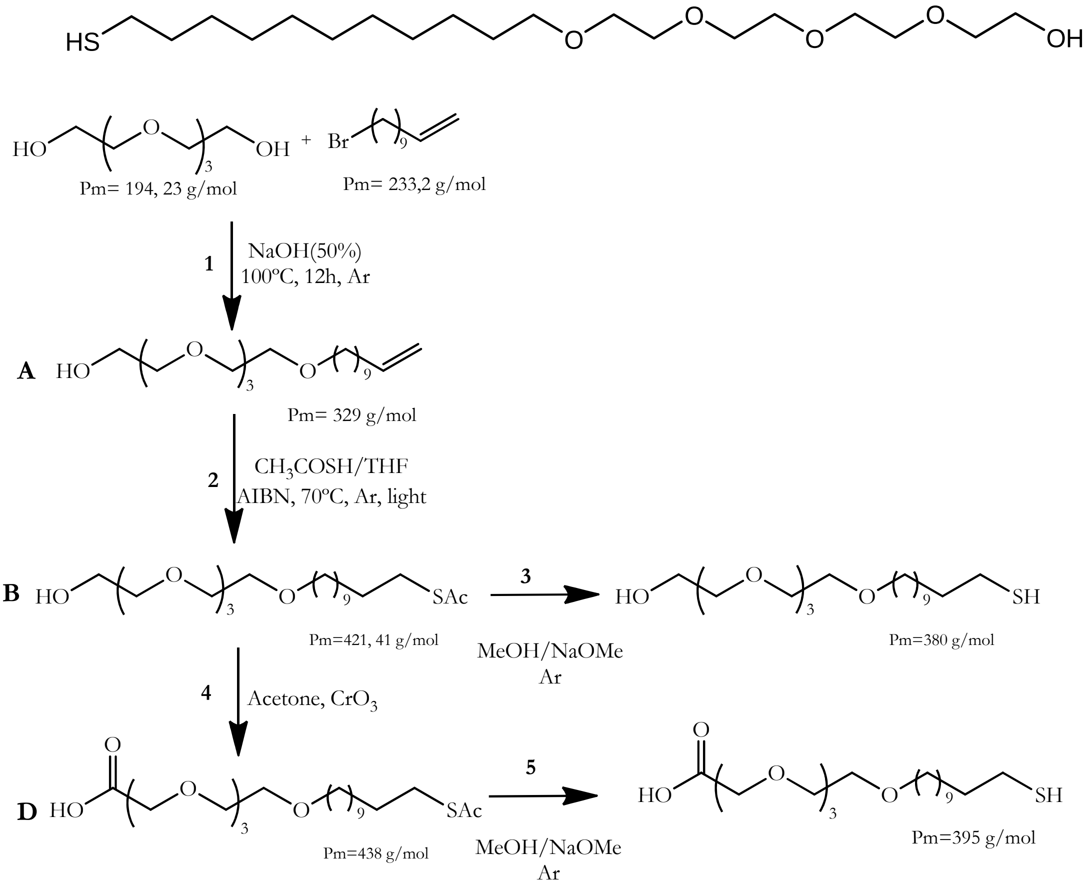

Step 1: Undecen-1-en-11-yl-tetra (ethylene glycol) (A) synthesis

A mixture of tetraethylenglycol (TEG) (15 g, 77.23 mmol) and NaOH (50%) (0.4 mL, 7.5 mmol) was stirred for 30 minutes at 100 ºC under argon atmosphere. The reaction was cooled down to room temperature and 11-Br-undecene (3.6 g, 15.45 mmol) was added. The reaction was heated up to 100 ºC and left 20 h under stirring. The mixture was diluted with dichlorometane (CH_2Cl_2, 10 ml), washed with water (20 mL) and extracted with hexane (3 x 20 ml). The hexane fractions were collected, dried over Na_2SO_4, filtered and the solvent evaporated at low pressure. The crude product was purified by flash column chromatography on silica gel (eluent: Ethyl Acetate or EtOAc) to give the undecen-1-en-11-yl-tetra(ethylene glycol) (A) (3.3 g, 65.4 % yield) as a yellow oil. **Rf** = 0.38 (EtOAc: Toluene 9:1); 'H NMR (300 MHz, $CDCl_3$) 6 1.3 (br s, 12H), 1.55 (qui, 2 H, ***J*** = 7 Hz), 2.0 (q, 2 H, ***J*** = 7 Hz), 2.85 (br **s,** 1 H), 3.4 (t, 2 H, ***J*** = 7 Hz), 3.5-3.75 (m, 16 H), 4.9-5.05 (m, 2 H), 5.75-5.85 (m, 1 H).

Step 2: 1-(Thioacetylundec-11-yl) tetra (ethylen glycol) (B) synthesis

To a solution of A (5 g, 15.2 mmol) in dry THF, thiolacetic acid (AcSH, 4.62 g, 60.8 mmol) and AIBN (cat.) were added. Reagents were dried under vacuum for 5 hours. The mixture was left under reflux for 4 hours (70 ºC). The reaction was diluted with 30 ml of EtOAc and a saturated solution of $NaHCO_3$ was added until neutral pH. The organic phase was washed with NaCl saturated solution, dried over Na_2SO_4 and the solvent was removed at low pressure. The residue was purified by flash column chromatography on silica gel (eluent: CH_2Cl_2: MeOH (2 %) to CH_2Cl_2: MeOH(5 %)) to obtain a light yellow oil (B). Pobt= 3.3g, %Rdto.= 53, 6%.**Rf** = 0.44 (CH_2Cl_2: MeOH (2 %)). **1H RMN** (CDCl3, 300 MHz) 1.24-1.36 (m, 14H); 1.53-1.67 (m, 4H); 2.66 (t,2H); 3.42 (t, 2H); 3.55-3.71 (m, 16H) ppm.

Step 3: (1-Mercaptoundec-1 I-yl) tetra(ethylene glycol) (C) synthesis

0.8 g of the protected product **B** were dissolved in 10 mL methanol and 0.2 g of sodium methoxide were added. The solution was stirred for 3 hours and then the pH was neutralized with Amberlite IR120. The reaction was filtrated, dried in the rotary evaporator and washed several times with diethyl ether. The final product **C** was obtained with a 92 % yield. **'H NMR** (300 MHz, $CDCl_3$) 6 1.2 (br s, 14 H), 1.3 (t, 1 H, J = 7 Hz), 1.5 (m, 4 H), 2.5 (q, 2 H, J = 7 Hz), 2.85 (br s, 1 H), 3.4 (t, 2 H, J = 7 Hz), 3.55-3.75 (m, 16 H)ppm.

Step 4: 22-(Thioacetyl)-2,5,8,11-tetraoxadocosan-1-oic acid (D) synthesis

0.9 g of **B** was dissolved in 4 mL acetone and Jones reagent was added drop by drop until red colour persisted. Then, the reaction was stirred for 1 hour and then it was stopped with 2-propanol, diluted with EtOAc, washed twice with water, and dried in the rotary evaporator. The purification was performed by column chromatography (CH_2Cl_2: MeOH 19:1) (49 % final yield). **1H NMR** (300 MHz,

$CDCl_3$), δ 1.2-1.4 (m, 14H), 1.55 (qui, 4H, *J* = 7.0 Hz), 2.3 (s, 3H), 2.84 (t, 2H, *J* = 7.0 Hz), 3.4 (t, 2H, *J* = 7.0 Hz), 3.5-3.8 (m, 12H), 4.0 (s, 2H) ppm.

Step 5: 22-Mercapto [2,5,8,11- tetraoxadocosan]-1-oic acid (E) synthesis

0.6 g of the protected product **D** were dissolved in 4 mL methanol and 0.15 g of sodium methoxide were added. The solution was stirred for 3 hours and then the pH was neutralized with Amberlite IR120. The reaction was filtrated, dried in the rotary evaporator and washed several times with diethyl ether. The final product **C** was obtained with a 89 % yield. **^{1}H NMR** (300 MHz, $CDCl_3$), δ 1.3-1.7 (m, 18H), 2.5 (t, 2H thiol, *J* = 7.0 Hz), 2.7 (t, 2H disulfide, *J* = 7.0 Hz) 3.5 (t, 2H, *J* = 14.0 Hz), 3.6-3.8 (m, 12H), 4.15 (s , 2H disulfide),4.19 (s, 2H thiol) ppm.

(1.2) Mixed chain sugar modified synthesis:

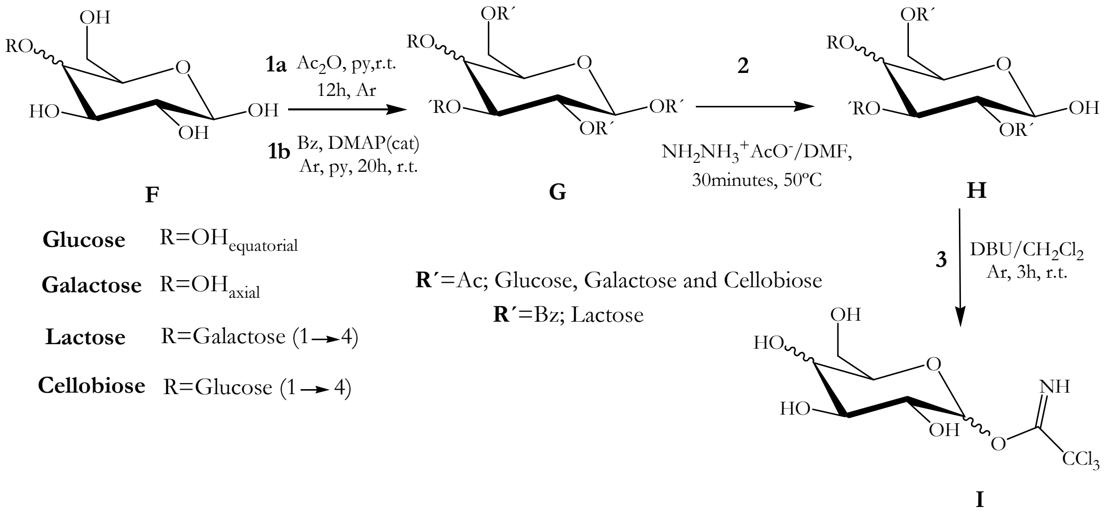

Protection of sugar hydroxilic groups (G):

Step 1a: Peracetilation of glucose, galactose and cellobiose(G).

Standard procedure was suspending the saccharide and acetic anhydride (1: 12 equivalents) in dry pyridine, the reaction was stirred for 20 h at room temperature. Then, dichloromethane was added and successively extractions with HCl (5%), saturated sodium carbonate solution and water were done. Organic phase was dried with sodium sulphate, filtered and concentrated.

1,2,3,4,6-Penta-*O*-acetyl-β-D-glucopyranose: 89.64 % of yield. ^{1}H-RMN ($CDCl_3$, 300MHz): δ 2- 2.21 (m, 15H, 5 Ac), 4- 4.3 (m, 4H, CH_2,H4, H5), 5.3 (m, 2H, H3, H4), 6.4 (s, 1H, H1) ppm.

1,2,3,4,6-Penta-*O*-acetyl-β-D-galactopyranose: 92.40 % of yield. ^{1}H-RMN ($CDCl_3$, 300MHz): δ 2- 2.3 (m, 15H, 5 Ac), 4- 4.3 (m, 4H, CH_2,H4, H5), 5.3 (m, 2H, H3, H4), 6.4 (s, 1H, H1) ppm.

2,3,4,6-Tetra-O-acetyl-β-D-glucopyranosyl-(1→4)-(1,2,3,6- (Tetra-O-acetyl) D-glucose: 91.20 % of yield. . **^{1}H NMR** (300 MHz, $CDCl_3$), δ 2-2.3 (m, 24H, Ac), 3.65 (m, 1H, H4), 4.12 (dd, 2H , H6,H6´, *J* = 7.1, 3.6 Hz), 4.35 (dd, 1H, *J* = 12.3, 1,2 Hz, H5´), 4.45- 4.62 (m, 2H, H3, H2´), 4.98 (m, 2H, H2, H3´),5.1-5.4 (m, 2H H3, H2´), 5.6 (d, 1H, *J* = 8.4 Hz, H1),6,3 (d, 1H, *J* = 3.6 Hz, H1´)ppm.

Step 1b: 2,3,4,6-Tetra-O-benzoyl-β-D-galactopyranosyl-(1→4)-1,2,3,6-tetra-O-benzoy-D-glucose: (G).

25 mL of pyridine were added to 5 g of lactose (13,85 mmol) at 0°C. Dimethylaminopyridine (DMAP) was also added as catalyst. Under argon atmosphere, 23.3 g of benzoil chloride (166.2 mmol) was added (1: 12 equivalents of lactose and benzoil clhoride). The reaction changes its color from with to brown. After 20 h of stirring, reaction product was extracted using 500 mL of AcOEt and washed with water, with sulfuric acid 2M and with a saturated sodium bicarbonate solution. Product solution was dried with magnesium sulphate, filtered and concentrated. The purification was performed by column chromatography (Hexane: AcOEt 1:3) (89.8 % final yield). ^{1}H-RMN ($CDCl_3$, 300MHz): δ 3.73- 3.83 (m, 2H, H5, H5´), 3.92 (m, 1H, H-6´), 4.31 (m, 1H, H-6´), 4.40 (t, 1H, J=9.0Hz, H4), 4.56 (s, 2H, H-6a, H6b), 4.96 (d, 1H, J=7.8Hz, H1´),5.39 (dd, 1H, J=10.2, 3.3Hz, H3´),5.62 (dd, 1H, J=10.2, 3.6Hz, H2), 5.74-5.8 (m, 2H, H2´, H4´),6.21 (dd, 1H, J=10.2, 9Hz, H3), 6.76 (d, 1H, J=3.6Hz, H1), 7.17-7.72 (m, 40H, Bz).

Step 2: Deprotection of anomeric hydroxyl group (H).

Standard procedure consist of in dissolved the saccharide and the hydrazine acetate (1: 1.2 equivalents) in dry dimethylformamide (DMF). The reaction was heated at 50 °C for 30 minutes. Then, a doble volume of AcOEt was added and removed by rotary evaporation. This procedure was repeated twice. Later on, five extractions with NaCl saturated solution were done. Solution was dried by sodium sulfate and concentrated. An extra purification was done was performed by column chromatography for dissacharides.

2,3,4,6-Tetra-*O*-acetyl-β-D-glucopyranose: 85,16%. of yield. **1H NMR** (300 MHz, CDCl3), δ 1.3-1.7 (m, 18H), 2.5 (t, 2H thiol, *J* = 7.0 Hz), 2.7 (t, 2H disulfide, *J* = 7.0 Hz) 3.5 (t, 2H, *J* = 14.0 Hz), 3.6-3.8 (m, 12H), 4.15 (s , 2H disulfide),4.19 (s, 2H thiol) ppm.

2,3,4,6-Tetra-*O*-acetyl-β-D-galactopyranose: 78% of yield. ^{1}H-NMR (300 MHz, $CDCl_3$): δ 5.50-5.30 (m, 3H), 5.20-5.00 (m, 2H), 4.69 (d, 0.4H,*J*= 6.6 Hz, H1), 4.43 (m, 1H, H4), 4.10-4.00 (m, 3H, H5), 4.00-3.90 (m, 0.4H, H5), 3.00-2.70 (m, 1H), 2.11, 2.06, 2.01, 1.96 (s, 12H, 4 OAc) ppm.

2,3,4,6-Tetra-O-acetyl-β-D-glucopyranosyl-(1→4)-2,3,6-tri-O-acetyl-D-glucose: Cromatography eluent from hexane:AcOEt (2:1), to hexane:AcOEt (1:2). 83,81 %.of yield. **^{1}H NMR** (300 MHz, $CDCl_3$), δ 1.9-2.3 (m, 22H, Ac), 3.65 (dd, 1H, *J*= 7.5, 0.9 Hz, H4), 4.2 (m, 4H , H6,H6´), 4.35 (dd, 1H, *J* = 12.6, 2.7 Hz, H5´), 4.45 (m, 1H, H5´),4.5 (m, 1H, H4), 4.65- 4.75 (m, 2H, H2´,H5), 4.9 (m, 2H,H2, H3´), 5.1-5.2 (m, 2H, H3, H1´), 5.4 (d, 1H, *J* = 3.6 Hz, H1) ppm.

2,3,4,6-Tetra-O-benzoyl-β-D-galactopyranosyl-(1→4)-2,3,6-tri-O-benzoyl-D-glucose: Chromatography eluent, Hexane :AcOEt (3:1), AcOEt. 77,96 % of yield. ^{1}H-RMN ($CDCl_3$, 300MHz): δ 3.94-3.67 (m, 2H,H5, H5´), 4.24 (t, 1H, J=9.6Hz, H4), 4.51 (dd, 1H, J=9.1, 3.3Hz, H6b), 4.59 (m, 1H, H6a), 4.94 (d, 1H, J=7.8Hz, H1´),5.24 (dd, 1H, J=7.2, 3.6Hz, H3´),5.40 (dd, 1H, J=10.3, 3.4Hz, H2), 5.62 (d, 1H, J=3.6Hz, H1), 5.68-5.77 (m, 2H, H2´, H4´),6.14 (t, 1H, J= 9.6Hz, H3), 8.07-7.25 (m, 35H, Bz) ppm.

Step 2: Trichloroacetimidate fomation (I).

Standard procedure starts dissolving in dry and deoxygenated dichloromethane the trichloroacetonitrile and the anomeric hydroxilic group deprotected sugar (H) in a ratio of 15: 1 equivalents respectively; finally, diazobicicleundecene (DBU) was added as catalyst. The reaction turns on dark yellow-orange color. After 3 h of stirring at room temperature, no starting product remained. Purification is performed by chromatography using passivated silica (hexane: triethylamine (1%)).

Tricloroacetimidate of 2,3,4,6-Tetra-*O*-acetyl-β-D-glucopyranose: Cromatography eluent, hexane: AcOEt (1:1). 72,43 % of yield. ^{1}H-RMN (300 MHz, $CDCl_3$): δ 2.1 (m, 12H, Ac), 4.05-4.19 (m, 2H,H6), 4.14 (dd, 1H, J=4, 12.5Hz), 5.04

(dd, 1H, J=10.5, 20Hz), 5.05 (t, 1H, J=10.5Hz), 5.42 (t, 1H, J=10Hz), 6.41 (d, 1H, J=3Hz), 8.65 (s, 1H, NH) ppm.

Tricloroacetimidate of 2,3,4,6-Tetra-*O*-acetyl-β-D-galactopyranose: Cromatography eluent, hexane :AcOEt (1 :1). 72. 74% of yield. ^{1}H-RMN (300 MHz, CDCl$_3$): δ 1.94-2.18 (m, 12H, Ac), 4.01-3.96 (m, 1H, J=12.5Hz), 4.43 (t, 1H, J=7.5, Hz, H4), 5.37 (d, 1H, J=3.6 Hz, H5), 5.4 (d, 1H, J=3 Hz, H3), 5.55 (dd, 1H, J=2.7, 0.9Hz, H2), 6.6 (d, 1H, J=3.3 Hz, H1), 8.66 (s, 1H, NH) ppm.

Tricloroacetimidate of 2,3,4,6-Tetra-O-acetyl-β-D-glucopyranosyl-(1→4)-2,3,6-tri-O-acetyl-D-glucose: Cromatography eluent hexane:AcOEt (2:1). 69 %.of yield. **^{1}H NMR** (300 MHz, CDCl$_3$), δ 1.9-2.05 (m, 22H, Ac), 3.65 (m, 1H, , H4´), 4.05-4.15 (m, 4H , H6,H6´), 4.37 (dd, 1H, *J* = 12.6, 4.5 Hz, H5), 5.02-5.18 (m, 4H, H2, H5,H2´,H3´),5.5 (t, 1H, *J* = 9.9 Hz, H1´), 6.47 (d, 1H, *J* = 3.6 Hz, H1) ppm.

Tricloroacetimidate of 2,3,4,6-Tetra-O-benzoyl-β-D-galactopyranosyl-(1→4)-2,3,6-tri-O-benzoyl-D-glucose: Cromatography eluent hexane:AcOEt (2:1).%Rdto.= 77,09 % of yield. ^{1}H-RMN (CDCl$_3$, 300MHz): δ 3.67-3.92 (m, 2H, H5, H5′), 4.24 (t, 1H, J=9.6Hz, H4), 4.34 (m, 2H, H6′), 4.57 (m, 2H, H6), 4.94 (d, 1H, J=7.8Hz, H1′), 5.39 (dd, 1H, J=7.2, 3.6Hz, H3′), 5.54 (dd, 1H, *J*=10.3, 3.4Hz, H2), 5.74 (m, 2H, H2′, H4′), 6.15 (m, 1H, H3), 6.70 (d, 1H, J=3.6Hz, H1), 7.16-8.03 (m, 35H, Bz), 8.56 (s, 1H, NH) ppm.

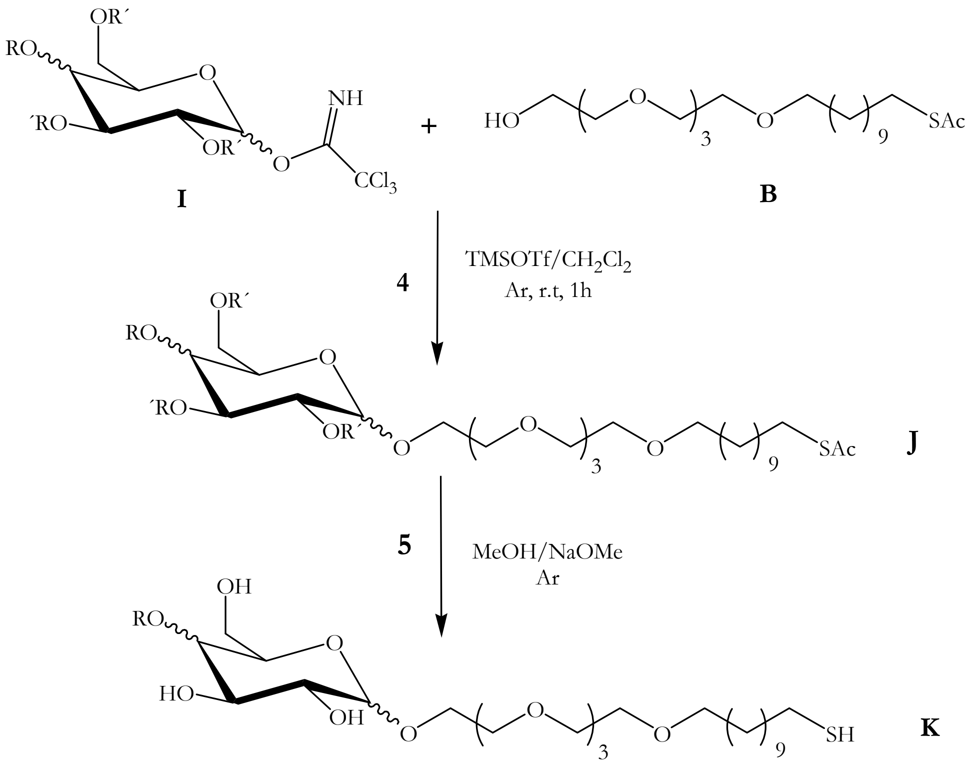

Step 4. Glycosilation of sugar with chain mixed (J).

Standard procedure starts with the dissolution of the activated sugar (I) and B in a ratio of 1: 1.5 equivalents, under inert atmosphere.0.05 equivalents of TMSOTf was also added. The mixture was stirred at this temperature and monitorized by TLC (hexane:AcOEt 1:1). After 4 h the pH was adjusted to 7 with Et_3N (50 µL), the solvent was removed at low pressure and the residue was purified by flash column chromatography (hexane:AcOEt 1:1) using passivated silica (hexane: triethylamine (1%)) to give the glycosilated product as a syrup.

11-thioacetyl [3,6,9,12-tetraoxaundecanyl] -(2,3,4,6-Tetra-*O*-acetyl)-β-D-glucopyranose: Flash column chromatography hexane:AcOEt 1:3. 61.4 % of yield. **^{1}H NMR** (300 MHz, $CDCl_3$): δ 1.06 (s, 3H); 1.29-1.55 (m 16H); 1.98 (s, 3H); 1.99 (s, 3H); 2.04 (s, 3H); 2.27 (s, 3H); 2.83 (t, 2H, *J* = 7.5 Hz); 3.3 (1H, m), 3.39 (2H, t, *J* = 6.8 Hz), 3.57-3.71 (m, 18H); 3.89 (m, 1H), 4.07 (dd, 1H, *J* = 12.3, 2.1 Hz); 4.20 (dd, 1H, *J* = 12.3, 4.6 Hz), 4.55 (d, 1H, *J* = 8 Hz); 4.93 (dd, 1H, J= 9.5, 8.0 Hz), 5.03 (t 1H, *J* = 9.8 Hz), 5.15 (t, 1H, *J* = 9.5 Hz) ppm.

11-thioacetyl [3,6,9,12 - tetraoxaundecanyl] - 2,3,4,6 -Tetra- *O* -acetyl – β -D-galactopyranose : Cromatography eluent, from hexane :AcOEt (2 :1) to hexane: AcOEt (1:2). 51% of yield. **^{1}H NMR** (300 MHz, $CDCl_3$): δ 1.18- 1.35 (m, 10 H); 1.45-1.55 (m ,6H); 1.93 (s, 2H); 1.96 -2.1 (m, 15H); 3.38 (t, 2H, *J* = 6.6 Hz); 3.48-3.61 (m, 14H), 3.53 (2H, t, *J* = 6.8 Hz), 3.57-3.71 (m, 26H); 4.26 (t, 1H, *J* = 12.3, 5.4 Hz, H2,H5), 5.1 (m, 1HH3); 5.76 (d, 1H, *J* = 4.5 Hz, H1) ppm.

11-thioacetyl[3,6,9,12-tetraoxaundecanyl]-(2,3,4,6-Tetra-O-acetyl-β-D-glucopyranosyl-(1→4)-(2,3,6- (tri-O-acetyl) D-glucose: Column chromatography eluent from hexane:AcOEt 2:1 to Hexane: AcOEt (1:2). Yield 45%. . ^{1}H NMR (300 MHz, $CDCl_3$): δ 1.1-1.3 (m, 10H); 1.48-1.56 (m, 6H); 2.33 (s,3H, Ac);1.85-2.03 (m, 2H,); 2.22-2.28 (m, 24H); 3.36 (t, 2H, *J* = 8.1 Hz); 3.48-3.65 (m,18 H); 3.92-4.16 (m, 4H, H6, H6´); 4.3 (dd, 1H, *J* = 12.6, 4.2 Hz); 4.38-4.52 (m, 2H); 4.85 (m, 2H, H2, H2´);5.05(dd, 1H, *J* = 9.6, 3.6 Hz, H3); 5.06 (m, 2H,H1, H3); 5.4(t,1H, *J* = 9.6) ppm.

11-thioacetyl[3,6,9,12-tetraoxaundecanyl]-2,3,4,6-(benzoyloxy(methyl))-β-D-galactopyranosyl-(1→4)-(2,3,6-(benzoyloxy (methyl)) D-glucose: Cromatography eluent hexane: AcOEt (2:1). 47.3 %.of yield. ^{1}H NMR (300 MHz, $CDCl_3$): δ 1.15-1.43 (m, 14H); 1.51-1.62 (m, 2H); 2.33 (s,3H, Ac);2.87 (t, 2H, *J* = 7.2 Hz); 3.33-3.8 (m, 19H); 4.27 (t, 1H, *J* = 9.3 Hz); 4.40 (dd, 1H, *J* =12,4 Hz); 4.52 (dd, 1H, *J* = 12.0, 1.5

Hz); 4.82 (d, 1H, *J* = 7.8 Hz); 4.88 (d, 1H, *J* = 8.1Hz);5.36 (dd, 1H, *J* = 10.5, 3.3 Hz); 5.47 (m, 1H,); 5.8 (m, 2H); 5.7(t,1H, *J* = 9.5); 7-8 (m, 35H) ppm.

Step 5. Deprotection of sugar modified chain mixed (K).

The glycosilated product was treated with NaOMe in methanol. The mixture was stirred for 3 hours under. TLC (CH_2Cl_2:MeOH 4:1) showed the appearance of a new product (Rf 0.7). The reaction was neutralised with Amberlist IR-120, filtered and evaporated to dryness

11-thio[3,6,9,12-tetraoxaundecanyl] -D-glucopyranose: 98 % of yield. **^{1}H NMR** (300 MHz, D_2O): δ; 1.16-1.53 (m, 14 H), 2.53 (bs, 2H); 3.12 (t, 1 H, *J* = 8.5 Hz), 3.24 (q, 1H, *J* = 9.4 Hz); 3.28-3.33 (m, 4H); 3.42-3.53 (m, 1H); 3.65 (m, 1H); 3.73 (d, 1H; *J* = 12.1 Hz); 3.89 (m, 1H); 4.4(d, 1H, *J* = 7.8 Hz) ppm

11-thio[3,6,9,12-tetraoxaundecanyl] -β-D-galactopyranose: 94% of yield.

^{1}H NMR (300 MHz, MeOD):δ 1.25-1.37 (m, 10 H), 1.4-1.7 (m, 8H); 2.67 (t, 1 H, *J* = 7.5 Hz), 2.67 (q, 1H, *J* = 9.4 Hz); 3.42-3.53 (m, 1H); 3.53-3.57 (m, 5H); 3.59-3.66(m, 16H); 3.7 (m, 3H); 4.24 (d, 1H, *J* = 7.2 Hz) ppm

11-thio[3,6,9,12-tetraoxaundecanyl] -(*ß*-D-galactopyranosyl)(1→4)-ß-D-glucopyranoside: 91% of yield . **^{1}H NMR** (300 MHz, MeOD):δ 1.25-1.45 (m, 14 H), 1.52-1.6 (m, 4H); 2.69 (t, 1 H, *J* = 7.2 Hz), 3.34 (t, 1H, *J* = 5.7 Hz, H4); 3.53-3.74 (m, 29H); 3.59-3.7(m, 16H); 3.88 (m, 1H, H5´); 4.36 (d, 1H, *J* = 7.5 Hz, H1´) ppm

11-thio[3,6,9,12-tetraoxaundecanyl]- (*ß*-D-galactopyranosyl) (1→4)-ß-D-glucopyranoside. In this case, final product must be washed repeatedly with diethylether to extract the free benzoil groups. After this product is dried and obtained with a 88% of yield. **^{1}H NMR** (300MHz, D_2O): δ 1.3-1.5 (m, 12H); 1.57 (m, 2H); 1.67 (q, 2H, *J* = 7.5 Hz); 2.48 (t, 2H, *J* = 7.5 Hz); 2.68 (t, 2H, *J* = 7.5 Hz); 3.2-4 (m, 30H); 4.34 (dd, 1H, *J* = 9.5, 8.0 Hz) ppm.

Synthesis of Lactose-C_2H_4-NH_2

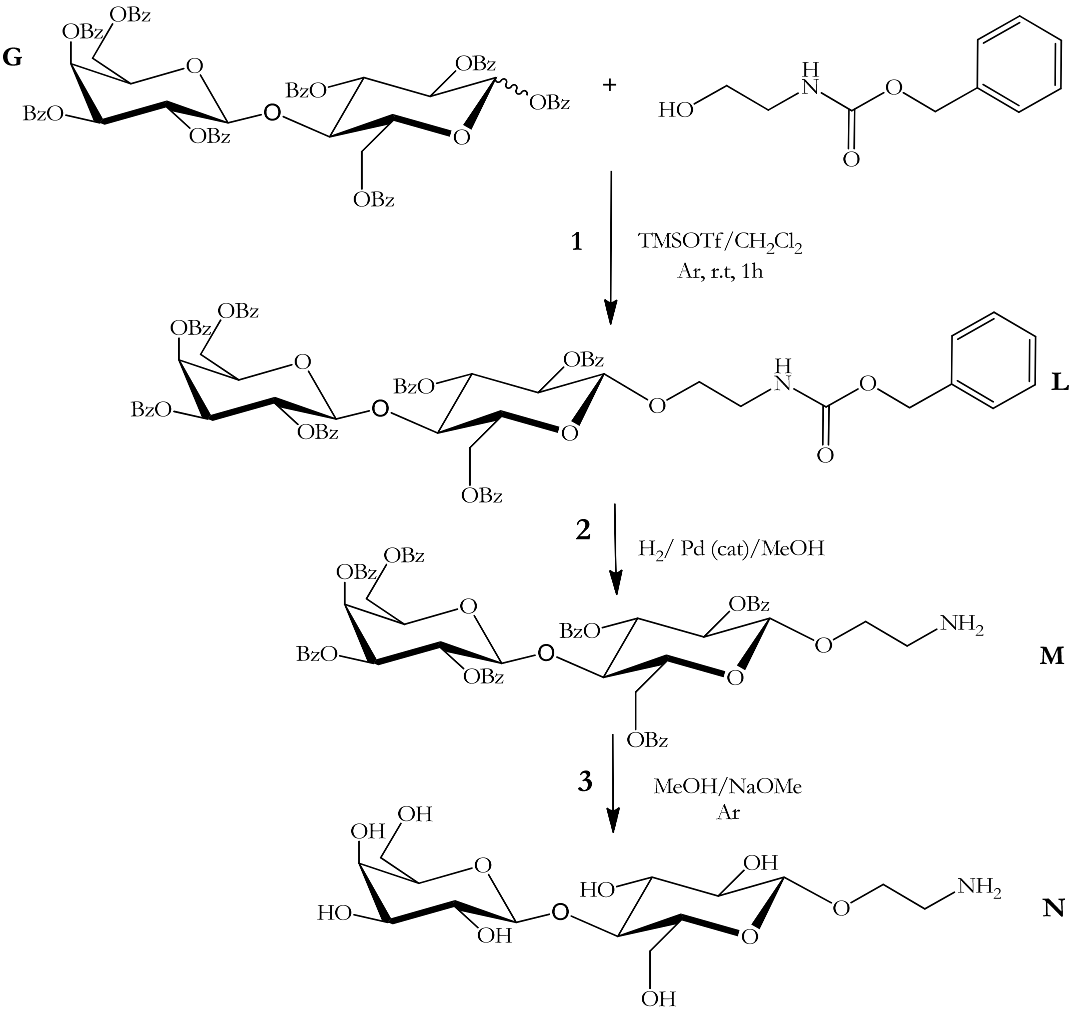

Step 1. 1-[(N-(2-amine)carbamic acid benzyl ester) ethoxy] [2,3,4,6-(benzoyloxy(methyl))]-β-D-galactopyranosyl-(1→4)-D-(2,3,6-benzoyloxy (methyl))-glucose (L). Perbenzoylated lactose (G) (2.6 g, 2.15 mmol) and benzyl N-(2 hydroxyethyl) carbamate (0.63g , 3.73 mmol) (Sigma) are dissolved in dichloromethane (10 mL) under inert atmosphere and 10.9 μL (0.086 mmol) of TMSOTf are also added. The mixture was stirred at room temperature and monitorized by TLC (hexane:AcOEt 2:1). After 4 h the pH was adjusted to 7 with Et_3N (50 μL), the solvent was removed at low pressure and the residue was purified by flash column chromatography using passivated silica (hexane: triethylamine (1%)) and as eluent from hexane:AcOEt 3:1 to AcOEt to give the glycosilation product as a syrup with a 81.3 % of yield. (1.9 g). ^{1}H NMR (300 MHz, $CDCl_3$), δ 3.3(m, 12H), 3.7 (m, 3H), 4.12 (m, 2H) 4.5(m, 3H), 3.6-3.8 (m, 12H), 4.65 (t , *J*= 14.1 Hz),4.8-5.02(m, 2H), 5.75 (m, 2H), 7-8 (m, 40H) ppm.

Step 2. 1- [2-aminoethoxy] [2,3,4,6- (benzoyloxy (methyl))] –β – D – galactopyranosyl -(1→4)-D-(2,3,6-benzoyloxy (methyl))-glucose (M). 350 mg of M was dissolved in 2 mL of methanol. Under inert atmosphere, a catalytic amount of Pd(C) was added to the solution and the reaction mixture was hydrogenated under vigorous stirring for 12h. Then, the reaction mixture was filtered over a pad of Celite. The solvent was evaporated to give the final product N in a yield of 73.9 %. ^{1}H NMR ^{1}H NMR (300 MHz, CDC_{l3}), δ 2.9 (m, 2H) 3.84(m, 3H), 4.21 (m, 2H, H6/H6´), 4.55 (m,2H), 4.65(m, 1H), 4.97 (m, 3H), 5.1(s ,2H), 5.62(m, 1H, H3), 5.75 (m, 2H), 7.1-8 (m, 35H) ppm.

Step 3. 1-[2-aminoethoxy]β-D-galactopyranosyl-(1→4)-D-glucose (N). 0.1g of L was treated with NaOMe in methanol. The mixture was stirred for 3 hours under. The reaction was neutralised with Amberlist IR-120, washed several times with ethyl ethet, filtered and evaporated to dryness This reaction is quantitative (100%). ^{1}H NMR (300 MHz, CDC_{l3}), δ 2.9 (m, 2H) 3.05(m,1H, H4´), 3.45 (m, 1H, H4), 3.4-4.8 (m,18H), 4.06(m, 1H, H5´), 5.06 (d, 2H,H1, H1´), 5.17(s ,2H).

(A1.2) Synthesis of Fe_3O_4@Au Nanoparticles

Monodisperse Fe_3O_4 NPs of 6nm mean diameter were synthesized following the seed-mediated growth method described by Sun and coworkers. Briefly, 6nm Fe_3O_4 NP seeds were synthesized by mixing 2mmol of $Fe(acac)_3$ (Sigma), 7.2mmol of 1,2-hexadodecanediol, 6mmol of oleic acid, 6mmol of oleylamine and 20ml of benzyl ether. The mixture was heated to 200ºC for 2 hours and afterwards heated to reflux (265ºC) under nitrogen atmosphere for 1 hour. The mixture was allowed to cool to room temperature by removing the heat source. The NPs were precipitated by adding ethanol, collected with a magnet and redispersed in hexane three times. Finally, particles were redispersed in 10ml hexane containing 75mM of oleic acid and 75mM of oleylamine.[2] The gold shell was synthesized using the protocol describes by Wang and coworkers. Briefly, 10ml of the previous -solution of Fe_3O_4 NPs were place in a flask and 1.12mmol of gold (III) acetate (Strem), 5.4 of mmol 1,2-hexadodecanediol (Sigma), 0.78mmol of oleic acid (Sigma), 4.57mmol of oleylamine (Sigma) and 20ml of benzyl ether (Sigma) were added in the same flask. Under argon atmosphere and vigorous stirring, the reaction solution was heated to 189-190 ºC at 10ºC/min and was kept at this temperature for 2 hours. After cooling to room temperature, ethanol was added in the solution. The NPs were washed three times and collected with a magnet. NPs were redispersed in 10ml hexane containing 75mM of oleic acid and 75mM of oleylamine.[3]

Fe_3O_4@Au water transfer: Synthesis of Fe_3O_4@Au@S$(CH_2)_{11}(OCH_2CH_3)_3$ CH_2CH_2OH (50%) @ (S$(CH_2)_{11}(OCH_2CH_3)_3CH_2CH_2O(C_xH_x)$. CM-Glucose, CM-Galactose; CM-Cellobiose and CM-Lactose.

In general, hexane soluble particles are precipitate and washed with EtOH, and resuspended in hexane. An equivalent volume of water is added to the particles containing a mixture 1:1 of the carboxylated mixed chain E and the corresponding modified sugar (K). NaBH4 was added to reduce the thiol group. Mixture was shaking until phase transfer was complete. After this, particles are cleaned by dialysis using a 5-10 cm piece of membrane (Pierce, 10000 MWCO), and placed in a 5 L recipient containing distillated water. Water from the recipient was changed three times per day during 72h. Cleaned particles were filtrated with a 0.2 μm cellulose filter and liophylizated.

NPs	Carboxylated Mixed chain	Modified Sugar (mg)	mg Fe_3O_4@Au hexane.	Final NPs(mg)
CM-Glucose	25(0.0636mmol)	23(0.0636mmol)	15	16.59
CM-Galactose	25(0.0636mmol)	23(0.0636mmol)	15	14.3
CM-Cellobiose	25(0.636mmol)	35(0.636mmol)	15	13.4
CM-Lactose	25(0.0636mmol)	35(0.0636mmol)	15	17.1

Synthesis of Fe_3O_4@Au@S$(CH_2)_{11}(OCH_2CH_2)_3CH_2CO_2H$ (CM-CO_2H)[4]

A 7 mg weight of Fe_3O_4@Au NPs were mixed with 0.03 mmol of $HS(CH_2)_{11}(OCH_2CH_2)_3CH_2CO_2H$ (E) and 0.20 mmol of $NaBH_4$. The reaction was carrying on both in hexane (1ml) and water (1ml). The mixture was agitated for 72 hours at room temperature. Functionalized NPs were in the aqueous phase whilst non-functionalized remained in organic phase. The water soluble NPs were loaded into 8cm segments of seamless cellulose ester dialysis membrane (Sigma, MWCO=10000), placed in 4l beakers of water, and stirred slowly, recharging with fresh water approximately every 10 hours over the course of 24 hours. The red wine solution was collected and liophylizated. UV/Vis(H_2O):v=524nm (surface plasmon band). IR (KBr): v=3433, 2925, 1722, 1644, 1531, 1384, 1199, 1014, 794 cm^{-1}

Synthesis of Fe_3O_4@Au@S $(CH_2)_{11}(OCH_2CH_2)_3CH_2CONH$@Tat (CM-tat)[4]

Finally, 7.9µmol of (N-(3-Dimethylaminopropyl)-N´-ethylcarbodiimide dihidrochloride), 18.7µmol of N-hydroxysuccinimide were added to 1.5mg of Fe_3O_4@Au@$(CH_2)_{11}(OCH_2CH_2)_3CH_2CO_2H$ solubilized in 2ml of 2[N-morpholino]ethanesulfonic acid (MES) (50mM, pH 6.5). The reaction proceeded for 30 min. Consequently, Tat peptide (0.06µmol) was added and the mixture was stirred for 24 hours. This solution was loaded into 6cm segments of seamless cellulose ester dialysis membrane (Sigma, MWCO=10000), placed in 4l beakers of water, and stirred slowly, recharging with fresh water approximately every 10 hours over the course of 24 hours. The red wine solution was collected and liophylizated.

(A1.3) Synthesis of NNs

Prior to use, all glassware was washed with aqua regia (caution: aqua regia is highly toxic and corrosive) and rinsed thoroughly with MilliQ water. In a typical synthesis, 100 mL of 2 mM (aq.) $HAuCl_4$ (Sigma) and 120 mL of freshly prepared 0.5 mM $Na_2S_2O_3$ (Sigma) are mixed, under mild stirring conditions for 9 minutes, prior to a second addition of 0.5 mM $Na_2S_2O_3$; the volume of the second addition can be varied from 20 – 50 mL for tuning the LSPR in the range of 750 – 1075 nm (NIR range).

Pegylation and Purification of NNs by gel-electrophoresis

The NPs produced by the synthetic method proposed here were derivatised with HS-C_2H_4-CONH-PEG-O-C_3H_6-COOH (M.W. 5000 g/mol; obtained from Rapp-Polymere) to increase their colloidal stability (NPs@PEG). Briefly, 10 mL of each sample (0.2*x* – 0.5*x*) was supplemented with 1 mg of thiolated PEG. The pH of the solution was adjusted to 12.0 with a concentrated solution of NaOH. Samples were left overnight to react (ligand-exchange) under mild stirring conditions. The increased colloidal stability allowed washing the NPs by centrifugation (centrifuged twice for 15 min at 10000 rpm and resuspending pellets in MilliQ water); prior to PEG-derivatisation, centrifugation aggregated the NPs irreversibly. Furthermore, PEG-derivatised NNs were stable in tris-borate-EDTA (1x TBE) buffer, among other buffers, which is used in gel-electrophoresis generally. Samples were loaded (mixed with loading buffer, i.e. 1x TBE, 10% glycerol) then in wells within an agarose gel (0.6x) immersed in an electrophoresis cuvette filled with TBE 1x. Electrophoresis separation was run at 100 V for 1 hour. Due to the increased electrophoretic mobility of NPs other than NNs, i.e. polyhedral Au-NPs, two bands were resolved in the gel. The band corresponding to the NNs were cut and introduced in TBE-filled dialysis membranes (cut-off 10 KDa). They were immersed in the electrophoresis cuvette. NNs were extracted from the gel-cut segments by application of 100 V for 2 hours.

Derivatisation of NNs with Glucose and TAMRA (NNs@T&Glc)

NNs were derivatised with glucose and 5-TAMRA cadaverine (Tetramethylrhodamine–5–carboxamide cadaverine; absorption/emission = 545/576 nm) was purchased from Anaspec; for promoting cellular uptake and fluorescence labeling, respectively. Briefly, 1 mg NNs@PEG were incubated with 1:3 mg of EDC(1-Ethyl-3-[3-dimethylaminopropyl] carbodiimide hydrochloride, Sigma):Sulfo-NHS (sulfo-NHS (N-hydroxysulfosuccinimide), Sigma) in 2 mL MES (2-Aminoethanol and 2-(N-morpholino)ethanesulfonic acid, Sigma)buffer pH 6 for 20 minutes at 37 ºC; activated NNs@PEG (bearing a semi-stable amine-reactive ester) were then incubated for 2 hours (room temperature) with 100 μg and 270 μg of TAMRA and glucose(Glc) (1:5 molar ratio), respectively. Derivatised NNs (NNs@T&Glc) were left (under mild stirring conditions) overnight; functional NNs were then washed out of ligand excess by centrifugal precipitation; functional NNs were centrifuged twice for 15 min at 10000 rpm and then, pellets were resuspended first in MilliQ water and finally, in PBS prior to cell culture studies.

Derivatisation of NNs with TAMRA (NNs@T)

NNs were derivatised 5-TAMRA cadaverine (Tetramethylrhodamine–5–carboxamide cadaverine; absorption/emission = 545/576 nm, Anaspec). Briefly, 1.5 mg NNs@PEG were incubated with 4.5 mg of EDC(1-Ethyl-3-[3-dimethylaminopropyl] carbodiimide hydrochloride, Sigma) and 6.75 mg of Sulfo-NHS (sulfo-NHS (N-hydroxysulfosuccinimide), Sigma) in 1.5 mL MOPS (3-(N-morpholino)propanesulfonic acid, Sigma) buffer pH 6 for 20 minutes at 37 ºC; activated NNs@PEG (bearing a semi-stable amine-reactive ester) were then incubated over night (room temperature) with 150 μg of TAMRA). NNs were then washed out of ligand excess by centrifugal precipitation; functional NNs were centrifuged twice for 15 min at 10000 rpm and then, pellets were resuspended first in MilliQ water and finally, in PBS prior to cell culture studies.

Derivatisation of NNs with Lactose and TAMRA (NNs@T&Lacto)

NNs were derivatised with [4-hydroxyethylamine]β-D-galactopyranosyl-(1→4)-D-glucose (N) and 5-TAMRA cadaverine (Tetramethylrhodamine–5–carboxamide cadaverine; absorption/emission = 545/576 nm, Anaspec). Briefly, 1.5 mg NNs@PEG were incubated with 4.5 mg of EDC (1-Ethyl-3-[3-dimethylaminopropyl] carbodiimide hydrochloride, Sigma) and 6.75 mg of Sulfo-NHS (sulfo-NHS (N-hydroxysulfosuccinimide), Sigma) in 1.5 mL MOPS (3-(N-morpholino)propanesulfonic acid, Sigma) buffer pH 6 for 20 minutes at 37 °C; activated NNs@PEG (bearing a semi-stable amine-reactive ester) were then incubated over night (room temperature) with 150 µg and 750 µg of TAMRA and the modified lactose (Lacto) , respectively. NNs were then washed out of ligand excess by centrifugal precipitation; functional NNs were centrifuged twice for 15 min at 10000 rpm and then, pellets were resuspended first in MilliQ water and finally, in PBS prior to cell culture studies.

Derivatisation of NNs with tat peptide and TAMRA (NNs@T&tat)

NNs were derivatised with tat-peptide and 5-TAMRA cadaverine (Tetramethylrhodamine–5–carboxamide cadaverine; absorption/emission = 545/576 nm, Anaspec). Briefly, 1.5 mg NNs@PEG were incubated with 4.5 mg of EDC(1-Ethyl-3-[3-dimethylaminopropyl] carbodiimide hydrochloride, Sigma) and 6.75 mg of Sulfo-NHS (sulfo-NHS (N-hydroxysulfosuccinimide), Sigma) in 1.5 mL MOPS (3-(N-morpholino)propanesulfonic acid, Sigma)buffer pH 6 for 20 minutes at 37 °C; activated NNs@PEG (bearing a semi-stable amine-reactive ester) were then incubated for 20 minutes with (room temperature) 84 µg of tat peptide, after this time 150 µg of TAMRA were added. After 2 hours at room temperature, overnight incubation was carry on at 4 °C. NNs were then washed out of ligand excess by centrifugal precipitation; functional NNs were centrifuged twice for 15 min at 10000 rpm and then, pellets were resuspended first in MilliQ water and finally, in PBS prior to cell culture studies.

Synthesis of rhodamin-Anti-HRP

1 mL of Anti-HRP (Sigma, 0.8 mg/mL previously dialyzed against $NaPO_3$ 0.1 M pH=8) was mixed with 100 µL of rhodamine B isothiocyanate (Sigma, 1 mg/mL) at pH 9.2. In these conditions, isothiocyanate reacts with α-amine groups from the anti-HRP. After 2 hours of reaction at 4 °C, product is gel-filtrated using a PD-10 column (GE Healthcare). Concentration was determined using Bradford colorimetric assay (Anexe B). Final product fluorescence was measured in a Fluorescence Spectrometer Perkin Elmer LS55 showing a λ(absorption, max) = 540 nm and λ(emission, max)= 580 nm. Modified anti-HRP was obtained in a 97% of yield.

A2. Colorimetric assays:

(A2.1) MTT viability assay

Cell viability and proliferation were analyzed by MTT colorimetric assay. HeLa or VERO cells (5 000 cells per well) were seeded in a 96 well plate at 37 °C in 5% CO_2. After 24 h, the medium was replaced with fresh medium containing the different NPs modifications in varying concentrations. After cultivation again for 24 h, NNs solutions were removed and cells were washed. 20 μL of MTT dye solution (5 mg/mL in PBS) solved in 100 μL of DMEM media was added to each well. After 4 h of incubation at 37 °C and 5% CO_2, the cells were centrifugated at 5000 rpm for 10 minutes and the medium was removed. Formazan crystals were dissolved in 100 μL of DMSO. The absorbance of each well was read on a microplate reader (D Biotek ELX800) at 570 nm. The spectrophotometer was calibrated to zero absorbance using culture medium without cells. The relative cell viability (%) related to control wells containing cell incubated without NNs was calculated by $[A]_{test}/[A]_{control}*100$. Each measurement was repeated at least five times to obtain the mean values and the standard deviation.

(A2.2) Coomasie protein detection assay (Bradford)[5]

This is a colorimetric assay which allows quantifying the solution protein concentration. It is based in the color change from blue to brown (465 to 595 nm) suffered by Coomasie reagent when gets binding to a protein. Protein concentration maintains a liner a behavior with the change color at two ranges, from 1 to 25μg/mL and from 100 to 1500 μg/mL which can be measured in an absorbance microplate-reader. Standard curve is done using bovine serum albumin (BSA). Samples are placed in a 96-well plate, and are prepared differently for each concentration range; for low concentration 150 μL of sample are mixed with 150 μL of Coomasie reagent, for high concentration 10 μL of sample are mixed with 300 μL of Coomasie. For both, 10 minutes are required to consider protein-Coomasie binding is finished. After this, absorbance values are read in a ELx800TM (BioTek) absorbance microplate-reader at 595 nm.

(A2.3) Colorimetric activity assay for determination of enzymatic activity of HRP

1.5mL of 2,2'-azino-bis(3-ethylbenzothiazoline-6-sulphonic acid) (ABTS, Sigma, 1 mg/mL in water); 10 μL of H_2O_2 (Sigma) 0.10 mM are mixed with 10 μL of sample in a cuvette. Absorbance chances with time are measured with a UV-visible spectrophotometer Varian Cary 50 at 414 nm. Enzymatic activity is directly related with the slope of the curve obtained printing absorbance *vs* time.

(A2.4) Colorimetric activity assay for determination of enzymatic activity GOX

1 mL of sodium phosphate buffer pH 6 0.1 M; 0.5 mL of 0.1 M glucose sodium phosphate buffer 0.1M; 0.1 mL of 2,2'-azino-bis(3-ethylbenzothiazoline-6-sulphonic acid) (ABTS, Sigma, 1 mg/mL in water); 0.1 mL of HRP (Sigma, 2mg/mL) sodium phosphate pH=6 0.1 M are mixed with 10 μL of sample in a cuvette. Absorbance chances with time are measured with a UV-visible spectrophotometer Varian Cary 50 at 414 nm. Enzymatic activity is directly related with the slope of the curve obtained printing absorbance *vs* time.

A3. Experimental Protocols of Sample Preparations

(A3.1) Cytoskeleton (F-actin and β-tubulin); clathrin and caveolin immunofluorescence

Cells incubated with NPs were fixed in 4% formaldehyde/PBS with 1% sucrose at 37 °C for 15 min. The samples were then washed in PBS and permeabilizing buffer was added at 4 °C for 5 min prior to being incubated for 5 min in 1% BSA/PBS. This was followed by the addition of anti-tubulin/anti-clathrin/anticaveolin primary antibody (1:50 in 1% BSA/PBS, monoclonal anti-human raised in mouse (IgG1) Sigma) for 1 h at 37°C. Simultaneously rhodamine conjugated phalloidin was added for the duration of this incubation (1:50 in 1% BSA/PBS, Invitrogen). The samples were then washed in 0.5% Tween20/PBS and a secondary biotin conjugated antibody (1:50 in 1% BSA/PBS monoclonal anti-mouse (IgG), Vector Laboratories, UK) was added for 1 h at 37°C followed by more washing. Finally fluorescein conjugated streptavidin was added (1:50 in 1% BSA/PBS, Vector Laboratories) at 4°C for 30 min followed by a final wash. Samples were then viewed using a Leitz fluorescence microscope for Fe_3O_4@Au NPs or a Olympus FV10-I in NNs case. [4]

(A3.2) Hoechst staining [6]

Hoechst 33342 (2'-[4-ethoxyphenyl]-5-[4-methyl-1-piperazinyl]-2,5'-bi-1H-benzimidazole trihydrochloride trihydrate) (Thermo scientific) is a cell-permeable DNA stain that is excited by ultraviolet light and emits blue fluorescence at 460 to 490nm. This dye can be used to mark nuclei of live-cells. Hoechst 33342 binds preferentially to adenine-thymine (A-T) regions of DNA. Dye is added diluted 1:100 in PBS with Ca^{2+} and Mg^{2+} directly on cells. After 30 minutes of incubation at 37 °C, 5% CO_2 nuclei can be observed under a fluorescence microscopy (Nikon Eclipse T*i*).

(A3.3) Western blotting analysis of caveolin and clathrin

Following NP incubations 1 ml PBS was added per sample, samples were lysed using 3 freeze/thaw cycles of 80°C for 20 min followed by 37 °C for 30 min. Total protein concentration of each sample was determined spectrophotometrically using the Nanodrop (Labtech, UK). Equal concentrations of all samples were reduced, then run on a 4–12% NuPAGE Novex Bis Tris Gel using the NuPage electrophoresis system, following manufacturer's instructions. Proteins were then transferred to Hybond-P PVDF Membrane following manufacturer's instructions ( ). After non-specific blocking, detection of clathrin and caveolin was performed using specific antibodies and the ECLWestern Blot System. X-ray film was exposed for 1 min prior to developing using Kodak developer.

(A3.4) SEM & TEM NPs samples preparation

SEM and TEM samples were prepared by concentrating the samples by centrifugation (centrifuged twice for 10 min at 8000 rpm and resuspending pellets in MilliQ water); in each case, 5 μL of the solution were immobilised on a Formvar–coated Cu grid for TEM and on a plate of silicon wafer (*ca.* 25 mm^2) for SEM. TEM samples were observed under FEI Tecnai T20, FEI Tecnai T30. SEM samples were observed under a INSPECT F50.

(A3.5) Cell preparation for scanning electron microscopy (SEM)

Following **MGNPs** incubations all samples were fixed with 1.5% glutaraldehyde (Sigma) buffered in 0.1M sodium cacodylate (Agar U.K.) (4 °C, 1 h). Samples were then postfixed in 1% osmium tetroxide for 1 h (Agar U.K.), and 1% tannic acid (Agar U.K.) was used as a mordanant. Samples were subsequently dehydrated thoug a series of alcohol concentrations (20%, 30%, 40%, 50%, 60%, 70%), stained with 0.5 uranyl acetate followed by further dehydration (90%, 100% 100% (dry)). The final dehydration was in hexamethyl-disilazane (Sigma), followed by air-drying. Once dry, the samples were coated with gold before examination with a Hitachi S800 field emission SEM at an accelerating voltage of 10 keV.

50000 Vero cells were seeded and after 24 hours of incubation **NNs** at different concentrations for 24 hours. The samples were prepared by fixing the cells with 4% glutaraldehyde in 0.2 M sodium cacodylate pH 7.2 for 2 hours at 4ºC. The dehydration process was conducted by incubating the cells for 5 min at room temperature with increasing concentrations of methanol (30, 50, 70 and 100%) and anhydride methanol for 10 min. All samples were sputter-coated with gold immediately before observation. Images were obtained with a FEI INSPECT F50 microscope.

(A3.6) Cell preparation for transmission electron microscopy

Following NP incubations all samples were fixed as for SEM, stained for 60 min with 1% osmium tetroxide and 0.5% uranyl acetate, then taken through the alcohol dehydration steps up to dried absolute alcohol. The coverslips were then treated with 1:1 propylene oxide:resin overnight to evaporate the alcohol. The following day the coverslips were embedded in araldyte resin, and ultrathin sections were cut and stained with lead citrate, prior to silver staining enhancement and viewed under a Zeiss 902 electron microscope at 80 kV.

(A3.7) XPS sample preparation

X–ray photoelectron spectroscopy (XPS) spectra were acquired by a Kratos AXIS ultra DLD spectrophotometer with Al Kα radiation. The spectra were collected with analyser pass energy of 20 eV. The vacuum in the test chamber was maintained below 1×10^{-9} Torr. The binding energies scale was calibrated taking, as a reference, the adventitious C 1s peak at 284.9 eV. XPS samples, in powder form previously lyophilized, were deposited in Cu tapes.

(A3.8) Z-potential sample preparation

To measurement Z-potential of NPs diluted solution of NPs (0.1 mg/mL) and 10 mM KCl filtered with a 0.2 μm cellulose filter. Each sample was measured three times, combining 10 runs per measurement.

(A3.9) TGA and SQUID sample preparation

Liophilizated samples were weighed and measured in a SQUID MPMS-XL 5T QUANTUM DESIGN and in a TA STD 2960 in air or under nitrogen athmosphere under a heating of 10 ºC / min, respectively. Both measurements were performed in the services of University of Zaragoza.

(A3.10) ICP sample preparation

Samples were digested with concentrated HCl or aquia regia, as function of the desired element under analysis for the particles of Fe_3O_4@Au. Digested samples were diluted 100 times in MilliQ water. Samples were measurement in the service from Instituto of Cerámica y Vidrio (CSIC, Madrid) using ICP-OES in an IRIS ADVANTAGE, Termo Jarrell Ash.

(A3.11) Cellular cycle analysis

NPs toxicity in the cellular cycle was assessed using flow cytometry. 500000 cells (Vero) were seeded using a standard 6-well plate (Falcon). NPs at a final concentration of 100 μg mL^{-1} were incubated for 24 hours at 37ºC in a humidified atmosphere containing 5% CO_2. Cells were harvested, washed with PBS and left in 1 mL of cold ethanol for 24 hours at 4ºC. After extensively washing with PBS, buffer containing propidium iodide (50 μg mL^{-1}) and RNase A (100 μg mL^{-1}) were added and incubated for 30 minutes. Samples were analyzed using a BD FACSArray (BD Biosciences). The study was performed using a fluorescent dye (propidium iodide) that interacts with DNA, leading to different peaks depending on the cellular cycle phase: the first prominent peak is attributed to cells in the G0/G1 phase, while the second peak corresponds to G2/M. Between those peaks is the S phase. If the NPs deregulated the cell cycle an accumulation of cells in one or more steps will occur, increasing the corresponding peak area. Vero cell line was tested with different NNs@T&Glc concentration (50 μg mL^{-1} and 100 μg mL^{-1}) with an incubation period of 12 hours where no significant changes were observed

(A3.12) Complement activation

Complement activation experiments were performed by Western Blot analysis. Equal volumes (20 μL each) of NPs (0.2 mg mL^{-1}), human serum from healthy donors (AB+) and veronal buffer were mixed together and incubated at 37°C for 60 minutes. As positive control 50 U of Cobra Venom Factor (CVF) (Quidel Corporation) was used, and as negative control, PBS. Proteins were resolved using SDS-PAGE. Before loading the samples on the gel, sample buffer containing 5% of sodium dodecyl sulfate (SDS) and 10% of β-Mercapthoethanol was mixed with the NPs and heated for 5 minutes at 90°C. The mixture was centrifuged at 13400 rpm for 30 minutes and 3 μL of the supernatant loaded on a 10% Tris-glycine gel. After running was completed (125 V, 1 hour), proteins were transferred to a membrane (Immunoblot PVDF membrane, BioRad) for 90 minutes at 100 mA using a semi-dry transfer cell (Trans blot SD, BioRad). The membrane was extensively washed with TBS-T (20mM Tris, 500mM NaCl, and

0.1% Tween-20) prior to incubating it overnight at 4ºC with 5% of non-fat dry milk in TBS-T (blocking buffer), on a rocking platform. The membrane was then washed and incubated with the primary antibody solution, consisting in a mouse monoclonal antibody against human C3/C3b (Abcam) diluted 1:1000 in blocking buffer for 90 minutes. After another washing step, it was incubated with a goat anti-mouse IgG antibody conjugated with alkaline phosphatase (Dako), diluted 1:2000 in blocking buffer for 90 minutes. The membrane was finally incubated with a solution containing NitroblueTetrazolium (NBT) and 5-Bromo- 4-Chloro-3-Indolyl Phosphate (BCIP) (Sigma). This substrate system produces an insoluble NBT diformazan end product that is blue to purple in color and can be observed visually.

(A3.13) Laser Set-ups for NNs irradiation experiments

DPSSL 809 nm system

For the heating experiments, a 2W continuous wave (CW) 808 nm was coupled to a fiber. Samples were positioned in front of the beam (*ca.* 10 W×cm^{-2}). Temperature was monitored in real time by a thermocouple which was placed at *ca.* 0.5 cm away from the beam spot. Sample volume was 500 µL and was placed at a 500 µL quartz cuvette with 0.5 cm of path.

DPSSL 1064 nm conditions

For the heating experiments, a 3W continuous wave (CW) 1064 nm Ventus laser from Laser Quantum was coupled to a TEM$_{00}$ fiber by means of fibre coupler (PAF–X–7–C from Thorlabs). Samples were positioned in front of the beam (*ca.* 30 W×cm^{-2}). Temperature was monitored in real time by a thermocouple which was placed at *ca.* 0.5 cm away from the beam spot. Sample volume was 1000 µL and was placed in a 3 mL quartz cuvette with 1 cm of path.

PTT in vitro studies

Vero cells were cultured in µ-Dishes from Ibidi (3.5 cm^2, ibiTreat coated for optimized adhesion of most cell types), and incubated for 24 h at 37 °C, 5% CO_2 in Dulbecco´s complete media. NNs@T&Glc (0.1 mg×mL^{-1}) was added in fresh media. After 8 h of incubation, NNs were removed and cells were washed gently several times with PBS. 300 µL of PBS with Ca^{2+} and Mg^{2+} was added. At this point cell marked with Hoescht or cells that will be study with Live/dead kit must be marked appropriately see corresponding annexes. Cells were laser irradiated (DPLSS 1064 nm) for 2 minutes, with a power of 30 W/cm^2. That is placing the cell-dish at 1 cm from the laser fibre ending, which means that laser spot diameter is 0.18 cm and the laser intensity was of 1.3 W.

Single-cell laser irradiation

3T3 cells were seeded on ibidi plates (3.5 cm^2, ibiTreat coated for optimized adhesion of most cell types) and incubated (37ºC, 5%CO_2) during 12 h with NN@T&Lacto (0.3 mg/mL). Cells were observed under confocal microscopy to evaluate and study NNs internalization. Then, cells were trypsinized and transferred to Petri plates; the transfer to Petri-dishes was motivated by experimental reason since these plates are better suited for NIR-laser-coupled microscope. After 3h on the Petri plates, laser irradiation experiments were carried out

NIR laser irradiation experiments were performed using a light source (809 nm, 100 mW) coupled to an upright microscope (Axitotech, Zeiss, 40× objective) leading to a focused light spot of a few micrometers in diameter in the image plane; by changing the operation voltage of the laser, the resulting power of the focused light spot could be tuned in the range of 0-35 mW (power densities up to *ca.* 10^6 W/cm^2). This equipment allows for observation of cell changes following extremely high irradiation *in situ*;[7] this homemade equipment is placed in the facilities of the Philipps-University of Marburg (Prof. Parak).

(A3.14) Live/dead assay [8]

In order to assess the cell viability of cells without NNs, loaded with NNs, laser irradiated or non irradiated, the live/dead® viability/cytotoxicity assay (Invitrogen) was used in selected samples; this test provides a two-color fluorescence cell viability assay that is based on the simultaneous determination of live and dead cells with two probes, calcein AM and ethidium homodimer (EthD-1), that measure recognised parameters of cell viability, i.e. intracellular esterase activity and plasma membrane integrity, respectively. Cells were incubated in ibidi® treated plate for 24 h, before NNs addition in complete Dulbeccos´s media. Incubation with particles was carry on for 12 h at 37 °C, 5% CO_2. Particles were removed and cells were cleaned few times with PBS with Mg^{2+} and Ca^{2+}. Before laser irradiation cells dead/live® kit was added (250 µL per dish) with a concentration of 2.5 μM of EthD-1 and 5 μM of calcein AM in PBS wit Ca^{2+} and Mg^{2+} and cells were incubated during 30 minutes at 37 °C, 5% CO_2. After this, cells were irradiated as is indicated in the laser set-up for cell-laser-irradiation experiment appendix. Fluorescence from this kit was observed under an inverted fluorescence microscope (Nikon Eclipse T*i*).

REFERENCES

(1) Pale-Grosdemange, C.; Simon, E. S.; Prime, K. L.; Whitesides, G. M.: Formation of self-assembled monolayers by chemisorption of derivatives of oligo(ethylene glycol) of structure HS(CH2)11(OCH2CH2)mOH on gold. *Journal of the American Chemical Society* **1991**, *113*, 12-20.

(2) Sun, S. H.; Zeng, H.; Robinson, D. B.; Raoux, S.; Rice, P. M.; Wang, S. X.; Li, G. X.: Monodisperse MFe2O4 (M = Fe, Co, Mn) nanoparticles. *Journal of the American Chemical Society* **2004**, *126*, 273-279.

(3) Wang, L. Y.; Luo, J.; Fan, Q.; Suzuki, M.; Suzuki, I. S.; Engelhard, M. H.; Lin, Y. H.; Kim, N.; Wang, J. Q.; Zhong, C. J.: Monodispersed core-shell Fe3O4@Au nanoparticles. *Journal of Physical Chemistry B* **2005**, *109*, 21593-21601.

(4) Smith, C. A. M.; de la Fuente, J.; Pelaz, B.; Furlani, E. P.; Mullin, M.; Berry, C. C.: The effect of static magnetic fields and tat peptides on cellular and nuclear uptake of magnetic nanoparticles. *Biomaterials* **2010**, *31*, 4392-4400.

(5) Coomassie (Bradford) Protein Assay Kit.

(6) Hoechst 33342 Fluorescent Stain

(7) Munoz Javier, A.; del Pino, P.; Bedard, M. F.; Ho, D.; Skirtach, A. G.; Sukhorukov, G. B.; Plank, C.; Parak, W. J.: Photoactivated Release of Cargo from the Cavity of Polyelectrolyte Capsules to the Cytosol of Cells. *Langmuir* **2008**, *24*, 12517-12520.

(8) LIVE/DEAD® Viability/Cytotoxicity Kit *for mammalian cells.

List of Abbreviations

acac	Acetylacetonate
AgNPs	Silver NPs
AMF	Alternating Magnetic Field
B_0	Magnetic Field
C_{abs}	Absorption Cross-Section area per NP
CM	Mixed Chains
CM-Celob	Cellobiose modified Mixed Chain
CM-Celob (NP)	Iron oxide@gold NP CM-Celob coated
CM-CO_2H	Carboxylic Mixed Chain
CM-CO_2H (NP)	Iron oxide@gold NP CM-CO_2H coated
CM-Galacto	Galactose modified Mixed Chain
CM-Galacto (NP)	Iron oxide@gold NP CM-Galacto coated
CM-Glc	Glucose modified Mixed Chain
CM-Glc (NP)	Iron oxide@gold NP CM-Glc coated
CM-Lacto	Lactose modified Mixed Chain
CM-Lacto (NP)	Iron oxide@gold NP CM-Lacto coated
CM-OH	Hidroxylated Mixed Chain
CM-OH (NP)	Iron oxide@gold NP CM-OH coated
CPP	Cell Penetratin Peptide
CR	silica@gold NP
CT	Computed Tomography
CTAB	Cetyl Trimethyl Ammonium Bromide
DMEM	Dulbecco's Modified Eagle Medium
DMSO	Dimethyl sulfoxide
DPSSL	Diode-pump solid-state laser
EDC	1-Ethyl-3-[3-dimethylaminopropyl] carbodi-imide hydrochloride
EELS	Electron Energy Loss Spectroscopy
EGRF	Epidermal Growth Factor Receptor
ELISA	Enzyme-Linked ImmunoSorbent Assay
EMF	External Magnetic Field
EPR effect	Enhanced Permeability and retention Effect
EthD-1	Ethidium Homodimer
f	frequency
FC	Field Cooled
FDA	Food and Drug Administration
Fe_3O_4	Magnetite
Fe_3O_4@Au NPs	Iron oxide@Gold Nanoparticles
FM	Ferrimagnetic Particles
GNPs	Gold Nanoparticles
GNRs	Gold Nanorods
GNSs	Gold Nanoshells
GOx	Glucose Oxidase
Hb	Hemoglobin
HbO_2	Oxyhemoglobin
H_C	Coercive Field
HG	Gold Hollow Shell

HR	High resolution
HRP	HorseRadish Peroxidase
HR-TEM	High Resolution Transmission Electron Microscopy
I	Power density
ICP	Inducted Coupled Plasmon
K_a	Magnetic Anisotropic Constant
LPEI	Linear Poly ethylenimine
LSPR	Localized Surface Plasmon Resonance
m	Mass of material
MD	Multi-domain
MFH	Magnetic Fluid Hyperthermia
MGNPs	Magnetic Gold NPs
MNPs	Magnetic Nanoparticles
M_R	Remanent Magnetization
MRI	Magnetic Resonance Imaging
M_S	Saturation Magnetization
MTT	3-(4,5-dimethylthiazol-2-yl)-2,5-diphenyltetrazolium
MUA	11-mercaptoundecanoic
MUA (NP)	Iron oxide@gold NP MUA coated
NHS	N-hydroxysuccinimide
NIR	Near-Infrarred
NNs	NanoNachos (Triangular Nanoprisms)
NNs@GOx	PEGylated NNs GOx modified
NNs@HRP	PEGylated NNs HRP modified
NNs@PEG	PEG coated NNs
NNs@T	PEGylated NNs TAMRA modified
NNs@T&Glc	PEGylated NNs TAMRA and Glucose modified
NNs@T&Lacto	PEGylated NNs TAMRA and Lactose modified
NNs@T&tat	PEGylated NNs TAMRA and tat modified
NNs^{1050}	PEGylated NNs ($\lambda_{maximum, absorption}$)= 1050)
NNs^{850}	PEGylated NNs ($\lambda_{maximum, absorption}$)= 850)
NPs	Nanoparticles
NR	Nanorod
O.D.	Optical Density
OA	Oleic Acid
OCT	Optical Coherence Tomography
PA	Photoacoustic
PBS	Phosphate Buffered Saline
PEG	Poly(ethylen)glycol
PEG (NP)	Iron oxide@gold NP PEG coated
PET	Positron Electron Tomography
PLGAs	Poly(lactic-*co*-glycolic) acid
P_{MF}	Heat produced per unit of volume
Pot Z	Zeta-Potential
PT	Photothermal
PTT	Photothermal Therapy
PVA	Poly (vinyl alcohol)
PVP	Poly(vinyl)alcohol
Q_{nano}	Heat Generated By Each Nanoparticle

$\mathbf{r_2}$	Relaxativity time
RES	Reticuloendothelial System
RF	Radiofrequency
$\mathbf{r_{SP}}$	Superparamagnetic radius
SAR	Specific Absorption Rate
SDS	Sodium Dodecylsulfate
SEM	Scanning Electron Microscopy
SERS	Surface Enhaced Resonance Spectroscopy
SP	Gold Sphere
SPECT	Single Photon Emission Computed Tomography
SPM-NPs	Superparamagnetic Nanoparticles
SPR	Surface Plasmon Resonance
SQUID	Superconducting Quantum Interference Device
STEM	Scannin Transmission Electron Microsopy
STEM-HAADF	Scanning Transmission Electron Microscopy-High-Angle Annular Dark Field
TAMRA	Tetramethylrhodamine - 5 - carboxamide cadaverine
tat	purified HIV transactivator of transcription
tat-MGNPs	Iron oxide@gold NP CM-CO_2H coated tat attached
TD	Time Domain
TEM	Transmission Electron Microscopy
TGA	thermogravimetric analysis
TPL	Two-Photon Luminiscence
VSM	Vibrating Sample Magnetometer
XPS	X-ray photoelectron spectroscopy
ZFC	Zero Field Cooled
α-TNF	Transcription Necrosis Factor
γ-$\mathbf{Fe_2O_3}$	Maghemite
$\Delta\mathbf{E}$	Anisotropic energy barrier
$\Delta\mathbf{T_{av}}$	Average Temperature
μ_0	Magnetic permeability in vacuum
μ_a	Absorption of light of a group of NPs under laser irradiation

•

Resumen & Conclusiones

Desde el descubrimiento de las particulares propiedades que poseen los materiales a escala nanométrica, y el desarrollo de nuevas técnicas para analizarlas, su utilización se ha implementado en todo tipo de áreas como química, óptica, energía, y por supuesto, biología. Para su uso en bioaplicaciones, la mayor ventaja que presentan estos materiales es su tamaño, ya que se encuentra en la misma escala que proteínas, enzimas, anticuerpos, ADN, virus, etc. Esta correspondencia en tamaño permite evaluar interacciones entre nanomateriales y moléculas activas lo que ha permitido adentrarse en el conocimiento de los mecanismos celulares con más detalle, así como el desarrollo de nuevas terapias y procedimientos de diagnóstico. Dentro de estos materiales destacan por su biocompatibilidad los óxidos de hierro, y el oro, material noble por excelencia.

El trabajo aquí expuesto está centrado en la utilización y desarrollo de nanomateriales para su uso en nanomedicina. Para ello, se han utilizado dos tipos de nanopartículas. El trabajo está dividido en dos secciones según el tipo de nanopartícula utilizada. En la primera sección se utilizará una estructura núcleo-corteza de óxido de hierro-oro, mientras que en la segunda se utilizarán nanoprismas triangulares aquí denominados como NanoNachos (NNs).

El trabajo presentado en la primera sección utilizando las estructuras núcleo-corteza está centrado en la síntesis por descomposición térmica en fase orgánica. Las partículas resultantes presentan un núcleo de Fe_3O_4 de 4 nm y una corteza de oro de 3 nm aproximadamente. La optimización de la estabilidad de estos sistemas en medio acuoso se llevó a cabo a través de una transferencia de fase mediante el uso de ligandos anfifílicos sintetizados en nuestro laboratorio como parte del trabajo. Estas cadenas les proporcionarán la estabilidad suficiente para poder liofilizarlas, centrifugarlas y realizar reacciones químicas sobre su superficie para unir moléculas con una funcionalidad determinada, como marcadores, carbohidratos, enzimas, etc. Se caracterizaron las propiedades físico-químicas de estas partículas una vez en fase acuosa. Además se realizaron estudios para evidenciar la estructura núcleo@corteza, aunque no fue posible determinarlo con una certeza del 100%. No obstante, las partículas muestran las propiedades ópticas del oro, así como un contraste uniforme de apariencia áurea bajo la observación de las partículas con STEM, y propiedades superparamgnéticas equivalentes a las que muestran núcleos de magnetita de tamaño similar al utilizado como núcleo.

Mediante el ensayo colorimétrico del MTT se evaluó la toxicidad sobre células HeLa de estas NPs con diferentes azúcares en su superficie, así como sin ellos, no encontrando toxicidad en ninguna de ellas. Además, se evaluó el potencial de estas partículas como vectores y como agentes para terapia de hipertermia magnética. Su uso como vectores se realizó utilizando partículas a las que se les unió un péptido de internalización (tat) que promueve la entrada de las nanopartículas al interior celular. Se estudió la vía de internalización de estas NPs cuando eran expuestas o no a un campo magnético externo. En ambos casos se encontró que la vía de entrada era mediada por caveolina, que es una proteína involucrada en algunos procesos de endocitosis, mostrando despreciable el efecto del campo magnético. No obstante, un anormal alineamiento de las fibras celulares como respuesta al campo magnético fue observado.

Las partículas modificadas con azúcares se evaluaron como posibles agentes para terapias de hipertermia magnética, que es una terapia basada en la generación de calor tras la aplicación de un campo magnético alterno sobre materiales superparamagnéticos. A día de hoy el uso de nanopartículas de óxido de hierro está muy extendido para este tipo de terapia. Por ejemplo el grupo de Jordan utiliza este tipo de materiales par terapias en humanos. No obstante, debido a que presentan un valor de SAR por debajo de los materiales comerciales relacionado con el pequeño tamaño de su núcleo magnético se descartó su uso para este tipo de aplicaciones.

En la segunda sección aparece compilado el trabajo relativo a la búsqueda y desarrollo de un nuevo proceso sintético de prismas triangulares de oro, aquí denominados NanoNachos (NNs). Estos NNs poseen la particularidad de absorber luz en el infrarrojo cercano (NIR), región en la cual se encuentra la denominada ventana biológica donde la penetración de radiación es máxima debido a la mínima absorción de los componentes biológicos en esa región. Este tipo de sistemas que absorben radiación poseen la capacidad de liberar la energía absorbida en forma de luz produciendo calor, lo que genera otro tipo de terapia térmica conocida como hipertermia óptica (PTT). El proceso de síntesis es una forma sencilla, directa y evitando el uso de surfactantes citotóxicos como el CTAB típicamente utilizados para generar este tipo de estructuras, que además generan posterioes problemas para su funcionalización. Además, se optimizó la síntesis para modular la absorción de la banda del infrarrojo cercano, esto se consigue mediante el control y variación del radio molar entre la sal de oro y el tiosulfato, que actúa como reductor. El método de síntesis surge como una variación del método descrito por Zhou y colaboradores para la obtención de estructuras núcleo-corteza Au-As_2S. El estudio de los productos de reacción y su composición fue realizado mediante el uso de XPS que confirmó la oxidación del tiosulfato a sulfato, así como que los NNs están compuestos de oro descartando de esta manera la posibilidad de que se estructuras como las descritas por Zhou fueran las responsables de la banda NIR de absorción.

Estos NNs fueron estabilizados mediante cadenas heterofuncionales tiol/carboxilo de polietilenglicol (PEG) que dejan abierta la posibilidad de futuras modificaciones químicas en su superficie, así como permite que las partículas sean estables incluso centrifugando a 13000 rpm. Las partículas PEGyladas (NNs@PEG) se separaron de otros subproductos de la reacción mediante electroforesis-gel. La estructura de estas partículas se estudió mediante microscopía electrónica (SEM, TEM, STEM e EELS). Los resultados muestran de manera concluyente que las partículas presentan una estructura plana de unos 9 nm de ancho. La estructura cristalina de los NNs se estudió mediante HRTEM, encontrando una orientación *fcc* del Au, además se pudieron indexar puntos que indican la presencia de planos de simetría y defectos de empaquetamiento que son los que van a determinar la estructura plana final de las partículas.

El potencial de estas partículas como "nanoesufas" o como generadores de calor se midió mediante la irradiación de soluciones de NNs@PEG con diferentes máximos de absorción NIR utilizando dos fuentes laser de diferentes longitudes de onda, 809 nm y 1064 nm. Los resultados demuestran la gran capacidad de estas partículas para generar calor incluso a concentraciones bajas. Los resultados muestran incrementos de temperatura de hasta 50 °C en tan sólo 2 minutos en las cercanías del punto de irradiación del láser, lo que es comparable a los mejores resultados presentados en literatura hasta el momento. Ese gran potencial abre un abanico de posibilidades de aplicación de estas partículas para terapias de hipertermia local o para provocar la liberación de fármacos, potencial que viene apoyado por el hecho de no necesitar CTAB para su síntesis, lo que evita muchos procesos de intercambio para eliminar la presencia de este surfactante altamente tóxico.

Como prueba de concepto para evaluar la capacidad de generar calor de manera local de los NNs se les unió una enzima (GOx). La actividad de este enzima unido a la superficie de los NNs se midió después de diferentes tratamientos térmicos, así como después de su irradiación con un láser NIR. Mientras que la actividad de la enzima sobre las partículas permanece estable incluso hasta cuando es calentada a 55 °C durante media hora, la actividad de la enzima unida a las partículas irradiadas con el láser desciende hasta un 40%. Este resultado indicaría que el calor generado en las cercanías de las partículas puede dañar de manera irreversible la actividad de la GOx. Aunque, considerando la intensidad del láser utilizada en el experimento, y los cálculos teóricos para este tipo de sistemas, no es posible confirmar si el responsable de la pérdida de actividad es el calor generado por un solo NN o por un efecto colectivo de varas partículas próximas e irradiadas simultáneamente.

Para determinar la viabilidad celular i*n vitro* de los NNs se realizaron el ensayo del MTT, del ciclo celular y de la activación del complemento. Adicionalmente se estudiaron posibles cambios en la morfología celular mediante microscopía de barrido. En ningún caso se observó efecto citotóxico, alteraciones del metabolismo o cambio de la morfología celular.

Se llevaron a cabo experimentos de internalización celular, para ello se utilizaron NNs diferentemente modificados, con un fluoróforo (TAMRA, NNs@T), con lactosa y fluoróforo (NNs@T&Lacto), o con un péptido de internalización (tat) y el mismo fluoróforo (NNs@T&tat). Se determinó que bajo las mismas condiciones el orden de internalización de máximo a mínimo era: NNs@T&tat > NNs@T&Lacto> NNs@T. Estas diferencias estarán últimamente determinadas por la presencia de los diferentes ligandos en la superficie de las partículas que tienen dos posibles efectos, (i) dirigir una internalización mediada por receptores, y/o (ii) producir un cambio en la carga de los NNs.

Por último, se estudió el efecto de la irradiación de las partículas con un láser *in vitro*. Primeramente se hizo analizando los efectos de la irradiación con un láser de 1064 nm sobre un continuo de células VERO cargadas con NNs@T&Glc. Los efectos del láser en este caso se estudiaron a nivel de viabilidad celular. Además se estudiaron cambios en la morfología celular mediante microscopía de barrido e inmunomarcaje del citoesqueleto. Los resultados muestran diferentes grados de daño relacionados directamente con la distancia del centro del área irradiada por el láser, aproximadamente 1 mm, lo que coincide con el perfil de potencia del láser. Experimentos a nivel de una única célula se realizaron con un sistema diferente, utilizando un láser de 809 nm y células 3T3 cargadas con NNs@T&Lacto. Los resultados preliminares mostraron el potencial de modular la liberación de fármacos de manera remota del interior de compartimentos celulares mediante el uso de NNs modificados con drogas.

List of Publications

Parts of this PhD dissertation were published or are in the process of preparation for submission; these are listed in the following:

Smith, C. A. M.; de la Fuente, J.; Pelaz, B.; Furlani, E. P.; Mullin, M.; Berry, C. C.: The effect of static magnetic fields and tat peptides on cellular and nuclear uptake of magnetic nanoparticles. *Biomaterials* **2010**, *31*, 4392-4400.

Moros, M.; Pelaz, B.; Lopez-Larrubia, P.; Garcia-Martin, M. L.; Grazu, V.; de la Fuente, J. M.: Engineering biofunctional magnetic nanoparticles for biotechnological applications. *Nanoscale* **2010**, *2*, 1746-1755.

Franca, A.; Pelaz, B.; Moros, M.; Sanchez-Espinel, C.; Hernandez, A.; Fernandez-Lopez, C.; Grazu, V.; de la Fuente, J. M.; Pastoriza-Santos, I.; Liz-Marzan, L. M.; Gonzalez-Fernandez, A.: Sterilization Matters: Consequences of Different Sterilization Techniques on Gold Nanoparticles. *Small* **2010**, *6*, 89-95.

Pelaz, B.; Grazu, V.; Ibarra, A; Magen, C.; del Pino, P.; de La Fuente, J. M.: Tailoring the Synthesis and Heating Ability of Gold Nanoprisms for Bioapplications. *Langmuir* **2012**, *just accepted manuscript.*

Pelaz, B. & del Pino, P.: Hyperthermia using Inorganic Nanoparticles. Chapter in the Elservier book: "Nanobiotechnology: Inorganic Nanoparticles *vs.* Organic Nanoparticles"; *submitted.*

Pelaz, B.; del Pino, P.: Bioapplications of Gold Nanoparticles; chapter in the Elservier book: "Nanobiotechnology: Inorganic Nanoparticles *vs.* Organic Nanoparticles"*; submitted.*

Rivera_Gil, P.; Jiménez de Aberasturi, D.; Wulf, V.; Pelaz, B.; del Pino, P.; Zhao, Y.; de la Fuente J.M.; Ruiz de Larramendi, I.; Rojo, T.; Liang, X-L.; Parak W.J.: The challenge to relate physico-chemical properties of colloidal nanoparticles to their cytotoxicity. *Accounts of Chemical Research; submitted.*

Salado J., Insausti M., Lezama L., Gil de Muro I., Moros M., Pelaz B., Grazú V., de La Fuente J.M., Rojo T.: Functionalized $Fe3O4@Au$ superparamagnetuc nanoparticles: in vitro bioactivity; *submitted.*

Pelaz, B. & del Pino, P.; de La Fuente, J. M.: Effects of NIR-laser Irradiation on Epithelial Cells Challenged with Gold Functional Nanoprisms; *in preparation.*

Tian, F.; Clift, M.J.D.; del Pino, P.; Pelaz, B.; Rothen-Rutishauser, B.; Estrada, G.; de la Fuente, J.M.; Stoeger, T.: Biocompatibility of three different shapes of gold nanoparticles on lung epithelial cells; *in preparation.*